

BROADBAND OPTICAL SOURCES BASED ON HIGHLY  
NONLINEAR QUASI-PHASEMATCHED INTERACTIONS

A DISSERTATION  
SUBMITTED TO THE DEPARTMENT OF ELECTRICAL  
ENGINEERING  
AND THE COMMITTEE ON GRADUATE STUDIES  
OF STANFORD UNIVERSITY  
IN PARTIAL FULFILLMENT OF THE REQUIREMENTS  
FOR THE DEGREE OF  
DOCTOR OF PHILOSOPHY

Christopher Richard Phillips

June 2012

© 2012 by Christopher Richard Phillips. All Rights Reserved.  
Re-distributed by Stanford University under license with the author.

This dissertation is online at: <http://purl.stanford.edu/gb541vv6573>

I certify that I have read this dissertation and that, in my opinion, it is fully adequate in scope and quality as a dissertation for the degree of Doctor of Philosophy.

**Martin Fejer, Primary Adviser**

I certify that I have read this dissertation and that, in my opinion, it is fully adequate in scope and quality as a dissertation for the degree of Doctor of Philosophy.

**James Harris**

I certify that I have read this dissertation and that, in my opinion, it is fully adequate in scope and quality as a dissertation for the degree of Doctor of Philosophy.

**Jelena Vuckovic**

Approved for the Stanford University Committee on Graduate Studies.

**Patricia J. Gumport, Vice Provost Graduate Education**

*This signature page was generated electronically upon submission of this dissertation in electronic format. An original signed hard copy of the signature page is on file in University Archives.*

# Abstract

Quasi-phasematching (QPM) is a powerful and versatile technique for manipulating coherent radiation. With current QPM media, we can perform a number of functionalities, including generating, amplifying, or spectrally broadening light across a wide range of frequencies. An advantage of QPM is that it allows us to engineer very strong nonlinear interactions with available commercial lasers. However, devices involving such strong nonlinearities can exhibit a number of subtle effects, necessitating careful numerical and theoretical modeling. In this dissertation, we consider a number of different applications of QPM, all of which share this common theme.

First, we consider supercontinuum (SC) generation in quasi-phasematching waveguides. SC generation was first demonstrated in this context in a bulk QPM crystal [1], and subsequently in a reverse-proton-exchanged (RPE) LiNbO<sub>3</sub> waveguide with commercial Er: and Yb: femtosecond lasers [2]. SC generation in QPM waveguides has several advantageous properties including relatively low energy requirements (compared to those required in bulk), automatic carrier envelope offset frequency ( $f_{\text{CEO}}$ ) detection, and the potential to engineer the QPM grating profile to produce a tailored output spectrum. We first study SC generation numerically, showing good agreement between simulations and existing experimental results. The two key ingredients to this study were the development of a general numerical model, and a careful calibration of both the second- and third-order nonlinear susceptibilities as well as inclusion of multiple waveguide modes and QPM orders. This calibration indicated a strong competition between  $\chi^{(2)}$  and  $\chi^{(3)}$  effects, significantly greater than had previously been assumed in LiNbO<sub>3</sub>. We showed that this competition led to an order-of-magnitude increase in energy requirements and in some cases degraded

coherence properties.

We performed SC generation experiments in QPM RPE waveguides using a Tm-doped fiber laser system. These experiments yielded a multiple-octave-spanning spectrum, and facilitated self-referencing of the laser directly from the waveguide with just a spectral filter and a silicon avalanche photodiode. We modeled the experiments numerically, showing good agreement between simulated and measured spectra. The several-nJ pulse energies required are well within reach of commercial Tm-doped fiber lasers. Next, in order to resolve the  $\chi^{(2)} - \chi^{(3)}$  competition and several other limitations of RPE waveguides, we studied dispersion-engineered LiNbO<sub>3</sub> ridge waveguides for the purpose of obtaining group velocity matching between the first and second harmonic pulses. We showed numerically that when properly designed, these ridge waveguides can facilitate SC generation with pump energies of around 50 pJ, as much as 50 times lower than in RPE waveguides. These results point the way towards compact, integrated, and versatile  $f_{\text{CEO}}$  detection and frequency comb generation in the near- and mid-infrared (IR) spectral regions.

There is significant interest in generating tunable, high-spectral-density frequency combs in the mid-IR for spectroscopic applications. To accomplish this goal, we demonstrated tunable mid-IR generation based on difference frequency generation (DFG) in orientation patterned gallium arsenide (OP-GaAs). The OP-GaAs sample had a fan-out QPM design, facilitating smooth tuning across the mid-IR from 6.7-12.7  $\mu\text{m}$ . The DFG system was based on a Tm-doped fiber laser producing 150-fs pulses at 1.95- $\mu\text{m}$ , and utilized the Raman soliton self frequency shift in a fluoride fiber to obtain a power-tunable 2.5- $\mu\text{m}$  seed for the DFG process. Average powers of up to 1.3 mW were obtained. We investigated the limitations of this approach theoretically and numerically, and showed that with realistic upgrades to the pump laser, high-gain optical parametric amplification (OPA) and high overall conversion efficiency can be obtained. This would allow for the generation of powers exceeding of as much as 100 mW, with a power spectral density sufficient for spectroscopic applications.

The last topic discussed in this dissertation is optical parametric chirped pulse amplification (OPCPA). There is significant interest in generating high-intensity, few-cycle pulses in the mid-IR for high-harmonic generation. However, there are few laser

systems with the required properties beyond  $3\ \mu\text{m}$ , which motivates the use of existing near-IR laser sources and nonlinear optics to generate and amplify light in this spectral region. Due to dispersion, amplification of few-cycle pulses is challenging unless one of several approaches is taken in order to facilitate broadband gain. Our approach is to utilize chirped (aperiodic) QPM gratings, in which the grating  $k$ -vector is varied monotonically through the length of the device. With these devices, the grating bandwidth can exceed the phasematching bandwidth of the input pulses, thereby allowing for ultra-broadband amplification.

We first study the properties of this type of OPA device, showing a number of interesting physical properties including adiabatic following solutions to the nonlinear three-wave mixing equations. We then give an overview of our OPCPA experimental results, demonstrating  $7\text{-}\mu\text{J}$ ,  $75\text{-fs}$  pulses centered at  $3.4\ \mu\text{m}$ , with a repetition rate of  $100\ \text{kHz}$ . With chirped QPM OPA devices, high-gain, broad-bandwidth amplification, and tailored spectral gain and phase profiles can be achieved. Furthermore, these devices enable a number of system-level improvements. For example, we are able to achieve highly efficient pulse compression by simply sending the amplified mid-IR pulses through low-loss, anti-reflection-coated bulk silicon. Any spectral phase not corrected by the silicon can be compensated by pre-distorting the  $1.56\text{-}\mu\text{m}$  seed laser with a pulse shaper. This approach is possible because the seed phase is parametrically transferred to the mid-IR pulses by the collinear pre-amplifier. Finally, we discuss in detail the design opportunities and constraints which arise when deploying chirped QPM gratings in OPCPA systems. The main system constraints are on the duration and peak power of the pump pulses. We show that recent upgrades to the pump laser allowed these constraints to be met. The compressed idler pulses were able to ionize xenon, indicating the system is now adequate for use in high-field experiments.

# Acknowledgements

The work in this dissertation would not have been possible without the support of many people.

First and foremost, I want to thank my research advisor, Professor Martin Fejer. It is primarily due to the breadth and depth of Marty's scientific understanding, and his incredible ability to convey that understanding to others, that I have been able to find success in research. Marty has given me the freedom to pursue many projects, and it is with the help of his guidance, ideas, and insightful appraisal of any new results that I have been able to converge on sensible solutions to experimental and theoretical problems.

I thank Professors James Harris and Jelena Vuckovic for reading this dissertation and giving me kind comments, and for being on my orals committee. I also thank Steve Harris for chairing my orals committee, and for his nonlinear optics class. The quality of Steve's teaching helped convince me to stick with nonlinear optics.

I am extremely grateful for our collaboration with Clemens Heese, Lukas Gallmann, and Professor Ursula Keller at ETH Zurich. The optical parametric chirped pulse amplification experiments described in this dissertation were performed at ETH, and were made possible by their experimental expertise and incredible efforts over many years. I've found my trips there very valuable, and have always been amazed when visiting Prof. Keller's group.

I am also extremely grateful for our collaboration with Jie Jiang, Ingmar Hartl, and Martin Fermann at IMRA America. We performed the supercontinuum generation and difference frequency generation experiments described in this dissertation at IMRA during my several visits. Their proficiency with fiber lasers and efficient

experimental work made my visits both enjoyable and highly productive.

I have worked with many talented people in the Byer-Fejer group over the years. Jason Pelc and I joined Marty's group within about a week of each other, and we ended up defending on adjacent days. The main themes of our research have often been very different: he works with single photons, while my work has usually required rather a lot of photons. Yet despite this contrast, getting our devices to work has relied in large part on understanding a similar set of nonlinear-optical effects. Working with Jason over the years has been a great experience.

Several projects I have worked on have involved using lithium niobate in ways which, in hindsight, were somewhat foolish. Yet discovering why has been very valuable, and it is thanks to Judith Schwesyg's insight and careful measurements that we figured out a number of important issues related to photorefraction and absorption.

The existence of reverse proton exchanged waveguides has been critical for all of our supercontinuum generation work, and for other collaborations and on-going projects that I've been involved with. It's thanks to Carsten Langrock's fabrication expertise that I've been able to work with these devices.

I greatly enjoyed many discussions on nonlinear optics with Joe Schaar. One of the things that I realized soon after starting work on nonlinear optics was the crucial role that general simulation tools would play during my time here. Discussions with Joe up to and around the time he graduated were invaluable in figuring out which effects to think about, and how to go about modeling them.

More recently, I've worked with Yu-Wei Lin, to whom I'm passing the torch on a number of projects. It is very comforting to know that one's research efforts will be left in capable hands. And I've very much enjoyed collaborating with Angie Lin on orientation-patterned GaAs, and on our recent work on some GaAs waveguide devices. Over the past several months I've also collaborated with Alireza Marandi and Stephen Wolf on modeling degenerate femtosecond optical parametric oscillators, and have appreciated the quick progress we've made thanks to their efforts. I would also like to thank all of the other members of the Byer-Fejer community, for creating such a friendly and effective environment for research.

Thanks to Tim Brand and Ryan Macdonald from the Ginzton crystal shop for

their successful efforts at polishing monolithic OPO samples. And thanks to Dieter Jundt and Djordje Djukic at Crystal Technology for fabricating the MgO:LiNbO<sub>3</sub> samples which made our OPCPA experiments possible.

Vivian Drew, our group administrator, and Amy Duncan, the EE degree progress officer, also deserve thanks. Planning the final stages of one's Ph.D can be tough, and so I have appreciated Amy's kind and helpful attitude in recent months.

Finally, I would like to thank my family and friends. It would seem strange to me to try and convey the extent of my appreciate here, so instead I will be brief, and simply say that everyone's support over the years is something for which I am truly grateful.

# Contents

<b>Abstract</b>	<b>iv</b>
<b>Acknowledgements</b>	<b>vii</b>
<b>1 Introduction</b>	<b>1</b>
1.1 Maxwell's Equations . . . . .	2
1.2 Nonlinear Mixing with Paraxial Diffraction . . . . .	6
1.3 Nonlinear Mixing Involving Waveguide Modes . . . . .	8
1.4 Quasi-Phasematching . . . . .	11
1.5 Plane-Wave Processes in QPM Gratings . . . . .	15
1.5.1 Second Harmonic Generation . . . . .	16
1.5.2 Three Wave Mixing . . . . .	18
1.5.3 Cascaded Phase Shifts . . . . .	19
1.6 Overview of this Dissertation . . . . .	21
<b>2 Modeling of Supercontinuum Generation</b>	<b>22</b>
2.1 Introduction . . . . .	22
2.2 Numerical Model . . . . .	24
2.3 Comparison to 1043-nm-Pumped Experiments . . . . .	30
2.4 Model Calibrations for 1043-nm-Pumped Experiments . . . . .	36
2.5 Comparison to 1580-nm-Pumped Experiments . . . . .	41
2.6 Discussion . . . . .	46
2.7 Appendix: Material Properties . . . . .	49
2.8 Appendix: Cascading Approximation for QPM Waveguides . . . . .	55

<b>3</b>	<b>QPM SC Generation with a Tm-Fiber Laser</b>	<b>60</b>
<b>4</b>	<b>GVD-Engineered QPM SC Generation</b>	<b>67</b>
<b>5</b>	<b>Multiple Nonlinear Envelope Model</b>	<b>75</b>
5.1	Introduction . . . . .	75
5.2	Generalized Coupled Wave Equations . . . . .	76
5.2.1	Propagation of Waveguide Modes . . . . .	77
5.2.2	Expansion in Harmonic Orders . . . . .	80
5.2.3	Assignment of Nonlinear Driving Terms . . . . .	82
5.2.4	Propagation of Harmonic Envelopes . . . . .	84
5.3	Model Simplifications . . . . .	88
5.3.1	Isolating Important Terms in $P_{NL}$ . . . . .	88
5.3.2	Highly Phase Mismatched Terms . . . . .	90
5.3.3	Highly Group-Velocity Mismatched Terms . . . . .	91
5.4	Numerical Example . . . . .	92
5.4.1	Minimal SHG Model . . . . .	94
5.4.2	Third and Fourth Harmonic Generation . . . . .	94
5.4.3	Intrapulse DFG Effects . . . . .	95
5.4.4	Envelopes $a_{n,N}$ with $N < 0$ . . . . .	97
5.4.5	Comparison with Single-Envelope Model . . . . .	97
5.5	Motivating Factors for a GCW Model . . . . .	99
5.5.1	Carrier Offset Frequency . . . . .	101
5.5.2	GCW Model for Optical Design . . . . .	101
5.5.3	Numerical Tractability . . . . .	102
5.5.4	Accuracy of the Nonlinear Coefficients . . . . .	103
5.6	Conclusions . . . . .	104
5.7	Appendix: Energy Conservation in the GCWE Model . . . . .	107
5.8	Appendix: Choice of Effective Susceptibilities . . . . .	111
<b>6</b>	<b>OPA in Orientation-Patterned GaAs</b>	<b>117</b>
6.1	Introduction . . . . .	117

6.2	Experiment . . . . .	118
6.3	Modeling . . . . .	122
6.4	Design . . . . .	124
6.4.1	Exponential Growth . . . . .	125
6.4.2	Interactions Involving Pulsed Beams . . . . .	126
6.5	Design Example . . . . .	132
6.6	Summary of This Chapter . . . . .	134
<b>7</b>	<b>Theory of OPA with Chirped QPM Gratings</b>	<b>135</b>
7.1	Introduction . . . . .	135
7.2	Coupled Wave Equations . . . . .	139
7.3	Signal Amplification . . . . .	146
7.4	Adiabatic Following Solutions . . . . .	147
7.5	Adiabaticity Constraint . . . . .	154
7.6	Efficiency and Phase . . . . .	158
7.7	Summary of This Chapter . . . . .	163
7.8	Appendix: Linearization and Adiabaticity of Reduced Equations . . .	164
7.8.1	Linearization . . . . .	165
7.8.2	Analogy to Quantum Systems . . . . .	167
<b>8</b>	<b>OPCPA with Chirped QPM Gratings</b>	<b>171</b>
8.1	OPCPA Using Chirped QPM Gratings . . . . .	172
8.2	Experimental System . . . . .	175
8.3	Design in the Limit of Non-Diffracting Beams and Highly Chirped Signal Pulses . . . . .	179
8.3.1	Pump Intensity and QPM Chirp Rate . . . . .	179
8.3.2	Nonlinear Chirp Profile . . . . .	183
8.3.3	Apodization . . . . .	191
8.4	Coincidentally-Phasematched Processes . . . . .	197
8.4.1	Phasematching . . . . .	197
8.4.2	Numerical Example . . . . .	200
8.5	Statistical Phasematching . . . . .	203

8.6	Noncollinear Processes . . . . .	209
8.6.1	Noncollinear Phasematching . . . . .	210
8.6.2	Noncollinear Gain: Outline . . . . .	211
8.6.3	Noncollinear Gain: Uniform Medium . . . . .	212
8.6.4	Noncollinear Gain: Linearly Chirped Medium . . . . .	213
8.6.5	System Implications . . . . .	217
8.7	Collinear Focusing . . . . .	220
8.7.1	Effective Lensing . . . . .	221
8.7.2	Example: Positive Chirp Rate, Undepleted-pump . . . . .	224
8.7.3	Example: Negative Chirp Rate, High Pump Depletion . . . . .	226
8.7.4	Spatiotemporal Coupling: Concept . . . . .	228
8.7.5	Spatiotemporal Coupling Example . . . . .	229
8.7.6	Summary of This Section . . . . .	235
8.8	Summary of Design Constraints . . . . .	235
8.9	Conclusions . . . . .	242
<b>9</b>	<b>Conclusions</b>	<b>244</b>
9.1	Summary of this dissertation . . . . .	244
9.2	Other contributions . . . . .	247
9.3	Future work . . . . .	249
	<b>Bibliography</b>	<b>251</b>

# List of Tables

2.1	Lorentzian Fit Parameters for $H_R(\Omega)$ . . . . .	49
2.2	Cascading Approximation Parameters at 1043 nm . . . . .	58
2.3	Cascading Approximation Parameters at 1580 nm . . . . .	58
8.1	OPCPA System Parameters . . . . .	177
8.2	Overview of Spatiotemporal Effects in Chirped QPM OPCPAs . . . . .	236
8.3	OPCPA Design Constraints and Parameters . . . . .	237

# List of Figures

1.1	Quasi-Phasematching . . . . .	13
2.1	Comparison Between Measured and Simulated Output Spectra (1043-nm-Pumped Experiments) . . . . .	32
2.2	Evolution of the 1043-nm Pulses in the Time Domain . . . . .	33
2.3	Spectrum Versus Position in the QPM Grating . . . . .	35
2.4	Spectrum for Several Values of $\chi_E$ , with $\chi_{R,pk} = 0$ . . . . .	39
2.5	Spectrum for Several Values of $\chi_{R,pk}$ with Fixed $\chi_E + H_R(0)\chi_{R,pk}$ . . . . .	40
2.6	Comparison Between Measured and Simulated Spectra (1580-nm-Pumped Experiments) . . . . .	42
2.7	LiNbO <sub>3</sub> Raman Transfer Function . . . . .	50
3.1	Setup of a Self-Referenced Tm-Doped Fiber and PPLN Waveguide System . . . . .	61
3.2	Amplified Pulse Characterization . . . . .	62
3.3	Power Spectral Density of the PPLN-Waveguide Supercontinuum . . . . .	65
3.4	RF Spectrum at 796 nm . . . . .	66
4.1	Schematic and Dispersion of LiNbO <sub>3</sub> Ridge Waveguide . . . . .	69
4.2	Input and output Spectra for Waveguide W1 (1950-nm Pump) . . . . .	71
4.3	Input and Output Spectrum for Waveguide W2 (1043-nm Pump) . . . . .	72
5.1	Schematic of Envelope Spectra and Interactions in the Generalized Coupled Wave Model . . . . .	78
5.2	Schematic and Dispersion of LiNbO <sub>3</sub> Ridge Waveguide . . . . .	93

5.3	Spectrum Predicted by a Second Harmonic Generation Model . . . . .	95
5.4	Spectrum Predicted by an Extended Coupled-Wave Model, Including Third and Fourth Harmonic Generation . . . . .	96
5.5	Spectrum Obtained by a Coupled-Wave Model Including Intrapulse Difference Frequency Generation . . . . .	98
5.6	Spectrum Obtained by a Generalized Coupled-Wave Model Including All Relevant Mixing Processes . . . . .	99
5.7	Comparison Between Single-Envelope and Multiple-Envelope Propa- gation Models . . . . .	100
5.8	Schematic of Coupling Between Small-Signal Components . . . . .	113
6.1	Experimental Setup of a Tm-Fiber DFG System . . . . .	119
6.2	Input Pulses for DFG in OP-GaAs . . . . .	120
6.3	Mid-IR Output Spectra and Power . . . . .	121
6.4	OPA Behavior Versus Normalized Parameters . . . . .	131
6.5	OPA Design Using 2-ps-Duration Pump Pulses . . . . .	133
7.1	Spatial Profile of a Chirped QPM Grating . . . . .	143
7.2	Signal Gain and Pump Depletion as a Function of Position in a Chirped QPM Grating . . . . .	145
7.3	Three-wave mixing: Geometric example . . . . .	151
7.4	Adiabatic Following Process . . . . .	153
7.5	Geometric Adiabaticity Constraint . . . . .	158
7.6	Pump Depletion as a Function of Pump and Signal Intensities . . . . .	160
7.7	Signal Phase Accumulation During Propagation . . . . .	162
7.8	Eigenvalues as a Function of Normalized Phase Mismatch . . . . .	168
7.9	Contours of Constant Conversion Efficiency and Comparison to Adia- baticity Constraints . . . . .	170
8.1	OPCPA Schematic; Mapping Between Signal Frequency and Pump Time	173
8.2	Experimental Schematic of a Mid-IR OPCPA System . . . . .	175
8.3	Nonlinear Chirp Design Example . . . . .	189

8.4	WKB-Based Apodization Example . . . . .	195
8.5	Coincidentally Phasematched Processes: QPM Periods . . . . .	199
8.6	Coincidentally Phasematched Processes: 3.8- $\mu\text{m}$ Example . . . . .	201
8.7	Coincidentally Phasematched Processes: 3.0- $\mu\text{m}$ Example . . . . .	202
8.8	Schematic of Gain-Guided Noncollinear Modes in Chirped QPM Gratings	215
8.9	Simulated Normalized Gain Rate $\Gamma/\gamma_{p0}$ of Noncollinear Gain-Guided Modes . . . . .	216
8.10	Geometric Mean Angle Versus Idler Wavelength . . . . .	218
8.11	Simulation Example for a Positively Chirped QPM Grating . . . . .	225
8.12	Simulation Example for a Negatively Chirped QPM Grating . . . . .	227
8.13	Spatiotemporal Coupling Effects for an Example Case with High Pump Depletion and a Negative Chirp Rate . . . . .	230
8.14	Nonlinear Idler Phase . . . . .	234

# Chapter 1

## Introduction

The main theme of this dissertation is highly nonlinear devices based on quasi-phasematching (QPM) gratings. In order to design, understand, or explain the behavior of these devices, careful numerical and analytical modeling is often required. In this chapter, we develop the main concepts and equations underlying the work discussed in later chapters. More specifically, we develop differential equations for modeling nonlinear interactions involving waves propagating in either bulk media or bound waveguide modes. By deriving these equations in the frequency domain, dispersion can be treated exactly, without the need for a series expansion. Similarly, all conventional second- and third-order nonlinear-optical interactions can be included in the nonlinear polarization. The equations we develop thus form a basis for further simplification (for example, to derive conventional coupled-wave equations), or they can be used directly in order to numerically simulate nonlinear-optical interactions.

In section 1.1, we introduce Maxwell's equations, the constitutive relations, the nonlinear polarization, and we derive the eigenmode equations which specify the linear-optical propagation of plane waves in homogeneous but anisotropic media. In section 1.2, we develop propagation equations for the electric field in a homogeneous medium in terms of the nonlinear polarization. In section 1.3, we develop propagation equations for each waveguide mode in terms of the nonlinear polarization. In section 1.4, we introduce quasi-phasematching, and describe its importance in achieving efficient frequency conversion via the second-order nonlinear susceptibility. In section

1.5, we introduce coupled wave equations which describe the interaction due to the second-order nonlinear susceptibility between waves which are continuous in time and planar in space. Finally, in section 1.6, we give an overview of the rest of this dissertation.

## 1.1 Maxwell's Equations

In many physical situations, Maxwell's equations support eigenmodes of linear propagation, i.e. electric field profiles which remain unchanged during propagation except for a constant rate of attenuation and phase accumulation with respect to position. It is often possible to greatly simplify Maxwell's equations by expanding the electric and magnetic fields around such eigenmodes. Following Ref. [3] and working in the frequency domain, Maxwell's equations are given by

$$\nabla \cdot \tilde{\mathbf{D}} = \tilde{\rho} \quad (1.1a)$$

$$\nabla \cdot \tilde{\mathbf{B}} = 0 \quad (1.1b)$$

$$\nabla \times \tilde{\mathbf{E}} = -i\omega\tilde{\mathbf{B}} \quad (1.1c)$$

$$\nabla \times \tilde{\mathbf{H}} = \tilde{\mathbf{J}} + i\omega\tilde{\mathbf{D}}. \quad (1.1d)$$

where tilde denotes a field quantity expressed in the frequency domain. In these equations,  $\mathbf{E}$  and  $\mathbf{H}$  are the electric field and magnetic field, respectively.  $\rho$  and  $\mathbf{J}$  are the electric charge density and electric current density, respectively.  $\mathbf{D}$  and  $\mathbf{B}$  are the electric displacement field and magnetic induction, respectively. Bold text denotes a vector or tensor quantity. The vectors  $\mathbf{D}$  and  $\mathbf{B}$  are given in terms of  $\mathbf{E}$  and  $\mathbf{H}$  via constitutive relations which are determined by the response of the medium to the electric and magnetic fields. In this dissertation, we consider dielectric media which are nonlinear, inhomogeneous, anisotropic, and non-magnetic. For these cases, the

constitutive relations are given by

$$\tilde{\mathbf{D}} = \boldsymbol{\epsilon} \tilde{\mathbf{E}} + \tilde{\mathbf{P}}_{NL} \quad (1.2a)$$

$$\tilde{\mathbf{B}} = \mu_0 \tilde{\mathbf{H}} \quad (1.2b)$$

where  $\mathbf{P}_{NL}$  is the nonlinear polarization and  $\boldsymbol{\epsilon}$  is the permittivity;  $\boldsymbol{\epsilon}$  is a rank-2 tensor and is a function of both position and frequency. The relative permittivity is defined as  $\boldsymbol{\epsilon}_r \equiv \boldsymbol{\epsilon}/\epsilon_0$ . We use the following definition of the Fourier transform:

$$\tilde{f}(\omega) \equiv \mathcal{F}[f](\omega) \equiv \int_{-\infty}^{\infty} f(t) e^{-i\omega t} dt. \quad (1.3)$$

Tilde's will not be used for quantities which are only used here in the frequency domain, such as the linear and nonlinear susceptibility tensors.

The matrix  $\boldsymbol{\epsilon}$  determines how light propagates linearly through a medium; its frequency dependence determines the dispersive properties of the medium, while its spatial dependence determines the waveguide modes (if any) which are supported. Through time-dependent perturbation theory, the frequency-dependence of  $\boldsymbol{\epsilon}$  can be expressed (for a wide range of cases) in terms of a sum of Lorentzians associated with the quantum-mechanical energy eigenstates (or resonances) of the medium [4, pp. 142]. When operating far from these resonances (in particular, within the transparency window of the material) the dispersion of  $\boldsymbol{\epsilon}$  can often be approximated by a Sellmeier equation [5]. Dispersion plays a very important role in nonlinear optics, since it determines the relative phase accumulated by the different spectral components as they interact coherently with each other. We discuss this issue in more detail in section 1.4.

The nonlinear polarization can often be written in the form of a power series in

the electric field. Including terms up to third order in this series,  $\mathbf{P}_{NL}$  is given by

$$\begin{aligned} \frac{\tilde{P}_{NL,i}(\omega)}{\epsilon_0} &= \sum_{j,k} \int_{-\infty}^{\infty} \chi_{ijk}^{(2)}(\omega, \omega', \omega - \omega') \times \\ &\quad \tilde{E}_j(\omega') \tilde{E}_k(\omega - \omega') d\omega' \\ &+ \sum_{j,k,l} \int_{-\infty}^{\infty} \int_{-\infty}^{\infty} \chi_{ijkl}^{(3)}(\omega, \omega', \omega'', \omega - \omega' - \omega'') \times \\ &\quad \tilde{E}_j(\omega') \tilde{E}_k(\omega'') \tilde{E}_l(\omega - \omega' - \omega'') d\omega' d\omega'' \end{aligned} \quad (1.4)$$

where  $\tilde{E}_j$  and  $\tilde{P}_{NL,j}$  denote the components of  $\tilde{\mathbf{E}}$  and  $\tilde{\mathbf{P}}_{NL}$  along coordinate  $j$ , respectively (with  $j \in \{x, y, z\}$ ). Each  $\chi^{(n)}$  denotes the  $n^{\text{th}}$ -order nonlinear susceptibility;  $\chi^{(n)}$  is a rank- $(n+1)$  tensor. These susceptibilities are parameterized by their  $n+1$  subscripts (which indicate the polarizations involved) and  $n$  independent frequency arguments. Their properties and symmetries have been discussed extensively [4]. Furthermore, as with the linear susceptibility, the nonlinear susceptibilities can often be derived through time-dependent perturbation theory [4, pp. 135–147]. As a result, the nonlinear susceptibilities  $\chi^{(n)}$  ( $n > 1$ ) have similar form and are related to the linear susceptibility  $\chi^{(1)}$ , although they are more complicated.

In many cases, such as those considered in later chapters, the complexity of  $\mathbf{P}_{NL}$  can be reduced significantly. For example, Eq (1.4) has a form resembling a convolution. In particular, if we assume that the nonlinear susceptibilities are non-dispersive, then Eq. (1.4) is explicitly a sum of convolutions of electric fields. If we also consider only a single polarization component of the electric field, then the nonlinear polarization can be expressed in the time domain as

$$\frac{P_{NL}(t)}{\epsilon_0} = \chi^{(2)} E(t)^2 + \chi^{(3)} E(t)^3. \quad (1.5)$$

Due to the quadratic or cubic dependence on the electric fields, for beams of low intensity, the nonlinear polarization is small and may be negligible. As a result, in order to achieve efficient frequency conversion, we usually need light with a reasonably high power (at least several mW, and often several Watts or more, depending on the

interaction). Such intensities are readily achieved by modern lasers, and especially by pulsed lasers. Note, however, that there is not always a need for high powers: for example, strong nonlinear-optical interactions have been demonstrated even at the single-photon level [6]. Nonetheless, the nonlinear interactions discussed in this dissertation involve, and require, pulses with kW- or even MW-level peak powers.

To understand nonlinear optics, we first need to understand linear optics. Linear-optical propagation is obtained by setting  $\mathbf{P}_{NL} = 0$ . Assuming  $\mathbf{P}_{NL} = 0$ , taking the curl of Eq. (1.1c), applying the constitutive relations in Eq. (1.2), and writing  $\nabla \times \tilde{\mathbf{H}}$  in terms of  $\tilde{\mathbf{E}}$  using Eq. (1.1d), we can obtain following the pair of equations

$$\nabla \cdot (\epsilon_r \tilde{\mathbf{E}}) = 0 \quad (1.6a)$$

$$\epsilon_r^{-1} \nabla \times \nabla \times \tilde{\mathbf{E}} = \left(\frac{\omega}{c}\right)^2 \tilde{\mathbf{E}}. \quad (1.6b)$$

With these equations, linear-optical propagation can be determined.

Consider first the case of a homogeneous medium (corresponding to a position-independent permittivity). In this case, the eigenmodes are plane-waves. Taking the three-dimensional spatial Fourier transform of Eq. (1.6) with spatial frequency vector  $\mathbf{k} \equiv k\mathbf{u}$ , we find that

$$\mathbf{u} \cdot \tilde{\mathbf{D}} = 0 \quad (1.7a)$$

$$(-\mathbf{u} \times \mathbf{u} \times \epsilon_r^{-1}) \tilde{\mathbf{D}} = \frac{\omega^2}{c^2 k^2} \tilde{\mathbf{D}}. \quad (1.7b)$$

Eq. (1.7a) indicates that only the components of  $\tilde{\mathbf{D}}$  perpendicular to  $\mathbf{k}$  are non-zero, and Eq. (1.7b) yields an eigenvalue equation for these components (at each propagation direction  $\mathbf{u}$ ). Denoting the eigensolutions by subscript  $n$ , Eqs. (1.7) yield eigenvectors  $\mathbf{D}_n$  and eigenvalues  $\omega^2/(c^2 k_n^2)$ , and hence electric field eigenvectors  $\mathbf{E}_n = \epsilon^{-1} \mathbf{D}_n$  and dispersion relations  $k_n(\omega)$ .

## 1.2 Nonlinear Mixing with Paraxial Diffraction

In this section, we determine a unidirectional scalar-wave propagation equation in the presence of the nonlinear susceptibility  $\tilde{\mathbf{P}}_{NL}$  for a homogeneous uniaxial medium. For such a material, the relative permittivity is given by

$$\tilde{\epsilon}_r(\omega) = \begin{bmatrix} n_e(\omega)^2 & 0 & 0 \\ 0 & n_o(\omega)^2 & 0 \\ 0 & 0 & n_o(\omega)^2 \end{bmatrix} \quad (1.8)$$

We will assume that the electric field is polarized parallel to the  $c$ -axis (direction  $\hat{\mathbf{x}}$ ; index  $n_e$ ), and has spatial frequency components lying close to the propagation direction ( $+\hat{\mathbf{z}}$ ); this assumption allows us to make the small-angle (paraxial) approximation. Since the nonlinear polarization is given in terms of the electric field, we determine a system of equations involving only  $\mathbf{E}$ . Applying the same analysis used for Eq. (1.6b) and also using the identity  $\nabla \times \nabla \times \mathbf{A} = \nabla(\nabla \cdot \mathbf{A}) - \nabla^2 \mathbf{A}$ , we find

$$\nabla(\nabla \cdot \tilde{\mathbf{E}}) - \nabla^2 \tilde{\mathbf{E}} = \left(\frac{\omega}{c}\right)^2 \left( \epsilon_r \tilde{\mathbf{E}} + \frac{\tilde{\mathbf{P}}_{NL}}{\epsilon_0} \right). \quad (1.9)$$

The term  $\nabla(\nabla \cdot \tilde{\mathbf{E}})$  can be simplified via Eq. (1.1a). By assuming a relatively weak nonlinear polarization, Eq. (1.1a) reduces to Eq. (1.6a). In turn, Eq. (1.6a) implies that  $\nabla \cdot \tilde{\mathbf{E}} = \nabla \cdot (\epsilon^{-1} \epsilon \tilde{\mathbf{E}}) = \nabla \cdot ((\epsilon^{-1} - \epsilon_{zz}^{-1} \mathbf{I}) \epsilon \tilde{\mathbf{E}})$  for identity matrix  $\mathbf{I}$ , since  $\epsilon_{zz}^{-1} = \hat{\mathbf{z}}^T \epsilon^{-1} \hat{\mathbf{z}}$  is a constant scalar and  $\nabla \cdot (\varphi \mathbf{I} \epsilon \tilde{\mathbf{E}}) = 0$  for any constant scalar  $\varphi$ . Given the permittivity in Eq. (1.8), the matrix  $(\epsilon^{-1} - \epsilon_{zz}^{-1} \mathbf{I}) \epsilon$  has only one non-zero element (the  $xx$  component). Therefore,  $\nabla \cdot \tilde{\mathbf{E}}$  has a simple form:

$$\nabla \cdot \tilde{\mathbf{E}} = \left(1 - \frac{n_e(\omega)^2}{n_o(\omega)^2}\right) \frac{\partial}{\partial x} (\tilde{\mathbf{E}} \cdot \hat{x}). \quad (1.10)$$

Substituting this equation into Eq. (1.9) and taking the dot product of both sides with  $\hat{x}$ , we arrive at the following equation for the  $x$ -component of  $\tilde{\mathbf{E}}$ :

$$\left[ \frac{\partial^2}{\partial z^2} + (1 - \delta) \frac{\partial^2}{\partial x^2} + \frac{\partial^2}{\partial y^2} + k_e(\omega)^2 \right] (\tilde{\mathbf{E}} \cdot \hat{\mathbf{x}}) = - \left( \frac{\omega}{c} \right)^2 \left( \frac{\tilde{\mathbf{P}}_{NL} \cdot \hat{\mathbf{x}}}{\epsilon_0} \right) \quad (1.11)$$

where  $\delta = 1 - (n_e/n_o)^2$ .  $\delta$  is close to zero in materials such as LiNbO<sub>3</sub>, so it can be convenient to make the approximation  $\delta = 0$ , since this renders the operator on the left hand side of Eq. (1.11) radially symmetric. A similar procedure to the one used here can be applied to obtain equations governing diffraction and nonlinear mixing in general anisotropic media with arbitrary propagation direction [7].

Eq. (1.11) supports waves propagating in all directions, and in particular in both the  $+\hat{\mathbf{z}}$  and  $-\hat{\mathbf{z}}$  directions. Often, all the spatial frequencies involved in a nonlinear-optical interaction correspond to a narrow angular range around  $+\hat{\mathbf{z}}$ . This condition applies, for example, to the positive-frequency components of beams propagating along the  $z$ -axis and having beam waists much larger than the wavelength. In such cases, we can replace the propagation operator in Eq. (1.11) with a simpler one corresponding to paraxial diffraction through the relations

$$\begin{aligned} \hat{L}_z &\equiv \frac{\partial^2}{\partial z^2} + k_e^2 \\ &= \left( \frac{\partial}{\partial z} - ik_e \right) \left( \frac{\partial}{\partial z} + ik_e \right) \\ &\approx -2ik_e \left( \frac{\partial}{\partial z} + ik_e \right). \end{aligned} \quad (1.12)$$

The first relation is the definition of  $\hat{L}_z$ , the second relation follows immediately from the first, and the third relation is accurate when  $\hat{L}_z$  is applied to waves having spatial frequencies  $\mathbf{k}$  in a narrow cone around  $k_e \hat{\mathbf{z}}$ . With Eq. (1.12) we can approximate Eq.

(1.11) to yield the following unidirectional propagation equation

$$\left[ \frac{\partial}{\partial z} + ik_e(\omega) + \frac{i}{2k_e(\omega)} \left( (1 - \delta) \frac{\partial^2}{\partial x^2} + \frac{\partial^2}{\partial y^2} \right) \right] (\tilde{\mathbf{E}} \cdot \hat{\mathbf{x}}) = -i \frac{\omega^2}{2c^2 k_e(\omega)} \left( \frac{\tilde{\mathbf{P}}_{NL} \cdot \hat{\mathbf{x}}}{\epsilon_0} \right). \quad (1.13)$$

This equation is appropriate for waves propagating around the  $+\hat{\mathbf{z}}$  direction and is first-order in the propagation coordinate  $z$ ; as such, it is considerably simpler and more tractable than Eq. (1.11). Since dispersion remains exact for on-axis wave components via the frequency-dependence of  $k_e(\omega)$ , and only minor approximations have been made on the diffraction and nonlinear terms, Eq. (1.13) is well-suited to modeling nonlinear-optical interactions involving pulsed beams in homogeneous uniaxial media, even when extremely wide bandwidths are involved. Since the negative-temporal-frequency components of the electric field can be determined from the positive-frequency components, it is useful to solve only for the positive-frequency components in Eq. (1.13).

### 1.3 Nonlinear Mixing Involving Waveguide Modes

In this section we determine a propagation equation for interactions involving a set of orthogonal waveguide modes. The  $z$ -axis is used to denote the direction of the waveguide; we assume a lossless non-magnetic medium that is homogeneous along coordinate  $z$  and inhomogeneous along the transverse coordinates  $x$  and  $y$ . The electric field can be written as a sum over the modes supported by the waveguide,

$$\tilde{\mathbf{E}}(x, y, z, \omega) = \sum_n \tilde{\Phi}_n(z, \omega) \mathbf{E}_n(x, y, \omega) e^{-i\beta_n(\omega)z}. \quad (1.14)$$

where the (vector) modes  $\mathbf{E}_n(x, y, \omega) \exp(-i\beta_n(\omega)z)$  are solutions to Maxwell's equations in the case when  $\mathbf{P}_{NL} = 0$ . Note that in general, a continuum of radiation modes must be included in order to form a complete basis for the electric field; the summation in Eq. (1.14) can thus be viewed as a summation over the bound modes plus integration over the radiation modes of the waveguide. However, in this dissertation

we always neglect the radiation modes.

A propagation equation for each of the scalar envelopes  $\Phi_n$  can be determined by applying the reciprocity relations for Maxwell's equations and orthogonality of the waveguide modes [8]. Consider any pair of solutions to Maxwell's equations for a given permittivity profile  $\epsilon(x, y, \omega)$ , with each solution  $j$  specified by the fields  $\mathbf{E}^{(j)}$  and  $\mathbf{H}^{(j)}$ , and by the corresponding nonlinear polarization  $\mathbf{P}_{NL}^{(j)}$ . The reciprocity relations are constraints which such pairs of solutions must obey, which can be determined from Eqs. (1.1c) and (1.1d). Following Ref. [8], the the reciprocity relations are given by

$$\nabla \cdot \left( \tilde{\mathbf{E}}^{(1)} \times \tilde{\mathbf{H}}^{(2)*} + \tilde{\mathbf{E}}^{(2)*} \times \tilde{\mathbf{H}}^{(1)} \right) = i\omega \left( \tilde{\mathbf{P}}_{NL}^{(2)*} \cdot \tilde{\mathbf{E}}^{(1)} - \tilde{\mathbf{P}}_{NL}^{(1)} \cdot \tilde{\mathbf{E}}^{(2)*} \right). \quad (1.15)$$

where we have assumed a lossless and non-gyrotropic medium and used the symmetry of  $\epsilon$ . The orthogonality condition for waveguide modes  $n$  and  $m$  at a particular frequency can be written as [9]

$$\int (\mathbf{E}_n \times \mathbf{H}_m^* + \mathbf{E}_m^* \times \mathbf{H}_n) \cdot \hat{\mathbf{z}} dx dy = \delta_{mn} \bar{g}_m \quad (1.16)$$

where  $\bar{g}_m(\omega)$  is a real-valued and frequency-dependent scale factor, and  $\delta_{mn}$  is the Kronecker delta.

The propagation equation for the scalar envelope of each mode can be obtained by taking one of the solutions in Eq. (1.15) to be the nonlinear-optical case being modeled (i.e.  $\mathbf{E}^{(1)} = \mathbf{E}$  and  $\mathbf{P}_{NL}^{(1)} = \mathbf{P}_{NL}$ ), and the other solution to be one of the linear-optical waveguide modes (i.e.  $\mathbf{E}^{(2)} = \mathbf{E}_m$  and  $\mathbf{P}_{NL}^{(2)} = 0$ ).  $\mathbf{E}^{(1)}$  is thus given by the modal expansion in Eq. (1.14). Substituting these choices into Eq. (1.15) and applying orthogonality [Eq. (1.16)], we find the following propagation equation for each scalar envelope

$$\frac{d\tilde{\Phi}_n}{dz} = -ie^{i\beta_n z} \frac{\omega}{\bar{g}_n} \int \tilde{\mathbf{P}}_{NL} \cdot \mathbf{E}_n^* dx dy \quad (1.17)$$

This equation applies for both forward and backward propagating modes of the waveguide (which correspond to positive and negative values of  $\beta_n$ , respectively). In the absence of any nonlinear polarization, each envelope  $\Phi_n$  propagates unchanged. Since

Eq. (1.17) yields a propagation equation for each individual mode, backward waves can be neglected simply by neglecting the corresponding set of equations.

In the conventional slowly-varying envelope approximation (SVEA), one first determines a second-order differential equation for a set of envelopes, and then neglects second-order derivatives to arrive at a first-order differential equation for those envelopes. Eq. (1.17) represents a more general and accurate approach: a set of first-order equations governing the evolution of any set of waveguide modes can be determined directly from Maxwell's equations. Instead of having a set of  $N$  second-order equations for modes including forward and backward components, Eq. (1.17) yields  $2N$  first-order equations, with each envelope corresponding to either a forward or a backward mode. In order to construct a tractable set of equations from Eq. (1.17), we then neglect radiation-mode and backward-wave envelopes (provided that they are indeed negligible).

For weakly-confining waveguides, the vector components of the electric and magnetic field lie primarily, but not entirely, in the plane perpendicular to the propagation direction. As a result, in the limit of weak confinement, the mode scale factor appearing in the orthogonality relation above can be approximated as

$$\begin{aligned}\bar{g}_n &= \frac{2\beta_n}{\omega\mu_0}g_n \\ &\approx \frac{2\beta_n}{\omega\mu_0} \int |\mathbf{E}_n|^2 dx dy,\end{aligned}\tag{1.18}$$

where  $g_n$  is defined by the first expression and approximated in the second. Substituting Eq. (1.18) into Eq. (1.17), we obtain the following set of propagation equations

$$\frac{d\tilde{\Phi}_n}{dz} = -ie^{i\beta_n z} \frac{\omega^2}{2\beta_n g_n c^2 \epsilon_0} \int \tilde{\mathbf{P}}_{NL} \cdot \mathbf{E}_n^* dx dy.\tag{1.19}$$

If coupling to radiation modes can be neglected, the resulting coupled-mode system will usually involve a relatively small number of modes; in some cases, only a single mode must be considered. The mode profiles and corresponding dispersion relations can be found through a variety of numerical techniques [10, 11]. Losses can be accounted for heuristically by adding an attenuation term to the left hand side of Eq.

(1.17) or (1.19). More generally, losses originate from absorption within the waveguide layers (which results in an imaginary part of the propagation constant of the unperturbed waveguide) and from scattering into different modes (including radiation modes) of the unperturbed structure due to  $z$ -dependent perturbations in the waveguide [12]; these effects are beyond the scope of this work.

## 1.4 Quasi-Phasematching

When light propagates through a linear-optical medium, each spectral component of the electric field accumulates a phase of the form  $\exp(-i\beta(\omega)z)$  for some propagation constant  $\beta$ , as discussed in the previous sections. In a nonlinear-optical medium, the electric field is modified by the nonlinear polarization, as shown in Eq. (1.13) for paraxially-diffracting beams and in Eq. (1.17) for waveguide modes. The phase accumulated by a spectral component during linear-optical propagation can differ from the phase accumulated by the corresponding nonlinear polarization. This difference is called phase mismatch. Phase mismatch limits the length over which energy can be transferred from one spectral component to another: when the electric field slips out of phase with the nonlinear polarization, energy is back-converted to the input wave.

As an example, consider a first harmonic (FH) wave of frequency  $\omega_1$  propagating linearly (i.e. unperturbed by  $\mathbf{P}_{NL}$ ) with phase  $\exp(-i\beta_1 z)$ . This FH results in a term in the nonlinear polarization at frequency  $\omega_2 = 2\omega_1$  through the  $\chi^{(2)}$  susceptibility. We denote the relevant component (or projection) of  $\chi^{(2)}$  as  $\chi_{\text{eff}}^{(2)}$ , the exact form of which will be discussed in section (1.5). The  $z$ -dependence of the second harmonic (SH) nonlinear polarization is given by  $\chi_{\text{eff}}^{(2)}(z) \exp(-2i\beta_1 z)$ , based on Eq. (1.4). The linear-optical phase factor accumulated at frequency  $2\omega_1$  is  $\exp(-i\beta_2 z)$ . If  $\chi_{\text{eff}}^{(2)}$  is  $z$ -independent, the difference between these two phase factors results in the following phase mismatch:

$$\Delta\beta_0 = \beta_2 - 2\beta_1. \quad (1.20)$$

Due to dispersion,  $\Delta\beta_0 \neq 0$  except in certain specific cases. Propagation of the SH envelope  $A_2$  takes the following form:

$$\frac{dA_2}{dz} \propto \chi_{\text{eff}}^{(2)} e^{i\Delta\beta_0 z}, \quad (1.21)$$

where this form arises by neglecting  $\chi^{(3)}$  and changes to the FH envelope  $A_1$ . Based on this equation, energy is transferred from the FH to the SH over a distance  $|\pi/\Delta\beta_0|$ . After this distance, energy is transferred back to the FH.  $|\pi\Delta\beta_0|^{-1}$  is often just a few microns, which is an insufficient distance to transfer a significant proportion of the energy from the FH to the SH, unless extremely high intensities are involved.

The phase mismatch can be overcome by modulating the nonlinear susceptibility  $\chi_{\text{eff}}^{(2)}$ . If the sign of  $\chi_{\text{eff}}^{(2)}$  is reversed at each point where the phase mismatch would cause the direction of energy transfer to change sign, then the changes in sign cancel and energy flows monotonically from the FH to the SH [13, 14, 15, 16]. This procedure is called quasi-phases-matching (QPM). The sign of  $\chi^{(2)}$  is often, but not always, reversed at positions  $N\pi/|\Delta\beta_0|$  for integers  $N$ . The resulting  $\chi_{\text{eff}}^{(2)}(z)$  profile is periodic, with period of  $2\pi/|\Delta\beta_0|$ .

It is useful to express the QPM grating structure in normalized form as

$$\bar{d}(z) = \frac{\chi_{\text{eff}}^{(2)}(z)}{\chi_0^{(2)}} \quad (1.22)$$

where  $\chi_0^{(2)}$  is the value of  $\chi_{\text{eff}}^{(2)}$  in the un-modified material. Periodic QPM gratings can be written in the form  $\bar{d}(z) = \text{sgn}(\cos(K_g z))$  for grating k-vector  $K_g$  (period  $2\pi/K_g$ ). More generally, arbitrary QPM gratings can be expressed in the form

$$\bar{d}(z) = \text{sgn}(\cos(\phi_G(z)) - \cos(\pi D(z))) \quad (1.23)$$

where the smooth and continuous grating phase profile  $\phi_G(z)$  can be written as

$$\phi_G(z) = \phi_0 + \int_0^z K_g(z') dz' \quad (1.24)$$

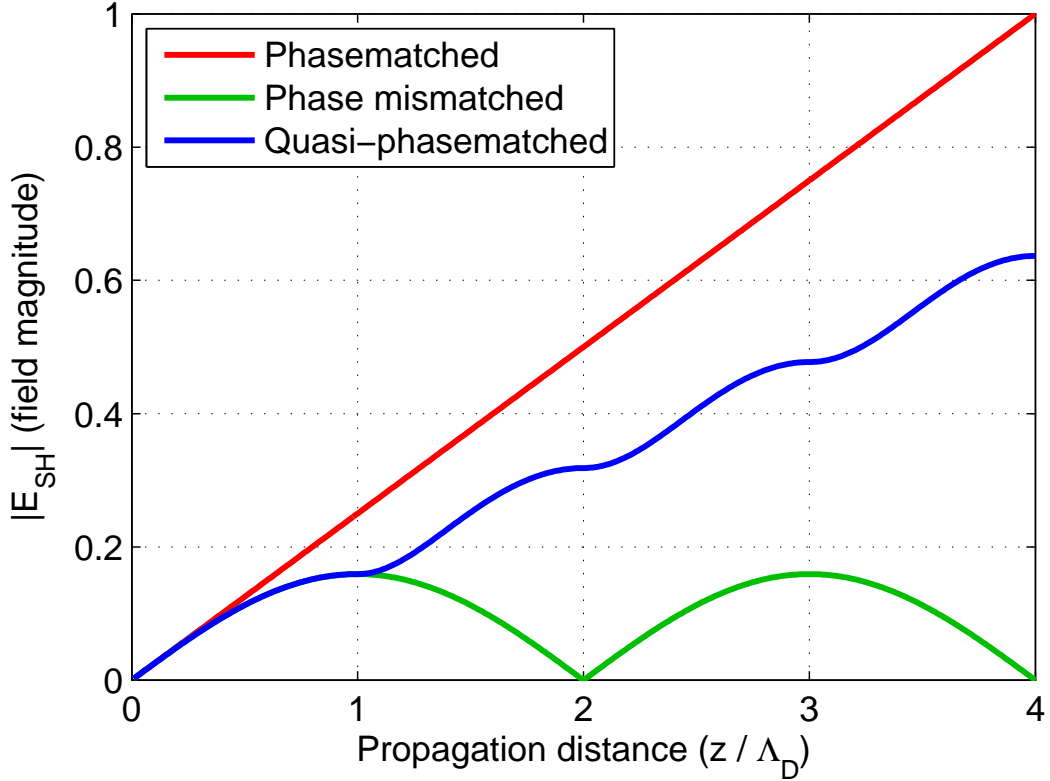


Figure 1.1: Evolution of the magnitude of the second harmonic *field* with position for three different cases. (1) Phasematched (red): linear growth of the field; quadratic growth of the intensity. (2) Phase mismatched (green): oscillatory; no net growth. (3) Quasi-phasematched (blue): linear growth of the field from the first Fourier order of the grating, plus oscillations from the other Fourier orders.

for local grating k-vector  $K_g(z)$  and initial phase  $\phi_0$ .  $D(z)$  is the local duty cycle. If we assume a constant grating k-vector satisfying  $K_g = \Delta\beta_0$ , then phasematching for the SH is satisfied by the Fourier order of the QPM grating whose phase evolves as  $\exp(-iK_g z)$ . This case is illustrated in Fig. 1.1, where we compare phasematched, phase mismatched, and quasi-phasematched second harmonic generation (SHG). In QPM SHG, the SH can grow monotonically with position  $z$  but at a reduced rate compared to the phasematched case, since only a single Fourier order of the grating satisfies phasematching.

In order to model the propagation of the electric field, it is useful to express the

QPM grating in terms of its Fourier coefficients. Since  $\bar{d}(z) = \pm 1$ , it can be expressed as

$$\bar{d}(z) = \sum_{m=-\infty}^{\infty} \bar{d}_m \exp(im\phi_G(z)), \quad (1.25)$$

where the Fourier coefficients are given by

$$\bar{d}_m = \frac{2 \sin(\pi m D)}{\pi m} \quad (1.26)$$

for  $m \neq 0$ , and  $\bar{d}_0 = (2D - 1)$ . Eq. (1.25) is a trigonometric identity; while resembling a Fourier series, it applies for smooth and continuous grating phase and duty cycle profiles. It is also sometimes convenient to expand the effective nonlinear coefficient  $d_{\text{eff}}$  in a Fourier series, i.e. without a separate normalization:

$$d_{\text{eff}}(z) = \sum_{m=-\infty}^{\infty} d_m \exp(im\phi_G(z)), \quad (1.27)$$

where  $d_m$  depend on the duty cycle. Substituting Eq. (1.25) into Eq. (1.21) and applying using the fact that  $\bar{d}_m = \bar{d}_{-m}$  yields an equation of the form

$$\frac{dA_2}{dz} \propto \sum_m \bar{d}_m e^{i\Delta\beta_m z} \quad (1.28)$$

where the  $m^{\text{th}}$ -order phase mismatch is given by

$$\Delta\beta_m(z) = \beta_2 - 2\beta_1 - mK_g(z) \quad (1.29)$$

for integers  $m$ . When  $K_g = \Delta\beta_0$ , the first-order phase mismatch  $\Delta\beta_1 = 0$ . As a result, the contribution to  $A_2$  from the  $m = +1$  term in Eq. (1.28) can grow over arbitrary distances. The remaining contributions to  $A_2$  lead to rapid (varying over a the length-scale  $|\Delta\beta_0^{-1}|$ ) but small oscillations in the SH with position. As a result, it is often appropriate to neglect these contributions to the SH polarization and consider just the  $m = +1$  term of Eq. (1.28).

QPM has been achieved in a number of materials including LiNbO<sub>3</sub> [17, 18, 19, 20, 21, 22], LiTaO<sub>3</sub> [23, 24], and GaAs [25]. In LiNbO<sub>3</sub> and LiTaO<sub>3</sub>, QPM is usually achieved through inversion of ferroelectric domains by applying a pulsed electric field with a well chosen profile, which exceeds the ferroelectric coercive field, to electrodes lithographically patterned on a substrate [26]. In GaAs and GaP, QPM can be achieved by growing layers of opposite crystal orientation (and hence opposite nonlinearity) [27]. QPM is used in a very wide variety of devices and applications [28], which we will not attempt to summarize here.

## 1.5 Plane-Wave Processes in QPM Gratings

The propagation equations established in sections 1.2 and 1.3 support a wide variety of interactions, with resulting nonlinear dynamics that can be complicated and difficult to interpret. Because of this complexity, it is useful to consider simpler limiting cases, such as interactions between plane- and continuous waves, in order to understand the most important processes involved. Therefore, in this section, we determine coupled wave equations (CWEs) for plane-wave  $\chi^{(2)}$  interactions.

In nonlinear media, many components of the nonlinear polarization are generated. Even with just a single input frequency  $\omega$  in a  $\chi^{(2)}$  medium, a non-zero spectral component at frequency  $2\omega_0$  is generated; the  $\omega_0$  and  $2\omega_0$  components can in turn generate a component at  $3\omega_0$ , and so on; such processes lead to spectral components at frequencies  $N\omega_0$  for each integer  $N \geq 0$ . However, usually only a small number or a small range of spectral components is significant in determining the important dynamical processes. The importance of different terms is frequently related to phasematching: when the process generating a spectral component is sufficiently phase mismatched, the resulting component and its corresponding polarization are negligible. Motivated by this argument, we can construct simplified sets of equations by ignoring all but a small number of spectral components. In this section, we introduce two of the simplest energy-conserving  $\chi^{(2)}$  cases: SHG involving a first and second harmonic (denoted by subscripts 1 and 2, respectively), and three-wave mixing (TWM) involving an idler, signal and pump (denoted by subscripts  $i$ ,  $s$  and  $p$ , respectively).

To determine the CWEs, we assume that the electric field is comprised of a small number of collinear, single-frequency components, and hence has the form

$$\mathbf{E}(z, t) = \frac{1}{2} \sum_j A_j(z) e^{i\omega_j t - k_j z} \mathbf{v}_j + c.c \quad (1.30)$$

where  $j \in \{1, 2\}$  (for SHG) or  $j \in \{i, s, p\}$  (for TWM).  $A_j(z)$  are time-independent,  $c.c$  denotes complex conjugate,  $\omega_j$  are carrier frequencies, and  $k_j = k(\omega_j)$  for wavevector  $k(\omega)$ . The vectors  $\mathbf{v}_j$  depend on the type of interaction, but are in general assumed to have unity magnitude and to correspond to a mode of linear-optical propagation, according to Eqs. (1.7). Each  $\mathbf{v}_j$  is allowed to be complex, to account for elliptical polarizations;  $\mathbf{v}_j$  are closely related to the Jones vectors. For SHG,  $\omega_2 = 2\omega_1$ ; for TWM,  $\omega_p = \omega_i + \omega_s$ . Substituting Eq. (1.30) into Eq. (1.4) yields several second-order contributions to the nonlinear polarization; we are interested in this section in the terms having carrier frequencies  $+\omega_j$  for  $j \in \{1, 2\}$  (for SHG) or  $j \in \{i, s, p\}$  (for TWM). These contributions are denoted  $\mathbf{P}_{NL,j}$  for carrier frequency  $j$ . Note that in general, one must calculate the nonlinear coupling between an orthogonal pair of polarizations at each carrier frequency. For nonlinear media with an isotropic linear-optical susceptibility (such as GaAs) this coupling can be particularly important [27], but here we consider only the simpler case corresponding to a single polarization state at each frequency.

### 1.5.1 Second Harmonic Generation

For SHG, the relevant contributions to  $\mathbf{P}_{NL}$  satisfy

$$\mathbf{P}_{NL,1} \cdot \mathbf{v}_1^* = \epsilon_0 d_{\text{eff}} A_1^* A_2 e^{i(\omega_1 - (k_2 - k_1)z)} \quad (1.31a)$$

$$\mathbf{P}_{NL,2} \cdot \mathbf{v}_2^* = \epsilon_0 d_{\text{eff}}^* \frac{A_1^2}{2} e^{i(\omega_2 - (2k_1)z)}. \quad (1.31b)$$

In these equations, the effective nonlinear coefficient  $d_{\text{eff}}$  is given by

$$\begin{aligned} d_{\text{eff}}(z) &= \frac{1}{2} \chi_{\text{eff}}^{(2)} \\ &= \frac{1}{2} \sum_{j_1, j_2, j_3} \chi_{j_1, j_2, j_3}^{(2)}(z, \omega_1, \omega_1, \omega_2) v_{1;j_1}^* v_{1;j_2}^* v_{2;j_3}, \end{aligned} \quad (1.32)$$

where  $v_{k;j} = \mathbf{v}_k \cdot \mathbf{e}_j$  for unit vector  $\mathbf{e}_j$ ; indices  $j_1$ ,  $j_2$  and  $j_3$  are summed over the  $x$ ,  $y$  and  $z$  Cartesian components. Third-order contributions to the nonlinear polarization can be obtained in the same way. We have used  $d_{\text{eff}}$  in the above equations instead of  $\chi_{\text{eff}}^{(2)}$  due to historical conventions. Throughout this dissertation, we use  $d_{\text{eff}}$  to refer to a tensor contraction based on a particular set of polarization components;  $d_{\text{eff}}$  is the sum of all the Fourier orders of the QPM grating. In writing Eq. (1.31) we have assumed that  $\chi^{(2)}$  is real. In more general cases where the imaginary part of  $\chi^{(2)}$  cannot be ignored, then  $\mathbf{P}_{NL,2}$  should be calculated with  $\chi^{(2)}$  and not  $(\chi^{(2)})^*$  [the latter form, which is implied by the  $d_{\text{eff}}^*$  factor in Eq. (1.31b), makes no difference if  $\chi^{(2)}$  is real].

In order to construct a coupled-wave system, each envelope  $A_j$  is assumed to be driven only by the nonlinear polarization term  $P_{NL,j}$ . Substituting Eqs. (1.31) into Eqs. (1.1) thus yields the following set of equations

$$\frac{dA_1}{dz} = -i \frac{\omega_1 d_{\text{eff}}(z)}{n_1 c} A_1^* A_2 e^{-i\Delta k_0 z} \quad (1.33a)$$

$$\frac{dA_2}{dz} = -i \frac{\omega_1 d_{\text{eff}}(z)^*}{n_2 c} A_1^2 e^{+i\Delta k_0 z} \quad (1.33b)$$

where  $d_{\text{eff}}$  contains all the Fourier orders and  $\Delta k_0 = k_2 - 2k_1$  is the material phase mismatch. The  $m^{\text{th}}$  order phase mismatch for SHG (i.e. associated with Fourier order  $m$  of the QPM grating) is given by

$$\Delta k_m = k_2 - 2k_1 - mK_g. \quad (1.34)$$

Analytical solutions to Eqs. (1.33) are given in Refs. [13, 29].

In a first-order QPM interaction, both the FH and SH are driven by the +1 order

of the grating. This type of combination (both FH and SH driven by the same QPM order, or set of QPM orders) arises from the use of  $d_{\text{eff}}^*$  in Eq. (1.33b) and is required for energy conservation. We can thus obtain coupled-wave equations for first-order QPM interactions by substituting Eqs. (1.22) and (1.25) into Eq. (1.32) and keeping only the  $m = 1$  term in the summation in Eq. (1.25). For a periodic QPM grating, where each  $\Delta k_m$  is  $z$ -independent, this procedure is equivalent to performing the substitutions  $d_{\text{eff}} \rightarrow d_{\text{eff}} \bar{d}_1$  and  $\Delta k_0 \rightarrow \Delta k_1$ .

### 1.5.2 Three Wave Mixing

For TWM, the relevant contributions to  $\mathbf{P}_{NL}$  satisfy

$$\mathbf{P}_{NL,i} \cdot \mathbf{v}_i^* = \epsilon_0 d_{\text{eff}} A_s^* A_p e^{i(\omega_i - (k_p - k_s)z)} \quad (1.35a)$$

$$\mathbf{P}_{NL,s} \cdot \mathbf{v}_s^* = \epsilon_0 d_{\text{eff}} A_p A_i^* e^{i(\omega_s - (k_p - k_i)z)} \quad (1.35b)$$

$$\mathbf{P}_{NL,p} \cdot \mathbf{v}_p^* = \epsilon_0 d_{\text{eff}}^* A_i A_s e^{i(\omega_p - (k_i + k_s)z)}. \quad (1.35c)$$

In these equations, the effective nonlinear coefficient  $d_{\text{eff}}$  is given by

$$\begin{aligned} d_{\text{eff}}(z) &= \frac{1}{2} \chi_{\text{eff}}^{(2)} \\ &= \frac{1}{2} \sum_{j_i, j_s, j_p} \chi_{j_i, j_s, j_p}^{(2)}(z, \omega_i, \omega_s, \omega_p) v_{i; j_i}^* v_{s; j_s}^* v_{p; j_p}, \end{aligned} \quad (1.36)$$

As in subsection 1.5.1,  $\chi^{(2)}$  is assumed to be real, and each envelope  $A_j$  is assumed to be driven only by nonlinear polarization term  $P_{NL,j}$ . Substituting Eqs. (1.35) into Eqs. (1.1) yields the following set of equations

$$\frac{dA_i}{dz} = -i \frac{\omega_i d_{\text{eff}}}{n_i c} A_s^* A_p e^{-i\Delta k_0 z} \quad (1.37a)$$

$$\frac{dA_s}{dz} = -i \frac{\omega_s d_{\text{eff}}}{n_s c} A_i^* A_p e^{-i\Delta k_0 z} \quad (1.37b)$$

$$\frac{dA_p}{dz} = -i \frac{\omega_p d_{\text{eff}}^*}{n_p c} A_i A_s e^{+i\Delta k_0 z}, \quad (1.37c)$$

where the phase mismatches for TWM are given by

$$\Delta k_m = k_p - k_s - k_i - mK_g. \quad (1.38)$$

Analytical solutions to Eqs. (1.37) are given in Ref. [13]. CWEs for first-order QPM are obtained via the same substitutions described in subsection 1.5.1.

The effective nonlinear coefficient defined in Eq. (1.36) is the same as the one defined in Eq. (1.32) if the idler and signal both correspond to the same FH and the pump corresponds to the SH. In the rest of this dissertation, we always assume that the waves are linearly polarized or correspond to a bound waveguide mode, and so  $d_{\text{eff}}$  is real. For an all-e-wave interaction in a uniaxial crystal,  $d_{\text{eff}} = d_{33}$  [4]; for 1.064- $\mu\text{m}$  SHG in  $\text{LiNbO}_3$ ,  $d_{33} \approx 25.2 \text{ pm/V}$  [30].

### 1.5.3 Cascaded Phase Shifts

The coupled-wave systems given by Eqs. (1.33) and (1.37) support solutions in which energy is transferred efficiently between the different waves provided that phasematching (or quasi-phasematching) is satisfied. The solutions behave very differently when there is a large phase mismatch: in such cases, the waves instead rotate each other's phases without much energy being transferred between them. The resulting interactions closely resemble self- and cross-phase-modulation effects that occur in pure  $\chi^{(3)}$  media. Because these phase shifts are an inevitable consequence of the repeated forward and back-conversion that occurs in phase-mismatched two- and three-wave interactions, they are termed cascaded phase shifts [31]. Cascaded phase shifts play an important role in many of the processes discussed in this dissertation. Therefore, in this subsection we introduce the simplest case of cascaded phase shifts: those corresponding to self phase modulation of the first harmonic in an SHG-like experimental configuration.

Consider Eq. (1.33b) in the limit of a large phase mismatch. The resulting SH is comprised of a rapidly-varying component whose phase evolves with the driving polarization [Eq. (1.31b)], and a slowly-varying component that propagates linearly (phase determined by  $k_2$ ). The rapidly-varying component, which we denote as  $A_2^{(1)}$ ,

is therefore given by

$$A_2^{(1)} \approx -\frac{1}{\Delta k_0} \frac{\omega_2 d_{\text{eff}}^*}{n_2 c} A_1^2 e^{+i\Delta k_0 z} \quad (1.39)$$

One way to arrive at this equation is from integration by parts, but more general approaches such as multiple scale analysis can be employed [32]. If we assume  $A_2 = A_2^{(1)}$  and substitute Eq. (1.39) into Eq. (1.33a) we obtain the following equation for the evolution of the FH

$$\begin{aligned} \frac{dA_1}{dz} &= i \frac{1}{\Delta k_0} \frac{\omega_1^2 |d_{\text{eff}}|^2}{n_1 n_2 c^2} |A_1|^2 A_1 \\ &= -i \frac{3\omega_1 \chi_{\text{cascade}}^{(3)}}{8n_1 c} |A_1|^2 A_1, \end{aligned} \quad (1.40)$$

where  $\chi_{\text{cascade}}^{(3)}$  is an effective third-order susceptibility that arises due to the cascaded  $\chi^{(2)}$  process, and is given by

$$\chi_{\text{cascade}}^{(3)} = -\frac{1}{\Delta k_0} \frac{8\omega_1 |d_{\text{eff}}|^2}{3n_2 c} \quad (1.41)$$

The form of Eq. (1.40) thus gives rise to self phase modulation (SPM) of the FH. Similar effective  $\chi^{(3)}$  coefficients can be derived for each order of the QPM grating [see section 2.8].

One consequence of Eq. (1.40) is that a high rate of SPM can be obtained by choosing a small  $\Delta k$ . Such phase shifts can facilitate QPM supercontinuum generation, as discussed in later chapters. Of course, the cascading approximation must break down in the  $|\Delta k| \rightarrow 0$  limit. The maximum rate of SPM that can be obtained in practice is limited and varies for different types of nonlinear interaction. For interactions which are both continuous-wave (CW) and plane-wave, insight into the behavior of SHG and TWM processes can be gained through the geometrical approach to describing frequency conversion introduced in Ref. [16] (we utilize this approach in chapter 7).

For pulsed interactions, group velocity mismatch and the resulting frequency dependence of the phase mismatch is an important limiting factor (discussed in chapter

4). For interactions involving focused beams, diffraction effects arising from cascaded phase shifts can be important (these effects are discussed in chapter 8). A more detailed comparison between different  $\chi^{(3)}$ -like susceptibilities, and a discussion of their absolute magnitudes for  $\text{LiNbO}_3$ , is given in appendices 2.7 and 2.8.

## 1.6 Overview of this Dissertation

The three main topics discussed in this dissertation are supercontinuum (SC) generation in  $\chi^{(2)}$  media, difference frequency generation (DFG) and optical parametric amplification (OPA) in orientation-patterned GaAs, and optical parametric chirped pulse amplification (OPCPA) using chirped QPM gratings.

In chapter 2, we introduce a general model for nonlinear-optical interactions in QPM waveguides, and use that model to describe existing SC generation experiments. In chapter 3, we experimentally demonstrate SC generation and self-referencing with a Tm-doped fiber laser system, and show good agreement with numerical simulations. In chapter 4, we use the results of chapter 2 to design and simulate significantly improved QPM SC generation devices by use of dispersion-engineered ridge waveguides. In chapter 6, we demonstrate mid-infrared generation in orientation-patterned GaAs via difference frequency generation, and explore theoretically the extension of our experimental results to the high-gain regime. In chapter 7, we theoretically investigate chirped QPM gratings in the operating regimes of high gain and high pump depletion, showing their advantageous properties including suppression of back-conversion. In chapter 8, we describe a system in which our chirped QPM OPCPA devices are currently implemented, give an overview of our experimental results, and draw on the results of chapter 7 to explore in detail the design constraints and opportunities afforded by chirped QPM gratings for OPCPA systems. In chapter 9, we summarize our results, discuss several other contributions which are not included in this dissertation, and highlight several future and ongoing research directions.

# Chapter 2

## Modeling of Supercontinuum Generation QPM Media

### 2.1 Introduction

The generation of coherent light in the infrared from mode-locked lasers is of considerable interest for applications including frequency comb generation, spectroscopy, and few-cycle pulse generation [1, 2, 33, 34]. Absolute frequency calibration is usually achieved by self-referencing, for example via 1f-2f or 2f-3f interferometry [2, 1]. To perform self-referencing and to reach spectral regions not accessible through suitable or well-developed laser gain media, nonlinear-optical methods are usually required. Much attention has been given to  $\chi^{(3)}$ -based supercontinuum generation in optical fibers. Due to the high nonlinearity and engineerable dispersion available in fibers, spectra spanning multiple octaves can be achieved with relatively low pulse energies [33]. A limiting factor for SC generation is the transparency window of the fiber, and extending supercontinuum generation to non-silica fibers transparent in the mid-IR is an active area of research [34].

Compared to fibers, relatively little attention has been given to supercontinuum generation via  $\chi^{(2)}$  processes in quasi-phasematched (QPM) media, even though very high nonlinearities are readily available in QPM waveguides [35], and supercontinuum generation has been demonstrated experimentally [1, 2]. In contrast to methods

employing bulk QPM media, QPM waveguides enable highly nonlinear interactions when pumping with commercial mode-locked lasers (including fiber lasers) with few-nJ pulse energies. Additionally, nonlinear interactions have been demonstrated in QPM waveguides using GaAs [36], which has transparency up to 17  $\mu\text{m}$  and therefore offers the possibility of generating a supercontinuum across the mid-IR. In order to reach this goal, a detailed understanding and quantitative modeling of the nonlinear dynamics involved is first required. Progress has been made recently in modeling broadband  $\chi^{(2)}$  interactions [37], but a complete analysis including waveguide effects, competing nonlinearities, and the role that chirped QPM gratings can play in modifying spectral broadening processes is needed [38]. In order to reach the full potential of QPM waveguides for continuum generation, these effects must be modeled so that appropriate QPM gratings and, where necessary, dispersion-engineered waveguides can be designed.

In this chapter, we develop a model to describe nonlinear interactions in QPM waveguides. In order to test and calibrate the model, we simulate the experiments of Ref. [2], which were performed in reverse-proton-exchanged (RPE) LiNbO<sub>3</sub> waveguides, and show good agreement between experiments and simulations. Our analysis reveals the importance of several effects including the second-order ( $\chi^{(2)}$ ), instantaneous third-order ( $\chi_E$ ) and stimulated Raman scattering (SRS;  $\chi_R$ ) nonlinearities, the interaction between multiple waveguide modes, and the dispersion of the waveguides and associated modal overlaps.

In section 2.2 we introduce our nonlinear waveguide model. In section 2.3, the results of this model are compared to the 1043-nm-pumped experiments of Ref. [2]. In section 2.4 and the appendices at the end of this chapter (appendices 2.7 and 2.8), we show the importance of different  $\chi^{(2)}$  and  $\chi^{(3)}$  terms in reproducing the experimental results, and discuss how the model parameters were estimated in cases where absolute values could not be determined from available literature data. In section 2.5, our model is compared to the 1580-nm-pumped experiments of [2].

## 2.2 Numerical Model

In this section, we introduce a model to simulate ultra-broadband nonlinear interactions between multiple waveguide modes using an analytic-signal formalism for forward-propagating waves, similar to that described in Refs. [37, 39, 40, 41], generalized to describe waveguide interactions with multiple nonlinear-optical effects and multiple guided modes. The model automatically accounts for all of the conventional  $\chi^{(2)}$  interactions including second harmonic generation (SHG), sum frequency generation (SFG), and difference frequency generation (DFG) including intrapulse DFG. All  $\chi^{(3)}$  interactions can be accounted for as well, but we consider only self and cross phase modulation (SPM and XPM), and SRS.

Since RPE LiNbO<sub>3</sub> waveguides are weakly guiding and have historically been analyzed within that limit, we begin with the propagation equations given by Eq. (1.19), and make the approximation that the modes are linearly polarized parallel to the crystal c-axis ( $\hat{\mathbf{x}}$  direction),

$$\mathbf{E}_n(x, y, \omega) \approx B_n(x, y, \omega)\hat{\mathbf{x}}. \quad (2.1)$$

The required modal properties are determined from the proton concentration profile, which is calculated using a concentration-dependent diffusion model. This diffusion model and other properties of RPE waveguides are discussed in Ref. [42].

Since the electric field is real, it is sufficient to consider only its positive frequency components. We thus define frequency domain analytic-signal envelopes  $\tilde{A}_n$  for each waveguide mode in relation to the modal amplitudes introduced in Eq. (1.14), via

$$\tilde{\Phi}_n(z, \omega)u(\omega) = \frac{1}{2}\tilde{A}_n(z, \omega - \omega_{\text{ref}}) \exp[i(\beta_n(\omega) - \beta_{\text{ref}} + \omega_{\text{ref}}/v_{\text{ref}})z]. \quad (2.2)$$

As a result of the Heaviside step function  $u(\omega)$  on the left hand side of this equation,  $\tilde{A}_n(z, \omega < 0) = 0$ . We have also introduced a reference propagation constant  $\beta_{\text{ref}}$ , a reference group velocity  $v_{\text{ref}}$ , and a carrier frequency  $\omega_{\text{ref}}$ ; appropriate choices for these reference quantities are discussed below. The  $\exp(i\beta_n(\omega)z)$  phase factor in Eq. (2.2) cancels the  $\exp(-i\beta_n(\omega)z)$  in Eq. (1.14); the  $\tilde{A}_n(\omega)$  envelopes therefore accumulate

the full frequency-dependent phase  $\exp(-i\beta_n(\omega)z)$  during linear propagation. We choose this form so that each  $A_n(t)$  can be substituted directly into the (approximate) nonlinear polarization in the time domain [see Eq. (2.12) below].

Based on the assumption of  $x$ -polarized modes, the modes are only driven by the  $\chi_{xxx}^{(2)}$  tensor element. Since the crystallographic  $c$ -axis lies along our  $x$ -direction, the corresponding material tensor element is  $\chi_{333}^{(2)}$ ; when Kleinmann's symmetry applies, contracted notation can be used to write  $\chi_{333}^{(2)} = 2d_{33}$  [4]. Since only a single tensor element is involved, we simplify the notation according to  $\chi_{xxx}^{(2)} \rightarrow \chi^{(2)}$  and  $\chi_{xxxx}^{(3)} \rightarrow \chi^{(3)}$ ; throughout this chapter, subscripts indicate waveguide mode indices rather than Cartesian coordinate indices.

With the above assumptions and substitutions, the nonlinear polarization [introduced in Eq. (1.4)] can be expressed in the frequency domain as

$$\begin{aligned} \tilde{P}_{NL}(\omega)/\epsilon_0 = & \int_{-\infty}^{\infty} \chi^{(2)}(\omega, \omega', \omega - \omega') \tilde{E}(\omega') \tilde{E}(\omega - \omega') d\omega' + \\ & \int_{-\infty}^{\infty} \int_{-\infty}^{\infty} \chi^{(3)}(\omega, \omega', \omega'', \omega - \omega' - \omega'') \tilde{E}(\omega') \tilde{E}(\omega'') \tilde{E}(\omega - \omega' - \omega'') d\omega' d\omega''. \end{aligned} \quad (2.3)$$

To calculate the nonlinear coupling between envelopes  $\tilde{A}_n$ , suitable integrations involving  $\tilde{P}_{NL}$  are performed over the transverse spatial dimensions  $x$  and  $y$  of the waveguide. For the  $\chi^{(2)}$  nonlinear term, these modal overlap integrals (which we term effective modal susceptibilities) are given by

$$\begin{aligned} X_{npq}(z, \omega, \omega') = & \int_{-\infty}^{\infty} \chi^{(2)}(x, y, z; \omega, \omega', \omega - \omega') \\ & \times B_n(x, y, \omega) B_p(x, y, \omega') B_q(x, y, \omega - \omega') dx dy. \end{aligned} \quad (2.4)$$

where each  $X_{npq}(\omega, \omega')$  is thus an effective second-order nonlinear susceptibility for interactions involving waveguide modal amplitudes  $\tilde{A}_n(\omega)$ ,  $\tilde{A}_p(\omega')$  and  $\tilde{A}_q(\omega - \omega')$ .  $\chi^{(2)}$  is allowed to vary in the propagation coordinate  $z$  to model QPM, and also in  $x$ ,  $y$ , and  $z$  in order to model arbitrary variations in  $\chi^{(2)}$  associated with fabrication processes. These non-uniformities typically correspond to  $z$ -independent modifications

to  $|\chi^{(2)}|$ , of the form  $\chi^{(2)}(x, y, z) = f(x, y)\bar{d}(z)$ , where  $\bar{d}(z) = \pm 1$  represents the QPM patterning [42]; however, other profiles of  $\chi^{(2)}(x, y, z)$  can also occur [43]. For RPE LiNbO<sub>3</sub> waveguides, this  $f(x, y)$  is negligible close to the upper surface of the crystal, down to a depth  $h_{\text{WG}}$  below the surface [42]. Therefore,  $\chi^{(2)}(x, y, z) = 0$  for  $x < h_{\text{WG}}$  and  $|\chi^{(2)}(x, y, z)| = \chi_0^{(2)}$  for  $x \geq h_{\text{WG}}$ , where  $x = 0$  denotes the upper surface of the crystal and  $\chi_0^{(2)}$  is the relevant tensor element in the unperturbed material.

The effective third-order modal susceptibilities  $X_{npqr}(\omega, \omega', \omega'')$ , corresponding to interactions involving  $A_n(\omega)$ ,  $\tilde{A}_p(\omega')$ ,  $\tilde{A}_q(\omega'')$  and  $\tilde{A}_r(\omega - \omega' - \omega'')$ , are given by

$$\begin{aligned} X_{npqr}(\omega, \omega', \omega'') &= \chi^{(3)}(\omega, \omega', \omega'', \omega - \omega' - \omega'') \\ &\quad \times \Theta_{npqr}(\omega, \omega', \omega''), \end{aligned} \quad (2.5)$$

where the frequency-dependent overlap integral  $\Theta_{npqr}$  is defined as

$$\Theta_{npqr}(\omega, \omega', \omega'') = \int_{-\infty}^{\infty} B_n(\omega) B_p(\omega') B_q(\omega'') B_r(\omega - \omega' - \omega'') dx dy. \quad (2.6)$$

In Eq. (2.5),  $\chi^{(3)}$  is assumed to be independent of position, as is usually the case even in QPM media.

Propagation equations for  $\tilde{A}_n(z)$  can be derived using Eqs. (2.3-2.5), but their numerical evaluation would involve time-consuming integrals in the frequency domain. To derive a simple yet accurate propagation equation, note that the scale of  $B_n(x, y, \omega)$  in Eq. (2.2) is arbitrary since any frequency-dependent scale factor applied to  $B_n$  can be absorbed into  $\tilde{A}_n$ . Hence,  $B_n$  can be chosen so as to minimize the frequency-dependence of the overlap integral for the fundamental waveguide mode,  $X_{000}$ , given in Eq. (2.4). We therefore introduce a frequency dependent normalization for the modes, according to

$$\int_{-\infty}^{\infty} |B_n(x, y, \omega)|^2 dx dy = g_n(\omega) \quad (2.7)$$

where the form of  $g_n(\omega)$  is chosen to simplify the numerics. To satisfy Eq. (2.7), we define  $B_n(x, y, \omega) \equiv (g_n(\omega))^{1/2} \bar{B}_n(x, y, \omega) / (\int_{-\infty}^{\infty} |\bar{B}_n(x, y, \omega)|^2)^{1/2}$ , where  $\bar{B}_n(x, y, \omega)$

are numerically-determined, un-normalized mode profiles. The strength of the nonlinear interactions will generally scale inversely with the mode area, which is defined as

$$A_{\text{eff},n}(\omega) \equiv \frac{\left(\int_{-\infty}^{\infty} |\bar{B}_n|^2 dx dy\right)^2}{\int_{-\infty}^{\infty} |\bar{B}_n|^4 dx dy} \quad (2.8)$$

for mode  $n$  at frequency  $\omega$ . In this chapter we choose  $g_n(\omega) = A_{\text{eff},n}(\omega)^{1/3}$ , since this choice renders  $X_{npq}$  dimensionless and  $X_{000}$  weakly dispersive. It is also possible to formally optimize the  $g_n(\omega)$  profile in order to minimize the frequency dependence of  $X_{npq}$  in various ways; these optimization problems (which are convex) will be discussed in appendix 5.8. With the above choice of  $g_n(\omega)$ , the  $\chi^{(3)}$  terms  $X_{npqr}$  are not dimensionless. As a result, a single set of functions  $g_n(\omega)$  cannot simultaneously account for the dependence of  $\chi^{(2)}$  and  $\chi^{(3)}$  modal overlap integrals on optical frequency. Despite this limitation, we find that with the above choice of  $g_n$  experiments can be described quantitatively while neglecting the dispersion of both the modal overlap integrals  $X_{npq}$  and  $X_{npqr}$ .

To determine a propagation equation for the modes of the RPE waveguide, we take the system of equations given by Eq. (1.19), neglect equations corresponding to backwards-propagating modes [39, 40], and approximate the nonlinear coupling coefficients. The second-order effective modal susceptibilities are approximated according to

$$X_{npq}(z, \omega, \omega') \approx \theta_{npq} \chi_0^{(2)} \bar{d}(z) \quad (2.9)$$

where each  $\theta_{npq}$  is a constant,  $\bar{d}(z) = \pm 1$  represents the spatial profile of the QPM grating,  $\chi_0^{(2)}$  is the nonlinear susceptibility of the unperturbed material, and  $\theta_{npq}$  is a modal overlap integral. Both  $\chi_0^{(2)}$  and  $\theta_{npq}$  are evaluated at a specific set of frequencies (typically at frequencies  $\omega_0$  and  $2\omega_0$  for input center frequency  $\omega_0$ , since the initial dynamics correspond to an SHG-like interaction). The (possibly smoothly-chirped) QPM grating profile  $\bar{d}(z)$  is expanded in a Fourier series according to Eq. (1.25). Based on the assumed form of  $\chi^{(2)}(x, y, z)$  discussed above, with  $|\chi^{(2)}(x, y, z)| =$

$f(x, y)$  for some function  $f$ , the Fourier coefficients of this series are given by Eq. (1.26) and the grating phase  $\phi_G(z)$  is given by Eq. (1.24).

The third-order susceptibility is approximated according to

$$\chi^{(3)}(\omega, \omega', \omega - \Omega, \Omega - \omega') \approx \chi_E + \chi_R(\Omega) \quad (2.10)$$

where  $\chi_E$  is the instantaneous (frequency-independent) electronic susceptibility, and  $\chi_R(\Omega)$  is the Raman susceptibility (which depends only on the Raman frequency shift  $\Omega$ ). In writing Eq. (2.10), the arguments of  $\chi^{(3)}$  have been expressed in terms of  $\Omega$  (representing a frequency shift),  $\omega$  (the driven optical frequency) and  $\omega'$  (another optical frequency). Given Eq. (2.10), the third-order effective susceptibilities are approximated according to

$$X_{npqr}(\omega, \omega', \omega - \Omega, \Omega - \omega') = \theta_{npqr} (\chi_E + \chi_R(\Omega)) \quad (2.11)$$

where each  $\theta_{npqr}$  is a constant. In making the above approximations, we neglect the dependence of the  $\chi^{(2)}$ ,  $\chi^{(3)}$ , and  $\chi_R$  susceptibilities on optical frequency, but the dependence of  $\chi_R$  on the Raman frequency shift, and hence the Raman response function, is retained.

Finally, by making use of the analytic signal formalism for the mode envelopes, the following set of propagation equations can be obtained by substituting Eqs. (2.1-2.11) into Eq. (1.19) [38]

$$\begin{aligned} \frac{\partial \tilde{A}_n}{\partial z} + i \left[ \beta_n - \beta_{\text{ref}} - \frac{\omega - \omega_{\text{ref}}}{v_{\text{ref}}} - i \frac{\alpha_n}{2} \right] \tilde{A}_n = \\ - i \frac{\omega^2 u}{g_n \beta_n c^2} \left\{ \sum_{p,q} \sum_m \bar{d}_m \theta_{npq} \mathcal{F} \left[ \frac{A_p A_q}{2} e^{i\phi_m} + A_p^* A_q e^{-i\phi_m} \right] + \right. \\ \left. \sum_{p,q,r} \frac{3\theta_{npqr} \chi_E}{8} \mathcal{F} [A_p A_q^* A_r] + \sum_{p,q,r} \frac{3\theta_{npqr} \chi_{R,pk}}{8} \mathcal{F} [\mathcal{F}^{-1} [\mathcal{F} [A_p A_q^*] H_R] A_r] \right\}, \end{aligned} \quad (2.12)$$

where  $\beta_n(\omega)$  is the modal propagation constant of mode  $n$ , and  $\alpha_n$  is the loss coefficient

of mode  $n$ , which we assume in this chapter to be non-dispersive except near the 2.85- $\mu\text{m}$  OH absorption feature of RPE LiNbO<sub>3</sub>. The envelope phase is given by  $\phi_m(z, t) = \omega_{\text{ref}}t - (\beta_{\text{ref}} - \omega_{\text{ref}}/v_{\text{ref}})z - m\phi_G(z)$ . Summation is performed over all the relevant positive and negative QPM orders  $m$ , with phases  $\exp(i\phi_m)$  for SFG terms (which have form  $A_p A_q$ ), and phases  $\exp(-i\phi_m)$  for DFG terms (form  $A_p^* A_q$ ). In this way, each QPM order is associated with both a corresponding conjugate SFG and DFG process; this association is required for energy conservation when the summation is performed over a finite range of index  $m$ .

For a particular input center frequency  $\omega_c$ , we usually choose  $\omega_{\text{ref}} \approx 2\omega_c$ ,  $\beta_{\text{ref}} = \beta_0(2\omega_c)$ , and  $v_{\text{ref}}^{-1} = (\partial\beta_0/\partial\omega)|_{\omega=\omega_c}$  (where this latter choice is appropriate since, in many cases, only energy which remains overlapped temporally with the input pulse contributes significantly to the nonlinear dynamics). The choice of  $\omega_c$  plays a relatively minor role in modeling SC generation, since the generated spectrum can span several octaves, and an additional numerical buffer region is required either at high frequencies where the envelopes are negligible, or at negative frequencies where the envelopes are identically zero, in order to avoid aliasing effects.

A useful property of Eq. (2.12) is that the nonlinear polarization can be calculated via products of time-domain mode envelopes  $A_n(z, t)$ . This property arises from the form of the envelopes defined in Eq. (2.2), and having neglected (or simplified, in the case of SRS) the frequency dependence of the modal overlap integrals and nonlinear susceptibilities.

Third-order nonlinear effects are described by the final two terms in Eq. (2.12). We define a normalized Raman transfer function according to

$$\chi_R(\Omega) \equiv \chi_{R,pk} H_R(\Omega) \quad (2.13)$$

where  $\chi_{R,pk}$  is the peak Raman susceptibility, and  $H_R(\Omega)$  is the Raman transfer function.  $H_R(\Omega)$  is the Fourier transform of the Raman temporal response function  $h(t)$ . The peak Raman frequency  $\Omega_{pk}$  is defined as the frequency shift for which  $|\Im[\chi_R]|$  is largest;  $H_R$  is normalized so that  $\Im[H_R(\pm\Omega_{pk})] = \mp 1$ , and the peak Raman susceptibility is defined as  $\chi_{R,pk} \equiv |\Im[\chi_R(\Omega_{pk})]|$ . The Raman transfer function is discussed

in appendix 2.7. The values we use for the  $\chi^{(2)}$  and  $\chi^{(3)}$  nonlinear susceptibilities are discussed in appendix 2.7 and section 2.4.

Most of the  $\chi^{(2)}$  interactions modeled by Eq. (2.12) are highly phase mismatched. In particular, for a given process (SHG, SFG or DFG involving a particular combination of waveguide modes), usually at most one QPM order, denoted  $m_0$ , is close to phasematching. To model a different QPM order  $m$ , the grid size required increases approximately in proportion to  $|m - m_0|$ , while the contribution to the pulse dynamics is (approximately) proportional to  $1/|m - m_0|^3$  [based on Eqs. (1.26) and (1.40)]. In appendix 2.8, we discuss these terms in more detail and calculate their contribution to the total SPM of the input pulse. In some cases, instead of including higher order terms explicitly in the simulations, their leading-order contributions to the pulse dynamics can be calculated analytically via the cascading approximation, which yields an effective instantaneous  $\chi^{(3)}$  coefficient for each term. These coefficients can then be added to the true instantaneous  $\chi^{(3)}$  coefficient  $\chi_E$  in Eq. (2.12), yielding an adjusted and possibly  $z$ -dependent effective value of  $\chi_E(z)$ .

In the following sections, Eq. (2.12) is evaluated numerically for several different cases. These equations are solved in the frequency domain, using a Runge Kutta method. Note that although the envelopes  $\tilde{A}_n$  yield a system of equations with a relatively intuitive form, for numerical robustness it is often advantageous to solve in terms of envelopes similar to  $\Phi_n$ , i.e. envelopes whose phase remains constant during linear-optical propagation; this is the approach we take in the numerical solutions.

## 2.3 Comparison to 1043-nm-Pumped Experiments

In this section, we test the nonlinear waveguide model given by Eq. (2.12) by comparing it to the 1043-nm-pumped experiments of Ref. [2]. In those experiments, broadband spectra were obtained when a particular chirped QPM grating profile was used, but not when a simple unchirped QPM grating was used. The pump pulses had a duration of 150 fs full-width at half-maximum (FWHM) and an energy of approximately 3.45 nJ inside the waveguide. The QPM grating had a length of 29 mm and the grating period was varied from 7  $\mu\text{m}$  to 11  $\mu\text{m}$  over this length by a linear

chirp (i.e.  $dK_g/dz = \text{constant}$ ). Based on waveguide fabrication parameters and the concentration-dependent diffusion model given in Ref. [42], the area of the  $\text{TM}_{00}$  mode (mode “0”) is  $16.30 \mu\text{m}^2$  at 1043 nm and  $6.37 \mu\text{m}^2$  at 521.5 nm. We label the waveguide modes in order of their eigenvalues, starting at “0” for the mode with the highest mode index (the “lowest-order” mode). For the modal overlap integrals,  $\theta_{000} \approx 0.817$ , and  $\theta_{0000} \approx 0.3925 \mu\text{m}^{-2/3}$  (evaluated for SPM at 1043 nm). For the  $\text{TM}_{10}$  mode (mode “4”), which is also included in the model explicitly for the results discussed in this section,  $\theta_{400} \approx 0.162$ , and the mode area at 521.5 nm is  $9.80 \mu\text{m}^2$ . We apply the waveguide cascading approximation described in appendix 2.8 to remove all but the first-order QPM interactions in Eq. (2.12). We assume a  $\text{sech}^2$  input pulse profile with flat spectral phase. Estimates for the relevant nonlinear susceptibilities are given in appendix 2.7.

In Figures (2.1a) and (2.1b) we show experimental and simulated output spectra corresponding to Fig. 4 of Ref. [2], respectively. The simulations are in quite good agreement with the experiments. For the 7-11  $\mu\text{m}$  chirped-QPM-period case, the simulation captures the main features seen experimentally, namely the high power spectral density (PSD) between 1  $\mu\text{m}$  and 1.2  $\mu\text{m}$ , and the “pedestal” generation between 1.4 and 1.75  $\mu\text{m}$ ; the reduction in PSD between 1.2 and 1.4  $\mu\text{m}$  in the experiment is also reproduced in the simulation (although there is a larger reduction in the latter). For the 7-8  $\mu\text{m}$  QPM period case, the simulated spectrum falls off at approximately the same rate as in the experiment, reaching  $10^{-6}$  of its peak at 1.45  $\mu\text{m}$ . The simulated spectra were averaged over five simulations with semiclassical quantum noise seeding added to the input pulse.

To understand how the spectral features in Fig. 2.1(b) arise, we first show in Fig. 2.2 the propagation of the pulse in the time domain for the case with 7-11  $\mu\text{m}$  QPM period. Fig. 2.2 represents a single simulation with no averaging. At the start of the QPM grating, the effective low-frequency  $\chi^{(3)}$ ,  $\chi_{\text{total}}^{(3)}$  [defined in Eq. (2.28)], is negative. This negative effective  $\chi^{(3)}$  arises from cascaded  $\chi^{(2)}$  interactions, and is discussed in detail in appendix 2.8 and section 2.4. Previous work has shown that cascaded quadratic nonlinearities by themselves can be used to support bright solitons and pulse compression, concepts closely related to supercontinuum generation

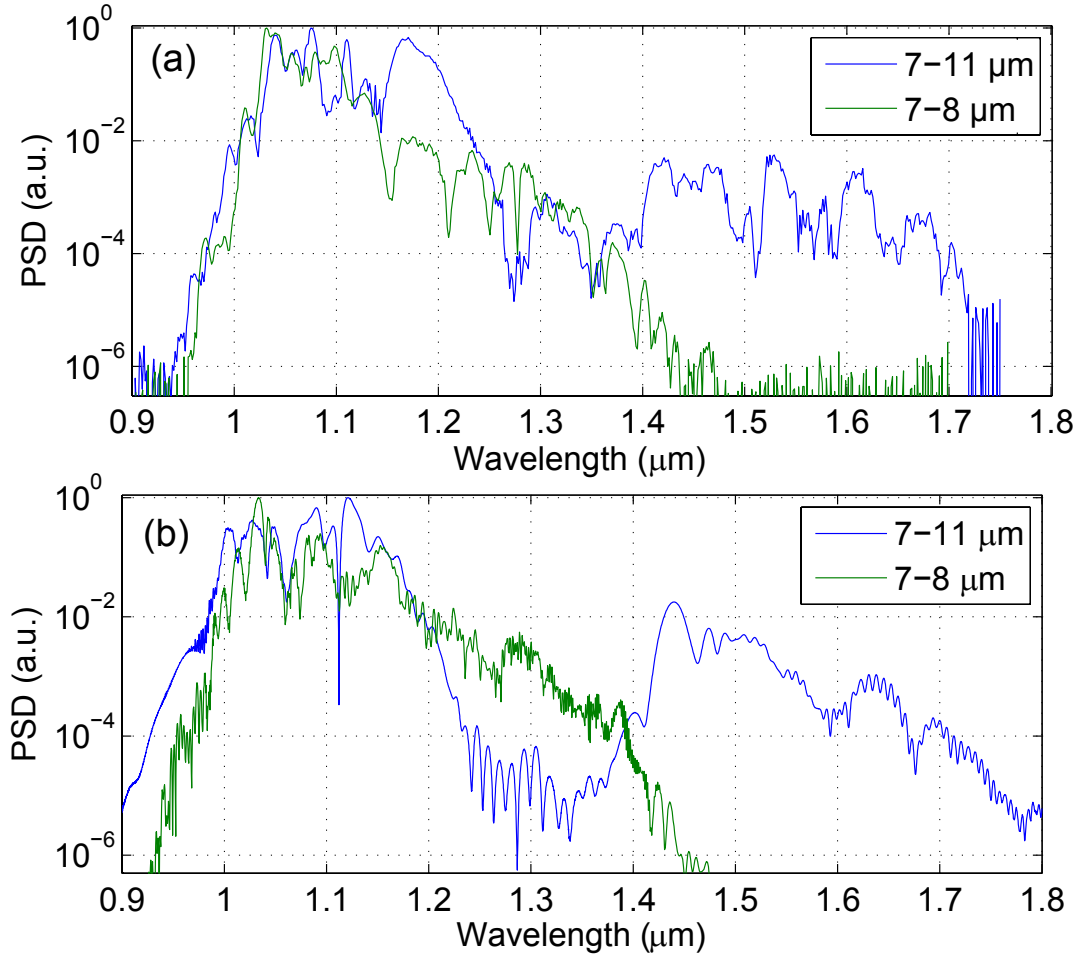


Figure 2.1: Output spectrum for the 1043-nm-case of Ref. [2], labeled with the range of periods in the linearly chirped QPM grating. The pulse energy is 3.45 nJ in all cases. (a) Experimentally measured, (b) numerically simulated using Eqs. (2.12). A QPM grating with a weak linear chirp from 7-8  $\mu\text{m}$  is included for comparison, showing reduced spectral broadening.

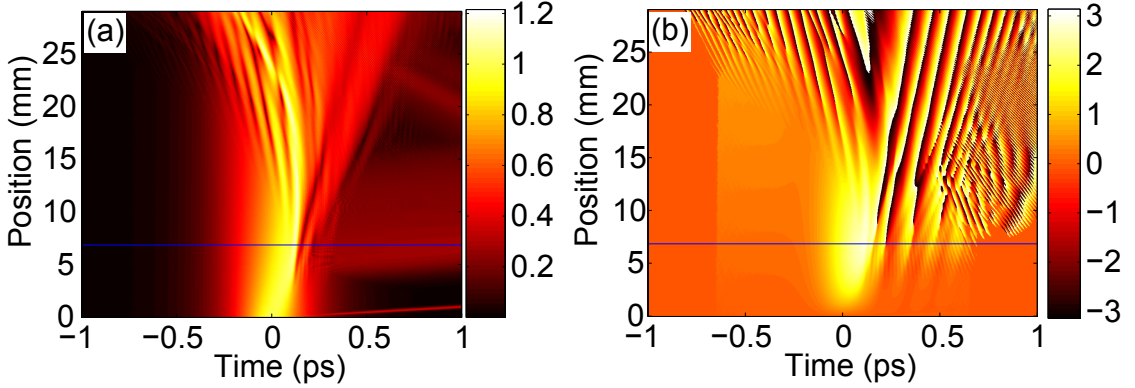


Figure 2.2: Pulse evolution in the time-domain for the simulation shown in Fig. 2.1(b), with QPM period varied from 7-11. (a) The pulse amplitude; the color bar represents  $|A_0(z, t)|$ . (b) The phase of the first harmonic part of the pulse (color bar in radians).

[44, 45, 46, 47, 48]. However, near the start of the QPM grating, there is only a relatively small amount of pulse compression evident in Fig. 2.2(a), and similarly only a small amount of nonlinear phase is evident in Fig. 2.2(b), much less than would be predicted from calculations based on  $\chi^{(2)}$  effects alone. This behavior occurs due to the competition between cascaded  $\chi^{(2)}$  and  $\chi^{(3)}$  SPM effects, which have opposite sign for this case. As a result,  $\chi_{\text{total}}^{(3)}$  is initially small, and actually changes sign as the pulse propagates due to the z-dependence of the contribution from the chirped QPM grating.

This change of sign of the effective  $\chi^{(3)}$  can be seen in Fig. 2.2(b), which shows the phase of the pulse after numerically filtering out the second harmonic spectral components. An intensity-dependent phase is accumulated near the start of the QPM grating, but after approximately 7 mm, the rate of phase accumulation changes sign, suggesting that  $\chi_{\text{total}}^{(3)}(z) \approx 0$  at that point. For comparison, we estimate  $\chi_{\text{total}}^{(3)}(z)$  analytically with Eq. (2.28), evaluated for the local grating k-vector  $K_g(z)$  and the local frequency of the pulse  $\omega_{FH}(z)$ . This latter quantity is defined by  $\omega_{FH}(z) = [\int \omega |\tilde{A}_0(z, \omega)|^2 d\omega] / [\int |\tilde{A}_0(z, \omega)|^2 d\omega]$ , where integration is performed only over the first harmonic (FH) spectral region. Eq. (2.28) is then evaluated using  $\omega_{FH}(z)$  for the frequency and  $K_g(z)$  for the local grating k-vector. The solid blue lines in Fig. 2.2

show the position at which  $\chi_{\text{total}}^{(3)} = 0$  according to this calculation. This position is close to where the simulated rate of phase accumulation changes sign. Thus, the initial behavior of the pulse in Fig. 2.2 is described quite well by this simplified picture.

Next, to understand the origin of the spectral components between 1.4 and 1.75  $\mu\text{m}$ , we show in Fig. 2.3(a) the propagation of the pulse in the frequency domain (plotted on a log scale). The generation of spectral components  $>1.4 \mu\text{m}$  can be seen to occur around 15 mm from the start of the QPM grating. To help explain this and other processes, we show in Fig. 2.3(b) a simulated cross-FROG (frequency resolved optical gating [49]) spectrogram at the output of the QPM grating, using a 150-fs Gaussian gate pulse. Due to a Raman self frequency shift (SFS) effect [50], the FH pulse shifts to lower frequencies and leaves behind a “trail” consisting of slower-group-velocity spectral components between 275 and 325 THz; simultaneously, a second harmonic (SH) wave is generated around a frequency determined by the spatial dependence of the QPM period, and also by the spatial dependence of the frequency, velocity, and propagation coefficient of the FH pulse. The generation of such waves is expected when there is a significant group index mismatch in addition to a large phase mismatch (in such a nearly-phasematched SHG interaction, SH components are not fully back-converted to the FH by the phase mismatch before they escape from the FH due to GVM). The group index difference between 521.5 and 1043 nm is  $\approx 0.287$  in this case, and the group velocity dispersion (GVD) is positive (and comparable to that of bulk  $\text{LiNbO}_3$ ); the phase mismatch is discussed in section 2.4. In Fig. 2.3 this SH wave is shown over a limited temporal range (with delay-dependent frequencies of around 460 THz), but it extends over approximately 24 ps (with frequency increasing with delay), corresponding to the relative delay accumulated between the SH and FH frequencies over the length of the waveguide.

Due to the presence of the self frequency shifted FH pulse, its Raman trail, and the generated SH pulse, spectral components between 1.3 and 1.75  $\mu\text{m}$  can be generated by at least two processes. One of these processes is optical parametric amplification (OPA) of quantum noise: spectral components between 1.4 and 1.75  $\mu\text{m}$  are generated via OPA between the SH pulse (which acts as the “pump”) and quantum noise

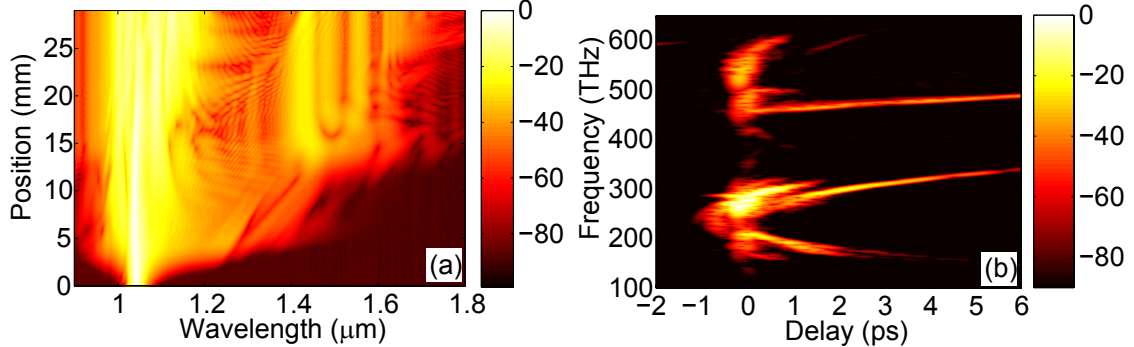


Figure 2.3: (a) Spectrum versus position in the QPM grating, showing spectral components  $>1.4 \mu\text{m}$  which are generated from the semiclassical quantum noise floor included in the simulation. (b) Simulated cross-FROG spectrogram (150 fs gate) of the pulse at the output of the QPM grating, plotted on a dB scale.

components around the input frequency. The generation of these spectral components from the (semiclassical) noise floor is evident in Fig. 2.3(a); when quantum noise is turned off in the simulation, these spectral components become much weaker (see Fig. 2.5). Because of the high SH intensities involved, the OPA process can have high gain, provided that phasematching is satisfied. The gain for this process is quite subtle, since the frequency and intensity of the generated SH wave depends on position  $z$  via the QPM chirp and Raman SFS of the FH pulse, and hence there is a spatially-dependent “pump” frequency and intensity; additionally, there is a spatially-dependent QPM period, and rapid temporal walk-off between pump, signal and idler spectral components. Thus, this situation differs from the chirped QPM OPA interactions studied elsewhere [51, 52, 53], where narrow-bandwidth pumps were assumed. Nonetheless, Eq. (2.12) captures this effect. In the spectrogram, the amplified noise can be seen in the crescent-like pattern around the FH which extends out to approximately (6 ps, 330 THz) (for the “signal” components) and (2 ps, 170 THz) (for the “idler” components). In addition to this noise-seeded OPA process, there is a coherent process by which spectral components  $>1.3 \mu\text{m}$  are generated. This process involves the generated SH pulse mixing with the FH pulse and its Raman trail according to phasematched DFG, and can be seen in the weaker “outer” crescent-like pattern which extends to approximately (0.8 ps, 150 THz) in Fig. 2.3(b).

Since the broad bandwidth of the pulses discussed in this section arises primarily from quantum noise, the pulses are of limited use for any frequency-comb-related applications. Coherent supercontinua are discussed and modeled in section 2.5 and chapter 3.

## 2.4 Model Calibrations for 1043-nm-Pumped Experiments

In this section, we discuss which effects modeled by Eq. (2.12) were important in the above simulations, the sensitivity of the simulations to those effects, and how we estimate the values of the  $\chi^{(3)}$  nonlinear coefficients.

In Fig. 2.2, we showed that the cascaded  $\chi^{(2)}$  and  $\chi^{(3)}$  SPM effects were of opposite sign and comparable magnitude. Here, we will quantify these terms, and hence the initial dynamics, by analyzing the  $\chi^{(3)}$  and cascaded  $\chi^{(2)}$  contributions to SPM near the input of the QPM grating. The effective low-frequency-shift third-order nonlinear susceptibility,  $\chi_{\text{total}}^{(3)}$ , is given in Eq. (2.28) as

$$\chi_{\text{total}}^{(3)}(z) = \chi_E + \chi_{R,pk} H_R(0) + \sum_{m,q} \chi_{\text{cascade}}^{(m,q)}(z). \quad (2.14)$$

This total susceptibility determines the initial rate of SPM for narrow-bandwidth pulses. There are contributions to  $\chi_{\text{total}}^{(3)}$  from  $\chi_E$ , SRS, and from each waveguide mode at each order of the QPM grating via cascaded  $\chi^{(2)}$  interactions. Each of these cascaded  $\chi^{(2)}$  contributions, labeled  $\chi_{\text{cascade}}^{m,q}$ , arises from an SHG interaction involving QPM order  $m$ , SH waveguide mode index  $q$  and FH waveguide mode index 0;  $\chi_{\text{cascade}}^{m,q}$  are given in appendix 2.8 in terms of the corresponding phase mismatches  $\Delta k_{m,q00}$  [defined in Eq. (2.26)]. The necessary parameters for calculating  $\chi_{\text{cascade}}^{m,q}$  for these experiments are given in table 2.2. There are also small but non-negligible nonlinear phase shifts due to cross phase modulation and cross Raman scattering from the SH acting on the FH pulse; these effects are captured by the numerical simulations (e.g. those shown in Fig. 2.1), but we neglect them in the following discussion.

At the input of the QPM grating (local QPM period  $7 \mu\text{m}$ ), and with  $d_{33} = 25.2 \text{ pm}^2/\text{V}^2$ ,  $\sum \chi_{\text{cascade}}^{m,q} = -9140 \text{ pm}^2/\text{V}^2$ . The largest-magnitude term is  $\chi_{\text{cascade}}^{1,0} = -7915 \text{ pm}^2/\text{V}^2$ , which corresponds to first-order QPM involving the lowest-order waveguide mode at the SH frequency. In appendix 2.7, we find that for congruent LiNbO<sub>3</sub>,  $\chi_E + H_R(0) = 6365 \text{ pm}^2/\text{V}^2$ . Based on this  $\chi^{(3)}$  contribution, the effective low-frequency  $\chi^{(3)}$  would be very small if only the lowest-order waveguide mode, first-order QPM interaction ( $\chi_{\text{cascade}}^{1,0}$ ) was included in Eq. (2.12). With all the  $\chi^{(2)}$  terms included,  $\chi_{\text{total}}^{(3)} \approx -2775 \text{ pm}^2/\text{V}^2$  is negative, but has much lower magnitude than predictions based on the  $\chi^{(2)}$  terms alone. The next two largest cascade terms are  $\chi_{\text{cascade}}^{-1,0} = -830 \text{ pm}^2/\text{V}^2$  (corresponding to a negative order of the QPM grating), and  $\chi_{\text{cascade}}^{1,4} = -413 \text{ pm}^2/\text{V}^2$ .

As the pulse propagates through the waveguide, the Raman SFS effect causes  $\Delta k_{0,000}$  (the phase mismatch for SHG involving the lowest-order waveguide modes and with QPM order 0) to decrease (the phase mismatch decreases with wavelength). Therefore, for a constant  $K_g(z)$  profile,  $\Delta k_{1,000} = \Delta k_{0,000} - K_g(z)$  would also decrease with  $z$ . However, the QPM chirp corresponds to a period increasing from  $7 \mu\text{m}$  (input) to  $11 \mu\text{m}$  (output), and hence to a decreasing  $K_g(z)$  profile; the presence of the QPM chirp therefore causes  $\Delta k_{1,000}$  to increase with  $z$ . The net result of the Raman SFS effect and the QPM chirp, for this particular case, is that  $\chi_{\text{cascade}}^{(3)}$  actually changes sign during propagation, as shown in Fig. 2.2(b). Since the cancellation between the cascaded  $\chi^{(2)}$  and  $\chi^{(3)}$  terms hindered conventional spectral broadening via SPM, the dominant mechanism for generating spectral components  $>1.4 \mu\text{m}$  was optical parametric amplification of quantum noise. This mechanism is consistent with the results of Ref. [2], where observation of the carrier-envelope-offset frequency  $f_{\text{CEO}}$  was reported when using a 1580-nm pump, but not for the 1043-nm-pumping case. For many applications, the coherence of the supercontinuum is important; if the cancellation of SPM effects were reduced, the intensity of the SH could be reduced and the rate of FH SPM increased, thereby allowing for coherent supercontinuum generation. We discuss such cases in chapter 4.

The above analysis of SPM effects depends on the low-frequency  $\chi^{(3)}$  terms  $\chi_E$  and  $H_R(0)\chi_{R,pk}$ , whose sum can be determined quite accurately (see appendix 2.7).

However, both  $\chi^{(3)}$  parameters must be known or estimated individually for the simulations; in appendix 2.7, we show that it is difficult to use available literature data to absolutely calibrate both  $\chi_E$  and  $\chi_{R,pk}$  simultaneously. To show the importance of these terms beyond the  $\chi^{(2)} - \chi^{(3)}$  competition calculated above, we first show that SRS must be included in the model in order to reproduce the experimental results. The importance of SRS is shown in Fig. 2.4, where we plot the output spectrum for several values of  $\chi_E$  while setting  $\chi_{R,pk} = 0$ . For the case with  $\chi_{R,pk} = 0$  and  $\chi_E = 0$ , there is a long-wavelength pedestal which extends to  $>2 \mu\text{m}$ ; this pedestal extends further than the spectra shown in Figs. (2.1a) and (2.1b). However, based on the results of appendix 2.7,  $\chi_E + H_R(0)\chi_{R,pk} \approx 6365 \text{ pm}^2/\text{V}^2$ . When  $\chi_E$  is increased towards this value (while still maintaining the false assumption that  $\chi_{R,pk} = 0$ ), the spectral broadening is reduced significantly. For the  $\chi_E > 3000 \text{ pm}^2/\text{V}^2$  cases in Fig. 2.4, the bandwidth is much narrower than in the experiments. Furthermore, for each case, there is no spectral “flattening” between 1 and  $1.2 \mu\text{m}$ , and no dip between  $1.2$  and  $1.4 \mu\text{m}$ ; both of these spectral features can be seen in Figs. (2.1a) and (2.1b).

The results of Fig. 2.4 show that simulations with SRS neglected differ significantly from the experimental results; the results of section 2.3 show that when all the terms in Eq. (2.12) are included, our model is sufficient to reproduce the spectral features observed experimentally, without any adjustments to known model parameters. We can therefore conclude that SRS plays an important role in the dynamics and must be included in the model. Note, in particular, that including SRS leads to the spectral “flattening” shown in Figs. (2.1a) and (2.1b). The frequency range over which the pulse spectrum is flattened is comparable to the Raman peak with largest frequency shift ( $\approx 19 \text{ THz}$ ) (see Fig. 2.7). Since this flattening also only occurs when SRS is included in the model, we can identify this effect as a Raman SFS.

Next, we consider the values of  $\chi_E$  and  $\chi_{R,pk}$ . To estimate these parameters, we performed simulations of the experiments discussed in section 2.3 for several values  $\chi_{R,pk}$  at fixed  $(\chi_E + H_R(0)\chi_{R,pk})$ , and compared the resulting simulated spectra to the experimentally observed spectrum in Fig. 2.1(a). In order to agree reasonably well, the spectrum should exhibit the spectral flattening between 1 and  $1.2 \mu\text{m}$  (SFS), and have a supercontinuum “pedestal” between  $1.4$  and  $1.75 \mu\text{m}$  with a PSD around  $10^{-3}$

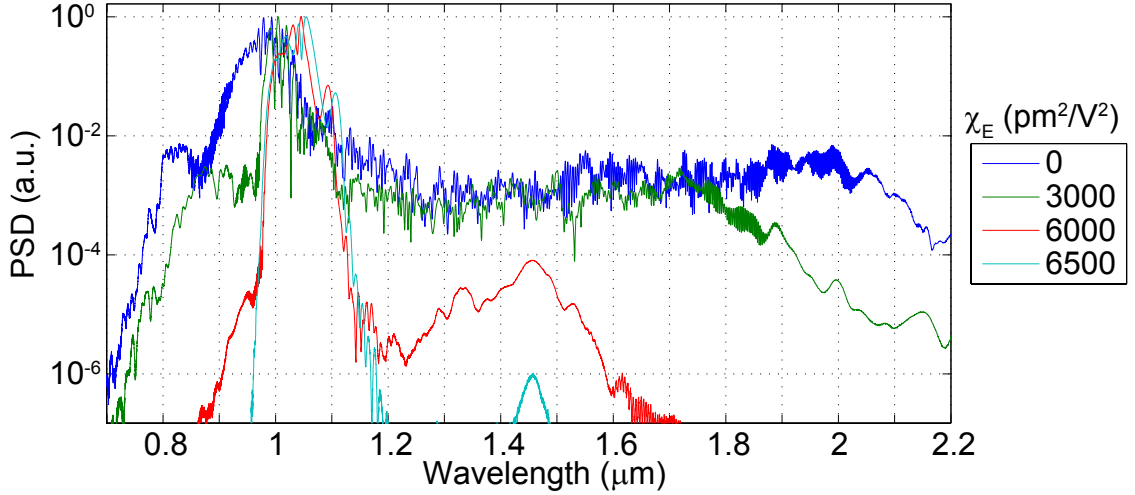


Figure 2.4: Spectrum for several values of  $\chi_E$ , with  $\chi_{R,pk} = 0$ . The values for  $\chi_E$  are given in the legend in units of  $\text{pm}^2/\text{V}^2$ ; the other model parameters are the same as those used in Fig. 2.1(b). The reduced broadening for larger values of  $\chi_E$  is a result of partial cancellation with the cascade  $\chi^{(3)}$ , which is of opposite sign.

smaller than the peak. To illustrate this numerical procedure, we show in Fig. 2.5 example spectra for several representative values of  $\chi_{R,pk}$  at fixed  $\chi_E + H_R(0)\chi_{R,pk}$ ; the spectra are averaged over five simulations (with different pseudo-random semiclassical quantum noise inputs) for each value of  $\chi_{R,pk}$ . For the dashed black line in Fig. 2.5, quantum noise was neglected. This case is plotted in order to indicate the importance of noise amplification in these simulations, as discussed in section 2.3. In comparing the spectrum as a function of  $\chi_{R,pk}$  to the experimental results in Fig. 2.1(a), we find that for values of  $\chi_{R,pk} < 5000 \text{ pm}^2/\text{V}^2$  the long-wavelength pedestal is weaker and extends to shorter wavelengths, and the spectral broadening between 1 and 1.2  $\mu\text{m}$  is reduced; for  $\chi_{R,pk} > 6000 \text{ pm}^2/\text{V}^2$ , the opposite trends hold. Based on simulations similar to those in Fig. 2.5, we estimate  $\chi_E = 5.46 \times 10^3 \text{ pm}^2/\text{V}^2$  and  $\chi_{R,pk} = 5.30 \times 10^3 \text{ pm}^2/\text{V}^2$ .

In relation to Fig. 2.3(b), increasing  $\chi_{R,pk}$  increases the intensity of the generated SH wave (the part of the SH which extends to  $>6$  ps in the spectrogram), and hence the OPA gain (since this SH wave acts as the pump for the OPA process), which in turn leads to a stronger  $>1.4\text{-}\mu\text{m}$  pedestal generation, which corresponds to the

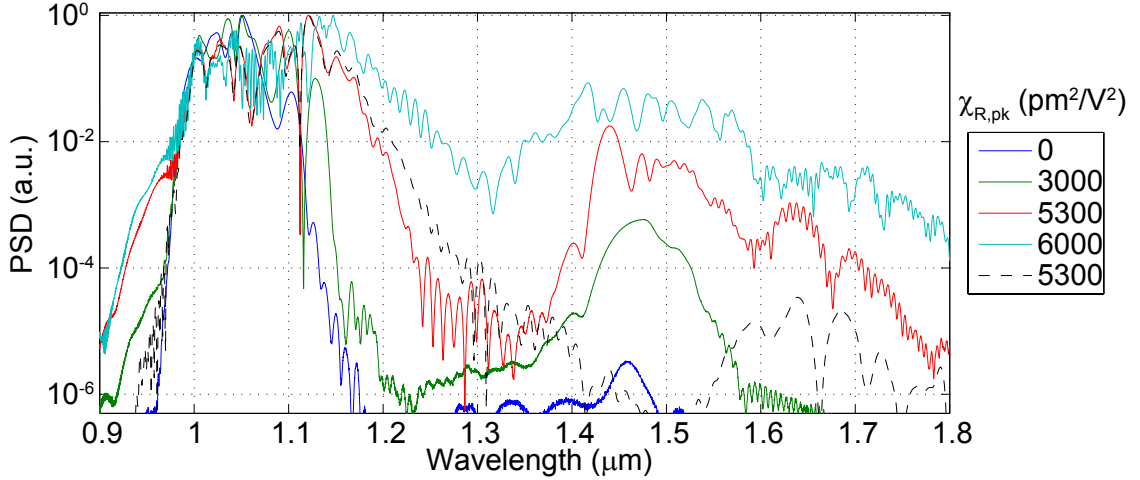


Figure 2.5: Spectrum for several values of  $\chi_{R,pk}$  (in  $\text{pm}^2/\text{V}^2$ ) with fixed sum  $\chi_E + H_R(0)\chi_{R,pk} = 6.365 \times 10^3 \text{ pm}^2/\text{V}^2$ ; the other model parameters are the same as those used in Fig. 2.1(b). For the dashed black line, quantum noise was neglected; the much lower PSD for  $1.4 \mu\text{m} < \lambda < 1.7 \mu\text{m}$  compared to the spectrum for  $\chi_{R,pk} = 5300 \text{ pm}^2/\text{V}^2$  with noise inputs included indicates the importance of parametric amplification of noise to the total output spectrum.

trends shown in Fig. 2.5. Since the Raman SFS process broadens the FH pulse bandwidth (primarily over the 1-1.2  $\mu\text{m}$  range), it might be interpreted as enhancing the non-local cascading response [47]; analogously, if the FH pulse is broadened by the SFS process such that it contains spectral components closer to phasematching, increased up-conversion can be expected, and hence a more intense SH.

In section 2.5, we show that  $\chi^{(3)}$  effects are also important for the 1580-nm-pumped experiments of Ref. [2], and use the same nonlinear coefficients there as those discussed in this section, with  $\chi_E$  scaled by a factor close to theoretical predictions [54], to accurately model those experiments as well; this agreement suggests that the  $\chi^{(3)}$  parameters estimated here are realistic. However, due to the  $\chi^{(2)} - \chi^{(3)}$  competition, our simulations are sensitive to relatively small deviations in the model parameters and input conditions from our assumptions. In particular, such variations could arise from differences in  $\chi^{(2)}$  and  $\chi^{(3)}$  between protonated and congruent  $\text{LiNbO}_3$ , the frequency-dependence of the  $\chi^{(2)}$  and  $\chi^{(3)}$  susceptibilities, and the input pulse chirp. Direct measurements of the nonlinear susceptibilities in future work would be of great

value for modeling supercontinuum generation in QPM media.

## 2.5 Comparison to 1580-nm-Pumped Experiments

To test the nonlinear waveguide model further, in this section we compare it to the 1580-nm-pumped experiments of [2]. Those experiments used pulses with a duration of 50 fs (FWHM) and energy of 1.2 nJ inside the waveguide. The QPM grating was 17.4-mm long with a grating period of  $27.5 \mu\text{m}$  and losses of approximately 0.1 dB/cm. The area of the  $\text{TM}_{00}$  mode at 1580 nm and 790 nm is estimated as  $28.48 \mu\text{m}^2$  and  $11.35 \mu\text{m}^2$ , respectively. The modal overlap integral  $\theta_{000} \approx 0.793$ , and  $\theta_{0000} \approx 0.3266 \mu\text{m}^{-2/3}$  (evaluated for self phase modulation at 1580 nm). For the  $\text{TM}_{02}$  mode (“mode 2”),  $\theta_{002} \approx 0.043$ ; for the  $\text{TM}_{10}$  mode (“mode 4”),  $\theta_{004} \approx 0.220$ ; the areas at 790 nm for these modes are  $17.55 \mu\text{m}^2$  and  $19.09 \mu\text{m}^2$ , respectively. The remaining terms  $\theta_{npq}$  are relatively small and mainly give rise to additional peaks in the pulse spectrum at short wavelengths without altering the spectral broadening very significantly.

In Fig. 2.6(a) we show the experimental results for continuum generation from Fig. 3 of Ref. [2]; in Fig. 2.6(b) we show simulations of these experiments using Eqs. (2.12) for three slightly different values of  $\chi_E$ , with the  $\text{TM}_{00}$  and  $\text{TM}_{10}$  modes and the QPM orders +1, +3, and +5 [index  $m$  in Eq. (2.12)] included in the model, and assuming a 1.2-nJ input pulse. The remaining modes and QPM orders are accounted for via the cascading approximation given by Eq. (2.28). The simulations capture the spectral broadening observed experimentally, particularly the  $\chi_E = 4368 \text{ pm}^2/\text{V}^2$  case; the evolution of the spectrum of the pulse for that case is shown in Fig. 2.6(c). Semiclassical quantum noise on the input pulses was included, as in sections (2.3) and (2.4), but did not change the output spectra on the scale of Fig. 2.6.

The initial dynamics (near the start of the QPM grating) can be described quite accurately via the cascading approximation, discussed in appendix 2.8 and applied in section 2.4. Table 2.3 gives the relevant parameters for evaluating the cascaded  $\chi^{(2)}$  terms,  $\chi_{\text{cascade}}^{m,q}$  (QPM order  $m$  and SH mode  $q$ ) for SHG of the 1580-nm input pulse. With  $d_{33} = 19.5 \text{ pm}/\text{V}$  [30],  $\sum \chi_{\text{cascade}}^{m,q} = -5900 \text{ pm}^2/\text{V}^2$ . The three largest-magnitude cascaded- $\chi^{(2)}$  terms are  $\chi_{\text{cascade}}^{1,0} = -4416 \text{ pm}^2/\text{V}^2$ ,  $\chi_{\text{cascade}}^{-1,0} = -1058$

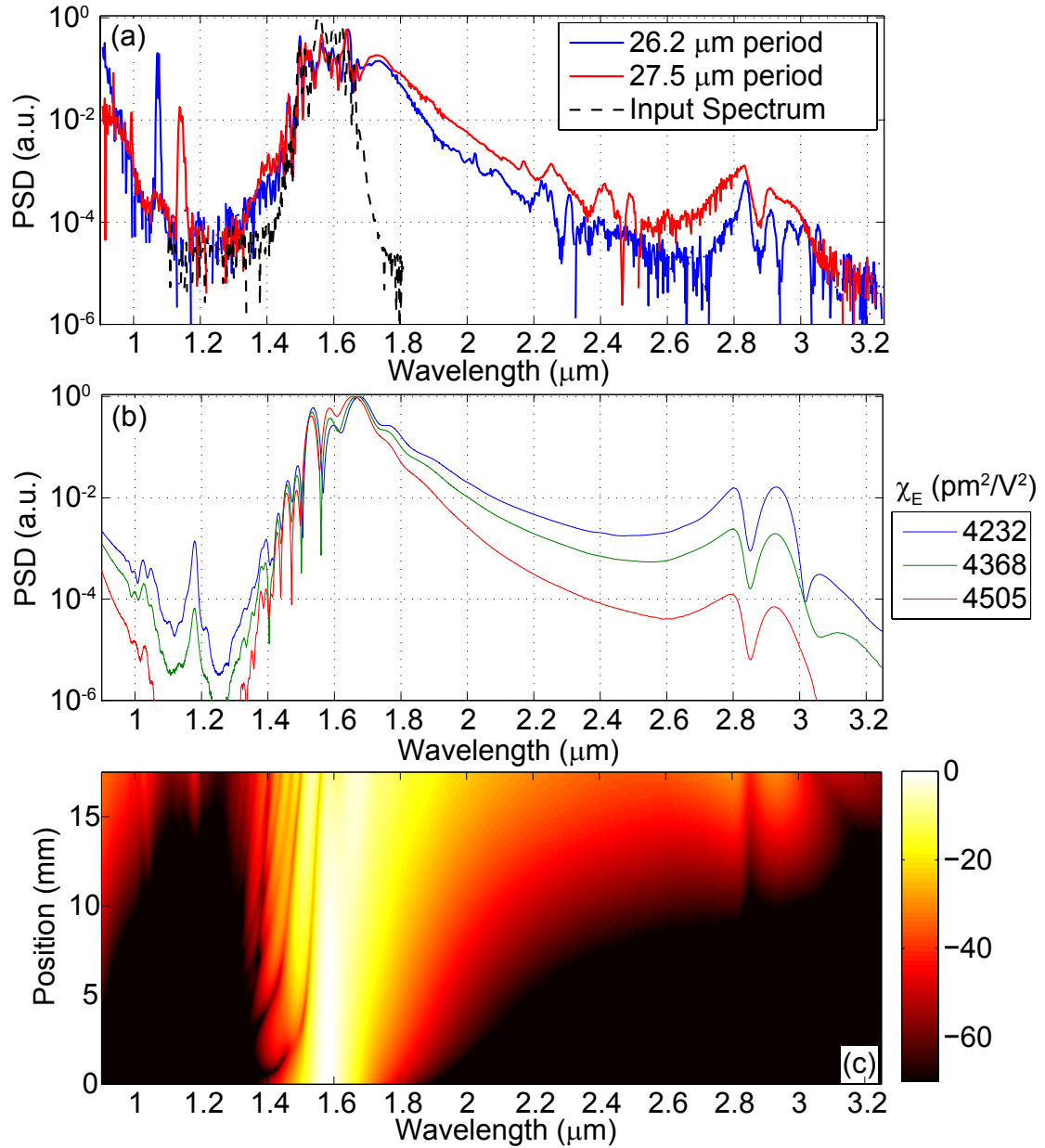


Figure 2.6: (a) Experimental data with 1580-nm-pumping from Ref. [2] (b) Simulated output spectrum corresponding to (a) for a simulation including the  $\text{TM}_{00}$ ,  $\text{TM}_{10}$ , and  $\text{TM}_{02}$  modes. Three slightly different values of  $\chi_E$  have been assumed; these values are explained in the text. (c) Evolution of the spectrum of the  $\text{TM}_{00}$  mode through the waveguide (dB scale normalized to 0 dB at the spectral peak of the input pulse).

$\text{pm}^2/\text{V}^2$ , and  $\chi_{\text{cascade}}^{1,4} = -473 \text{ pm}^2/\text{V}^2$ . With the value of  $\chi_E + H_R(0)\chi_{R,pk}$  determined in appendix 2.7 combined with these cascade contributions, the total effective  $\chi^{(3)}$  is  $\chi_{\text{total}}^{(3)} = 465 \text{ pm}^2/\text{V}^2$ , of the wrong sign for soliton formation. However, based on a theoretical two-band model, it is predicted that  $\chi_E$  should decrease with wavelength [54]. When such a scaling of  $\chi_E$  with frequency is included such that  $\chi_E(1580 \text{ nm}) \approx 4368 \text{ pm}^2/\text{V}^2$ ,  $\chi_{\text{total}}^{(3)} = -626 \text{ pm}^2/\text{V}^2$ , which then supports soliton formation given the positive GVD of  $\text{LiNbO}_3$  (and RPE waveguides) at 1580 nm. With this value of  $\chi_E$ , the simulations are in good agreement with the experimental results. This scaling corresponds to  $\chi_E(1580 \text{ nm})/\chi_E(1043 \text{ nm}) = 0.8$ , which is very close to the predictions from the (oversimplified) two-band model of Ref. [54]. Note, however, that due to the almost complete cancellation of  $\chi^{(3)}$  and  $\chi^{(2)}$  contributions to the total SPM,  $\chi_{\text{total}}$  and hence the output spectrum is sensitive to errors in  $\chi_E$  and  $d_{33}$  of as little as 2%. This sensitivity is illustrated in Fig. 2.6(b), where the three  $\chi_E$  cases shown correspond to values for  $\chi_E(1580 \text{ nm})/\chi_E(1043 \text{ nm})$  of 0.775, 0.8, and 0.825. For more accurate modeling, it would be necessary to know the model parameters precisely, or to operate in a regime where the  $\chi^{(2)} - \chi^{(3)}$  cancellation is not so complete.

With the above scaled values of  $\chi_E$ , the 1580-nm pulse broadens in spectrum and compresses in time due to the negative  $\chi_{\text{total}}^{(3)}$ , positive dispersion, and high intensity. This process is determined by the combined effects of SPM, group velocity dispersion (GVD), group velocity mismatch (GVM), and SRS. Once enough spectral broadening has occurred, various short-wavelength peaks in the spectrum are generated via phasematched processes involving different waveguide modes and QPM orders.

In the experiments, a peak in the PSD occurred around  $2.85 \mu\text{m}$  and was of comparable magnitude and wavelength for different QPM periods, as shown in Fig. 2.6(a). Similarly, we found that the wavelength of the long-wavelength peak in the simulations is only weakly dependent on QPM period (i.e. a peak occurs at the same wavelength for a relatively wide range of QPM periods, as long as there is sufficient spectral broadening). For conventional DFG of frequency  $\omega_{DFG} = \omega_1 - \omega_2$ , one normally would anticipate  $\Delta k = \beta(\omega_1) - \beta(\omega_2) - \beta(\omega_{DFG}) - K_g$ , and thus a wavelength for the phasematched peak that would depend strongly on the QPM period, in contrast

to the observed behavior. However, for a DFG process involving a phase mismatched SH component as one of the participating waves, the phasematching condition differs from the conventional one.

Consider a FH propagating with an effective dispersion relation  $\beta_{\text{eff}}^{(FH)}(\omega)$  which may differ from the linear dispersion relation of the lowest-order mode,  $\beta_0(\omega)$ , due to nonlinear-optical processes. A relevant example of such an effective dispersion relation is that of a soliton-like pulse, in which all spectral components propagate with a particular propagation constant and group velocity. If this propagation constant and group velocity are similar to those corresponding to linear-optical propagation of a pulse centered at carrier frequency  $\omega_{FH}$ , then the effective soliton dispersion relation is given, approximately, by  $\beta_{\text{eff}}^{(FH)}(\omega) \approx \beta_0(\omega_{FH}) + (\omega - \omega_{FH})/v_{FH}$ , with group velocity  $v_{FH} \approx (\partial\beta_0(\omega_{FH})/\partial\omega)^{-1}$ . Given this FH pulse and a highly phase mismatched SHG process, the effective propagation coefficient for the SH pulse at frequencies  $\omega$  in the vicinity of  $2\omega_{FH}$  is given approximately by  $\beta_{\text{eff}}^{(SH)}(\omega) \approx 2\beta_0(\omega_{FH}) + K_g + (\omega - 2\omega_{FH})/v_{FH}$ . This form arises for a SH pulse  $\pi/2$  radians out of phase with its driving polarization, aligned temporally with the FH pulse at group velocity  $v_{FH}$ . For the DFG process involving such a SH spectral component with frequency  $\omega_2$ , a FH spectral component with frequency  $\omega_1$ , and a generated wave at frequency  $\omega_{DFG} = \omega_2 - \omega_1$ , the effective  $\Delta k$  is given by

$$\Delta k_{\text{eff}}(\omega_{DFG}, \omega_2) = \beta_{\text{eff}}^{(SH)}(\omega_{DFG} + \omega_1) - \beta_{\text{eff}}^{(FH)}(\omega_1) - \beta_0(\omega_{DFG}) - K_g. \quad (2.15)$$

With the approximate forms of the propagation constants  $\beta_{\text{eff}}^{(j)}$  described above,

$$\Delta k_{\text{eff}}(\omega_{DFG}) \approx \beta_0(\omega_{FH}) + \frac{\omega_{DFG} - \omega_{FH}}{v_{FH}} - \beta_0(\omega_{DFG}), \quad (2.16)$$

independent of  $K_g$ , in contrast to the conventional phasematching relation. This type of phasematching relation was discussed in [55]. There is a dip in the spectra at  $2.85 \mu\text{m}$ : this dip occurs due to OH absorption, which we included in the model as a complex Lorentzian perturbation to the effective index, with a corresponding peak absorption of  $3 \text{ mm}^{-1}$ . This value of absorption is comparable to absorptions measured in protonated  $\text{LiNbO}_3$  samples [42]. Furthermore, the change in refractive

index corresponding to this value of absorption determines the width of the 2.8- $\mu\text{m}$  “peak” (and dip) in the simulated spectrum, both of which are consistent with the measured spectrum.

The wavelength of the above cascaded-DFG peak depends sensitively on the waveguide dispersion. With the dispersion relation for the lowest-order mode calculated from our concentration-dependent proton-diffusion model and the dispersion relation for protonated lithium niobate given in Ref. [42], the wavelength of the cascaded DFG peak is  $>3 \mu\text{m}$ , longer than observed experimentally. However, this waveguide model is calibrated primarily for wavelengths  $< 2 \mu\text{m}$ . Furthermore, small changes in fabrication parameters could also lead to shifts in the effective phase mismatch given by Eq. (2.16). Therefore, some discrepancy with experiments can be expected for processes involving longer wavelengths. Due to these uncertainties, For Fig. 2.6(b) we added a small, smooth and monotonic frequency-dependent offset to the effective index in order to shift the cascaded DFG peak to 2.85  $\mu\text{m}$ . We chose a functional form  $\delta n(\omega) = \frac{1}{2}[1 + \tanh((\omega_L - \omega)/\Delta\omega)][(\omega - \omega_L)/(\omega_{OH} - \omega_L)]^2 \delta n_0$ , where  $\omega_L$  and  $\omega_{OH}$  corresponding to 2  $\mu\text{m}$  and 2.85  $\mu\text{m}$ , respectively,  $\Delta\omega = 2\pi \times 5 \text{ THz}$ , and  $\delta n_0 = -8 \times 10^{-4}$ . This functional form was chosen so that  $\delta n \approx \delta n_0$  at 2.85  $\mu\text{m}$ , and so that  $\delta n \approx 0$  for wavelengths  $< 2 \mu\text{m}$ , where our waveguide dispersion model is well-calibrated. This latter constraint helps to ensure that the pulse dynamics are not artificially altered by the effective index offset. Provided the above constraints are met, we have found that the spectrum is relatively insensitive to the functional form of  $\delta n(\omega)$ . With improved characterization of the RPE waveguide dispersion and the nonlinear parameters of the model, and the input pulse, this offset might not be required. The wavelength of the cascaded DFG peak also depends on the pulse frequency, which changes due to the Raman SFS. This SFS depends on the value of  $\chi_{R,pk}$  (which we only estimate via the approach of section 2.4) and on the input electric field profile (which is not known for these experiments).

In comparing this work with prior modeling of the experiments of Ref. [2], we note that Refs. [37, 41] also show good agreement between single-envelope simulations and the 1580-nm-pumped experiments we have discussed in this section, despite their neglect of the waveguide mode profiles and Raman nonlinearities. Without both the

$\chi_E$  and  $\chi_{R,pk}$  terms, only the cascaded- $\chi^{(2)}$  interactions contribute to the total SPM, and so  $\chi_{\text{total}}^{(3)}$  is much larger. For a plane-wave model,  $\chi_{\text{cascade}}^{1,0} = -5170 \text{ pm}^2/\text{V}^2$  [this value is found via appendix 2.8), specifically from table 2.3, Eq. (2.28), and with  $c_q = \delta_{0,q}$ ]. We found earlier in this section that  $\chi_{\text{total}}^{(3)} \approx -626 \text{ pm}^2/\text{V}^2$ . Therefore, neglecting  $\chi^{(3)}$  and waveguide modes yields an effective low-frequency  $\chi^{(3)}$  that is an order of magnitude too large for these particular experiments. If  $\chi^{(3)}$  and waveguide effects are neglected, the SPM is increased by a similar factor, which will substantially alter the dynamics. For some cases, the measured spectrum can still be recovered by treating the pulse intensity as an unconstrained fit parameter in the simulations, as appears to have been done in Refs [37, 41], but such an approach would not work in other spectral ranges, such as those considered in section 2.3.

In contrast to the plane-wave models of previous work, for Fig. 2.6(b) we included appropriate modal overlaps and  $\chi^{(3)}$  terms according to Eq. (2.12), and we assumed a pulse energy of 1.2 nJ at the input to the waveguide, the same as the experimental value. In section 2.4, we also showed that properly-calibrated third-order nonlinear effects, particularly SRS, are required to model the 1043-nm-pumped experiments of [2]. These experiments were not modeled in Refs. [37, 41]; from the results of this chapter, it would not seem possible to model these experiments without the inclusion of all the effects and calibrations we have discussed.

## 2.6 Discussion

We have shown that our nonlinear waveguide model, given in Eq. (2.12), is in good agreement with the experimental results of Ref. [2] for both 1580-nm and 1043-nm pumps, and both uniform and chirped QPM gratings. The  $\chi^{(2)}$ , instantaneous  $\chi^{(3)}$ , and stimulated Raman scattering nonlinearities are all essential for accurately modeling the supercontinuum generation process.

To improve the accuracy of the simulations, the size of the various nonlinear terms (the susceptibilities themselves, and subsequent modal overlap integrals) in RPE waveguides must be known more precisely, especially the third-order nonlinear susceptibilities. Determining  $\chi_E$  and  $\chi_{R,pk}$  more accurately via direct measurements

will be the subject of future work. The dispersion of the nonlinear susceptibilities is important as well, as shown in section (2.5). It may also be important to determine the dispersion of the RPE waveguides at long wavelengths with greater accuracy. In addition to the model parameters in Eq. (2.12), measurements of the complex input electric field are needed; plausible values of the pulse chirp, which we assumed to be zero in our simulations, can have a significant impact on the output spectrum. Measurement of the spatial mode content of the output electric field would also be useful since this information would help to indicate which waveguide modes are important and must be included in the model.

Despite the difficulties in fully calibrating the parameters entering into Eqs. (2.12), our model is sufficiently accurate to be used to analyze and design QPM gratings and waveguides in order to improve spectral broadening or to perform other ultrafast functionalities such as nonlinear pulse compression. For example, we have shown that for both of the experiments of Ref. [2], the cascaded- $\chi^{(2)}$  and  $\chi^{(3)}$  susceptibilities were of comparable magnitude but opposite sign, and hence competed with each other. This cancellation of contributions to  $\chi_{\text{total}}^{(3)}$  significantly reduces the rate of SPM and hence increases the energy requirements for supercontinuum generation. Furthermore, based on our simulations, in the 1043-nm-pumped case the reduced rate of SPM meant that a strong FH pulse had to be used, which in turn led to a strong generated SH pulse; this SH pulse amplified quantum noise, which led to incoherent supercontinuum generation.

In fiber-based SC generation, the zero-GVD wavelength,  $\lambda_{\text{GVD}}$ , is often shifted by waveguide design to be nearby the input wavelength,  $\lambda$ . We have seen from simulations based on Eqs. (2.12) that shifting  $\lambda_{\text{GVD}}$  to be comparable to the input wavelength is one way to significantly enhance the spectral broadening processes for  $\chi^{(2)}$ -based continua as well, since generated spectral components would then remain overlapped temporally. Furthermore, if the GVD at the input wavelength is negative ( $\lambda > \lambda_{\text{GVD}}$ ) or negligible ( $\lambda \approx \lambda_{\text{GVD}}$ ), supercontinuum generation could be achieved with a positive  $\chi_{\text{total}}^{(3)}$ ; for this case, by choosing  $\Delta k_{1,000} < 0$  the contributions of  $\chi^{(2)}$  and  $\chi^{(3)}$  to SPM would add rather than cancel while still being of appropriate sign to support  $\chi^{(3)}$ -like bright solitons at the input wavelength.

Since RPE waveguides are weakly guiding, significant shifts in  $\lambda_{\text{GVD}}$  cannot be obtained. However,  $\lambda_{\text{GVD}}$  is conveniently located near  $2 \mu\text{m}$ , making Tm-based laser sources promising candidates for increased spectral broadening in RPE waveguides, as discussed in chapter 3. An alternative approach is to use tightly confining waveguides, in which a high index contrast could enable shifting  $\lambda_{\text{GVD}}$  to the  $1.55\text{-}\mu\text{m}$  and  $1\text{-}\mu\text{m}$  spectral regions, discussed in chapter 4. There is also the possibility of using AlGaAs QPM waveguides, which can be tightly confining and are transparent in the mid-IR. With simultaneous engineering of the waveguide dispersion and the QPM grating, supercontinuum generation may be possible across the mid-IR. With the model of nonlinear interactions in QPM waveguides we have developed here, strategies can be developed for reaching spectral regions not accessible to silica-fiber-based supercontinuum sources, and for performing optimizations made possible by the versatility of QPM gratings [52, 56], suggesting a path towards compact and robust traveling-wave frequency-comb sources in the IR and mid-IR spectral regions.

## 2.7 Appendix: Material Properties

In this appendix, we discuss the nonlinear coefficients contained in Eqs. (2.12); these must be known accurately in order to quantitatively predict experimental results. For the second-order nonlinear terms in this appendix, we assume  $d_{33} = 25.2$  pm/V for 1064-nm-SHG [30]; for modeling the experiments of Ref. [2], we assume  $d_{33} = 25.2$  pm/V for 1043-nm-pumping and  $d_{33} = 19.5$  pm/V for 1580-nm-pumping [30]. We also assume that  $\chi^{(2)}(x, y) = 0$  close to the upper surface of the crystal, as described in Ref. [42] and section 2.2.

We determined the imaginary part of the normalized Raman transfer function,  $\Im[H_R]$ , by measuring the spontaneous Raman scattering cross section of congruent LiNbO<sub>3</sub> (CLN). The Raman spectrum of LiNbO<sub>3</sub> has been measured previously [57, 58], but in some cases large relative errors have been reported [57]; an additional measurement across the Raman spectrum could prove to be useful. For the measurement, we used a WiTec Alpha300 S Raman microscope in the XZZ $\bar{X}$  configuration and at 295 K. The resulting spectrum is shown in Fig. 2.7 (blue line). To determine  $\Re[H_R]$  we fitted the measured  $\Im[H_R]$  to a sum of Lorentzians; this reconstructed Raman susceptibility is also shown in Fig. 2.7. The parameters for the fit are given in Table 2.1. The terms of the Lorentzian fit have form  $a_j/(f_j^2 - f^2 + 2i\gamma_j f)$  for optical frequency  $f$  (not angular frequency). The small measured peak at around -4.6 THz ( $\approx -153$  cm<sup>-1</sup>) was neglected in the fit since it does not correspond to the  $e$ -wave polarization component [59]: its presence indicates imperfect polarization discrimination during the measurement.

Table 2.1: Lorentzian Fit Parameters for  $H_R(\Omega)$ .

$f_j$ (THz)	7.59	8.28	9.93	18.98	20.93	21.52	20.62
$\gamma_j$ (THz)	0.453	0.222	0.255	0.461	0.278	0.485	0.282
$a_j$ (a.u.)	0.268	0.085	0.019	1.000	0.013	0.014	0.012

Calibrating the  $\chi^{(3)}$  coefficients in LiNbO<sub>3</sub> can be challenging, as noted in Ref. [60]. In the remainder of this appendix, we discuss the absolute scale of the third-order nonlinear coefficients  $\chi_{R,pk}$  and  $\chi_E$ . The nonlinear refractive index,  $n_2$ , is related to the third-order nonlinear susceptibility. However, there are at least three significant

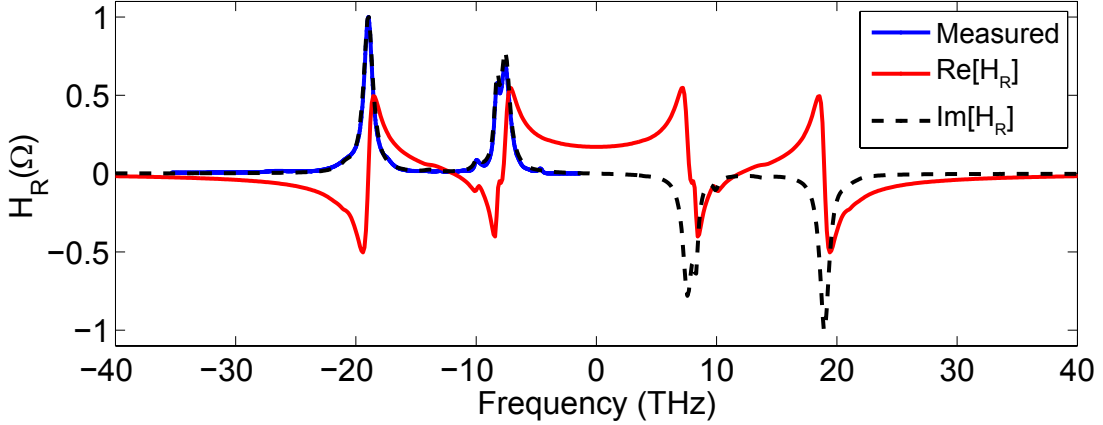


Figure 2.7: Measured imaginary and complex reconstructed stimulated Raman scattering transfer function for  $e$ -wave interactions in  $\text{LiNbO}_3$ , based on our measurement of the  $XZZ\bar{X}$  spontaneous Raman scattering spectrum. The quality of the fit implies that a sum of Lorentzians is a suitable model for  $\Im[H_R]$ , so we calculate  $\Re[H_R]$  from these fit parameters (red line).

contributions to  $n_2$ : the instantaneous  $\chi_E$  susceptibility, the real part of the  $\chi_R$  susceptibility, and also an effective  $\chi^{(3)}$  susceptibility, denoted  $\chi_{\text{eff}}^{(3)}$ , which arises due to the phase mismatched second-order nonlinear interaction, i.e. the cascaded  $\chi^{(2)}$  process [31, 60]. In order to determine  $\chi_E$  from  $n_2$ , each of these contributions must be accounted for.

In Ref. [54],  $n_2$  was measured for  $\text{LiNbO}_3$  with the Z-scan method using 30-ps (FWHM) pulses with a center wavelength of  $1.064 \mu\text{m}$ . Since the reconstructed  $\text{LiNbO}_3$  Raman spectrum in Fig. 2.7 does not vary significantly for frequencies  $< 1$  THz, and assuming the 30-ps pulses had bandwidths  $\leq 1$  THz, the measured  $n_2$  represented the total low-frequency-shift  $\chi^{(3)}$  susceptibility, given by

$$\chi_0^{(3)} = \chi_E + \chi_{R,pk} H_R(0) + \chi_{\text{cascade}}^{(3)}. \quad (2.17)$$

This total susceptibility can be calculated from  $n_2$  as

$$\chi_0^{(3)} = \frac{4}{3} n_2 n_{FH}^2 \epsilon_0 c, \quad (2.18)$$

which in LiNbO<sub>3</sub> is given by  $\chi_0^{(3)} \approx 1535 \text{ pm}^2/\text{V}^2$  for  $n_2 = 0.933 \times 10^{-6} \text{ cm}^2/\text{GW}$  [54]. The contribution to  $\chi_0^{(3)}$  from the cascaded  $\chi^{(2)}$  interaction is given by Eq. (1.41). We repeat this result here, for convenience:

$$\chi_{\text{cascade}}^{(3)} = -\frac{16\pi d_{\text{eff}}^2}{3n_{SH}\lambda_{FH}} \frac{1}{\Delta k}. \quad (2.19)$$

For the Z-scan configuration used for LiNbO<sub>3</sub> in Ref. [54],  $d_{\text{eff}} = d_{33}$  and  $\Delta k = k(2\omega) - 2k(\omega) = 0.927 \text{ } \mu\text{m}^{-1}$  for 1.064- $\mu\text{m}$  pumping [61], and so  $\chi_{\text{cascade}}^{(3)} \approx -4831 \text{ pm}^2/\text{V}^2$ . Importantly,  $\chi_{\text{cascade}}^{(3)}$  is of opposite sign to the electronic and Raman contributions. After subtracting the contribution of the cascading term (which can be characterized more easily since  $d_{33}$  is relatively well-known), we find that  $\chi_E + \chi_{R,pk} H_R(0) = 6365 \text{ pm}^2/\text{V}^2$ , much larger than  $\chi_0^{(3)}$ .

Additional measurements are needed to determine both  $\chi_E$  and  $\chi_{R,pk}$ . One way to determine  $\chi_{R,pk}$  separately from  $\chi_E$  is by measuring the SRS gain at  $\Omega_{pk}$ . However, tabulated values for the Raman gain coefficient are inconsistent with the  $n_2$  measurements described above. Consider the Raman gain coefficient,  $(g_S/I_L)$ , evaluated at Stokes frequency  $\omega_S = \omega_L - \Omega_{pk}$  for some pump laser frequency  $\omega_L$ . It can be shown from Eq. (2.12) that

$$\chi_{R,pk} = \frac{n_S n_L \epsilon_0 c \lambda_S}{3\pi} \frac{g_S}{I_L}, \quad (2.20)$$

where the reduction in gain due to Stokes-anti-Stokes coupling effects are neglected when defining  $(g_S/I_L)$ , and  $n_S$  and  $n_L$  are the refractive indices at the Stokes and pump wavelengths, respectively. In LiNbO<sub>3</sub> with a 1.064- $\mu\text{m}$  pump laser, the gain coefficient corresponding to a contribution of 100% from SRS to the value of  $\chi_0^{(3)} - \chi_{\text{cascade}}^{(3)} = 6365 \text{ pm}^2/\text{V}^2$  calculated above is given by  $(g_S/I_L)_{\text{max}} \approx 2.51 \text{ cm/GW}$ , using  $H_R(0) = 0.17$  from Fig. 2.7. However, the gain coefficient tabulated in Ref. [4] is 9.4 cm/GW at 694 nm, which corresponds to 6.1 cm/GW at 1.064  $\mu\text{m}$  (by scaling with optical frequency); this value is more than twice as large as the upper bound for  $(g_S/I_L)$  provided by the  $n_2$  measurement (assuming  $\chi_E > 0$ ).

The tabulated values for  $(g_S/I_L)$  are also inconsistent with our experiments with

intense IR pulses (discussed in chapter 8). The Raman gain rate  $g_R$ , in  $\text{cm}^{-1}$ , can be approximated as [4]

$$g_R \approx 2\Re \left[ \sqrt{-ig_S \Delta k_R / 2 - (\Delta k_R / 2)^2} \right], \quad (2.21)$$

where  $g_S$  is the coupling coefficient between the intensity at the Stokes shifted wave at  $\omega_S$  and the pump laser at  $\omega_L = \omega_S + \omega_{R,pk}$ , and the phase mismatch  $\Delta k_R \equiv 2k(\omega_L) - k(\omega_S) - k(\omega_{AS})$  for anti-Stokes frequency  $\omega_{AS}$ . In turn,  $g_S$  is determined via the Raman gain coefficient ( $g_S/I_L$ ). In Refs. [53, 62], a 1-cm-long MgO:LiNbO<sub>3</sub> crystal was pumped with 1.064- $\mu\text{m}$  pulses with intensities of  $> 7 \text{ GW}/\text{cm}^2$  and durations of 12 ps (FWHM); the corresponding pulse bandwidth was significantly narrower than the linewidth of the main peaks of  $H_R(\Omega)$  shown in Fig. 2.7. Assuming  $(g_S/I_L) = 6.1 \text{ cm}/\text{GW}$ , Eq. (2.21) predicts an SRS gain in this case of 136 dB (185 dB if  $\Delta k_R \rightarrow \infty$ ). Despite this high predicted gain, no Stokes wave was observed experimentally. If we instead assume the above upper bound on  $(g_S/I_L)$  of 2.51 cm/GW (inferred from the  $n_2$  measurements of Ref. [54] under the assumption that  $\chi_E = 0$ ), the gain at the Stokes frequency would be approximately 69 dB.

Based on the above considerations, it is difficult to use available literature data to absolutely calibrate the third-order nonlinear coefficients in LiNbO<sub>3</sub> (which could also be different from those of RPE LiNbO<sub>3</sub>). The peak Raman susceptibility  $\chi_{R,pk}$  can be bounded above by the nonlinear refractive index and by the absence of SRS in the high intensity experiments discussed, and  $\chi_{R,pk}H_R(0) + \chi_E$  can be estimated from the measured value of  $n_2$ . For this paper, we further constrain the susceptibilities to yield output spectra in quantitative agreement with the supercontinuum generation experiments of Ref. [2], which we model in Sections (2.5) and (2.3). The  $\chi^{(3)}$  values that we use are given by

$$\begin{aligned} \chi_{R,pk} &= 5.3 \times 10^3 \text{ pm}^2/\text{V}^2, \\ \chi_E(1043\text{nm}) &= 5.46 \times 10^3 \text{ pm}^2/\text{V}^2. \end{aligned} \quad (2.22)$$

These parameters are discussed further in section 2.4. For the 1580-nm-pumping case

discussed in section 2.5,  $\chi_E$  is scaled according to theoretical predictions [54], such that  $\chi_E(1580 \text{ nm})/\chi_E(1043 \text{ nm}) \approx 0.8$ .

Another way to estimate the third-order nonlinear susceptibility is by using measurements of  $n_2$  to infer both the electronic and Raman components of the susceptibility via Eq. (2.17). For each measured value of  $n_2$  there is a corresponding value of the total low-frequency susceptibility  $\chi_0^{(3)}$ , given by Eq. (2.18). As in Eq. (2.17), we assume that  $\chi_0^{(3)}$  is comprised of contributions from the electronic, low-frequency Raman, and cascaded  $\chi^{(2)}$  susceptibilities. In Ref. [54],  $n_2$  of LiNbO<sub>3</sub> was measured at 1064 and 532 nm. There are two data points from the  $n_2$  measurements, and our goal is to determine the two unknown parameters  $\chi_E(1064 \text{ nm})$  and  $\chi_{R,pk}$ ; we therefore need to know how each term in the total susceptibility changes between 1064 and 532 nm. First, consider the  $\chi_E$  contributions. In Ref. [54], a theoretical prediction of the ratio of the electronic susceptibilities at different wavelengths was provided via a two-band model: based on this (oversimplified) model and the band gap of LiNbO<sub>3</sub>,  $\chi_E(532 \text{ nm})/\chi_E(1064 \text{ nm}) \approx 2.5$ . For the  $\chi_R$  contributions, we assume here that the peak Raman susceptibility and the Raman transfer function is independent of the optical frequency. Lastly, consider the  $\chi_{\text{cascade}}$  contributions. Since 532 nm lies above half the band-gap of LiNbO<sub>3</sub>, it has a very large phase mismatch with its second harmonic at 266 nm (which is also strongly absorbed) [63], and so the contribution to  $n_2$  from  $\chi_{\text{cascade}}^{(3)}$  is much smaller than at 1064 nm; therefore, we assume for simplicity that  $\chi_{\text{cascade}}^{(3)}(532 \text{ nm}) = 0$ . With the above assumptions,  $\chi_E$  and  $\chi_{R,pk}$  can be expressed as follows:

$$\begin{bmatrix} \chi_0^{(3)}(1064 \text{ nm}) \\ \chi_0^{(3)}(532 \text{ nm}) \end{bmatrix} = \begin{bmatrix} 1 & H_R(0) \\ \frac{\chi_E(532 \text{ nm})}{\chi_E(1064 \text{ nm})} & H_R(0) \end{bmatrix} \begin{bmatrix} \chi_E(1064 \text{ nm}) \\ \chi_{R,pk} \end{bmatrix} + \begin{bmatrix} \chi_{\text{cascade}}^{(3)}(1064 \text{ nm}) \\ \chi_{\text{cascade}}^{(3)}(532 \text{ nm}) \end{bmatrix} \quad (2.23)$$

where  $H_R(0) = 0.17$ ,  $\chi_E(1064 \text{ nm})/\chi_E(532 \text{ nm}) = 2.5$ ,  $\chi_{\text{cascade}}^{(3)}(1064 \text{ nm}) = -4830 \text{ pm}^2/\text{V}^2$ ,  $\chi_{\text{cascade}}^{(3)}(532 \text{ nm}) = 0$ ,  $\chi_0^{(3)}(1064 \text{ nm}) = 1535 \text{ pm}^2/\text{V}^2$ , and  $\chi_0^{(3)}(532 \text{ nm}) = 14578 \text{ pm}^2/\text{V}^2$ . By solving Eq. (2.23), we find values of  $\chi_E(1064 \text{ nm}) = 5476 \text{ pm}^2/\text{V}^2$

and  $\chi_{R,pk} = 5233 \text{ pm}^2/\text{V}^2$ . These values are very close to those we inferred via numerical simulations in sections 2.3 and 2.4; with the assumed frequency-dependence,  $\chi_E(532 \text{ nm}) = 13689 \text{ pm}^2/\text{V}^2$ .

In Ref. [54], there was a significant discrepancy between the measured and theoretically-predicted scaling of  $n_2$  between 1064 and 532 nm: at 532 nm, the measured  $n_2$  was approximately  $9.1\times$  the value at 1064 nm, while the two-band theory predicted a scaling factor of only 2.5 (as assumed above). Our analysis provides a possible resolution to this discrepancy: there is a large negative contribution to  $n_2$  from  $\chi_{\text{cascade}}^{(3)}$  in the 1064-nm case but not in the 532-nm case. In principle, Eq. (2.23) can be used to determine the susceptibilities unambiguously via  $n_2$  measurements alone. However, the solutions are highly sensitive to the value of  $\chi_E(532 \text{ nm})/\chi_E(1064 \text{ nm})$ , and this parameter is not known very accurately. Therefore, we can only assert consistency between the susceptibilities we have inferred, the two  $n_2$  measurements, and the oversimplified two-band theoretical model. Direct measurement of the susceptibilities, and their wavelength dependence, would be of great use for future work.

## 2.8 Appendix: Cascading Approximation for QPM Waveguides

In the limit of a large phase mismatch,  $\chi^{(2)}$  interactions can be approximated by  $\chi^{(3)}$ -like self- and cross-phase-modulation (SPM and XPM) terms; this approach is termed the cascading approximation, and has been discussed extensively [31]. In section 1.5.3 we introduced the simplest version of this approximation for SHG, and in Appendix 2.7, we used it to constrain the  $\chi^{(3)}$  susceptibilities given a known nonlinear refractive index. In this appendix, we determine the cascading approximation for the case of QPM waveguide SHG interactions. This calculation gives a total effective  $\chi^{(3)}$ , denoted  $\chi_{\text{total}}^{(3)}$ , which determines the rate of SPM for narrow-bandwidth pulses. In the experiments modeled in sections 2.3 and 2.5 the conditions for the validity of the approximation are not always satisfied for all of the waveguide modes and QPM orders, but it nonetheless provides valuable insight into the pulse propagation dynamics (especially near the start of the QPM grating).

In Ref. [32], the cascading approximation was determined from coupled wave equations for SHG via a multiple-scale analysis. A similar procedure can be used to determine the cascading approximation for QPM waveguides based on Eq. (2.12). To proceed with the analysis, we first split each mode envelope  $A_n$  into first and second pulse components  $A_{n,FH}$  and  $A_{n,SH}$ , with carrier frequencies  $\omega_{FH}$  and  $\omega_{SH} = 2\omega_{FH}$ , respectively. In principle, Eq. (2.12) can give rise to pulses around carrier frequencies  $m\omega_{FH}$  for all positive integers  $m$ . However, for pulses with a bandwidth  $\Delta\Omega$  less than an octave, i.e. for  $\Delta\Omega \ll \omega_{FH}$ , often only the components around  $\omega_{FH}$  and  $\omega_{SH}$  are relevant, to lowest order in the perturbation. Furthermore, higher order modes around  $\omega_{FH}$  can often be neglected, for example in the case when the waveguide only supports a single mode at that frequency.

With these assumptions, Eq. (2.12) yields the following simplified time-domain

coupled wave equations for SHG,

$$\begin{aligned}
\frac{\partial A_{0,FH}}{\partial z} + \hat{D}_{0,FH} A_{0,FH} &= -i \left( \frac{\omega^2 u}{g_0 \beta_0 c^2} \right)_{\omega_{FH}} \times \\
&\quad \left[ \sum_{q,m} d_m \theta_{q00} e^{-i \int \Delta k_{m,q00}(z') dz'} A_{0,FH}^* A_{q,SH} \right. \\
&\quad \left. + \frac{3(\chi_E + H_R(0)\chi_{R,pk})}{8} \theta_{0000} |A_{0,FH}|^2 A_{0,FH} \right] \\
\frac{\partial A_{q,SH}}{\partial z} + \hat{D}_{q,SH} A_{q,SH} &= -i \left( \frac{\omega^2 u}{g_q \beta_q c^2} \right)_{\omega_{SH}} \times \\
&\quad \left[ \sum_m d_m \theta_{q00} e^{i \int \Delta k_{m,q00}(z') dz'} \frac{A_{0,FH}^2}{2} \right. \\
&\quad \left. + \frac{6(\chi_E + H_R(0)\chi_{R,pk})}{8} \theta_{qq00} |A_{0,FH}|^2 A_{q,SH} \right] \quad (2.24)
\end{aligned}$$

where  $\hat{D}_q$  are dispersion operators. The FH and SH envelopes are given in terms of the following approximate form for the spectrum of the total electric field

$$\begin{aligned}
\tilde{E}(x, y, z, \omega) &\approx \frac{1}{2} \tilde{B}_0(x, y, \omega_{FH}) A_{0,FH}(z, \omega - \omega_{FH}) e^{-i(\beta_0(\omega_{FH}) - \omega_{FH}/v_{ref})} \\
&\quad + \frac{1}{2} \sum_q \tilde{B}_q(x, y, \omega_{SH}) A_{q,SH}(z, \omega - \omega_{SH}) e^{-i(\beta_q(\omega_{SH}) - \omega_{SH}/v_{ref})} \quad (2.25)
\end{aligned}$$

and  $\theta_{q00}$  introduced in Eqs. (2.9) is evaluated at the carrier frequencies; similarly  $\theta_{qq00} = \Theta_{qq00}(\omega_{SH}, \omega_{SH}, \omega_{FH})$ , where  $\Theta_{npqr}$  is defined in Eq. (2.6). In Eqs. (2.24) and (2.25), the spatial mode profiles and coupling coefficients have also been evaluated at the optical carrier frequencies. Furthermore, we have assumed that the intensity of the SH pulse is much lower than that of the FH pulse, and have therefore neglected the  $\chi^{(3)}$  terms involving  $|A_{n,SH}|^2$ . For the purposes of this simplified analysis, we assume that the pulse bandwidth is narrow enough that  $H_R(\Omega)$  can be approximated as  $H_R(0)$ ; this approximation does not apply for supercontinuum generation [in the simulations, we use  $H_R(\Omega)$ ], but is useful for estimating the rate of SPM for the FH pulse at the start of the QPM grating. The coupled-wave system given in Eqs.

(2.25) closely resembles conventional coupled-wave equations for SHG, see e.g. [29], except for the inclusion of many waveguide modes at the SH. Eqs. (2.25) are also an approximate form of a specific case of the generalized coupled-wave approach derived in chapter 5. We use subscripts “FH” and “SH” in this appendix (a slightly different notation to the one introduced in chapter 5) for simplicity.

The phase mismatch terms in Eqs. (2.24) are given by

$$\Delta k_{m,q00}(z) = \beta_q(2\omega_{FH}) - 2\beta_0(\omega_{FH}) - mK_g(z) \quad (2.26)$$

for QPM order  $m$  and waveguide mode  $q$  of the SH pulse.

If the characteristic length defined by  $L_{m_1,m_2} \equiv |\Delta k_{m_1,q00} - \Delta k_{m_2,q00}|^{-1}$  is much shorter than any other characteristic lengths of the problem for all  $m_1 \neq m_2$ , the multiple-scale analysis can be applied. In Ref. [32], where the linear operators represented diffracting beams, the Rayleigh range would be a relevant characteristic length. For pulses, the group velocity mismatch length between the FH and SH pulses is one of several important characteristic length scales. Given a sufficiently small value of  $L_{m_1,m_2}$  for all  $m_1 \neq m_2$ , and assuming that there is no SH pulse input at the start of the interaction, multiple scale analysis of Eq. (2.24) yields

$$\begin{aligned} \frac{A_{0,FH}}{\partial z} + \hat{D}_{0,FH} A_{0,FH} &= i \frac{\omega_{FH}}{g_{0,FH} n_{0,FH} c} \left( \sum_{m,q} \frac{d_m^2 \theta_{q00}^2 \omega_{FH}}{g_{q,SH} n_{q,SH} c} \frac{1}{\Delta k_{m,q00}(z)} \right) |A_{0,FH}|^2 A_{0,FH} \\ &\quad - i \frac{\omega_{FH}}{g_{0,FH} n_{0,FH} c} \left( \frac{3\theta_{0000}(\chi_E + H_R(0)\chi_{R,pk})}{8} \right) |A_{0,FH}|^2 A_{0,FH}, \end{aligned} \quad (2.27)$$

where  $n_{q,j} = \beta_q(\omega_j)c/\omega_j$  and  $g_{n,j} = g_n(\omega_j)$  for wave  $j$  ( $j = FH$  or  $j = SH$ ) and mode normalization coefficient  $g_n(\omega)$  given by Eq. (2.7). To analyze the different terms, it is convenient to introduce a simpler normalization of the mode profiles than the one used in sections 2.3 and 2.5 to analyze broadband pulses. If we choose  $g_n(\omega) = a_n(\omega)$  instead of  $g_n(\omega) = a_n(\omega)^{1/3}$ , the mode profiles  $B_n(x, y, \omega)$  are dimensionless. With

this definition of  $g_n$ ,  $\theta_{0000}/g_0(\omega_{FH}) = 1$ , and the total effective  $\chi^{(3)}$  is given by

$$\begin{aligned}\chi_{\text{total}}^{(3)}(z) &= \chi_E + \chi_{R,pk} H_R(0) - \sum_{m,q} c_q \frac{16\pi d_m^2}{3n_{q,SH} \lambda_{FH}} \frac{1}{\Delta k_{m,q00}(z)} \\ &\equiv \chi_E + \chi_{R,pk} H_R(0) + \sum_{m,q} \chi_{\text{cascade}}^{(m,q)}(z)\end{aligned}\quad (2.28)$$

where the cascading reduction factors  $c_q$  are given by

$$c_q = \frac{(\int \bar{\chi} B_{FH}^2 B_{q,SH} dx dy)^2}{(\int |B_{FH}|^4 dx dy) (\int |B_{q,SH}|^2 dx dy)}, \quad (2.29)$$

independent of the choice of normalization of the spatial mode profiles  $B_j$ ;  $\bar{\chi}(x, y)$  is the transverse spatial profile of the second order nonlinear susceptibility, which appears in Eq. (2.4). The  $\chi^{(2)}$  contributions to  $\chi_{\text{total}}^{(3)}$  have, in this waveguide case, forms analogous to Eq. (2.19) (which applies to plane waves). In sections 2.3 and 2.5 the values for these terms are discussed, and we show that almost complete cancellation of  $\chi_{\text{total}}^{(3)}$  can occur. The parameters  $c_q$  and  $\Delta k_{0,q00}$  are given in Tables 2.2 and 2.3 for the 1043-nm and 1580-nm pumped calculations discussed in sections 2.4 and 2.5, respectively.

Table 2.2: Cascading Approximation Parameters at 1043 nm

Mode number	0	1	2	3	4	5	6	7
$2\pi/\Delta k_{0,q00}$ ( $\mu\text{m}$ )	5.671	5.765	5.870	5.985	6.064	6.108	6.164	6.240
$c_q$	0.912	0.000	0.003	0.000	0.031	0.000	0.000	0.000

Table 2.3: Cascading Approximation Parameters at 1580 nm

Mode number $q$	0	1	2	3	4	5	9
$2\pi/\Delta k_{0,q00}$ ( $\mu\text{m}$ )	16.871	17.665	18.624	19.723	19.879	20.924	22.531
$c_q$	0.854	0.000	0.002	0.000	0.056	0.000	0.003

For bulk interactions,  $\chi_{\text{cascade}}^{(3)}$  can be found by taking  $c_q = \delta_{q0}$  and  $d_m = \delta_{m0} d_{33}$  where  $\delta_{ij}$  is the Kronecker delta. To calculate the cascaded phase shifts, we assumed a pulse centered around a particular carrier frequency. However, some care should

be taken with this procedure since during the supercontinuum generation process the center frequency of the pulse can shift. This frequency shift can reduce the accuracy of the cascading approximation for terms that are nearly phasematched. For the simulations performed here, we add  $\sum \chi_{\text{cascade}}^{m,q}$  to the instantaneous third-order nonlinear coefficient  $\chi_E$ , with summation performed over all terms except those which are either explicitly included in a given model derived from Eq. (2.12) or for which  $m = 1$  (since the  $m = 1$  terms are too close to phasematching for the cascaded- $\chi^{(2)}$  approximation to be accurate in numerical simulations of supercontinuum generation experiments).

## Chapter 3

# Supercontinuum Generation in Quasi-Phasematched $\text{LiNbO}_3$ Waveguides Pumped by a Tm-Doped Fiber Laser System

The choice of pump frequency, pulse duration, and waveguide group velocity dispersion (GVD) is of great importance in SC generation [33], and mid-IR generation in general. The zero group-velocity-dispersion (GVD) of RPE waveguides is at approximately 2000 nm, and so Tm-doped fiber lasers, which typically operate around 1950 nm, represent an interesting pump choice for PPLN-based supercontinuum generation [64]. Additionally, sources with wavelengths  $>1800$  nm are required in order to avoid two photon absorption in mid-IR materials such as GaAs and Si. Tm-doped fiber lasers are thus more compatible with mid-IR generation than established Er and Yb fiber comb technology, but until now Tm-fiber combs have remained elusive due to the long pulse widths generated with previous Tm-fiber oscillators (173 fs) [65], leading to degraded coherence properties of any generated SC. In this chapter, we use a high-power, near-linear 100-fs-level Tm-doped fiber oscillator-amplifier system to demonstrate for the first time self-referencing of a Tm-fiber-laser-pumped source. We use a single periodically poled lithium niobate (PPLN) waveguide to perform both

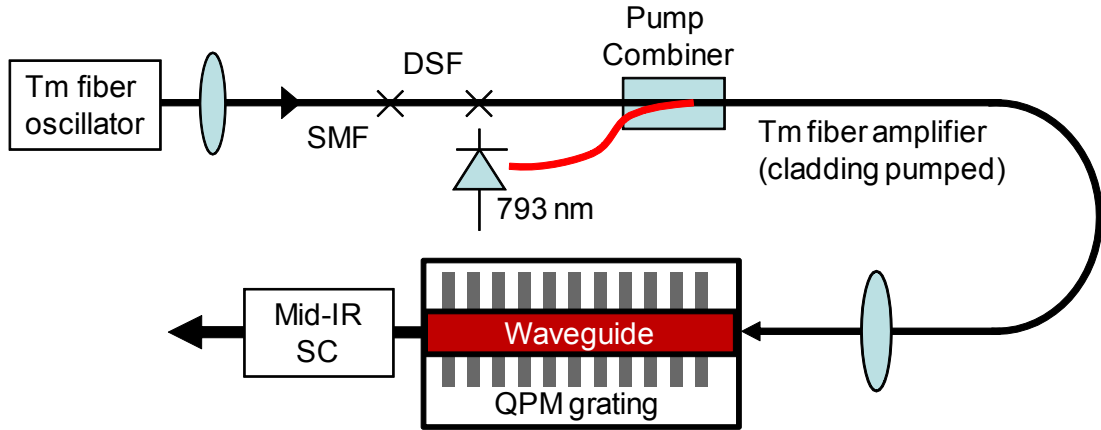


Figure 3.1: Setup of a self-referenced Tm-doped fiber and PPLN waveguide system. SMF: single-mode fiber; DSF: dispersion shifted fiber.

octave spanning SC generation as well as carrier-envelope-offset frequency sensing, and we numerically model the SC generation process in the QPM waveguide.

The experimental setup is shown in Fig. 3.1. The experiments were performed at IMRA America. The fiber oscillator is mode-locked by nonlinear polarization rotation and generates pulses as short as 70 fs with an average power of 30 mW at 72 MHz. These pulses are chirped in a positive dispersion fiber and subsequently amplified and compressed through a 2.0-m length of a large-mode-area Tm-doped fiber. The amplifier is cladding-pumped with up to 23 W at 793 nm by diode lasers, yielding amplified pulse energies up to 25 nJ. In this fiber, the large core diameter (25  $\mu\text{m}$ ), wide amplifier bandwidth and large fiber dispersion facilitate near linear amplification (B-integral  $<5$ ) without the use of any external bulk pulse compressor, providing a very compact setup [66].

We characterized the complex field profile of the amplified pulses using second harmonic generation frequency resolved optical gating (SHG FROG). The temporal profile is shown in Fig. 3.2(a), reconstructed via the principle components generalized projections algorithm (PCGPA). The FROG measurement was performed with a 100- $\mu\text{m}$ -long BBO crystal. The pulse duration is 97 fs (FWHM) at 1.8 W average power (25 nJ pulse energy). We also measured the amplified pulse spectrum with a Fourier transform infrared spectrometer (FTIR), as shown in Fig. 3.2(b). The spectrum

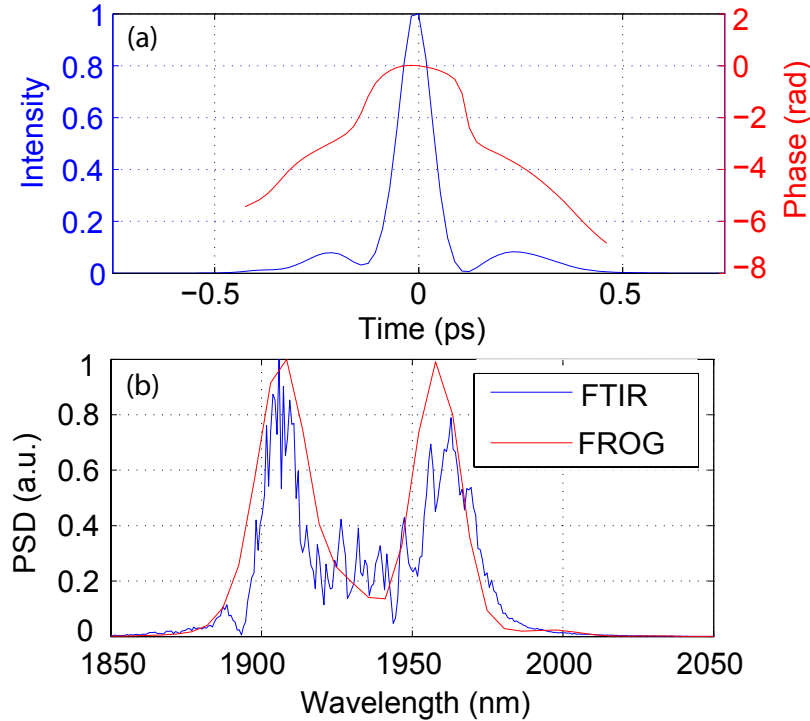


Figure 3.2: Amplified pulse characterization. (a) Time-domain amplitude and phase profile based on SHG FROG. (b) Pulse spectrum measured with an FTIR (blue) and reconstructed via the FROG algorithm (red).

returned by the FROG algorithm is plotted for comparison; the ripples in the FTIR spectrum indicate spurious reflections ( $\approx 1\%$  of pulse energy) not captured by the FROG measurement.

To perform SC generation, we coupled approximately 7 nJ of the amplified pulses into a reverse proton exchanged (RPE) LiNbO<sub>3</sub> waveguide. The waveguide is designed with fabrication parameters (proton-exchange depths and annealing times [42]) to support wavelengths up to 4000 nm and (approximately) minimize the mode area around 2000 nm. Excitation of the lowest-order mode at 2000 nm is achieved by use of an adiabatic input taper [67]. The pulses propagate through an 18.5-mm-long QPM grating with a period of 22.11  $\mu\text{m}$ , which leads to SC generation. We measured the spectrum using an FTIR for wavelengths  $>1750$  nm and an optical spectrum analyzer (OSA) for shorter wavelengths; these measurements were performed simultaneously.

The measured power spectral density (PSD) of the SC is shown in Fig. 3.3. The SC spans from 1350 to 2800 nm at the -40 dB level, and is continuous and easily observable on the OSA down to 400 nm, corresponding to nearly three octaves of bandwidth. Data  $> 2800$  nm corresponds to the noise floor of the FTIR measurement; there is considerable OH-absorption in RPE waveguides around 2850 nm [42], which may have limited further spectral broadening. Note that some spectral components at shorter wavelengths correspond to sum frequency generation (SFG) into higher order modes of the PPLN waveguide, so there is some frequency dependence to the coupling efficiency into the single-mode fiber input to the OSA.

It is necessary to have an accurate model of the SC generation process in order to design optimized QPM and waveguide profiles. As discussed in detail in chapter 2, we have developed a numerical model to describe nonlinear interactions in QPM waveguides; this model is also discussed in detail in Ref. [38]. The model accounts for the  $\chi^{(2)}$ , instantaneous  $\chi^{(3)}$ , and stimulated Raman scattering nonlinearities, including appropriate noise terms. Modal dispersion to all orders, nonlinear interactions between multiple waveguide modes, and multiple QPM orders are also included. The time (or frequency) dependence of the amplitude of each waveguide mode can be modeled with a single envelope [37]. The modes of the RPE waveguides are determined by modeling the concentration-dependent proton diffusion process during fabrication, and the proton-concentration- and wavelength-dependent refractive index shift [42]. In the input taper there is no QPM grating, and so the cascaded  $\chi^{(2)}$  and  $\chi^{(3)}$  contributions to the total SPM (almost) cancel each other (see chapter 2 or Ref. [38]); furthermore, GVD in the taper is small since the input wavelength is very near the zero-GVD wavelength of the waveguide. The taper is therefore neglected in the simulation.

A simulation from our model is shown in Fig. 3.3 on top of the experimental data. The simulation is in good agreement with the experiment. We assumed losses of 0.3 dB/cm except near the 2850-nm OH-absorption peak, and included the  $\text{TM}_{00}$  and  $\text{TM}_{01}$  modes; additional modes are supported, but these modes do not alter the nonlinear dynamics substantially. As the input to the simulation, we used the profile of the output pulse of the amplified Tm: fiber laser, reconstructed via the SHG

FROG algorithm as shown in Fig. 3.2. The simulated spectrum that most closely corresponds to the experimental spectrum for 7 nJ launched into the waveguide was obtained for a simulation assuming 2.8 nJ in the waveguide. Possible contributions to this discrepancy could be a lower value of  $d_{33}$  than assumed (we assumed  $d_{33} = 18.8$  pm/V, based on constant-Miller-delta scaling of the 1319 nm measurement of [30]), variations from our model assumptions during waveguide fabrication, photorefractive effects in the waveguide, and absorption in the waveguides between 2.2 and 2.9  $\mu\text{m}$ : no additional absorption in this spectral region was assumed in our simulations except for the OH peak itself, but there are additional proton-related absorption features in bulk LiNbO<sub>3</sub> [68]; these features are likely to be enhanced in proton-exchanged waveguides such as those used for these experiments, and therefore warrant further study.

From the simulation, the spectral broadening that occurs near the start of the QPM grating results from cascaded phase shifts associated with phase mismatched SHG [38]. However, as discussed in chapter 2, the cascading approximation quickly breaks down (so full numerical simulations were necessary to obtain the results shown in Fig. 3.3). As discussed above, the center wavelength of our pump pulse, 1930 nm, is close to the zero-GVD wavelength of RPE LiNbO<sub>3</sub> waveguides. Due to the low GVD around the center wavelength of the input pulses, pulse self-compression does not occur, even though we can obtain a negative total low-frequency  $\chi^{(3)}$  [ $\chi_{\text{total}}^{(3)}$ , defined in Eq. (2.28)] by an appropriate choice of QPM period. The absence of self-compression leads to a higher energy requirement for SC generation than with a 1580-nm pump wavelength [2]. However, the flat group index profile around the FH still reduces pulse spreading, which simulations show is one way to obtain a broad and relatively flat SC spectrum (such as the one seen in Fig. 3.3).

In addition to the cascaded phase shifts, spectral broadening is enhanced by stimulated Raman scattering (SRS), and self phase modulation (SPM) from the instantaneous  $\chi^{(3)}$  nonlinearity. Because the QPM period (22.11  $\mu\text{m}$ ) is shorter than that corresponding to phasematched SHG around the input wavelength (23.88  $\mu\text{m}$ ), SPM due to  $\chi^{(3)}$  has the same sign as SPM due to the cascaded  $\chi^{(2)}$  process. The broadening mechanisms can be identified numerically: turning off  $\chi^{(2)}$  ( $\chi^{(3)}$ ) leads to a

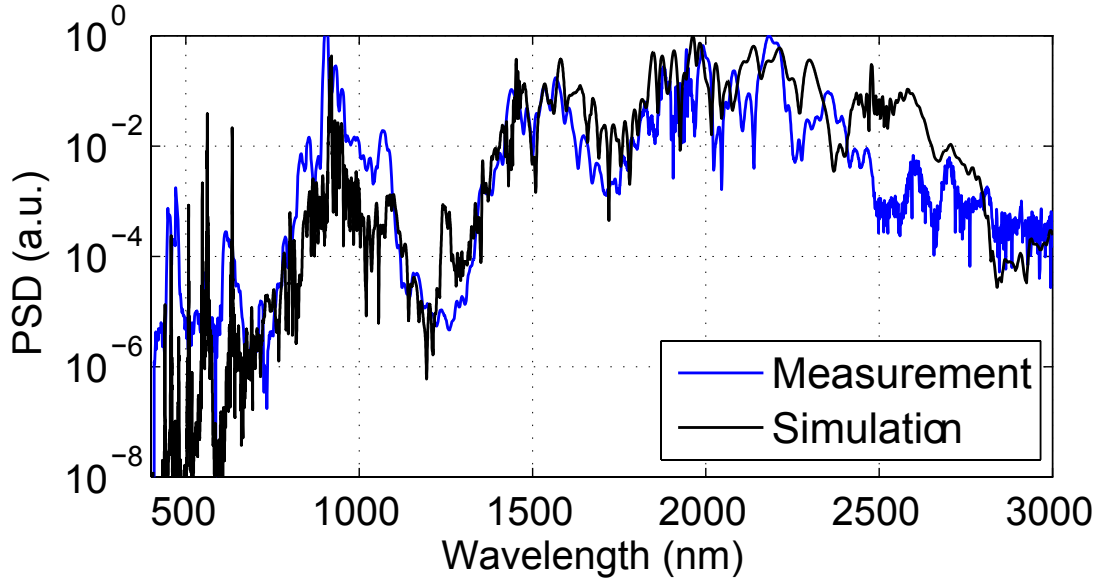


Figure 3.3: Power spectral density of the Tm-fiber-laser pumped SC generated in a PPLN waveguide. Measurements above and below 1750 nm were performed with an FTIR and an OSA, respectively.

major (minor) reduction in spectral broadening. In addition to the broadening effects described above, spectral components around  $2f$ ,  $3f$ , and  $4f$  (optical frequency  $f$ ) are generated via second harmonic generation (SHG) and other SFG processes. Peaks in the spectrum correspond to quasi-phased-matched interactions, but the PSD is significant even for processes with a relatively large phase mismatch, due to the high intensities involved.

Once sufficient broadening occurs, there is overlap between the  $f$ ,  $2f$ ,  $3f$ , and  $4f$  spectra. This overlap allowed  $f_{\text{CEO}}$  to be observed directly from the PPLN waveguides, without a separate interferometer or any adjustments to the input pulse [69]. The pulses were spectrally filtered with a grating spectrometer before  $f_{\text{CEO}}$  detection. With an InGaAs PIN diode, we observed  $f_{\text{CEO}}$  beats in the RF spectrum in the 1050 - 1250 nm range ( $f-2f$ ). With a Si avalanche photodiode (APD), we observed  $f_{\text{CEO}}$  beats around 796 nm ( $2f-3f$ ), and around 566 nm ( $3f-4f$ ). The  $f_{\text{CEO}}$  beat signal at 796 nm ( $2f-3f$ ), shown in Fig. 3.4, had the highest S/N ratio. The signal was 30dB above the noise floor at a resolution of 100 kHz (the  $f_{\text{CEO}}$  signal bandwidth was  $<100$

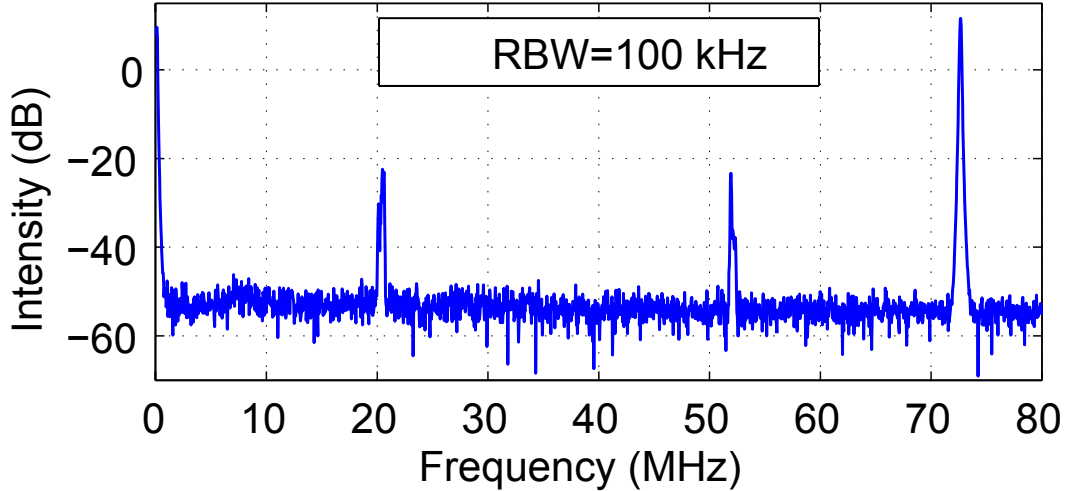


Figure 3.4: RF spectrum at 796 nm (filtered via a grating spectrometer) measured on a silicon APD, showing the repetition rate at 72 MHz, and  $f_{\text{CEO}}$  at 20 and 52 MHz.

kHz), and hence is suitable for feedback control. This measurement represents the first self-referenced Tm-fiber frequency comb, to the best of our knowledge.

In conclusion, our results show that QPM waveguides are a promising route towards compact mid-IR frequency combs based on Tm-fiber lasers. Our numerical model is in good agreement with the 1930-nm-pumped experiments discussed in this chapter, as well as the 1043-nm- and 1580-nm-pumped experiments of Ref. [2] which we discussed in chapter 2), even though the nonlinear dynamics differ significantly between each of these cases. Our model will help us exploit the high degree of engineerability of QPM gratings in the future. Significant improvements in bandwidth, energy requirements, and  $f_{\text{CEO}}$  signal can therefore be expected with improved QPM and waveguide designs; a promising approach towards such improvements is discussed in chapter 4. With mid-IR QPM media such as OP-GaAs [70], there is great potential to extend these methods to longer wavelengths in order to generate compact and low-cost frequency combs in the molecular fingerprint region.

## Chapter 4

# Dispersion-Engineered QPM Waveguides for Low-Energy Supercontinuum Generation

As discussed in the preceding chapters, one way to obtain spectral broadening in QPM media is via the cascaded  $\chi^{(2)}$  process. In this process, a Kerr-like self phase modulation (SPM) arises through phase mismatched SHG, with an effective third-order susceptibility  $\chi_{\text{cascade}}^{(3)} \propto -(\chi^{(2)})^2/\Delta\beta$  for large SHG phase mismatch  $\Delta\beta$ . In chapters 2 and 3, we showed that experimental demonstrations of QPM SC generation have so far been hampered by the strong competition between the cascaded  $\chi^{(2)}$  and  $\chi^{(3)}$  SPM effects [2, 38], and by the small dispersion at 2  $\mu\text{m}$  in  $\text{LiNbO}_3$  (which, for example, hinders pulse self-compression) [64]. In the 1580-nm-pumped experiments of [2], the sum of the cascaded  $\chi^{(2)}$  and  $\chi^{(3)}$  SPM terms yielded a rate of SPM that was almost an order of magnitude smaller than that due to the cascaded  $\chi^{(2)}$  term by itself (as shown in chapter 2).

The competition between nonlinear effects occurred in previous work because the pump was in the region of positive group velocity dispersion (GVD): in this case, the negative effective  $\chi^{(3)}$  susceptibility from  $\chi^{(2)}$  cascading must overcome the positive  $\chi^{(3)}$  susceptibility before bright soliton formation, an important step in SC generation, can occur [38, 54]. A large negative  $\chi_{\text{cascade}}^{(3)}$  could be obtained by

choosing a small and positive  $\Delta\beta$ . However, while such a reduction in  $|\Delta\beta|$  increases the rate of SPM, it also increases the rate of up-conversion of the first harmonic (FH) pulse to the second harmonic (SH) [47]. For SC generation, this up-conversion is a nonlinear loss mechanism for the FH, and hence limits how small  $|\Delta\beta|$  can usefully be made. In this chapter, we show that with the dispersion engineering made possible by tightly confining QPM waveguides, the energy requirements for octave-spanning SC generation can be reduced by two orders of magnitude compared to previous QPM-based approaches ( $\approx 30$  pJ compared to  $\approx 3$  nJ). To explain this improvement, we first discuss useful properties of tightly confining waveguides for QPM SC generation.

Given a large index contrast between the core and cladding layers of the waveguide, the zero-GVD frequency  $\omega_{\text{GVD}}$  can be increased substantially by changing the size of the core region [71]. By engineering a negative GVD at the input wavelength, soliton formation is possible with the  $\chi^{(2)}$  and  $\chi^{(3)}$  nonlinearities having the same (positive) sign, thereby avoiding competition between these effects. This procedure is analogous to GVD engineering in SC generation in  $\chi^{(3)}$  media, where the positive electronic  $\chi^{(3)}$  (and lack of any cascaded  $\chi^{(2)}$ ) requires engineering of the waveguide dispersion for operation in the negative-GVD regime [33, 71].

Another important property that can be achieved by waveguide design is group velocity (GV) matching of the FH and SH pulses. Consider the SHG interaction involving waveguide mode “0” of the FH and waveguide mode  $q$  of the SH. In Eq. (2.26) we defined the phase mismatch associated with this interaction as  $\Delta\beta_{m,q00}(z, \omega) \equiv \beta_q(2\omega) - 2\beta_0(\omega) - mK_g(z)$ , where  $\beta_j(\omega)$  is the propagation constant of mode  $j$  at frequency  $\omega$ . The group index mismatch associated with this interaction is given by

$$\delta n_{g,q}(\omega) \equiv n_{g,q}(2\omega) - n_{g,0}(\omega), \quad (4.1)$$

where the group index is given by

$$n_{g,j}(\omega) \equiv c(d\beta_j(\omega)/d\omega). \quad (4.2)$$

Assuming mode “0” for both the FH and SH mode, we define a zero-GVM frequency  $\omega_{\text{GVM}}$  as one satisfying  $\delta n_{g,0}(\omega_{\text{GVM}}) = 0$ .

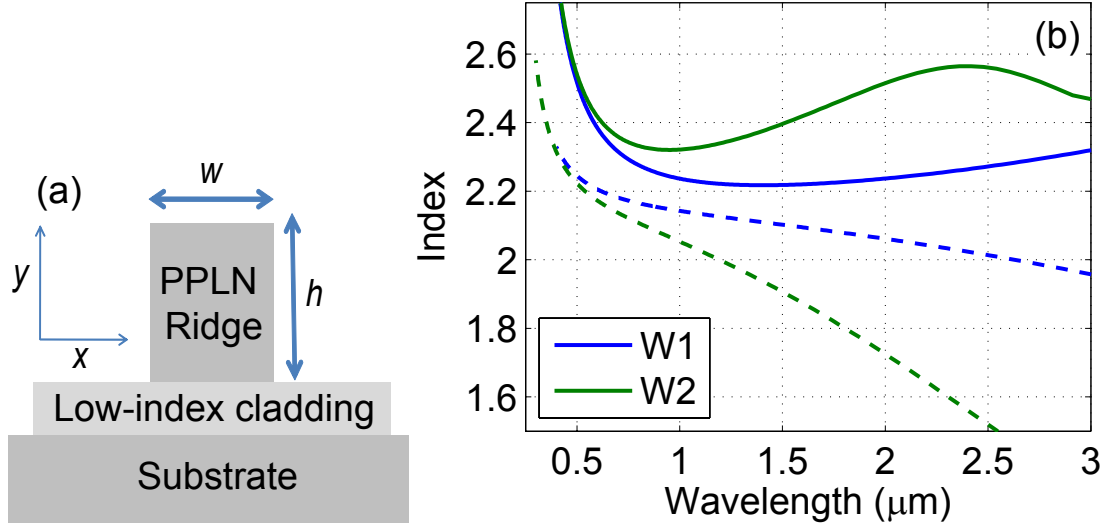


Figure 4.1: (a) Ridge waveguide schematic. Here, we assume a LiNbO<sub>3</sub> ridge, a low-index silica cladding, and air on the other sides of the ridge. (b) Modal effective index  $n$  (dashed lines) and group index  $n_g$  (solid lines) for waveguides W1 [ $w = h = 2.5 \mu\text{m}$ ], used for Fig. 4.2] and W2 [ $w = 0.8 \mu\text{m}$ ,  $h = 1.5 \mu\text{m}$ ], used for Fig. 4.3].

Up-conversion occurs for combinations spectral components close to phasematching. When GV matching is satisfied,

$$d\Delta\beta_{1,000}/d\omega \approx 0, \quad (4.3)$$

thereby minimizing the range of phase mismatches associated with a given pulse bandwidth (up to soliton effects, and higher orders in the dispersion relation). Thus, when the input frequency  $\omega_{FH} \approx \omega_{GVM}$ , the carrier phase mismatch  $|\Delta\beta_{1,000}(\omega_{FH})|$  can be made smaller (at a given pulse bandwidth) than at other input frequencies while still avoiding up-conversion at the edges of the spectrum; in turn, this reduction in  $|\Delta\beta_{1,000}|$  increases  $|\chi_{\text{cascade}}^{(3)}|$ , enabling a large SPM at low pulse energies.

To avoid up-conversion into SH mode  $q$  from FH mode 0, the phase mismatch  $|\Delta\beta_{1,q00}|$  must also be sufficiently large (or the relevant modal overlap integral must be sufficiently small). If the GVD is negative, then in order to obtain the positive  $\chi_{\text{cascade}}^{(3)}$  required to support bright solitons via the interaction between the lowest

order FH and SH modes, it is necessary that

$$\Delta\beta_{1,000}(\omega) < 0. \quad (4.4)$$

For higher order modes (i.e. for increasing mode index  $q$ ) at the SH, the propagation constant  $\beta_q$  is lowered towards that of the cladding(s), implying that  $\Delta\beta_{1,q00} < \Delta\beta_{1,000} < 0$ . Therefore, if  $|\Delta\beta_{1,000}|$  is large enough to avoid excessive up-conversion into SH mode 0, the  $|\Delta\beta_{1,q00}|$  are automatically large enough to avoid up-conversion into SH modes with  $q > 0$ .

Based on the above considerations, a suitable design procedure for QPM SC generation is to choose a waveguide size such that, for a given input frequency  $\omega$ ,

$$\omega \approx \omega_{\text{GVM}}. \quad (4.5)$$

The resulting GVD will be negative if the third order dispersion is positive, as is usually the case in the transparency window of the material and away from the cut-off wavelength of the (asymmetric) waveguide. A negative GVD can be seen in Fig. 4.1(b) by the positive slope of the group index with respect to wavelength for wavelengths  $\lambda$  longer than the zero-GVD wavelength  $\lambda_{\text{GVD}}$  (for example, at  $2 \mu\text{m}$  and  $1.5 \mu\text{m}$  for the solid blue and green lines, respectively). With an appropriate choice of QPM period (i.e. so that the associated  $\chi_{\text{cascade}}^{(3)} > 0$ ),  $\chi^{(2)}$ - $\chi^{(3)}$  competition is therefore avoided while still supporting bright solitons. Furthermore, SPM can be maximized by choosing a value of  $|\Delta\beta_{1,000}|$  just large enough to avoid excessive up-conversion into the lowest-order mode of the SH; given this choice of  $\Delta\beta_{1,000}$ , nonlinear loss via up-conversion into higher order SH modes is avoided automatically. In contrast, for cases with  $\omega > \omega_{\text{GVD}} > \omega_{\text{GVM}}$  [2], each of the above effects is detrimental to the SC generation process [38].

We demonstrate the above design concepts by considering SC generation examples with  $\text{LiNbO}_3$  ridge waveguides with the layout depicted in Fig. 4.1(a). This configuration is generally similar to that used in Refs. [72, 73] for efficient SHG devices. For the first example, we assume a center wavelength of 1950 nm, and waveguide dimensions  $w = h = 2.5 \mu\text{m}$ ; this waveguide is denoted W1. The corresponding dispersion

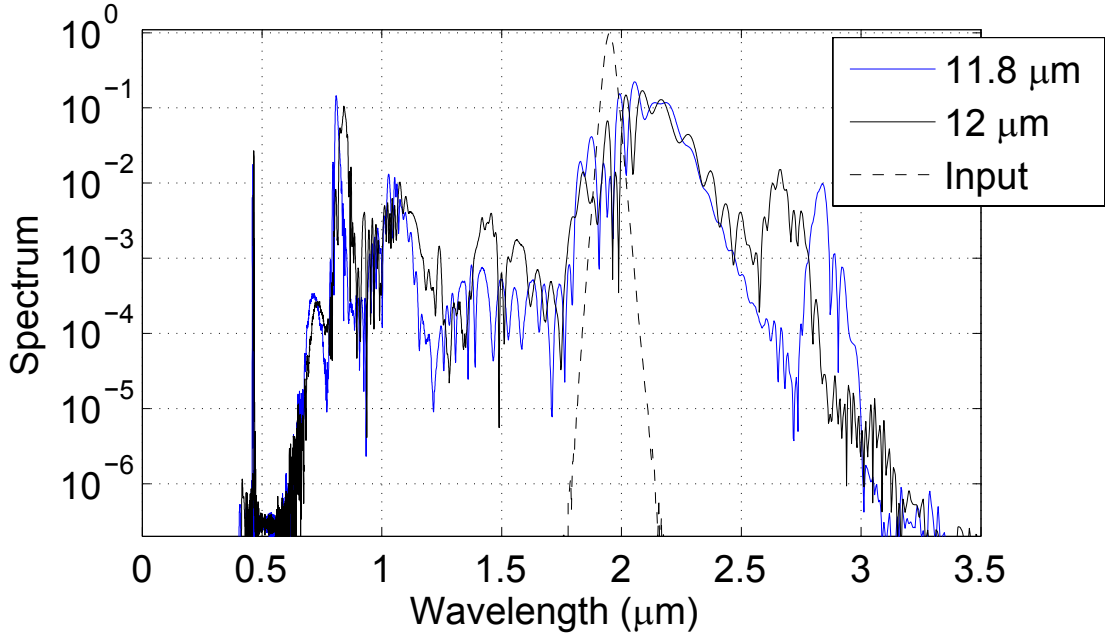


Figure 4.2: Input (pump) and output (SC) spectra for waveguide W1 ( $w = h = 2.5 \mu\text{m}$ ), whose dispersion profile is shown in Fig. 4.1(b). Two different cases, with QPM periods of 11.8 and 12.0  $\mu\text{m}$ , are plotted as the blue and black curves, respectively.

relation for the lowest-order  $y$ -polarized mode is shown via the blue curves in Fig. 4.2(b): for this mode, GV-matching occurs between the FH and SH, with zero-GVD wavelength  $\approx 1.4 \mu\text{m}$ . The mode profiles were calculated as in [11]. The E-field of the mode is polarized (primarily) along the crystalline  $c$ -axis; in our simulations, we therefore neglect all non- $e$ -wave-polarized  $\chi^{(2)}$  and  $\chi^{(3)}$  tensor elements for simplicity.

To simulate SC generation we use the model and nonlinear parameters described in chapter 2; this model captures both  $\chi^{(2)}$  and  $\chi^{(3)}$  interactions between multiple bound waveguide modes. Figure 4.2 shows the multiple-octave-spanning spectra that result from using waveguide W1 with two different choices of QPM grating period (11.8 and 12.0  $\mu\text{m}$ ); the period for QPM SHG of the input 1950-nm pulse is 12.3  $\mu\text{m}$ . The input  $\text{sech}^2$  pulse had FWHM duration of 100 fs and energy of 60 pJ. The QPM periods were chosen to yield SC generation spectra with low energy requirements (given a periodic grating). Fig. 4.2 indicates that with an appropriate waveguide design, low-energy SC generation can be obtained with a relatively wide range of

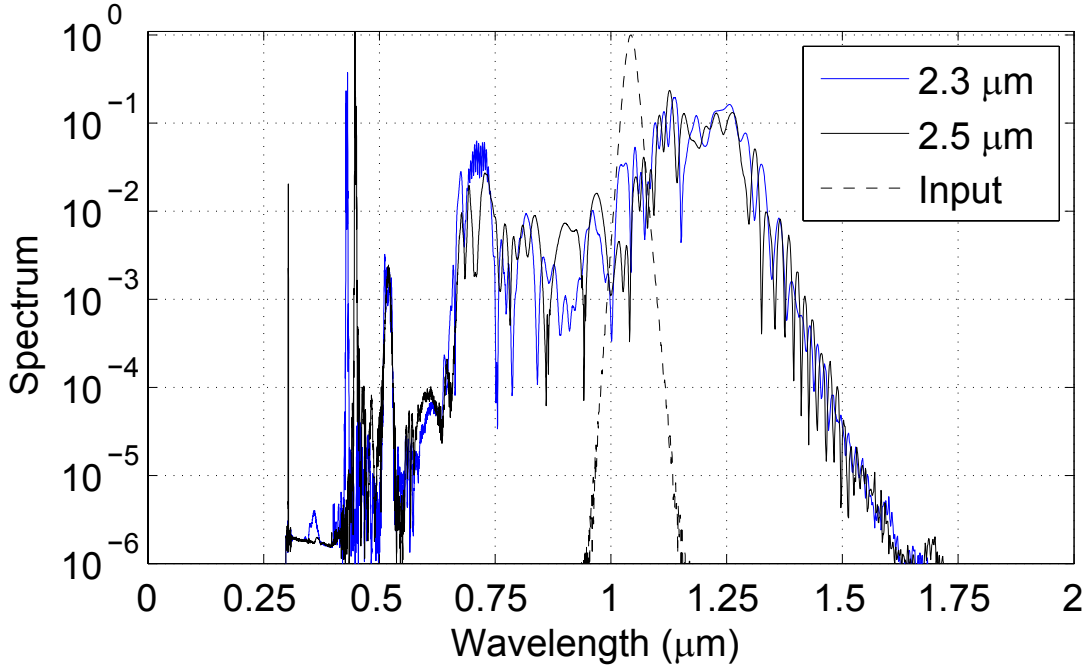


Figure 4.3: Input and output spectrum for waveguide W2 ( $w = 0.8 \mu\text{m}$ ,  $h = 1.5 \mu\text{m}$ ), whose dispersion profile is shown in Fig. 4.1(b). Two different cases, with QPM periods of 2.3 and 2.5  $\mu\text{m}$ , are plotted as the blue and black curves, respectively.

QPM periods.

To demonstrate the limits of the approach, we next consider a 1043-nm-pumped example. In Ref. [2], SC generation was demonstrated with 1043-nm-pumping, but, as discussed in section 2.3, this SC was incoherent. As discussed there, the reason for the incoherence is related to the large GV mismatch and the large  $\chi^{(2)}$ - $\chi^{(3)}$  competition in the waveguide, which required high pulse energies, leading to significant SHG which in turn led to high-gain OPA of vacuum noise. By engineering the waveguide dispersion, SC generation can be achieved with much lower pulse energies and without significant noise amplification. However, for the y-polarized mode of the waveguide layout shown in Fig. 4.1(a), the index contrast is insufficient to shift the zero-GVD wavelength  $\lambda_{\text{GVD}}$  significantly below 1043 nm, as required for low-energy SC generation. Therefore, we turn to the x-polarized mode, which offers greater waveguide dispersion since it is polarized primarily along the direction of tightest confinement

(air). To use  $d_{33}$  with this mode, the  $x$ -axis must correspond to the crystalline  $c$ -axis, adding to the fabrication challenges associated with machining waveguides of such small transverse dimensions.

We assume a waveguide design with  $w = 0.8 \mu\text{m}$  and  $h = 1.5 \mu\text{m}$ , and denote this design as waveguide W2. We note that fabrication of the waveguide dimensions as small as those required here may present practical difficulties. The dispersion relation for the lowest-order  $x$ -polarized mode of W2 is shown in Fig. 4.1(b). The zero-GVD wavelength  $\lambda_{\text{GVD}} \approx 0.9 \mu\text{m}$ , and the GVD is negative at the input wavelength. However, even for this mode, GV matching cannot be obtained for a 1043-nm pump. We assume a pulse with 50-fs (FWHM) duration, 30-pJ energy, and center wavelength of 1043 nm. The resulting octave-spanning output spectrum is shown in Fig. 4.3 for QPM periods of 2.3 and 2.5- $\mu\text{m}$ ; the period for QPM SHG is 3.16  $\mu\text{m}$ . The energy requirements are comparable to the 1950-nm pump assumed for Fig. 4.2: while the nonlinearity is enhanced by the smaller mode areas and higher frequency, the FH and SH group velocities are not matched, and hence a larger phase mismatch is required to avoid up-conversion to the SH. Figure 4.3 shows that low-energy 1- $\mu\text{m}$ -pumped SC generation can be obtained with LiNbO<sub>3</sub> ridge waveguides, but with strict fabrication requirements. For a pump wavelength around 1.55  $\mu\text{m}$ , these requirements are relaxed: the  $y$ -polarized mode of a waveguide with dimensions  $w = h = 1.1 \mu\text{m}$  could be used, similar to the 1950-nm example of Fig. 4.2.

In conclusion, our results show that group-velocity-engineered QPM waveguides are a promising route towards compact and low-pulse-energy frequency combs. We have simulated SC generation in realistic ridge waveguide designs with a validated numerical model [38]. Multiple-octave-spanning SC generation can be achieved in these QPM waveguides with pulse energies two orders of magnitude lower than in previous demonstrations; such pulse energies represent a small fraction of the energy available in modern ultrafast fiber lasers [66]. For LiNbO<sub>3</sub>, the approach described here is suited to pump wavelengths between approximately 1 and 3  $\mu\text{m}$ . To obtain GV-matching at longer wavelengths, materials such as GaAs and GaP could be used. With simultaneous dispersion and QPM engineering, waveguides which concentrate the SC energy into specific spectral regions or prepare the pulses for subsequent

nonlinear mixing stages might be realized. Since the bandwidth can be maximized around a given input frequency, this approach also holds great potential for a wide variety of applications in addition to IR and mid-IR frequency comb generation. With dispersion engineering, it may also be possible to optimize the coherence properties of the supercontinuum. Since the modulation instability (MI) of three-wave mixing processes differs substantially from those associated with true SPM and XPM effects [74], the coherence of QPM supercontinua warrants investigation in future work.

# Chapter 5

## Multiple Nonlinear Envelope Model of Pulse Propagation in Nonlinear Media

### 5.1 Introduction

In chapter 2, we introduced a single-envelope (SE) approach to describing arbitrary-bandwidth forward-propagating waves in QPM gratings. This SE model extends the numerical models developed for  $\chi^{(3)}$  media (see for example Refs. [39, 40]) to QPM waveguides. Good agreement with experimental results could be obtained provided that  $\chi^{(2)}$ ,  $\chi^{(3)}$  and multiple waveguide modes were all included in the model [38], justifying the use of these models for a wide range of QPM interactions.

However, a limitation of SE models is that they do not account for the generation of higher harmonic components explicitly: instead, these components are contained implicitly in the single envelope. As a result, several limitations emerge when using this approach to model nonlinear-optical interactions, and QPM interactions in particular. These issues include loss of information (frequency comb lines do not emerge unambiguously from a single simulation), computational issues (negligible interactions that can slow simulations down substantially are included automatically and unavoidably), difficulties in interpreting results or using the simulations as a design

tool (since with only a single envelope, all the individual sum and difference frequency generation processes are not distinguished from each other), and physical assumptions (with a SE approach, inaccurate approximations on the frequency dependence of the nonlinear coupling coefficients may be required). More generally, SE approaches do not allow the structure of many nonlinear interactions to be exploited effectively.

In this chapter, we introduce generalized coupled wave equations (GCWEs) to describe interactions in nonlinear media in which the electric field of each waveguide mode is decomposed into a series of envelopes centered at each harmonic order. With this GCW approach, the above issues with SE approaches are resolved, resulting in a model that is more general, more tractable numerically, and significantly simplifies the interpretation of numerical results. We focus on interactions involving discrete waveguide modes, but the same model we develop could be applied to bulk interactions as well. We first introduce this model in section 5.2. In section 5.3, we discuss several simplifications that make numerical simulations more tractable. In section 5.4, we demonstrate the model with a specific numerical example. In section 5.5, we discuss the advantages of the GCW model over existing SE approaches. In the appendices at the end of this chapter (sections 5.7 and 5.8) we discuss some important details about the GCWE model.

## 5.2 Generalized Coupled Wave Equations

In this section, we introduce GCWEs to model interactions in nonlinear media, with emphasis on QPM media. The electric field in each waveguide mode is first split into a series of harmonic envelopes centered at carrier frequencies  $N\omega_0$  for integer  $N$  and suitably chosen optical frequency  $\omega_0$ . Then, each term of the nonlinear polarization resulting from the mixing of these envelopes is associated with the envelope with the corresponding carrier frequency. In this way, we can construct a versatile, tractable, and accurate model in which all nonlinear processes have clear meaning and where no processes are neglected *a priori* or approximated inaccurately. We account for processes involving the  $\chi^{(1)}$ ,  $\chi^{(2)}$ , and  $\chi^{(3)}$  susceptibilities; higher order susceptibilities could be included in the same way.

Some of the resulting  $\chi^{(2)}$  interactions are illustrated in Fig. 5.1. First, consider the case of a narrow-bandwidth pulses shown in Fig. 5.1(a). An incident first harmonic (FH) pulse (carrier frequency  $\omega_0$ ) generates a second harmonic (SH) pulse component with carrier frequency  $2\omega_0$  through SHG; simultaneously, a third harmonic (TH) pulse component is generated through sum frequency generation (SFG) of the FH and SH pulses. Additionally, intrapulse difference frequency generation (DFG) of each pulse occurs, generating pulse components at low frequencies. In principle, these interactions lead to pulse components (harmonics) with carrier frequencies  $N\omega_0$  for all  $N \geq 0$ ; each of these harmonics can be associated with a different electric field envelope. Similarly, in a pulse train, each harmonic has a carrier envelope offset (CEO) frequency  $f_{\text{CEO}}^{(N)} = Nf_{\text{CEO}}^{(1)}$ , where  $f_{\text{CEO}}^{(N)}$  denotes the CEO frequency of the  $N^{\text{th}}$  harmonic [75]. Eventually, the envelopes become negligible for  $N > N_{\text{max}}$ , where integer  $N_{\text{max}}$  is determined by the nonlinear dynamics. In Fig. 5.1(a), terms up to  $N = 3$  are shown.

For interactions involving pulses which are sufficiently broadband that their spectra overlap, more complicated dynamics can arise, as illustrated in Fig. 5.1(b). For example, in addition to the types of processes illustrated in Fig. 5.1(a), DFG can occur between spectral components of the FH exceeding those of the SH. The GCW model developed in this section accounts for these additional interactions, and is used in subsection 5.4.4 to show that they are often negligible, even in an example involving highly nonlinear and ultrabroadband pulse propagation.

### 5.2.1 Propagation of Waveguide Modes

In this subsection, we determine equations for nonlinear coupling between forward-propagating waveguide modes. We start from the results given in chapter 1, and take a similar approach to the one given in chapter 2. The nonlinear polarization  $P_{NL}$  is given by Eq. (1.4). As in chapter 2, in this chapter we will neglect all but a single element of the nonlinear susceptibilities and a single Cartesian component (or projection) of the electric field, and hence use the simplified form of  $P_{NL}$  given by Eq. (2.3). For QPM interactions in  $\text{LiNbO}_3$ , this approximation would typically

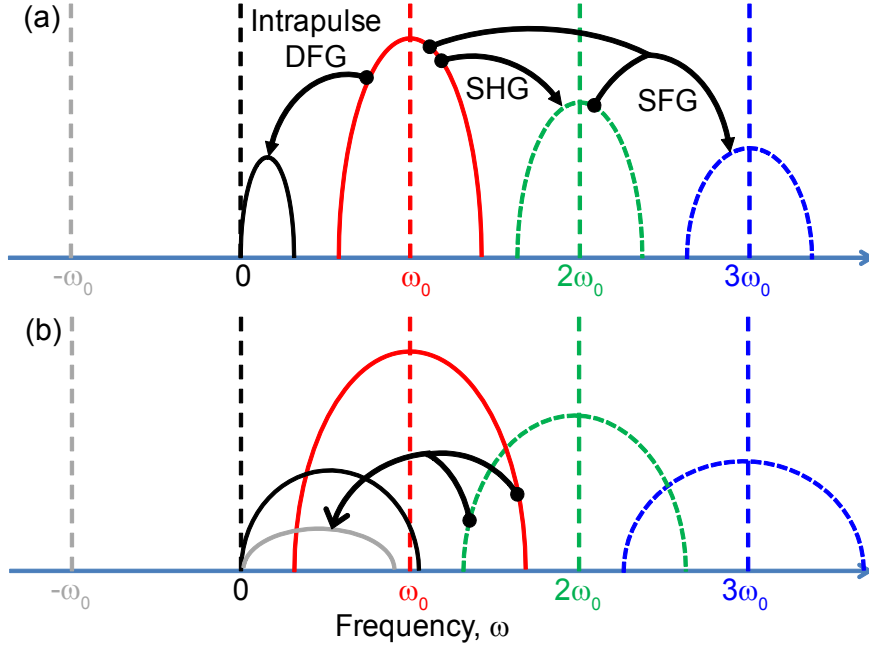


Figure 5.1: Schematic of envelope spectra and interactions in the generalized coupled wave model. The vertical dashed lines indicate the carrier frequencies of the different envelopes. Black arrows indicate nonlinear-optical processes. (a) Case with non-overlapping spectra, and corresponding sum and difference frequency generation processes. (b) Case with overlapping spectra, illustrating the additional DFG process between spectral components of the FH exceeding those of the SH, which results in a non-zero amplitude for the  $N = -1$  envelope (solid gray curve). Note that since all the envelopes are defined as analytic signals, their negative frequency components explicitly vanish.

correspond to including only  $\chi_{333}^{(2)}$ ,  $\chi_{3333}^{(3)}$ , and  $E_3$  in the analysis; the subscript 3 denotes the crystalline c axis, which in the coordinate system used in chapters 1 and 2 corresponds to the  $x$  axis. Of course, in certain cases, such as accidental near quasi-phasematching to an orthogonally polarized mode, or a Type-II interaction, more than one Cartesian component will have to be included. With Eq. (1.17), the equations developed here could be generalized straightforwardly to include the required tensor elements and polarizations.

We define an envelope for each waveguide mode through the relations

$$\tilde{A}_n(z, \omega) = 2\tilde{\Phi}_n(z, \omega)u(\omega)e^{-i\beta_n(\omega)z} \quad (5.1)$$

where the electric field is given in terms of  $\tilde{\Phi}_n$  by Eq. (1.14). This is the same as the form assumed in Eq. (2.2), but with the reference frequency and propagation constant set to zero. As in chapter 2,  $\tilde{A}_n$  are analytic signals, i.e.  $\tilde{A}_n(\omega < 0) = 0$ . Based on Eqs. (1.14) and (5.1), the electric field is given by

$$\tilde{\mathbf{E}}(x, y, z, \omega)u(\omega) = \frac{1}{2} \sum_n \tilde{A}_n(z, \omega)\mathbf{E}_n(x, y, \omega). \quad (5.2)$$

As in chapter 2, we assume weakly-guiding waveguides for simplicity and approximate the mode profiles using Eq. (2.1). Based on Eq. (1.19), the propagation equation for the amplitude of each waveguide mode is given by

$$\frac{\partial \tilde{A}_n}{\partial z} + i \left[ \beta_n - i \frac{\alpha_n}{2} \right] \tilde{A}_n = -i \frac{\omega^2 u}{g_n \beta_n c^2} \tilde{\mathcal{P}}_n, \quad (5.3)$$

where the attenuation coefficients  $\alpha_n$  for each waveguide mode have been added heuristically. Each effective modal driving polarization  $\tilde{\mathcal{P}}_n$  is defined as an overlap integral of the nonlinear polarization  $\tilde{P}_{NL}(x, y, z, \omega)$  and modal profile  $B_n(x, y, \omega)$  [introduced in Eq. (2.1)],

$$\tilde{\mathcal{P}}_n(z, \omega) = \int_{-\infty}^{\infty} \tilde{P}_{NL}(x, y, z, \omega) B_n(x, y, \omega) dx dy, \quad (5.4)$$

where we will use symbol  $\mathcal{P}$  in general to denote various types of modal overlap integrals involving contributions to the nonlinear polarization. The frequency-dependent mode normalization factors  $g_n$  are given by Eq. (2.7).

To evaluate  $\tilde{\mathcal{P}}_n$  in Eq. (5.4), we use the effective modal susceptibilities defined in Eqs. (2.4) and (2.5). As discussed in chapter 2, the scale of the modal spatial profiles  $B_n(x, y, \omega)$  is arbitrary, since any frequency-dependent scale factor applied to  $B_n$  can be absorbed into  $\tilde{A}_n$ . For most cases, the choice  $g_n(\omega) = A_{\text{eff},n}(\omega)^{1/3}$  (which we made

in chapter 2) is sufficiently accurate. However, in some cases it is important to choose  $g_n(\omega)$  more systematically; these cases are discussed in section 5.8.

### 5.2.2 Expansion in Harmonic Orders

Equation (5.3) is sufficient to model general nonlinear interactions, but does not represent a particularly tractable model since it does not exploit any of the structure of the processes involved (except for the presence of waveguide modes). In this section, we split each modal amplitude  $\tilde{A}_n$  into a set of harmonic envelopes  $A_{n;N}$  at each harmonic order  $N$  (first harmonic, second harmonic, and so on), and write Eq. (5.4) using these harmonic envelopes. We decompose the modal amplitude  $\tilde{A}_n$  in harmonic envelopes  $\tilde{A}_{n;N}$  according to

$$\tilde{A}_n(z, \omega) = \sum_N \tilde{A}_{n;N}(z, \omega) \quad (5.5)$$

where  $\tilde{A}_{n;N}$  denotes an envelope representing spectral content in waveguide mode  $n$  centered around frequency  $N\omega_0$  for integer  $N$ , with  $\omega_0$  an (arbitrary) reference frequency (for example, the center frequency of the input pulse). We use capital sub- and superscripts to denote a harmonic order  $N$ , and lower case sub- and superscripts to denote a waveguide mode index  $n$  (corresponding to envelope  $a_{A;N}$ ). We refer to  $A_{n;1}$  as the first harmonic,  $A_{n;2}$  as the second harmonic, and  $A_{n;3}$  as the third harmonic envelope of mode  $n$ . Eventually, we will shift each envelope  $\tilde{A}_{n;N}$  to explicitly be centered around optical frequency  $N\omega_0$  (while still being zero for negative optical frequencies), but this procedure is deferred until subsection 5.2.4 in order to simplify the intermediate steps.

Given Eq. (5.5), the effective modal driving polarizations  $\tilde{\mathcal{P}}_n$  defined in Eq. (5.4) can be split up into several different types of terms. The integrals over transverse coordinates  $x$  and  $y$  in Eq. (5.4) result in the frequency-dependent coefficients  $X_{npq}$  and  $X_{npqr}$  defined in Eqs. (2.4) and (2.5), respectively. The second-order terms of  $\mathcal{P}_n$  correspond to sum and difference frequency generation (SFG and DFG, respectively).

The components of  $\tilde{\mathcal{P}}_n$  corresponding to SFG are given by

$$\begin{aligned} \tilde{\mathcal{P}}_{(npq);(P,Q)}^{(SFG)}(\omega) = \\ \int_0^\omega X_{npq}(\omega, \omega', \omega - \omega') \tilde{A}_{p;P}(\omega') \tilde{A}_{q;Q}(\omega - \omega') d\omega', \end{aligned} \quad (5.6)$$

where the integration limits arise from using analytic signals. The components corresponding to difference frequency generation (DFG) are given by

$$\begin{aligned} \tilde{\mathcal{P}}_{(npq);(P,Q)}^{(DFG)}(\omega) = \\ \int_0^\infty X_{npq}(\omega, \omega', \omega + \omega') \tilde{A}_{p;P}^*(\omega') \tilde{A}_{q;Q}(\omega + \omega') d\omega'. \end{aligned} \quad (5.7)$$

The  $\chi^{(3)}$  terms of the nonlinear polarization can be split up based on the number of negative Fourier components involved in the integrand in Eq. (2.3), and hence the number of complex conjugate  $A_{n;N}$  factors. Terms with no negative Fourier components correspond to  $\chi^{(3)}$  SFG (e.g. third harmonic generation, THG); those with one negative Fourier component correspond to various four-wave mixing (FWM) processes (e.g. cross-phase modulation, XPM), while those with two negative Fourier components correspond to  $\chi^{(3)}$  DFG (e.g. depletion of the FH in THG). There are no terms with three negative Fourier components, since we have assumed analytic signals.

The contributions to  $\tilde{\mathcal{P}}_n$  corresponding to  $\chi^{(3)}$  SFG are given by

$$\begin{aligned} \tilde{\mathcal{P}}_{(npqr);(P,Q,R)}^{(SFG)}(\omega) = \\ \int_0^\omega \int_0^{\omega-\omega'} X_{npqr}(\omega, \omega', \omega'', \omega - \omega' - \omega'') \times \\ \left. \tilde{A}_{p;P}(\omega') \tilde{A}_{q;Q}(\omega'') \tilde{A}_{r;R}(\omega - \omega' - \omega'') d\omega' d\omega'' \right], \end{aligned} \quad (5.8)$$

the FWM contributions are given by

$$\begin{aligned} \tilde{\mathcal{P}}_{(npqr);(P,Q,R)}^{(FWM)}(\omega) = & \\ & \int_0^\infty \int_0^{\omega+\omega'} X_{npqr}(\omega, -\omega', \omega'', \omega + \omega' - \omega'') \times \\ & \tilde{A}_{p;P}^*(\omega') \tilde{A}_{q;Q}(\omega'') \tilde{A}_{r;R}(\omega + \omega' - \omega'') d\omega' d\omega'', \end{aligned} \quad (5.9)$$

and the  $\chi^{(3)}$  DFG contributions are given by

$$\begin{aligned} \tilde{\mathcal{P}}_{(npqr);(P,Q,R)}^{(DFG)}(\omega) = & \\ & \int_0^\infty \int_0^\infty X_{npqr}(\omega, -\omega', -\omega'', \omega + \omega' + \omega'') \times \\ & \tilde{A}_{p;P}^*(\omega') \tilde{A}_{q;Q}^*(\omega'') \tilde{A}_{r;R}(\omega + \omega' + \omega'') d\omega' d\omega'', \end{aligned} \quad (5.10)$$

With Eqs. (5.6-5.10), the effective modal driving polarization for each waveguide mode  $n$ , defined in Eq. (5.4), can be expressed as a sum of the different types of terms,

$$\begin{aligned} \tilde{\mathcal{P}}_n = & \frac{1}{4} \sum_{p,q} \sum_{PQ} \left[ 2\tilde{\mathcal{P}}_{(npq);(P,Q)}^{(DFG)} + \tilde{\mathcal{P}}_{(npq);(P,Q)}^{(SFG)} \right] + \\ & \frac{1}{8} \sum_{p,q,r} \sum_{P,Q,R} \left[ 3\tilde{\mathcal{P}}_{(npqr);(P,Q,R)}^{(FWM)} \right. \\ & \left. + 3\tilde{\mathcal{P}}_{(npqr);(P,Q,R)}^{(DFG)} + \tilde{\mathcal{P}}_{(npqr);(P,Q,R)}^{(SFG)} \right], \end{aligned} \quad (5.11)$$

where summation is performed over all waveguide modes and harmonic orders.

### 5.2.3 Assignment of Nonlinear Driving Terms

In this subsection, we assign the effective modal driving polarization terms defined in Eqs. (5.6-5.10) to equations describing the propagation of the harmonic envelopes  $A_{n;N}$ . Since each  $A_{n;N}$  will have carrier frequency  $N\omega_0$ , we assign to the propagation

equation for  $A_{n;N}$  all the terms of the polarization  $\tilde{\mathcal{P}}_n$  which also have carrier frequency  $N\omega_0$ . Note that this assignment includes negative integers  $N$ , e.g.  $A_{n;-1}$ , but we will maintain the assumption of analytic signals, such that for optical frequency  $\omega$ ,  $\tilde{A}_{n;N}(\omega < 0) = 0$ ; as a result,  $A_{n;N}$  for  $N < 0$  is only non-zero for octave spanning spectra. With this assignment, Eq. (5.3) can be expanded as

$$\frac{\partial \tilde{A}_{n;N}}{\partial z} + i \left[ \beta_n - i \frac{\alpha_n}{2} \right] \tilde{A}_{n;N} = -i \frac{\omega^2 u}{g_n \beta_n c^2} \tilde{\mathcal{P}}_{n;N} \quad (5.12)$$

where the effective harmonic polarizations  $\tilde{\mathcal{P}}_{n;N}$  are defined as

$$\begin{aligned} \tilde{\mathcal{P}}_{n;N} = & \frac{1}{4} \sum_{p,q,P} \left[ 2\tilde{\mathcal{P}}_{(npq),(P,N+P)}^{(DFG)} + \tilde{\mathcal{P}}_{(npq),(P,N-P)}^{(SFG)} \right] + \\ & \frac{1}{8} \sum_{p,q,r,P,Q} \left[ 3\tilde{\mathcal{P}}_{(npqr),(P,Q,N+P-Q)}^{(FWM)} + \right. \\ & \left. 3\tilde{\mathcal{P}}_{(npqr),(P,Q,N+P+Q)}^{(DFG)} + \tilde{\mathcal{P}}_{(npqr),(P,Q,N-P-Q)}^{(SFG)} \right]. \end{aligned} \quad (5.13)$$

To illustrate the meaning of Eqs. (5.12) and (5.13), consider the case of SHG in the fundamental waveguide mode, hence involving only the envelopes  $A_{0;N}$ , and involving only the FH and SH envelopes, further limiting consideration to  $A_{0;1}$  and  $A_{0;2}$ . In this case, and for the SH, Eq. (5.12) becomes

$$\begin{aligned} \frac{\partial \tilde{A}_{0;2}}{\partial z} + i \left[ \beta_0 - i \frac{\alpha_0}{2} \right] \tilde{A}_{0;2} = & -i \frac{\omega^2 u}{g_0 \beta_0 c^2} \\ & \times \left[ \frac{1}{4} \tilde{\mathcal{P}}_{(000),(1,1)}^{(SFG)} + \frac{3}{8} \tilde{\mathcal{P}}_{(0000),(2,2,2)}^{(FWM)} + \frac{6}{8} \tilde{\mathcal{P}}_{(0000),(1,1,2)}^{(FWM)} \right], \end{aligned} \quad (5.14)$$

which includes effective polarization terms for SHG, as well as terms for SPM (prefactor 3/8) and XPM (prefactor 6/8); these factors arise from summation over  $P$  and  $Q$  in Eq (5.13).

### 5.2.4 Propagation of Harmonic Envelopes

In this subsection, we introduce appropriate carrier frequencies and phases into the electric field envelopes, simplify the effective nonlinear susceptibilities, and arrive at a propagation equation for each of the envelopes. We first define frequency-shifted envelopes  $\tilde{a}_{n;N}$  using carrier frequencies  $N\omega_0$ , carrier propagation constants  $\beta_0(N\omega_0)$ , and assume a reference group velocity  $v_{\text{ref}}$ . The same reference propagation constant for the carrier,  $\beta_0(N\omega_0)$ , is used for all modes  $n$ , and hence with each envelope  $a_{n;N}$ . The relation  $\beta_n(-\omega) = -\beta_n(\omega)$  is used to evaluate  $\beta_0(N\omega)$  for envelopes with  $N < 0$ . The reference group velocity is typically chosen to correspond to the group velocity of the lowest-order mode of the FH. The shifted envelopes  $a_{n;N}$  are related to the envelopes  $\tilde{A}_{n;N}$  according to

$$\begin{aligned} \tilde{A}_{n;N}(z, \omega) = & \tilde{a}_{n;N}(z, \omega - N\omega_0) \times \\ & \exp[-i(\beta_0(N\omega_0) - N\omega_0/v_{\text{ref}})z]. \end{aligned} \quad (5.15)$$

Before applying these shifted envelopes, we simplify the effective susceptibilities by approximating them as independent of frequency within the integrands defined by Eqs. (5.6-5.10). With this assumption, all of the components of  $\tilde{\mathcal{P}}_n$  can be calculated efficiently via products of time-domain envelopes  $a_{n;N}(t)$  [38].

For QPM interactions, it is also convenient to expand the grating in terms of its (local) Fourier coefficients [14]. As discussed in chapter 2, the nonlinear susceptibility can vary in position  $(x, y, z)$  due to waveguide and QPM fabrication non-uniformities [42, 43]. Usually, it can be assumed that these changes in  $\chi^{(2)}$  are separable in transverse coordinate  $(x, y)$  and propagation coordinate  $z$ , and that  $\chi^{(2)}(x, y, z) = \pm|\chi^{(2)}(x, y, 0)|$ , where  $\chi^{(2)}(x, y, z)$  is the local  $\chi^{(2)}$  tensor element. In these cases, the QPM grating can be expressed according to Eqs. (1.25) and (1.26).

Inserting Eq. (1.25) for  $\chi^{(2)}$  into Eq. (2.4) for the effective susceptibility, we can

define approximate  $\chi^{(2)}$  nonlinear coefficients as

$$\begin{aligned} \bar{X}_{m;(n,p,q)}^{(N,P,N-P)}(z) &\equiv X_{npq}(\omega_N, \omega_P, \omega_N - \omega_P) \\ &\times \bar{d}_m \exp [i(\Delta\beta_{N;P}z - m\phi_G(z))]. \end{aligned} \quad (5.16)$$

where  $\bar{X}_{m;npq}^{N,P,Q}$  represents the contribution of the  $m^{\text{th}}$  Fourier component of the QPM grating to the coupling coefficient between envelope  $a_{n;N}$  (spectral components of the envelope of mode  $n$  and with carrier frequency  $N\omega_0$ ) to envelopes  $a_{p;P}$  and  $a_{q;Q}$ . To determine these coefficients, the effective susceptibilities  $X_{npq}$  are evaluated at frequencies  $\omega_N$ ,  $\omega_P$ , and  $\omega_N - \omega_P$  in Eq. (5.16); these frequencies can in general be different for each  $\bar{X}$  coefficient, but are not unconstrained. The most “natural” choice,  $\omega_J = J\omega_0$ , is often (but not always) appropriate. Appropriate choices of these frequencies for different types of problems are discussed in the appendices at the end of this chapter (sections 5.7 and 5.8). The phase mismatch terms are given by

$$\Delta\beta_{N;P} = \beta_0(N\omega_0) - \beta_0(P\omega_0) - \beta_0((N - P)\omega_0). \quad (5.17)$$

For the  $\chi^{(3)}$  terms, the different types of contributions to the third-order susceptibility must be considered. Here we will assume that  $\chi^{(3)}$  is comprised of a “fast” electronic component  $\chi_E$  and a “slow” Raman component  $\chi_R$ , as discussed in section 2.2. Although other contributions (such as Brillouin scattering) exist,  $\chi_E$  and  $\chi_R$  are likely to be the most relevant for broadband interactions. Thus we assume that the third-order susceptibility can be approximated according to Eq. (2.10). In section 5.8, the dispersion of  $\chi_E$  is discussed, since related quantities such as the nonlinear refractive index  $n_2$  can increase substantially for frequencies close to half the band gap [54].

Given the above form of  $\chi^{(3)}$ , we introduce effective susceptibilities similar to  $\bar{X}$  defined in Eq. (5.16) to model the  $\chi^{(3)}$  terms in Eq. (5.13). We first define  $\chi^{(3)}$  carrier

phase mismatch terms as

$$\begin{aligned} \Delta\beta_{N;P,Q} = & \beta_0(N\omega_0) - \beta_0(P\omega_0) - \\ & \beta_0(Q\omega_0) - \beta_0((N - P - Q)\omega_0). \end{aligned} \quad (5.18)$$

For SPM and XPM effects, these phase mismatch terms are zero. Using this form of  $\Delta\beta$ , for the FWM-type terms of Eq. (5.13) (which includes SPM and XPM terms) we can define coefficients

$$\begin{aligned} \bar{X}_{E;npqr}^{N,P,Q,N+P-Q}(z) = & \chi_E \theta_{npqr}(\omega_N, -\omega_P, \omega_Q) \\ & \times \exp(i\Delta\beta_{N;-P,Q}z) \end{aligned} \quad (5.19)$$

for the fast  $\chi^{(3)}$  component,  $\chi_E$ . Similarly for the slow  $\chi^{(3)}$  component,  $\chi_R$ , we define

$$\begin{aligned} \bar{X}_{R;npqr}^{N,P,Q,N+P-Q}(z, \Omega) = & \chi_R(\Omega) \theta_{npqr}(\omega_N, -\omega_P, \omega_Q) \\ & \times \exp(i\Delta\beta_{N;-P,Q}z) \end{aligned} \quad (5.20)$$

which maintains the dependence of the effective susceptibility on the frequency shift variable  $\Omega$ . For SFG-like terms such as third harmonic generation, we define coefficients

$$\begin{aligned} \bar{Y}_{npqr}^{N,P,Q,N-P-Q}(z) = & \chi_E \theta_{npqr}(\omega_N, \omega_P, \omega_Q) \\ & \times \exp(i\Delta\beta_{N;P,Q}z). \end{aligned} \quad (5.21)$$

As with the  $\chi^{(2)}$  nonlinear coefficients, the frequencies  $\omega_N, \omega_P, \omega_Q$  at which  $\theta_{npqr}$  is evaluated can vary for each nonlinear coefficient  $\bar{X}$  and  $\bar{Y}$ , but are not unconstrained; appropriate choices of these frequencies for different types of problems are also discussed in sections 5.7 and 5.8.

With the envelopes  $a_{n;N}$  defined in Eq. (5.15) and the nonlinear coefficients  $\bar{X}$  and  $\bar{Y}$  defined in Eqs. (5.16) and (5.19-5.21), Eq. (5.3) can be re-written in terms of

$\tilde{a}_{n;N}(z, \omega)$  as

$$\frac{\partial \tilde{a}_{n;N}}{\partial z} + iK_{n;N}a_{n;N} = -i \frac{\omega^2 u}{g_n \beta_n c^2} \tilde{p}_{n;N}, \quad (5.22)$$

where linear-optical propagation is determined by  $K_{n;N}$ , defined as

$$K_{n;N}(\omega) = \beta_n(\omega) - \beta_0(N\omega_0) - \frac{\omega - N\omega_0}{v_{\text{ref}}} - i \frac{\alpha_n(\omega)}{2}, \quad (5.23)$$

which includes dispersion to all orders. Under the assumption that the nonlinear susceptibilities  $\chi^{(2)}$  and  $\chi_E$  are real, the effective polarizations  $\tilde{p}_{n;N}$  are given by

$$\begin{aligned} \tilde{p}_{n;N} = & \frac{1}{4} \sum_{\substack{p,q \\ P,m}} \left[ \left( \bar{X}_{m;npq}^{N,P,N-P} \right) \mathcal{F} [a_{p;P} a_{q;N-P}] + \right. \\ & \left. 2 \left( \bar{X}_{m;qnp}^{N+P,N,P} \right)^* \mathcal{F} [a_{p;P}^* a_{q;N+P}] \right] + \\ & \frac{1}{8} \sum_{p,q,r,P,Q} \left[ 3 \left( \bar{X}_{E;npqr}^{N,P,Q,N+P-Q} \right) \mathcal{F} [a_{p;P}^* a_{q;Q} a_{r;N+P-Q}] + \right. \\ & \mathcal{F} \left[ \mathcal{F}^{-1} \left[ 3 \left( \bar{X}_{R;npqr}^{N,P,Q,N+P-Q} \right) \mathcal{F} [a_{p;P}^* a_{q;Q}] \right] a_{r;N+P-Q} \right] + \\ & \left( \bar{Y}_{npqr}^{N,P,Q,N-P-Q} \right) \mathcal{F} [a_{p;P} a_{q;Q} a_{r;N-P-Q}] + \\ & \left. 3 \left( \bar{Y}_{rnpq}^{N+P+Q,N,P,Q} \right)^* \mathcal{F} [a_{p;P}^* a_{q;Q}^* a_{r;N+P+Q}] \right] \end{aligned} \quad (5.24)$$

where  $\mathcal{F}$  denotes the Fourier transform, defined in Eq. (1.3); since the  $\tilde{a}_{n;N}$  are defined with a frequency shift corresponding to harmonic order  $N$ , their frequency argument  $\Omega$  corresponds to optical frequencies  $\omega = \Omega + N\omega_0$ . SFG terms such as third harmonic generation arising from  $\chi_R$  have been neglected, on the assumption that the Raman bandwidth is narrow compared to the optical carrier frequencies. Note that Eq. (5.24) contains many repeated terms within the summations; these terms can be calculated once and multiplied by appropriate scale factors in other parts of the summand.

The GCWEs defined by Eq. (5.22) capture all relevant second and third-order

nonlinear effects. For a particular CEO phase shift  $\varphi$  of the input electric field, each envelope  $a_{n,N}$  acquires phase shift  $N\varphi$  (assuming the input corresponds to  $a_{n,1}$ ), and so a complete reconstruction of the real-valued electric field is possible from a single simulation with zero CEO phase, in contrast to single-envelope approaches, as will be discussed in section 5.5.

The energy conservation of these equations is discussed in section 5.7; together with the numerical example we discuss in section 5.4, these considerations allow us to specify in section 5.8 general rules for the choices of the nonlinear coefficients  $\bar{X}$  and  $\bar{Y}$ . The assumption that  $\chi^{(2)}$  and  $\chi_E$  are real (lossless) helped to simplify Eq. (5.24). For example, this assumption allows SFG- and DFG-like driving terms to be written with coefficients  $\bar{X}_{m;npq}^{N,P,N-P}$  and  $(\bar{X}_{m;npq}^{N,P,N-P})^*$ , respectively. However, for two-photon absorption, an imaginary component of  $\chi_E$  is required. In section 5.8, we discuss minor modifications to  $\chi^{(3)}$  and Eq. (5.24) which allow such effects to be accounted for.

## 5.3 Model Simplifications

In this section, we discuss some simplifications which can significantly reduce computation time without substantial loss of accuracy. With the approximations we describe, the number of operations required to simulate a given interaction can be reduced by orders of magnitude in some cases.

### 5.3.1 Isolating Important Terms in $P_{NL}$

In deriving Eqs. (5.22), we made no assumption about the sign of  $N$  in envelopes  $a_{n,N}$ . In fact, there are inevitably polarization terms driving envelopes with negative values  $N$  whenever the bandwidth exceeds one octave. For example,  $a_{0,-1}$  is driven by spectral components of  $a_{0,1}$  (FH) which exceed those of  $a_{0,2}$  (SH); such components only exist when the spectral regions spanned by  $a_{0,1}$  and  $a_{0,2}$  overlap, as indicated in Fig. 5.1. In general, for pulses with bandwidths strictly less than an octave,  $a_{n,-1}$  is identically zero (as are all  $a_{n,N}$  with  $N < 0$ ). For typical ultrabroadband spectra (e.g.

those arising in supercontinuum generation), where the bandwidth exceeds an octave, the envelopes with  $N < 0$  are of finite amplitude. However, an important point is that they will usually be negligible. In order for these terms to be non-negligible, several conditions must be met: there must be components in different envelopes (e.g.  $a_{0;1}$  and  $a_{0;2}$ ) which are simultaneously overlapped spectrally and temporally, and are close to phasematched. In section 5.4, the magnitude of these envelopes is shown for a particular example.

Identifying negligible terms is important, since any simulation must use a finite number of envelopes (chosen by setting the remaining envelopes to zero). For example, Eq. (5.22) can be approximated by neglecting envelopes  $a_{n;N}$  with  $N > N_{\max}$  or  $N < 0$  for some positive integer  $N_{\max}$ . The resulting set of coupled wave equations contains terms corresponding to all of the conventional SFG and DFG interactions, including intrapulse DFG;  $N_{\max}$  can be chosen based on considerations of phasematching and material transparency. For a given set of envelopes, there are also many terms in Eq. (5.24) which may be negligible or not relevant in different contexts; these can be eliminated explicitly and self-consistently from the simulation by setting the relevant effective susceptibility to zero.

As a simple example, we can reduce Eqs. (5.22) to the conventional coupled wave equations for SHG by including only the envelopes  $a_{0;1}$  (FH) and  $a_{0;2}$  (SH), only the first order of the QPM grating ( $m = 1$ ), only the lowest order waveguide mode ( $n = 0$ ), neglecting  $\chi^{(3)}$  effects, scaling the waveguide modal profiles  $B_n(x, y, \omega)$  such that  $g_0(\omega) = 1$  in Eq. (2.7), and assuming sufficiently narrow-bandwidth pulses that the prefactor of  $\tilde{p}_{n;N}$  in Eq. (5.22) can be evaluated at the nearest carrier frequency. Under these assumptions, Eqs. (5.22) can be written as

$$\begin{aligned} \frac{d\tilde{a}_{0;1}}{dz} + iK_{0;1}\tilde{a}_{0;1} &= -i\frac{\omega_0 d_{\text{eff}}(z)^*}{n_0(\omega_0)c} \mathcal{F} [a_{0;2}a_{0;1}^*] \\ \frac{d\tilde{a}_{0;2}}{dz} + iK_{0;2}\tilde{a}_{0;2} &= -i\frac{\omega_0 d_{\text{eff}}(z)}{n_0(2\omega_0)c} \mathcal{F} [a_{0;1}^2] \end{aligned} \quad (5.25)$$

where  $n_0(\omega) = \beta_0(\omega)c/\omega$  and  $d_{\text{eff}}(z) = \bar{X}_{1,000}^{2,1,1}(z)/2$ . These equations closely resemble conventional coupled wave equations [76], except that dispersion effects are treated

exactly on the left hand sides through the  $K_{0,N}$  factors, the equations are evaluated in the frequency domain, and the carrier phase mismatch is incorporated into  $d_{\text{eff}}(z)$ . Note that care should be taken in general when neglecting envelopes, in order to avoid artificial amplification processes. We discuss these processes in sections 5.4 and 5.8, and show how they can be evaded.

For problems where  $\chi^{(2)} = 0$  such as supercontinuum generation in fibers, it may be sufficient to include only the  $N = 1$  envelopes,  $a_{n,1}$ ; if in addition only a single mode is supported, only  $a_{0,1}$  is required. In this case, Eqs. (5.22-5.24) reduce to a nonlinear envelope equation of the form often used to model  $\chi^{(3)}$  media [39, 40]. The resulting effective polarization is given, in the time domain, by

$$p_{0,1} = \frac{3\theta_0}{8} \mathcal{F}^{-1} \left[ (\chi_E + \chi_R(\Omega)) \mathcal{F} [|a_{0,1}|^2] \right] a_{0,1}, \quad (5.26)$$

where  $\theta_0 = \theta_{0000}(\omega_0, -\omega_0, \omega_0)$ , and where  $\chi_E$  is assumed to be frequency-independent, as in Eq. (2.10). The additional complexity in Eq. (5.24) compared to Eq. (5.26) is needed primarily because  $\chi^{(2)}$  media, and QPM media in particular, have a greater tendency to generate second, third, and higher-order harmonics.

### 5.3.2 Highly Phase Mismatched Terms

There are an infinite number of terms in Eq. (5.22), because QPM gratings are described by an infinite sum of spatial Fourier components. A simple way to evade this problem is to truncate the summation. However, for some situations, the inaccuracy incurred by simple truncation of the Fourier series is too large [38]. Instead of simply neglecting terms, it is possible to apply multiple-scale analysis, as introduced in Ref. [32], in order to determine the contributions of highly phase mismatched terms semi-analytically. This procedure is discussed in appendix 2.8, and yields cascaded phase shifts which have forms similar to SPM and XPM terms [31].

Here, we briefly describe how highly phase mismatched terms in Eq. (5.22) can be accounted for in the cascading approximation by modifying the  $\chi^{(3)}$  nonlinear coefficients. In contrast to a SE approach, where the cascading approximation must be applied at all frequencies or not at all, here we can assign to each nonlinear

interaction between a set of envelopes the full coupled evolution [Eqs. (5.22) and (5.24)], a corresponding set of cascading interactions if the interaction is highly phase mismatched, or a vanishing coupling coefficient if the interaction is negligible.

Consider as an example phase-mismatched SHG between the  $n = 0$  FH mode and the  $n = q$  SH mode, i.e. between the envelopes  $a_{0;1}$  and  $a_{q;2}$ ; each of the Fourier orders  $m$  of the QPM grating contribute to this interaction according to the effective susceptibilities  $\bar{X}_{m;q00}^{2,1,1}$ . In order to apply the SHG cascading approximation to one of these processes, a component can be added to  $\bar{X}_{E;0000}^{1,1,1,1}$  [38]:

$$\bar{X}_{E;0000}^{1,1,1,1} \rightarrow \bar{X}_{E;0000}^{1,1,1,1} - \frac{4\omega_0^2}{3g_q(2\omega_0)\beta_q(2\omega_0)c^2} \frac{|X_{m;q00}^{2,1,1}|^2}{\delta\beta_{m;q00}} \quad (5.27)$$

while simultaneously removing terms involving  $\bar{X}_{m;q00}^{2,1,1}$  from Eq. (5.24). The phase mismatch for these interactions is given by  $\delta\beta_{m;q00}(z) = \beta_q(2\omega_0) - 2\beta_0(\omega_0) - mK_g(z)$ .

Equation (5.27) is appropriate when there is a large  $\delta\beta_{m;q00}$  and no “leading-order” (slowly-varying) SH component [32]. If SH components are generated with non-negligible intensity compared to the FH due to a nearly-phaseshifted interaction (for example, due to the  $\bar{X}_{m;000}^{2,1,1}$  SHG interaction), then those components can also give rise to cascaded phase shifts via highly phase mismatched  $\bar{X}_{m;q00}^{2,1,1}$  interactions. Similarly, cascade phase shifts can arise from non-SHG processes (any highly phase mismatched  $\bar{X}_{m;npq}^{N,P,N-P}$  interaction). In these cases, a more general multiple-scale analysis can be performed to approximate phase mismatched  $\chi^{(2)}$  interactions with effective SPM and XPM interactions [52]. Some care must be taken with such analyses, however, since the SH generated due to a phase mismatched  $\bar{X}_{1;000}^{2,1,1}$  interaction often has form  $a_{0;2} \propto \bar{X}_{1;000}^{2,1,1} a_{0;1}^2$ , i.e.  $a_{0;2}$  inherits the phase of the dominant contribution to its nonlinear polarization, as opposed to the phase it would accumulate through linear propagation.

### 5.3.3 Highly Group-Velocity Mismatched Terms

Equation (5.22) supports the generation of numerous harmonics. These harmonics travel at different group velocities than the input pulse; especially for the higher

harmonic orders, this difference can be significant. Therefore, as the harmonic order increases, the temporal window required to capture the generated components usually increases substantially. However, the significance and intensity of the pulse components often decreases with harmonic order. Instead of substantially extending the time window to resolve such components, in this subsection we note that they can instead be removed adiabatically from the time window if they are weak and weakly-interacting, thus allowing for much faster approximate calculations.

A wide range of absorbing boundary conditions can be applied without substantially altering the results: the absorption rate due to the boundary simply needs to be negligible in the temporal region where the fields still interact nonlinearly, and should occur over a temporal region wide enough that the pulse is not artificially broadened in spectrum. Note that if filtered components are intense enough to non-negligibly amplify quantum noise, then this temporal filtering is not appropriate.

## 5.4 Numerical Example

In this section, we consider a specific example to illustrate some of the important features of the generalized coupled wave equations defined by Eqs. (5.22) and (5.24). This example is used to show how these propagation equations can be used in practice to define reduced GCW models. We start with simulations based on reduced forms of the GCWEs, and then build up to more general cases. Note that reduced models which include any desired set of interactions between a set of envelopes  $a_{n;N}$  can be defined automatically via Eqs. (5.22) and (5.24).

The example we consider is supercontinuum generation in a tightly confining LiNbO<sub>3</sub> ridge waveguide. We assume input pulses with energy 60 pJ, a FWHM duration of 100 fs (sech<sup>2</sup> profile), and a center wavelength of 1950 nm. Based on these pulse parameters, we assume a LiNbO<sub>3</sub> waveguide, diagrammed in Fig. 5.2(a), consisting of a 2.5 x 2.5  $\mu\text{m}$  LiNbO<sub>3</sub> ridge, with an infinite silica cladding layer below the ridge and air on the remaining three sides, similar to those described in Refs. [72, 73]; the modal electric field is polarized predominantly in the  $y$  direction. The

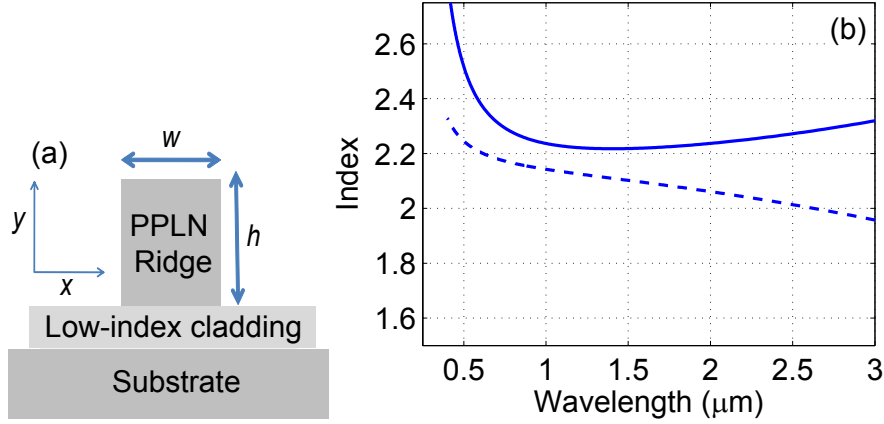


Figure 5.2: The same structure described in Fig. 4.1. (a) Schematic of ridge waveguide. We assume a  $\text{LiNbO}_3$  ridge, a low-index silica cladding, and air on the other sides of the ridge. (b) Modal effective index  $n$  (dashed line) and group index  $n_g$  (solid line) for the  $2.5 \times 2.5 \mu\text{m}$  waveguide described in the text.

length of the QPM grating is 7.5 mm. The corresponding dispersion of the lowest-order mode is given in Fig. 5.2. The waveguide dimensions were chosen to match the group velocities of the FH and SH pulses in the lowest-order mode. This group velocity matching approach enables low-energy QPM supercontinuum generation, as discussed in chapter 4.

In all simulations in this section, QPM orders  $m = 1$  and  $m = 3$  are included in the model;  $\chi^{(3)}$  effects are neglected for illustrative purposes, although in practice they can make significant contributions [38]. Similarly, we consider only the lowest-order waveguide mode, assume this mode to be lossless, and neglect noise on the input pulse. We assume that  $\bar{X}_{m;000}^{N,P,N-P} = \bar{X}_{m;000}^{2,1,1}$  for all interactions in Eq. (5.16). This assumption is implicit in SE models [38], and is made here in order to allow for direct comparison between GCW and SE results simulations [see Fig. 5.7]; additionally, this assumption simplifies the analysis, and is often sufficient in practice provided that the effective modal susceptibilities  $X_{npq}$  and  $X_{npqr}$  are weakly dispersive over the spectral regions of interest.

### 5.4.1 Minimal SHG Model

We first model only the first and second harmonic envelopes,  $a_{0;N}$  and  $a_{0;2}$  (or  $a_{0;N}$  with  $N \in \{1, 2\}$ ). Modeling a finite set of envelopes means that all other envelopes are assumed to be zero in Eq. (5.24). Equivalently, this assumption corresponds to setting to zero all nonlinear coefficients not involving coupling between the assumed set of envelopes, and also assuming that the other envelopes are initially zero.

The power spectral density (PSD) of each envelope obtained from Eq. (5.22) with this reduced model is shown in Fig. 5.3. The complete output pulse has an octave-spanning spectrum and overlapping FH and SH envelopes. Note that we have calculated the PSD associated with the square magnitude of the individual envelopes, as in Eq. (5.32). The actual power spectrum at the output of the waveguide would be given by first summing the envelopes and then squaring, as in Eq. (5.29); the result in the region of spectral overlap depends on the carrier-envelope phase. The QPM period ( $11.8 \mu\text{m}$ ) is slightly shorter than the period required for SHG phasematching ( $12.3 \mu\text{m}$ ); this choice of QPM period yields nonlinear phase shifts which, as discussed in subsection 5.3.2, give rise to SPM and spectral broadening. Additionally, the effective  $\chi^{(3)}$  nonlinearity resulting from cascaded phase shifts has the same sign of the true  $\chi^{(3)}$  nonlinearity.

### 5.4.2 Third and Fourth Harmonic Generation

Due to the high intensity of the pulses involved in this interaction, additional processes neglected in Fig. 5.3, such as the generation of third, fourth and higher harmonic pulse components, can be significant. To show these effects, we next simulate the same numerical example but with envelopes  $a_{0;N}$  with  $N \in \{1, 2, 3, 4\}$ . In Fig. 5.4(b), the output spectrum of each of these envelopes is plotted. The  $N \in \{1, 2\}$  case considered in Fig. 5.3 is shown in Fig. 5.4(a) versus frequency, for comparison. The spectrum of the FH and SH are modified only slightly by the presence of the additional harmonics. The spectra are shown in the frequency domain in order to make the third and fourth harmonic content easier to see. The peak around 650 THz (460 nm) corresponds to a phasematched process via third-order QPM.

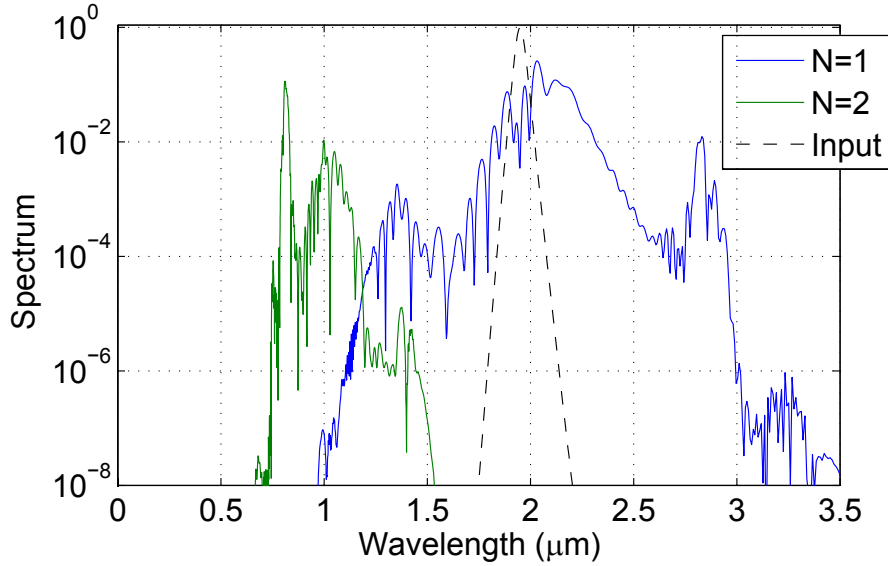


Figure 5.3: Normalized PSD of the envelopes obtained by solution of Eq. (5.22), including envelopes  $a_{0,N}$  with  $N \in \{1, 2\}$ . Normalization is performed with respect to the peak PSD of the input pulse (dashed line). Parameters are given in the text.

### 5.4.3 Intrapulse DFG Effects

For pulses of sufficient bandwidth and intensity, such as those considered in this example, intrapulse DFG can be significant. Intrapulse DFG effects are captured by interactions involving the envelopes  $a_{n,0}$ . In this case, intrapulse DFG leads to a peak in  $a_{0,0}$  around  $2.6 \mu\text{m}$ , shown in Fig. 5.5(b).

When including envelopes  $a_{n,0}$  in the simulations, however, artificial amplification effects can arise unless some care is taken to ensure that a consistent set of interactions is included in the model. This issue is illustrated in Fig. 5.5(a), which shows the spectrum obtained with the  $N \in \{0, 1, 2\}$  model. There is a prominent peak in  $a_{0,0}$  and  $a_{0,2}$  around  $\omega_0$  (wavelength  $2 \mu\text{m}$ ); this peak occurs because spectral components of these two envelopes experience OPA due to the intense SH pulse centered at frequency  $2\omega_0$ ; the effective susceptibility corresponding to this process is  $\bar{X}_{1;(000)}^{2,2,0}$ . However, this OPA process is artificial, and is in fact strongly suppressed by the strong FH pulse, which up-converts spectral components around  $\omega_0$  before they can be amplified (in an SFG-like process). This SFG process is not captured in Fig. 5.5(a) because some

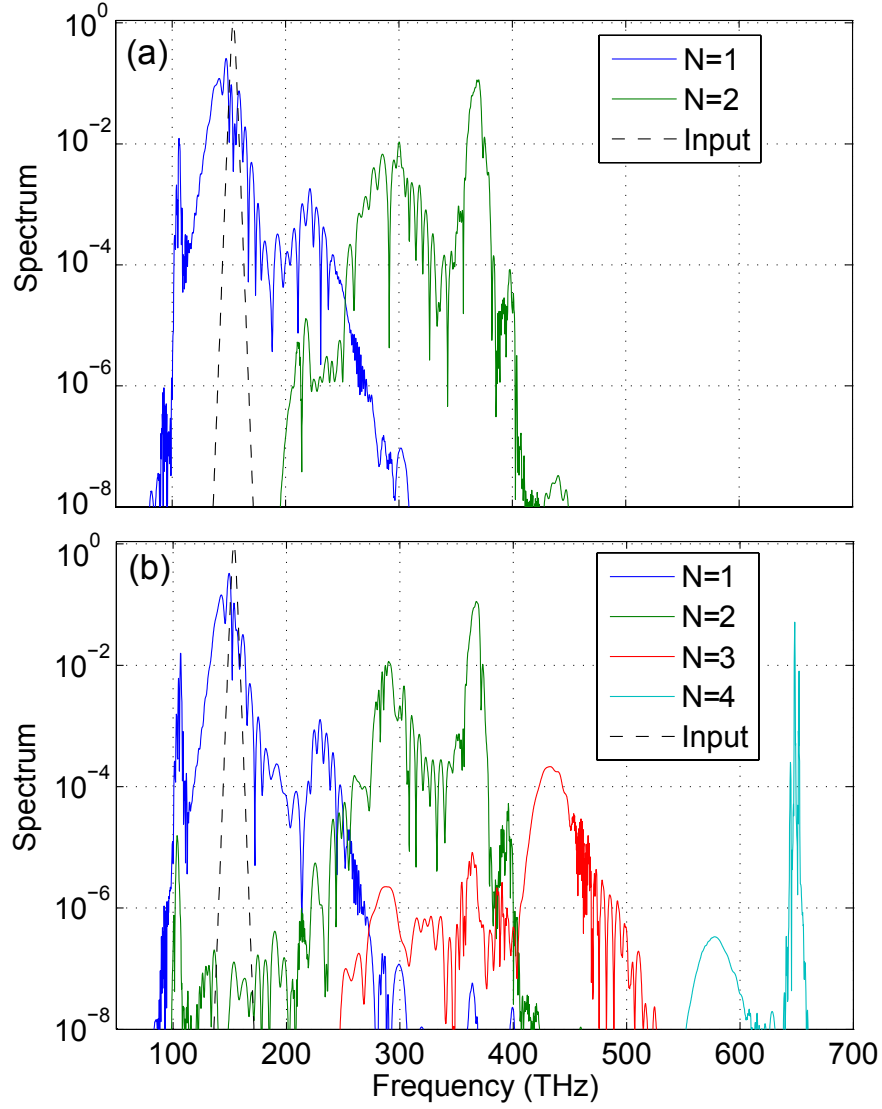


Figure 5.4: Normalized PSD of the envelopes obtained by solution of Eq. (5.22), including envelopes  $a_{0;N}$  with (a)  $N \in \{1, 2\}$ , and (b)  $N \in \{1, 2, 3, 4\}$ .

significant terms were neglected in the  $N \in \{0, 1, 2\}$  reduced model.

In contrast, when the third-harmonic envelope and the interaction  $\bar{X}_{1;000}^{3,2,1}$  is also included, the small contributions to both  $a_{0;0}$  and  $a_{0;2}$  which undergo OPA in Fig. 5.5(a) also experience SFG, driven by the strong FH pulse (via the interactions  $\bar{X}_{1;000}^{1,1,0}$  and  $\bar{X}_{1;000}^{3,2,1}$  for  $a_{0;0}$  and  $a_{0;2}$ , respectively). The correct suppression of the artificial

OPA process is illustrated in Fig. 5.5(b), which shows the output spectra when envelopes  $a_{0;N}$  for  $N \in \{0, 1, 2, 3\}$  are included in the model, i.e. no peak in  $a_{0;0}$  and  $a_{0;2}$  occurs near  $2 \mu\text{m}$ . Thus, in order to accurately capture the growth of small-signal components, all of the strong interactions involving those components must be included; in this case, the FH and SH pulses interact strongly with small-signal spectral components around  $2 \mu\text{m}$ . We consider this issue in more detail in section 5.8. In particular, a simplified description is given by Eqs. (5.35) and (5.36), which show the coupling between small spectral components in the vicinity of  $\omega_0$  and  $2\omega_0$  due to strong narrowband spectral components at  $\omega_0$  and  $2\omega_0$ .

Comparing Fig. 5.5(b) to Fig. 5.3 shows that when first-order QPM interactions between envelopes  $a_{0;N}$  ( $N \in \{0, 1, 2, 3\}$ ) are included, the spectrum is similar to the minimal SHG model ( $N \in \{1, 2\}$ ) but with an additional spectral peak due to phasematched intrapulse DFG (which occurs in this case around  $2.6 \mu\text{m}$ ), and the presence of a weak third harmonic pulse component.

#### 5.4.4 Envelopes $a_{n;N}$ with $N < 0$

In subsection 5.3.1, we argued that envelopes  $a_{0;N}$  with  $N < 0$  can often be neglected. To show that this is the case even for the broadband and highly nonlinear example under consideration, we show the  $-1 \leq N \leq 5$  case in Fig. 5.6. The envelope  $a_{0;-1}$  can be seen at around the  $10^{-10}$  level (PSD normalized to peak PSD of the input pulse), and is therefore negligible. Such  $N < 0$  terms will be negligible in a wide variety of cases, since their driving polarization is proportional to the product of the weak spectral wings of two different envelopes.

#### 5.4.5 Comparison with Single-Envelope Model

Under an identical set of assumptions, the GCW model discussed here should produce the same results as the SE models discussed elsewhere [37, 38, 41]. In Fig. 5.7, we compare the results obtained for the present example analyzed with the  $-1 \leq N \leq 5$  GCW model to those obtained with the single-envelope (SE) model described in Ref. [38]. The two are in good agreement, including near regions such as  $2.6 \mu\text{m}$ , where

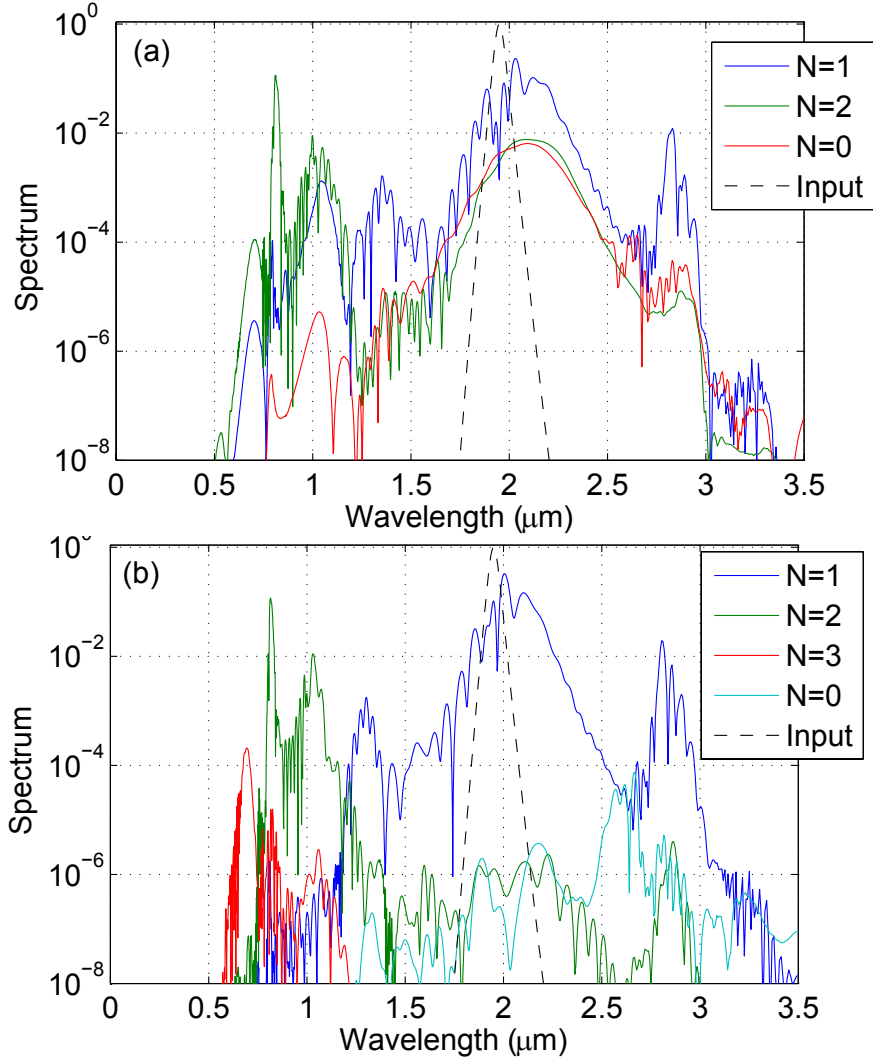


Figure 5.5: Normalized PSD of the envelopes obtained by solution of Eq. (5.22), including envelopes  $a_{0;N}$  with (a)  $N \in \{0, 1, 2\}$ , and (b)  $N \in \{0, 1, 2, 3\}$ . In (a), there are prominent and artificial spectral peaks in  $a_{0;0}$  and  $a_{0;2}$  around 2  $\mu\text{m}$ ; in (b), these peaks are suppressed by inclusion of envelope  $a_{0;3}$ .

multiple envelopes have comparable magnitude and hence the output spectrum is sensitive to the CEO phase  $\varphi$  of the input pulse; for the case shown in Fig. 5.7,  $\varphi = 0$ . The small residual differences are likely due to approximations made to the nonlinear polarization at the edges of the transparency window. The  $N = 1, 2$  case is also included in Fig. 5.7(b) for comparison.

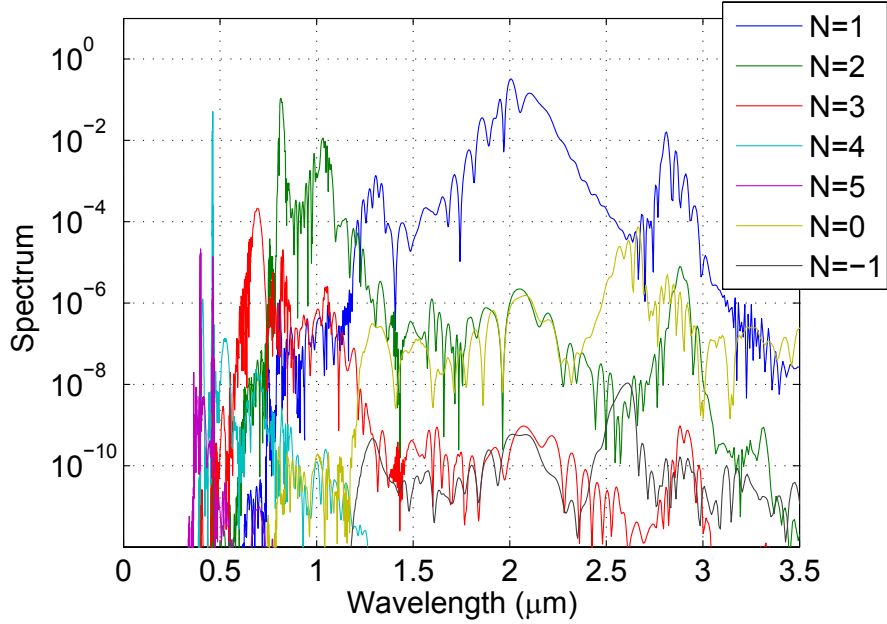


Figure 5.6: Normalized PSD of the envelopes obtained by solution of Eq. (5.22), including envelopes  $a_{0,N}$  with  $N \in \{-1, 0, 1, 2, 3, 4, 5\}$

The example discussed in this section shows some of the main features of Eqs. (5.22) and how they can be used to analyze and design highly nonlinear interactions. A wide variety of designs can be analyzed, including phasematched SFG, DFG, and SHG interactions, or interactions dominated by  $\chi^{(3)}$  effects. Many of the important spectral features are captured by the minimal SHG model, but additional processes can be accounted for straightforwardly given Eq. (5.24). For cases such as those discussed in Ref. [38], additional competing  $\chi^{(3)}$  processes are particularly important, and cause significant changes compared to the minimal SHG model, or even general  $\chi^{(2)}$  models, if either  $\chi_E$  or  $\chi_R$  is neglected.

## 5.5 Motivating Factors for a GCW Model

In this section, we discuss the advantages of the model given by Eq. (5.22) over single-envelope models. Specifically, we make comparisons to Eq. (5) of Ref. [38], which has a comparable level of generality.

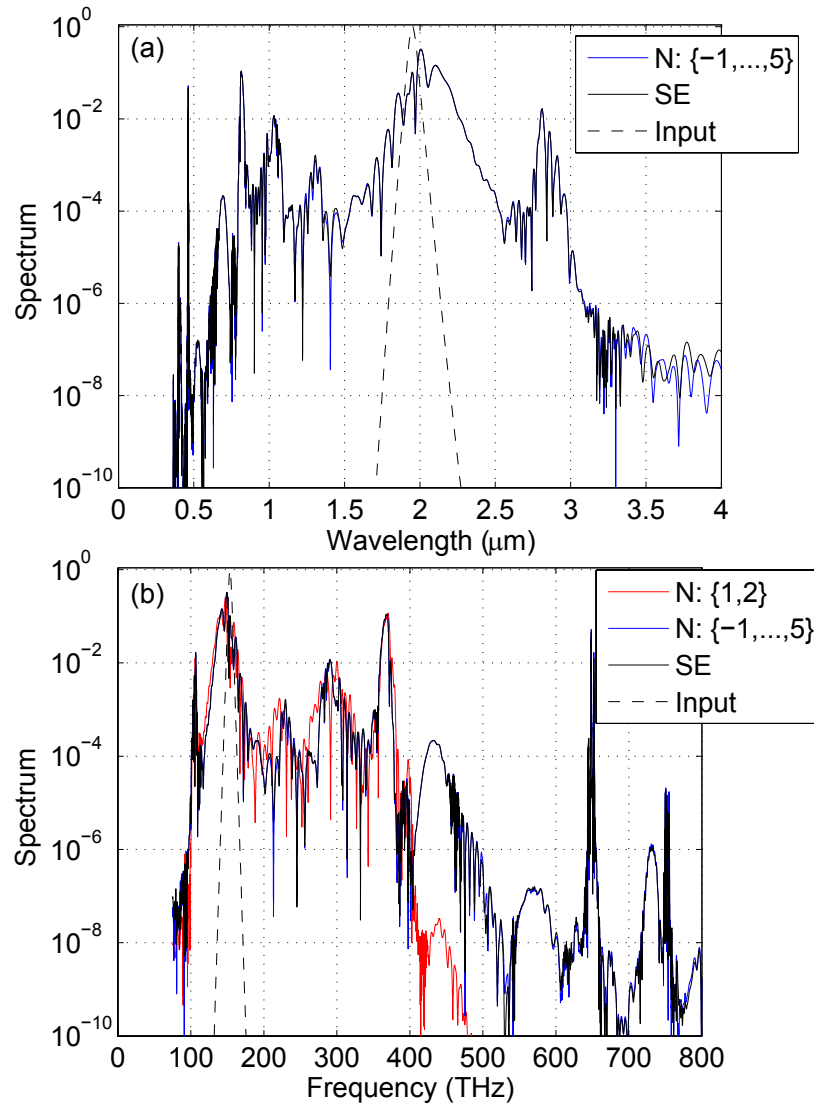


Figure 5.7: Comparison of simulations with different assumptions. The legends show the envelopes included; the spectra for the single envelope (SE) and  $N \in \{-1, 0, 1, 2, 3, 4, 5\}$  cases are in agreement across the entire wavelength range. The spectra are shown versus wavelength in (a), and versus frequency in (b). Note that the  $N \in \{1, 2\}$  model is quite accurate below 400 THz, but differs by four orders of magnitude around 450 THz (since the TH is not included in the model), and differs even more at higher frequencies.

### 5.5.1 Carrier Offset Frequency

A common application of ultra-broadband interactions is to generate or manipulate frequency combs. The defining feature of a frequency comb is the existence of discrete spectral lines which are spaced by the repetition rate of the laser source and are offset from DC by a CEO frequency  $f_{\text{CEO}}$ . Single-envelope simulations of  $\chi^{(2)}$  interactions do not preserve the properties of the frequency comb. When the different types of envelopes (FH, SH, etc.) are not distinguished, it cannot be determined unambiguously in a single simulation to which envelope a given spectral component of a pulse belongs, and hence what the associated signal would be at each comb line. In order to reconstruct all of the pulse's phase information (and hence all of the comb lines) in a SE model, it would be necessary to perform several simulations of the same interaction but with input pulses with different CEO phases, and then interfere the numerical results (if  $M$  envelopes would be needed in a GCW model, as many as  $M$  simulations with different input phases would be needed to unambiguously separate these envelopes in a SE model). For cases incorporating semi-classical noise, the situation would be complicated further. This unsatisfactory situation is avoided entirely by Eq. (5.22), since each envelope  $a_{n;N}$  inherits a factor  $N$  of the (possibly unknown) input phase, and hence can be unambiguously associated with spectral components having carrier offset  $Nf_{\text{CEO}}$ . Therefore, the GCW model overcomes a significant limitation of SE models, while still accounting for the same set of nonlinear interactions.

### 5.5.2 GCW Model for Optical Design

In designing optical devices, it is often useful to model a minimal set of interactions initially, for example only the coupled wave equations for SHG. With the GCW model, a design determined in this oversimplified limit can then easily be tested and optimized against a more general set of equations. Similarly, cases where the initially-neglected terms have a dramatic impact on the device operation compared to the idealized limit can be identified and resolved. Conversely, weak interactions can be identified and neglected before exploring a large design parameter space; for processes that are relatively simple or involve disparate length scales, analytical or semi-analytical

approximations such as those described in section 5.3.2 can be used to aid in the design process. Since all the different coupling terms appear directly, it is straightforward to identify the cause and contribution to different effects by performing simulations with different combinations of interactions included; such functionality is not supported by SE approaches, which treat all the different SFG and DFG processes as essentially the same.

For the above reasons, Eq. (5.22) can serve as an efficient tool for developing and analyzing designs, thereby reducing the amount of experimental iteration required to construct a useful device. While Eq. (5.22) models nonlinear interactions in waveguides, plane-wave or non-diffracting beams can be modeled by assuming only a single “waveguide” mode and applying slight modifications to the envelopes  $a_{n;N}$  and coefficients  $\bar{X}$  and  $\bar{Y}$ . For diffracting paraxial beams, a diffraction operator could be added straightforwardly.

### 5.5.3 Numerical Tractability

In this subsection, we briefly discuss numerical issues associated with modeling Eq. (5.22). The spectral bandwidth required in simulations naturally reflects the bandwidth of the different pulse components, and so is comparable in GCW and SE approaches when modeling octave-spanning spectra. The GCW approach offers a significant improvement for narrower-bandwidth pulses, as SE approaches are extremely poorly suited to model CW or narrow-bandwidth SHG interactions (since multiple octaves of bandwidth must be incorporated). Thus, the GCWEs scale gracefully from the CW to the multiple-octave-spanning-spectrum regimes, and is therefore suited to any  $\chi^{(2)}$  or  $\chi^{(3)}$  interaction, at many levels of approximation.

A significant advantage even for octave-spanning spectra is in spatial resolution. Many nonlinear interactions can occur simultaneously, many of which are highly phase mismatched, particularly in QPM media. With a single envelope, these interactions must be resolved in order to avoid aliasing. In contrast, highly phase mismatched terms in Eq. (5.22) can be solved semi-analytically using the approach discussed in subsection 5.3.2, or neglected entirely where appropriate: only terms relatively close

to phasematching must be resolved numerically.

While the number of points in each coherence length required for accurate simulation depends on the intensity (and therefore it is usually more appropriate to check for discretization-related errors directly by varying the  $z$ -step size or by using an adaptive discretization scheme), removing the possibility of aliasing issues improves robustness and reduces the required spatial resolution. For example, for the case considered in section 5.4, the  $N \in \{1, 2\}$  model shown in Fig. 5.3 captures most of the spectral structure and only requires a resolution of 2 fs in time, 10  $\mu\text{m}$  in propagation coordinate  $z$ , and a wide enough time window to capture the FH and SH; in contrast, the SE model requires a resolution of  $< 0.5$  fs and  $< 0.5$   $\mu\text{m}$ , and a wide enough time grid to resolve up to the fourth or even higher harmonics. Thus, by systematically removing terms from the simulation which are weakly interacting due to a large phase mismatch or a large group velocity mismatch (or both), improvements in computation time of several orders of magnitude are often possible.

Note that interactions involving multiple input waves can be modeled as well, for example by lumping the inputs into the relevant harmonic envelopes. Alternatively, the envelopes could be divided into components centered at intermediate carrier frequencies. For example, to model OPA one could assume pump and signal carrier frequencies  $\omega_p$  and  $\omega_s$ , respectively, and then define a set of carrier frequencies corresponding to all the sum and different frequencies involving  $\omega_p$  and  $\omega_s$  (such as the idler frequency  $\omega_i = \omega_p - \omega_s$ , the signal SH,  $2\omega_s$ , and so on). A similar approach to the one given in section 5.2 could then be used to determine coupling between envelopes associated with these carrier frequencies. However, this analysis is beyond the scope of this work.

#### 5.5.4 Accuracy of the Nonlinear Coefficients

The second- and third-order effective susceptibilities  $X_{npq}$  and  $X_{npqr}$  defined in Eqs. (2.4) and (2.5) can be strongly dispersive, particularly due to the changes in waveguide mode shape and size with optical frequency. In the most general forms of the SE and GCW approaches, this dispersion can be accounted for by integration over

all frequencies contributing to the nonlinear polarization, as in Eq. (2.3). However, in the much more tractable approach given by Eq. (5.24) or the corresponding approximation for the SE approach [38], the nonlinear polarization can be determined by calculating various products of the electric field envelopes in the time domain, and then multiplying the Fourier transform of these time-domain products by an appropriate coefficient that depends only on the driven (but not the driving) optical frequency. This procedure was also applied in Eq. (5) of [38].

In this approach, much of the dispersion of the effective susceptibilities is approximated by evaluating a (suitably normalized) overlap integral at a specific frequency. For higher harmonics (such as the third or fourth harmonic) and for higher order waveguide modes, this approximation can become inaccurate. In contrast, in the GCW approach each  $\bar{X}$  can be approximated around a set of harmonic frequencies involved in a particular interaction involving a set of modes. In this approximation, it is not necessary to assume that the effective susceptibilities remain constant over multiple octaves of bandwidth, and so more accurate coefficients can be used.

While some freedom in this regard is provided by the GCW model, choices of  $\bar{X}$  and  $\bar{Y}$  can still be constrained by the requirement to suppress artificial OPA effects, as discussed in detail in appendix 5.8. For particularly constrained cases, a number of alternatives are also possible, for example the electric field can be sub-divided into additional envelopes associated with different spectral regions (e.g. THz and optical regions), in order to account for the large differences in the nonlinear susceptibilities for frequencies below and above the material phonon resonances. Furthermore, the mode normalization profiles  $g_n(\omega)$  can be optimized in order to minimize the dispersion of  $X_{npq}$  or  $X_{npqr}$ ; this procedure is also discussed in section 5.8.

## 5.6 Conclusions

In this chapter we developed a general and versatile coupled-wave model to describe interactions between bound waveguide modes in nonlinear media. With this GCW model, simplified sets of coupled-wave equations can be derived, which allows for faster calculations and better understanding of the dynamical processes involved

compared to single-envelope models. With the same model, an arbitrary number of interactions can be included, so the accuracy of single-envelope models is also maintained. In many cases, the GCW model enables increased accuracy, since assumptions made on the nonlinear coefficients made by single-envelope models can be relaxed. Eqs. (5.22-5.24) show the underlying harmonic structure of the nonlinear mixing processes. It is this harmonic structure which allows approximate models to be defined, by neglecting different sets of terms. Additionally, the role of CEO phase and frequencies emerges independently of the dynamical processes, since an overall phase shift  $N\varphi$  can be extracted from each envelope  $a_{n;N}$  and corresponding polarization  $p_{n;N}$ . In contrast, in SE models, this harmonic structure not captured. As a result, individual processes are not isolated, and multiple simulations are required to determine the output spectrum for different absolute phase shifts of the input pulse. For interactions involving pulses of any bandwidth, the GCW model thus offers significant advantages compared to both conventional coupled wave equations and to SE models.

We considered in Section 5.4 a numerical example in order to show some of the advantageous properties of the GCW model. The example showed supercontinuum generation in a LiNbO<sub>3</sub> ridge waveguide, with spectral broadening based on the  $\chi^{(2)}$  nonlinearity. The most important process involved was phasemismatched SHG, which could be simulated using a minimal model. This minimal model could then be generalized to include additional harmonic generation processes and the resulting dynamics, and further generalized to show agreement with the corresponding SE model. The particular example we considered is a promising candidate for  $\chi^{(2)}$ -based SC generation through the matching of the group velocities of the FH and SH; the advantageous properties of this approach were discussed in chapter 4.

We discussed some of the complexities which arise when specifying GCW models, and in particular how the choice of susceptibilities and envelopes is constrained. Much of this complexity is related to the dispersion of the effective nonlinear susceptibilities. We show in appendix 5.8 that these susceptibilities can be rendered non-dispersive along an arbitrary trajectory of frequencies; this procedure allows for the nonlinear coupling to be captured accurately while avoiding instabilities that can result from

inappropriate choices of coupling coefficients.

When discussing application of the GCW model we focused on input fields consisting of a single pulse or a pulse train in which nonlinear interactions between adjacent pulses in the train can be neglected. This assumption applies very well in a wide variety of cases, but may not hold for high repetition rate systems. In such cases, periodic boundary conditions could be applied; this analysis is beyond the scope of this work.

The model developed here should help in simulating and understanding the complicated dynamical processes which inevitably arise when pulses of high intensity or broad bandwidth (or both) propagate through nonlinear media. With this understanding, novel devices with lower energy requirements, improved coherence properties, or new nonlinear-optical functionalities can be considered. This modeling is likely to play an important role in enhancing ultrafast laser technology and its applications.

## 5.7 Appendix: Energy Conservation in the GCWE Model

In this appendix, we consider energy conservation in the GCWEs defined by Eqs. (5.22-5.24). An important constraint is intrinsic permutation symmetry [4], which for the nonlinear coefficients defined in Eq. (5.16) implies that  $\bar{X}_{m;npq}^{N,P,N-P} = \bar{X}_{m;nqp}^{N,N-P,P}$ . In this appendix, we consider only the  $\chi^{(2)}$  terms of Eq. (5.24), and assume  $\chi^{(2)}$  to be real, for simplicity; the analysis could be extended straightforwardly to include  $\chi^{(3)}$  interactions.

We will show here that for non-overlapping envelope spectra, energy conservation is satisfied for any set of  $\bar{X}$  coefficients, provided that intrinsic permutation symmetry is satisfied. A simple case in which envelope spectra are non-overlapping is for narrow-bandwidth pulses. Another important case is for a pulse train with non-degenerate CEO frequencies, i.e. whenever the  $Nf_{\text{CEO}}$  are distinct for integer  $N$ , modulo the repetition rate. Since only a few envelopes are non-negligible in most practical cases, this non-degeneracy will almost always be the case when dealing with a pulse train that is not locked to  $f_{\text{CEO}} = 0$ . For cases with overlapping spectra, maintaining energy conservation places constraints on the nonlinear coefficients  $\bar{X}$ . However, even if these constraints are not met, the important nonlinear dynamics can still usually be captured accurately.

To illustrate these points, we first define  $P_n(z, t)$  as the power in waveguide mode  $n$  flowing through a plane  $z$ , and assume orthogonal waveguide modes. Energy conservation can then be determined via the Fourier transform of this power, evaluated at zero frequency, i.e.  $U_n(z) = \lim_{\omega \rightarrow 0} \int_{-\infty}^{\infty} P_n(z, t) \exp(-i\omega t) dt$ . We refer to  $U_n(z)$  as the modal energy. For a single pulse,  $U_n$  is the energy in mode  $n$ ; for an infinite pulse train,  $U_n$  has the form  $P_{n0}\delta(0)$  for average power  $P_{n0}$  in mode  $n$ . By writing  $U_n$  as a Fourier transform in this way, arbitrary types of pulses and pulse trains can be considered.  $U_n$  can be written as an integral in the frequency domain as

$$U_n(z) = \int_0^{\infty} W_n(z, \omega) d\omega. \quad (5.28)$$

where  $W_n$  is the energy spectral density (ESD) of waveguide mode  $n$ . Evaluating the temporal Fourier transform of the (total) Poynting vector  $\mathbf{S} = \mathbf{E} \times \mathbf{H}$  at zero frequency and applying orthogonality [Eq. (1.16)] yields the form of the ESD:

$$W_n(\omega) = \frac{g_n(\omega)\beta_n(\omega)c^2\epsilon_0}{2\omega} |\tilde{A}_n(\omega)|^2 \quad (5.29)$$

where  $A_n$  is defined in Eq. (5.1). Each modal amplitude  $A_n$  is determined from a coherent sum of harmonic envelopes  $A_{n;N}$  [see Eq. (5.5)], and these harmonic envelopes are related to the frequency-shifted envelopes  $a_{n;N}$  by Eq. (5.15).

In Eq. (5.24) a real  $\chi^{(2)}$  was assumed. Here we further assume that the waveguide modes are lossless. With these assumptions, energy conservation corresponds to the sum of the modal energies  $U_n$  being  $z$ -independent. The  $z$ -dependence of  $W_n$  (and hence  $U_n$ ) can be determined from Eq. (5.22), and is given by

$$\frac{dW_n(\omega)}{dz} = \epsilon_0\omega \sum_{M,N} \text{Im} [\tilde{p}_{n;N}(\omega)\tilde{a}_{n;M}^* e^{i(\beta_0(M\omega_0) - \beta_0(N\omega_0))z}] \quad (5.30)$$

where summation occurs over all indices  $M$  and  $N$ . The  $\exp[i(\beta_0(M\omega_0) - \beta_0(N\omega_0))z]$  factor originates from converting between the  $\tilde{a}_{n;N}$  and  $\tilde{A}_{n;N}$  envelopes and has no physical significance. Summing over waveguide modes, substituting for  $\tilde{p}_{n;N}$  in Eq. (5.30) with Eq. (5.24), applying intrinsic permutation symmetry of  $\chi^{(2)}$ , and integrating  $W_n(\omega)$  [as in Eq. (5.28)], the total change in energy  $U = \sum U_n$  can be written as

$$\begin{aligned} \frac{dU}{dz} = & \frac{\epsilon_0}{2} \sum_m \int \text{Im} \left[ \sum_{\substack{n,p,q \\ N,P,Q}} (|\bar{X}_{m;npq}^{Q+P,P,Q}| - |\bar{X}_{m;npq}^{N,N-Q,Q}|) \right. \\ & \left. \times \Omega \tilde{A}_{p;P}(\Omega) \tilde{A}_{q;Q}(\omega - \Omega) \tilde{A}_{n;N}(\omega)^* e^{-im\phi_G} \right] d\Omega d\omega \end{aligned} \quad (5.31)$$

where summation over indices  $n$ ,  $p$  and  $q$  denotes waveguide modes, summation over index  $m$  denotes QPM orders, and summation over  $N$ ,  $P$ , and  $Q$  denotes harmonic orders. Eq. (5.31) implies that  $dU/dz = 0$  if the nonlinear coefficients satisfy

$|\bar{X}_{m;npq}^{Q+P,P,Q}| = |\bar{X}_{m;npq}^{N,Q,N-Q}|$  whenever the product  $\tilde{A}_{p;P}(\Omega)\tilde{A}_{q;Q}(\omega - \Omega)\tilde{A}_{n;N}(\omega)^*$  is non-zero. One way to satisfy this condition is to set  $|\bar{X}_{m;npq}^{Q+P,P,Q}| = |\bar{X}_{m;npq}^{2,1,1}|$  for all harmonic indices  $P$  and  $Q$ .

As stated above, another case with  $dU/dz = 0$  is when the envelopes have non-overlapping spectra, so that  $\tilde{a}_{n;M}(\omega)\tilde{a}_{n;N}^*(\omega) = 0$  for all  $\omega$  unless  $N = M$ . When this condition is met, all terms with  $Q \neq N - P$  in Eq. (5.31) are zero. The remaining terms, for which  $Q = N - P$ , vanish identically, since intrinsic permutation symmetry implies that  $\bar{X}_{m;npq}^{N,P,N-P} = \bar{X}_{m;nqp}^{N,N-P,P}$ . There are two particularly important cases with non-overlapping envelope spectra. The first case is for sub-octave-spanning spectra, since each envelope then corresponds to a distinct spectral region. The second case is for arbitrary-bandwidth pulse trains, provided that the envelopes have non-degenerate carrier offset frequencies, i.e. if  $\text{mod}(Nf_{\text{CEO}}, f_{\text{rep}}) \neq f_{\text{rep}}$  for all integers  $N$  for which an envelope  $a_{n;N}$  is non-negligible.

Even when neither of these conditions are satisfied, and thus  $dU/dz \neq 0$ , the resulting  $z$ -dependence of  $U$  may be negligible. The GCW approach shows that there is an underlying set of interactions between the harmonic envelopes that determines the dynamics. Neglecting interactions and envelopes allows the most important dynamical processes, such as nearly-phasematched SHG, to be isolated. However, when envelopes are neglected, they no longer interfere with the remaining envelopes which, for overlapping spectra, results in the  $z$ -dependence of the energy described by Eq. (5.31). Similarly, an overall phase shift  $N\varphi$  of each envelope  $a_{n;N}$  has no effect on the dynamics, but does alter the interference between the envelopes when reconstructing the output spectrum. Despite these interference effects, the structure of the remaining equations (e.g. the coupled wave equations for SHG) is maintained, regardless of whether the spectra overlap or not. For example, in section 5.4.4, additional processes which occur for overlapping spectra (those involving the  $N = -1$  envelope) were shown to be negligible.

A related result which emerges due to the harmonic structure of Eqs. (5.22-5.24) is that the sum of the energies of each harmonic envelope ‘by themselves’ (i.e. neglecting interference with envelopes of different harmonic order in the same waveguide mode) is conserved in general. To show this result, we first define an ESD corresponding to

each harmonic envelope as

$$W_{n;N}(\omega) = \frac{g_n(\omega)\beta_n(\omega)c^2\epsilon_0}{2\omega} |\tilde{A}_{n;N}(\omega)|^2, \quad (5.32)$$

which yields a harmonic energy given by  $U_{n;N} = \int W_{n;N}(\omega)d\omega$ . Eq. (5.32) is defined in analogy to Eq. (5.29). The sum of these harmonic energies over all waveguide modes and harmonic orders is  $z$ -independent, since the sum  $\sum(dU_{n;N}/dz)$  corresponds to the sum over all the terms in Eq. (5.31) satisfying  $Q = N - P$ . Thus,

$$\frac{d}{dz} \left( \sum_{n,N} \int W_{n;N}(\omega)d\omega \right) = 0 \quad (5.33)$$

for any choice of nonlinear coefficients  $\bar{X}$  obeying intrinsic permutation symmetry. Because of Eq. (5.33), the  $z$ -dependence of  $U$  derived in Eq. (5.31) is due to interference effects with neglected interactions; provided that these terms play a negligible role in the dynamics, the fluctuations in energy are also negligible. In section 5.8, we consider the conditions which have to be met in order for an interaction to be negligible.

## 5.8 Appendix: Choice of Effective Susceptibilities

In Eqs. (5.16) and (5.19-5.21), nonlinear coefficients  $\bar{X}$  and  $\bar{Y}$  were introduced to describe coupling between envelopes  $a_{n;N}$  due to the  $\chi^{(2)}$  and  $\chi^{(3)}$  nonlinear susceptibilities. A natural choice of frequency arguments to use when calculating these coefficients is  $\omega_N = N\omega_0$  for integers  $N$ , where  $\omega_0$  is the carrier frequency of the FH. However, for envelopes  $a_{n;N}$  with  $N \leq 0$ , this choice is not necessarily appropriate. For example, the waveguide modes are either unbound or of infinite size at zero frequency ( $N = 0$ ). Furthermore, in section 5.4 we showed that inappropriate choices of nonlinear coefficients could lead to an artificial increase in the rate at which certain spectral components are amplified, which we termed an artificial OPA process. In that case, setting  $\bar{X}_{1;000}^{3,2,1} = 0$  for Fig. 5.5(a) led to artificial OPA around  $2 \mu\text{m}$ . However, any inappropriate choice of  $\bar{X}_{1;000}^{3,2,1}$  can lead to artificial OPA. In this appendix, we discuss how such effects can be evaded by appropriate choices of nonlinear coefficients and the waveguide normalization factor  $g_n(\omega)$  [defined in Eq. (2.7)]. It is often sufficient to choose  $g_n(\omega) = A_{\text{eff}}^{1/3}$  (to yield a weakly dispersive effective susceptibility), set  $\bar{X}_{m;npq}^{N,P,N-P} = \bar{X}_{m;npq}^{2,1,1}$  (approximating the effective susceptibilities as constant), and include all envelopes that interact strongly with other envelopes that are included (to avoid artificial OPA effects); here, we discuss these parameters in more detail.

We first provide a simple picture of the  $2\text{-}\mu\text{m}$  artificial OPA process apparent in Fig. 5.5(a), and its suppression in Fig. 5.5(b), by performing a linear stability analysis of Eqs. 5.22. For this analysis, we assume each envelope can be written as

$$a_{n;N} = \left( a_N^{(0)} + a_N^{(1)} \right) \exp[i(\beta_0(\omega) - K_N(\omega))z] \quad (5.34)$$

where  $a_N^{(0)}$  is a CW zeroth-order component frequency  $N\omega_0$ , and  $a_N^{(1)}$  is a weak and time-dependent first-order component which is expressed in the frequency domain for the following analysis. For the zeroth-order fields, we assume that only  $a_1^{(0)}$  and  $a_2^{(0)}$  are non-zero; for the first-order analysis we neglect products of two or more first-order fields. With these assumptions, coupling between the first-order components can be written as a simple linear system in the frequency domain. In order to construct this

linear system, we introduce a sideband vector  $\tilde{v}_\Delta$ , given by

$$\tilde{v}_\Delta(\Omega) = \begin{bmatrix} a_{1-\Delta}^{(1)}(\omega_0 - \Omega)^* \\ a_{1+\Delta}^{(1)}(\omega_0 + \Omega) \\ a_{2-\Delta}^{(1)}(2\omega_0 - \Omega)^* \\ a_{2+\Delta}^{(1)}(2\omega_0 + \Omega) \end{bmatrix}, \quad (5.35)$$

where  $\Omega$  is an arbitrary sideband frequency. The subscript  $\Delta$  is used to distinguish between different sets of envelopes which are coupled to each other. The simplest case has  $\Delta = 0$ , which corresponds to the linear system describing coupling between spectral components of  $a_{0;1}$  at frequencies  $\omega_0 \pm \Omega$  and spectral components of  $a_{0;2}$  at frequencies  $2\omega_0 \pm \Omega$ . Other integer values of  $\Delta$  indicate coupling between different sets of envelopes, but the same set of optical frequencies [e.g. for  $\Delta = 1$ , coupling is between  $a_0(\omega_0 - \Omega)$ ,  $a_2(\omega_0 + \Omega)$ ,  $a_1(2\omega_0 - \Omega)$ , and  $a_3(2\omega_0 + \Omega)$ ]. By substituting Eq. (5.34) for the modal envelopes into Eq. (5.22), and neglecting terms involving products of first order quantities, we obtain for the evolution of the sideband vectors  $\tilde{v}_\Delta$  the result

$$\frac{d\tilde{v}_\Delta}{dz} = iM_\Delta \tilde{v}_\Delta, \quad (5.36)$$

To write down the coupling matrices  $M_\Delta$ , we split the matrix into two parts in order to fit within the page width, i.e.  $M_\Delta = \begin{bmatrix} M_{\Delta,l} & M_{\Delta,r} \end{bmatrix}$ .  $M_{\Delta,l}$  and  $M_{\Delta,r}$  are given by

$$M_{\Delta,l} = \begin{bmatrix} \beta_0(\omega_0 - \Omega) & \left(\gamma_{2,1-\Delta}(\omega_0 - \Omega)a_2^{(0)}\right)^* \\ -\gamma_{2,1-\Delta}(\omega_0 + \Omega)a_2^{(0)} & -\beta_0(\omega_0 + \Omega) \\ 2\left(\gamma_{2-\Delta,1}(2\omega_0 + \Omega)a_1^{(0)}\right)^* & 0 \\ 0 & -2\gamma_{2+\Delta,1}(2\omega_0 + \Omega)a_1^{(0)} \end{bmatrix}$$

$$M_{\Delta,r} = \begin{bmatrix} \gamma_{2-\Delta,1}(\omega_0 - \Omega)a_1^{(0)} & 0 \\ 0 & -\left(\gamma_{2+\Delta,1}(\omega_0 + \Omega)a_1^{(0)}\right)^* \\ \beta_0(2\omega_0 - \Omega) & 0 \\ 0 & -\beta_0(2\omega_0 + \Omega) \end{bmatrix}, \quad (5.37)$$

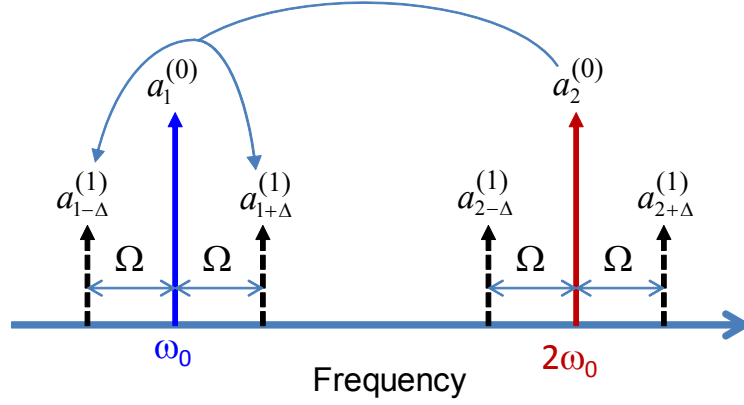


Figure 5.8: Schematic of sidebands (dashed arrows) and strong CW carrier waves at  $\omega_0$  and  $2\omega_0$  (blue and red arrows, respectively). The sidebands are coupled to each other via the CW carrier waves, based on Eqs. (5.35) and (5.36). A particular process is shown, in which the SH carrier ( $a_2^{(0)}$ ) mixes with the sideband  $a_{1-\Delta}^{(1)}$  ( $\omega_0 - \Omega$ ) to generate a sideband  $a_{1+\Delta}^{(1)}$  ( $\omega_0 + \Omega$ ) (and vice versa). The coupling coefficient for this process is given by the  $\gamma_{2,1-\Delta}$  terms in Eq. (5.37).

where the coupling coefficients  $\gamma_{N,P}(\omega)$  are given by

$$\gamma_{N,P}(\omega) = \frac{\omega^2}{g_0 \beta_0 c^2} \left| \bar{X}_{1,000}^{N,P,N-P} \right| e^{i\phi_G(z)}. \quad (5.38)$$

The above linear system is shown schematically in Fig. 5.8, which illustrates coupling between the first-order fields due to the zeroth-order fields.

There is a linear system corresponding to each integer value of  $\Delta$ . If the dispersion of the effective susceptibility can be neglected, then the  $\Delta = 0$  case is physically accurate; this assumption holds in particular for small  $\Omega$ . In contrast, and even for small  $\Omega$ , the  $\Delta \neq 0$  cases can represent artificial modifications that arise from evaluating the nonlinear coefficients at distant carrier frequencies. Thus, if Eq. (5.35) supports exponential growth for components  $\omega_0 \pm \Omega$ , this growth rate can be artificially altered in the  $\Delta = \pm 1$  systems, for any components of  $a_{0,0}$  and  $a_{0,2}$  around  $\omega_0$ , unless  $M_{\pm 1} = M_0$ , and hence

$$\bar{X}_{1,(000)}^{2,2,0} = \bar{X}_{1,(000)}^{3,2,1} = \bar{X}_{1,(000)}^{1,1,0} = \bar{X}_{1,000}^{2,1,1}. \quad (5.39)$$

The significance of the constraints in Eq. (5.39) depends on the problem being considered: specifically, on the magnitude of spectral components of  $a_{0;0}$  and  $a_{0;2}$  around  $\omega_0$ , the total gain for these components with and without the above constraint, and whether another aspect of the problem would be made more accurate by choosing different effective nonlinear coefficients for different interactions. The most important cases are when the amplification rate from  $M_{\pm 1}$  exceeds that of  $M_0$ , since this can lead to artificial exponential growth of weak spectral components, which can then distort the output spectrum.

For example, in Fig. 5.5(a) [ $N \in \{0, 1, 2\}$ ], the presence of an intense SH, ultra-broadband spectra, and the assumption that  $\bar{X}_{1;000}^{3,2,1} = 0$  [and hence  $\gamma_{24} = 0$  in Eq. (5.37)], led to a large artificial gain around  $2 \mu\text{m}$  that was suppressed in Fig. 5.5(b), in which  $a_{0;3}$  was included and thus Eq. (5.39) was satisfied. This suppression can be viewed heuristically as the competition between OPA due to the intense SH and SFG due to the intense FH; in Fig. 5.5(a), one of the SFG processes was not included in the model because  $\bar{X}_{1;000}^{3,2,1}$  was set equal to zero.

While Eq. (5.39) may appear restrictive, it can be satisfied in a natural way, via the smooth but otherwise arbitrary waveguide mode normalization function  $g_n(\omega)$  defined in Eq. (2.7). The single-argument function  $g_0(\omega)$  can be used to ensure that the two-argument function  $X_{npq}(\omega, \omega')$  defined in Eq. (2.4) is constant over a particular trajectory of frequency arguments. Such a trajectory could include, for example, the frequencies associated with  $X_{1;000}^{2,1,1}$ ,  $X_{1;000}^{3,2,1}$ , and the relevant frequencies for intrapulse DFG effects, corresponding to  $X_{1;000}^{1,1,0}$ . Thus, Eq. (5.39) can be reduced to  $\bar{X}_{1;000}^{2,2,0} = \bar{X}_{1;000}^{1,1,0}$ , which is much less restrictive. For the  $N \leq 0$  terms, we may choose  $\bar{X}_{1;000}^{N,P,N-P} = \bar{X}_{1;000}^{2,1,1}$  as needed to suppress artificial OPA of the type discussed above, and then choose a  $g_n(\omega)$  profile to yield an appropriate driving polarization for intrapulse DFG effects.

To see how  $g_n(\omega)$  can be determined, it is useful to first write the effective susceptibilities  $X_{npq}$  defined in Eq. (2.4) in the form

$$X_{npq}(\omega, \omega') = \sqrt{g_n(\omega)g_p(\omega')g_q(\omega - \omega')}C_{npq}(\omega, \omega') \quad (5.40)$$

where  $C_{npq}$ , which involves the frequency dependent mode shapes and the nonlinear susceptibility, is independent of the choice of the  $g_n(\omega)$  functions. From Eq. (5.40), in order to yield a non-dispersive  $X_{000}(\omega, \omega')$ ,  $g_0(\omega)$  must satisfy

$$\begin{aligned} g_0(\omega)g_0(\omega')g_0(\omega - \omega') &= \left| \frac{\pi}{2} \frac{\bar{X}_{1;000}^{2,1,1}}{C_{000}(\omega, \omega')} \right|^2 \\ &\equiv f(\omega, \omega'). \end{aligned} \quad (5.41)$$

Since the right hand side involves  $C_{000}(\omega, \omega')$ , a function of two variables, but the left hand side involves only  $g_0(\omega)$ , a function of one variable, Eq. (5.41) cannot in general be satisfied for all combinations of frequencies. However, Eq. (5.41) can be satisfied over a finite number of frequency trajectories of form  $\omega'(\omega)$ .

If we specify a trajectory  $\omega'(\omega) = \omega + \omega_0$ , assume an arbitrary positive value for  $g_0(\omega_0)$ , and define  $h_0(\omega) = \ln[g_0(\omega)]$  and  $F(\omega) = \ln[f(\omega, \omega'(\omega))/g_0(\omega_0)]$ , Eq. (5.41) can be re-written as

$$h_0(\omega) + h_0(\omega + \omega_0) = F(\omega). \quad (5.42)$$

This equation can be solved numerically; more generally, the deviation of  $g_n$  across an arbitrary number of trajectories can be minimized. One suitable approach is to pose a convex optimization problem with two constraints [Eq. (5.41) and monotonicity of  $h_0(\omega)$ ] and minimize  $\int d\omega |dh_0/d\omega|$  (with the integral replaced by a discrete summation).

Based on the above considerations, we can specify some guidelines for the nonlinear coefficients  $\bar{X}$ . Setting  $\bar{X}_{m;npq}^{N,P,N-P} = \bar{X}_{m;npq}^{2,1,1}$  for all  $N$  and  $P$  evades OPA-related instabilities of the type discussed above (provided a sufficient set of envelopes are included in the model), and is directly comparable to SE models (see Fig. 5.7), where this assumption is implicit since there is only a single envelope whose evolution is governed by a frequency independent coupling coefficient for each waveguide mode. Where equating nonlinear coefficients is inaccurate for some important nonlinear processes, evaluating  $\bar{X}_{m;npq}^{N,P,N-P}$  at the carrier frequencies may be more appropriate. In

order to evade instabilities here,  $g_n(\omega)$  should be chosen such that Eq. (5.39) is satisfied; a suitable approach for choosing these  $g_n(\omega)$  is illustrated in Eqs. (5.40-5.42). As a related general rule, when an envelope is strong enough to cause significant OPA by itself, care should be taken to ensure that other strong interactions which modify that OPA process are also included in the model, particularly when these interactions can substantially alter the gain rate (or eigenvalues, in the context of a MI). When the role of certain terms is not clear by inspection or by adding additional envelopes to the GCWEs, linear stability analysis of the form given above can help to determine their significance.

The dispersion of the  $\chi^{(3)}$  susceptibility can be also important, for example due to the increase in  $n_2$  near half the band gap. The form for  $\chi^{(3)}$  assumed in Eq. (2.10) does not account for these changes. A more accurate approximation to  $\chi^{(3)}$  which can captures some of its dispersion is

$$\chi^{(3)}(\omega, \omega', \omega - \Omega, \Omega - \omega') \approx \chi_E(\omega + \omega') + \chi_R(\Omega), \quad (5.43)$$

This form is compatible with the Fourier-transform-based propagation given by Eqs. (5.22-5.24). Replacing Eq. (2.10) with Eq. (5.43), the resulting  $\bar{X}_E$  and  $\bar{Y}$  terms would have forms similar to the  $\bar{X}_R$  terms in Eq. (5.24), but involving  $\mathcal{F}[a_{p;P}a_{q;Q}]$  instead of  $\mathcal{F}[a_{p;P}^*a_{q;Q}]$ . With a complex  $\chi_E$  profile in Eq. (5.43), the dispersion of the nonlinear refractive index and two photon absorption can be accounted for. In deriving the  $\bar{Y}$  terms in Eq. (5.24), a real  $\chi_E$  was assumed. Modified forms of these terms could be derived from Eq. (5.13) in order to account for a complex  $\chi_E$ .

The procedures discussed in this appendix should be sufficient for most problems of practical interest. However, for particularly constrained problems, the full frequency dependence of the effective susceptibilities can be included by taking the more computationally intensive approach of calculating  $\tilde{\mathcal{P}}_{n;N}$  by integrals in the frequency domain, as in Eqs. (5.6-5.10).

# Chapter 6

## Optical Parametric Amplification in Orientation-Patterned GaAs

### 6.1 Introduction

There is much interest in developing robust and compact sources in the mid-IR spectral region from 2-12  $\mu\text{m}$  for frequency metrology, biological, and medical applications [77]. In previous chapters, we focused on supercontinuum generation as a means of generating new spectral components in the IR and mid-IR spectral regions. A complementary technique, and one which holds much promise for generating light in the mid-IR, is difference frequency generation (DFG) of two infrared laser sources. With DFG, established broadband laser gain media such as Er- and Tm-doped fibers can be utilized to generate light in the mid-IR [78, 79]. Orientation-patterned gallium arsenide (OP-GaAs) is a good nonlinear material for accessing this spectral range due to its wide transparency range, high nonlinearity, and the broadband tunability enabled by quasi-phasesmatching (QPM) [25, 27, 36, 70, 80, 81, 82, 83, 84].

Compared to DFG employing continuous wave inputs, the use of femtosecond input pulses enables a wide-bandwidth, higher output power and conversion efficiency, and precise control of the optical frequency via the implementation of frequency comb lasers [75]. In order to avoid two-photon absorption in GaAs, a pump wavelength  $>1.7 \mu\text{m}$  is required [85]. Therefore, femtosecond Tm-doped-fiber lasers, which have a

typical center wavelength of around  $1.95\text{-}\mu\text{m}$ , are ideally suited to mid-IR generation in OP-GaAs. Furthermore, with the high peak powers available from such laser sources [66], efficient nonlinear conversion can be achieved.

Starting from a  $1.95\text{-}\mu\text{m}$  pump source, several nonlinear-optical approaches can be taken to generate the necessary near-IR spectral components to seed the DFG process. One approach is via supercontinuum (SC) generation [64, 86]. Although this approach yields a seed with low spectral density, with a broadband seed spectrum only the QPM period or crystal temperature needs to be varied in order to tune the generated mid-IR light. A different approach is to use synchronously-pumped (SP) optical parametric oscillators (OPOs) [87]. OPOs are versatile, high-power, and widely tunable, but they can be experimentally quite complex since a free space optical cavity is usually required, and they can be subject to spectral instabilities [87, 74]. The drawbacks of the above approaches can be avoided by the use of Raman soliton self frequency shift (SFS) sources [50, 88, 89, 90], in which a substantial portion of the energy of an input pulse can be down-shifted to the spectral range of interest. SFS followed by DFG offers the potential for broad tuning, a simple single-pass experimental configuration, and high conversion efficiency.

## 6.2 Experiment

Based on the above considerations, in the work discussed in this chapter we used a high power 150-fs-level,  $1.95\text{-}\mu\text{m}$  Tm-doped fiber oscillator-amplifier system to first generate a  $2.5\text{-}\mu\text{m}$  seed via SFS in a fluoride fiber, followed by mid-IR generation via DFG in a fan-out OP-GaAs crystal. The mid-IR light has an average power of 1.3 mW, and is tunable between  $6.7$  and  $12.7\ \mu\text{m}$ .

The experimental setup is shown in Fig. 6.1. The experiments were performed at IMRA America. The oscillator was mode-locked by nonlinear polarization rotation and generates pulses as short as 100 fs with an average power of 20 mW at 72 MHz. The pulses were chirped in a positive dispersion fiber and subsequently amplified in a 1.6-m length of large-mode-area cladding-pumped Tm-doped fiber. The pulses were then compressed in a large-mode-area fiber. We characterized the intensity and phase

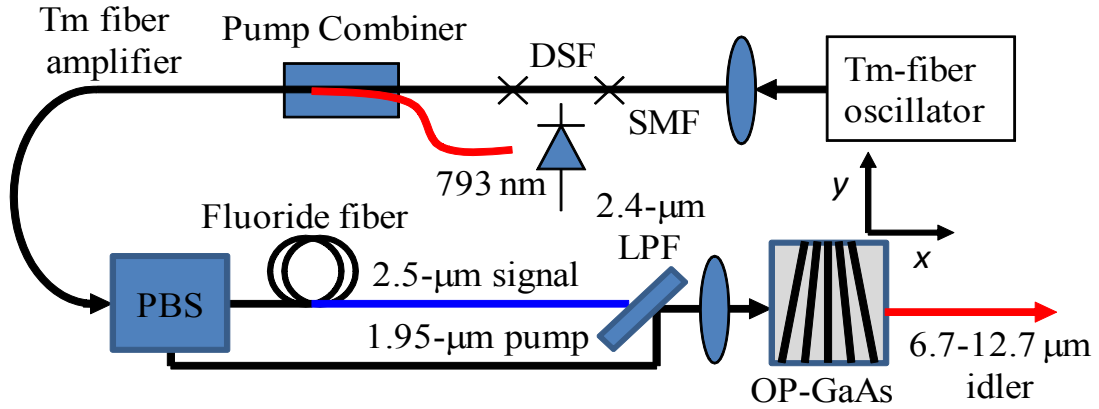


Figure 6.1: Setup of a Tm-fiber DFG system. SMF: single-mode fiber; DSF: dispersion-shifted fiber.

of the compressed pulses using second harmonic generation (SHG) frequency resolved optical gating (FROG). The reconstructed pulse duration was 145 fs (FWHM) at 1-W average power. The reconstructed pulse profile is shown in Fig. 6.2(a). The pre- and post-pulses are likely due to self phase modulation (SPM) in the multi-mode compression fiber, and can therefore be avoided with optimized fiber designs.

Next, the compressed pulses were split into two parts with a polarizing beam splitter (PBS); we denote these parts as the pump and signal arms. The pulses from the signal arm were coupled into a single-mode fluoride fiber in order to facilitate Raman SFS from  $1.95\ \mu\text{m}$  to  $2.5\ \mu\text{m}$ . This  $2.5\text{-}\mu\text{m}$  signal was then recombined with the  $1.95\text{-}\mu\text{m}$  pump using a  $2.4\text{-}\mu\text{m}$  long-pass filter (LPF); the corresponding spectrum is shown in Fig. 6.2(b). The total power before and after the fluoride fiber was 200 mW and 150 mW, respectively. After the LPF, the  $2.5\text{-}\mu\text{m}$  signal power was 30 mW (reduced from the input power primarily due to the inefficiency of the SFS process) and the  $1.95\text{-}\mu\text{m}$  pump power was up to 430 mW. The pulse duration is an important parameter in the process; with further optimization of the input pulses, SFS to longer wavelengths should be possible.

Both the pump and signal beams were focused to a  $30\text{-}\mu\text{m}$   $1/e^2$  radius inside an uncoated OP-GaAs sample. The sample had a fan-out QPM grating design, with QPM period ranging linearly from 52 to  $82\ \mu\text{m}$ , with 22 periods; the sample length

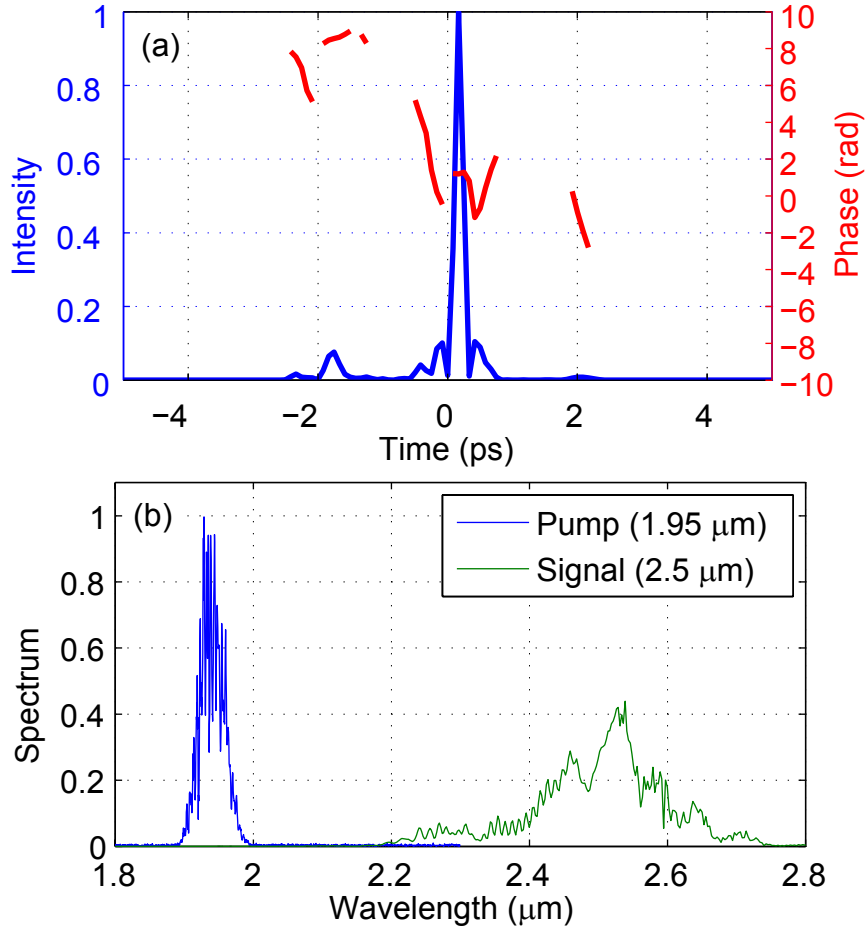


Figure 6.2: (a) FROG reconstruction of the 1.95- $\mu\text{m}$  pump, (b) Spectrum of the pump and Raman-self-frequency shifted signal after the LPF, measured with an FTIR.

and width were 2 and 10 mm, corresponding to the  $x$  and  $y$  directions indicated in Fig. 6.1, respectively. The sample was fabricated by molecular beam epitaxy (MBE) of an orientation-patterned template, followed by hydride vapor phase epitaxy (HVPE) for growth of a 1-mm-thick film suitable for bulk DFG [81].

The output mid-IR beam was collimated with an off-axis parabola. At optimal phasematching, the mid-IR output power was 1.3 mW. Tuning around this operating point was obtained by lateral translation of the fan-out QPM grating, which yielded a tuning range of 6.7-12.7  $\mu\text{m}$ . Spectra measured with an FTIR at several different QPM periods are shown in Fig. 6.3(a). At the edges of the tuning range, the delay

and the power in the fluoride fiber were adjusted, in addition to the QPM period, in order to shift the wavelength of the seed pulses (and hence the generated mid-IR wavelength) while still maintaining phasematching and temporal alignment with the pump in the OP-GaAs crystal. Further tuning could likely be obtained with an increase in pump power and shorter pump pulses. Next, we measured the average output DFG power as a function of average input pump power on a thermal power meter, as shown in Fig. 6.3(b). The position of the crystal for this measurement was chosen to maximize the output power at the highest pump energy.

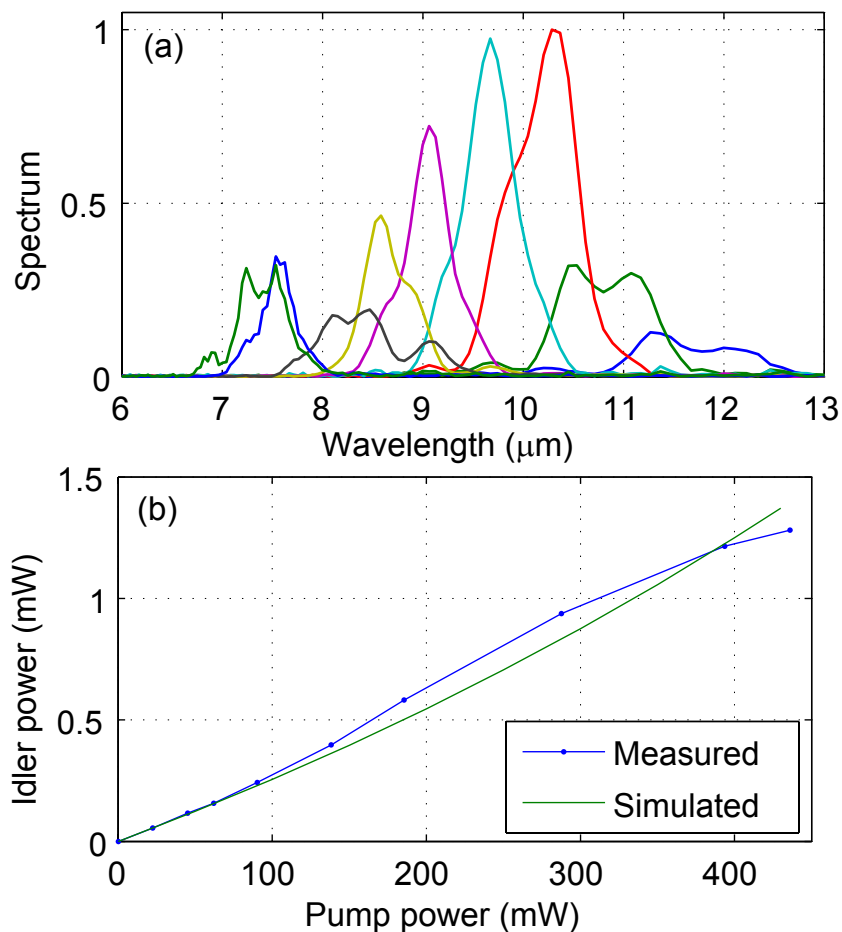


Figure 6.3: (a) Mid-IR output spectra measured with an FTIR at several different positions in the fan-out QPM grating. (b) Average mid-IR output power as a function of average pump power inside the OP-GaAs sample.

### 6.3 Modeling

To compare the above results to theoretical predictions, we modeled the bulk three-wave mixing process numerically with a split-step method, including the effects of diffraction, dispersion,  $\chi^{(2)}$ , and self and cross phase modulation (SPM and XPM, respectively). Coupled-wave equations describing nonlinear mixing between the pump, signal, and idler waves can be determined from Eq. (1.13). Since the permittivity of GaAs is isotropic,  $\delta = 0$ . In GaAs, all the components of  $\chi^{(2)}$  are zero except for the element  $\chi_{xyz}^{(2)}$  and terms related to it by permutation symmetries. In the experiments discussed above, the QPM grating k-vector is along the [110] direction ( $\hat{\mathbf{z}}$ ). To obtain efficient mixing, one of the input waves was polarized along [001] ( $\hat{\mathbf{x}}$ ) and the other along  $[\bar{1}\bar{1}0]$  ( $\hat{\mathbf{y}}$ ). From Eq. (1.4), the resulting nonlinear polarization is along direction  $[\bar{1}\bar{1}0]$  (perpendicular to the grating k-vector).

To derive a set of CWEs, we begin with Eq. (1.13) and follow the approach used in section 1.5. We thus assume the electric field has the same form given by Eq. (1.30),

$$\mathbf{E} = \frac{1}{2} \sum_j A_j e^{i\omega_j t - k_j z} \mathbf{v}_j + c.c \quad (6.1)$$

where  $j \in \{i, s, p\}$ . As in section 1.5, the envelopes  $A_j(x, y, z, t)$  are defined as analytic signals, but in contrast to section 1.5 they are allowed to vary in transverse coordinates as well as time. The vectors  $\mathbf{v}_j$  are given by  $\mathbf{v}_i = [-1, 1, 0]^T / \sqrt{2}$ ,  $\mathbf{v}_s = [1, -1, 0]^T / \sqrt{2}$ , and  $\mathbf{v}_p = [0, 0, 1]^T$ . Substituting Eq. (6.1) into Eq. (1.4) yields several second-order contributions to the nonlinear polarization; we are interested here in the terms having carrier frequencies  $+\omega_j$  for  $j \in \{i, s, p\}$ . These contributions are denoted  $\mathbf{P}_{NL,j}^{(2)}$  for carrier frequency  $j$ , and are given by

$$\mathbf{P}_{NL,i}^{(2)} = \frac{\epsilon_0}{2} \chi_{xyz}^{(2)} A_p A_s^* e^{i(\omega_i - (k_p - k_s)z)} \mathbf{v}_i \quad (6.2a)$$

$$\mathbf{P}_{NL,s}^{(2)} = \frac{\epsilon_0}{2} \chi_{xyz}^{(2)} A_p A_i^* e^{i(\omega_s - (k_p - k_i)z)} \mathbf{v}_s \quad (6.2b)$$

$$\mathbf{P}_{NL,p}^{(2)} = \frac{\epsilon_0}{2} \chi_{xyz}^{(2)} A_i A_s e^{i(\omega_p - (k_i + k_s)z)} \mathbf{v}_p, \quad (6.2c)$$

where  $\chi_{xyz}^{(2)}/2 = d_{14}$ . Third-order contributions to the nonlinear polarization, denoted  $\mathbf{P}_{NL,j}^{(3)}$ , can be obtained in the same way.  $\chi^{(3)}$  is anisotropic in GaAs [85], but we assume that it is isotropic for simplicity [87], i.e.  $\chi_{ijkl}^{(3)} = \chi_0^{(3)}$  for scalar  $\chi_0^{(3)}$ .

In order to construct a coupled-wave system, each envelope  $A_j$  is assumed to be driven only by nonlinear polarization term  $P_{NL,j}^{(2)} + P_{NL,j}^{(3)}$ , on the basis that the other interactions are sufficiently phase mismatched that conversion and cascade phase shifts are both negligible. The electric field and corresponding polarization components are in the same direction, and from Eq. (1.36),  $d_{\text{eff}} = d_{14}$ . Before writing out the coupled wave equations, it is useful to make several simplifications. Starting from Eq. (1.13), we set  $\delta = 0$  and  $k_e(\omega) = k(\omega)$  (since  $\epsilon$  is isotropic in GaAs), and simplify the diffraction operator by approximating  $i/(2k(\omega))$  as  $i/(2k_j)$  for each wave  $j$ . The nonlinear coupling can be simplified by assuming that the  $A_j$  have non-overlapping spectra and bandwidths which are significantly narrower than an octave around the carrier frequencies: this assumption allows  $\chi^{(2)}$  to be approximated as non-dispersive, and the factor  $\omega^2/(k(\omega)c^2)$  on the right hand side of Eq. (1.13) to be evaluated at each carrier frequency. We consider only the +1 order of the QPM grating. These simplifications yield the following set of coupled-wave equations

$$\begin{aligned} \left[ \frac{\partial}{\partial z} + i(k(\omega) - k_i) + \frac{i}{2k_i} \nabla_{\perp}^2 \right] \tilde{A}_i &= -i \frac{\omega_i d_1}{c n_i} \mathcal{F} [A_p A_s^*] e^{-i\Delta k_1 z} \\ &\quad - i \frac{3\omega_i}{8c n_i} \chi_0^{(3)} \mathcal{F} [ (|A_i|^2 + 2|A_s|^2 + 2|A_p|^2) A_i ] \end{aligned} \quad (6.3a)$$

$$\begin{aligned} \left[ \frac{\partial}{\partial z} + i(k(\omega) - k_s) + \frac{i}{2k_s} \nabla_{\perp}^2 \right] \tilde{A}_s &= -i \frac{\omega_s d_1}{c n_s} \mathcal{F} [A_p A_i^*] e^{-i\Delta k_1 z} \\ &\quad - i \frac{3\omega_s}{8c n_s} \chi_0^{(3)} \mathcal{F} [ (|A_s|^2 + 2|A_i|^2 + 2|A_p|^2) A_s ] \end{aligned} \quad (6.3b)$$

$$\begin{aligned} \left[ \frac{\partial}{\partial z} + i(k(\omega) - k_p) + \frac{i}{2k_p} \nabla_{\perp}^2 \right] \tilde{A}_p &= -i \frac{\omega_p d_1}{c n_p} \mathcal{F} [A_i A_s] e^{i\Delta k_1 z} \\ &\quad - i \frac{3\omega_p}{8c n_p} \chi_0^{(3)} \mathcal{F} [ (|A_p|^2 + 2|A_i|^2 + 2|A_s|^2) A_p ] \end{aligned} \quad (6.3c)$$

where  $\Delta k_1 = k_p - k_s - k_i - K_g$  is the carrier phase mismatch,  $n_j = k_j c / \omega_j$  is the refractive index of wave  $j$ , and  $d_1 = (\chi_{xyz}^{(2)} / 2) \times (2 / \pi)$  is the relevant nonlinear coefficient for first-order QPM. The operator  $\nabla_{\perp}^2 = \partial^2 / \partial x^2 + \partial^2 / \partial y^2$ .

The relevant nonlinear coefficients are given by  $d_{\text{eff}} = \chi_{xyz}^{(2)} / 2 = 94 \text{ pm/V}$  and  $n_2 = 1.5 \times 10^{-4} \text{ cm}^2/\text{GW}$  [83]. The third-order susceptibility can be related to the nonlinear refractive index by Eq. (2.18). The temporal profile of the pump pulses is given by the FROG reconstruction shown in Fig. 6.2(a). For the signal, we assumed transform-limited Gaussian pulses (possibly an oversimplification) with a FWHM duration of 50 fs, based on the signal bandwidth shown in Fig. 6.2(b). The beam waists were assumed to be  $30 \text{ }\mu\text{m}$  ( $1/e^2$ ), with beam waists and temporal overlap of the pulses at the center of the crystal; we also assumed radial symmetry. We note also that for 150-fs pulses, the group velocity walk-off length between the signal and pump pulses is 0.75 mm, based on the difference between the group velocities between 1.95 and  $2.5 \text{ }\mu\text{m}$ ; this length is shorter than the length of the crystal (2 mm).

The simulations, which had no adjustable parameters, are in good agreement with experiment. The nonlinearity of the two curves arises through several effects, including pump depletion, SPM, and XPM. Since the B-integral is approximately  $0.6\pi$  at the highest pump power (430 mW), and the signal gain is approximately 1.1 dB, these effects are relatively minor at the intensities involved here.

## 6.4 Design

With realistic improvements to the energy and quality of the input pulses, and anti-reflection (AR)-coated OP-GaAs samples, it should be possible to achieve  $>10 \text{ mW}$  mid-IR power without significant changes to the Tm-doped fiber laser system (i.e. with comparable pump pulse durations). Higher pump powers are of particular interest in order to obtain high-gain OPA, which would allow a high-power idler to be generated even with a weak signal seed. At these higher power levels, however, nonlinear phase shifts will be important and motivate the use of longer pump pulses. Longer pump pulses are advantageous because the plane-wave OPA signal gain scales as  $I_p^{1/2} L$ , for pump intensity  $I_p$  and interaction length  $L$ , while the B-integral scales

as  $I_p L$ . Therefore, the ratio of gain to B-integral scales as  $I_p^{-1/2}$ , which favors longer pump pulses at a given pump energy. In order to achieve a high gain without a large B integral, this scaling favors lower intensities and hence longer pulse durations, provided that the focusing conditions and grating length are chosen optimally at a given pulse duration. At the optimal crystal length and focusing, the B-integral scales inversely with the pulse duration. To show the above dependencies, it is useful to consider Eqs. (6.3) under a number of different approximations.

### 6.4.1 Exponential Growth

First, we show the OPA solutions which are supported by Eqs. (6.3). If each envelope  $A_j$  is both plane-wave (PW) and continuous-wave (CW), then the diffraction and dispersion operators in these equations are zero. If in addition the  $\chi^{(3)}$  terms are neglected, Eqs. (1.37) are obtained. To identify relevant properties of these simplified equations, it is useful to first non-dimensionalize them. Consider fields  $\bar{A}_j$  defined as  $\bar{A}_j = A_j \sqrt{n_j / \omega_j}$ . Coupling between these fields due to  $\chi^{(2)}$  is determined by a single coupling coefficient; this is in contrast to Eqs. (6.3), where a different coefficient,  $\omega_j d_{\text{eff}} / (c n_j)$ , is associated with each envelope. It is also convenient to normalize the envelopes to the input pump, since energy is transferred from the pump to the signal and idler. Based on these considerations, we define normalized envelopes  $a_j$  according to

$$A_j = \sqrt{\frac{\omega_j n_p}{n_j \omega_p}} A_{p0} a_j \quad (6.4)$$

where  $A_{p0}$  is the magnitude of the input pump envelope. Each  $|a_j|$  is proportional to the photon flux of wave  $j$ . Note that these  $a_j$  envelopes are not the same as any of those discussed in chapter 5. Substituting Eq. (6.4) into Eq. (6.3) and assuming

plane, continuous waves yields the following normalized CWEs

$$\begin{aligned}\frac{da_i}{dz} &= -i\gamma_0 a_p a_s^* e^{-i\Delta kz} \\ \frac{da_s}{dz} &= -i\gamma_0 a_p a_i^* e^{-i\Delta kz} \\ \frac{da_p}{dz} &= -i\gamma_0 a_i a_s e^{i\Delta kz}\end{aligned}\tag{6.5}$$

where the (real-valued) coupling coefficient  $\gamma_0$  is given by

$$\gamma_0 = \sqrt{\frac{\omega_i \omega_s}{n_i n_s}} \frac{d_1}{c} A_{p0}.\tag{6.6}$$

In the case of an undepleted pump ( $da_p/dz = 0$ ;  $a_p = 1$ ), coupling between the signal and idler is linear (in the sense that the output fields are linear in the input fields). The resulting equations can be written in the form of a linear dynamical system:

$$\frac{d}{dz} \begin{bmatrix} a_i^* e^{i\Delta kz/2} \\ a_s e^{-i\Delta kz/2} \end{bmatrix} = i \begin{bmatrix} -\frac{\Delta k}{2} & \gamma_0 \\ -\gamma_0 & \frac{\Delta k}{2} \end{bmatrix} \begin{bmatrix} a_i^* e^{i\Delta k/2} \\ a_s e^{-i\Delta kz/2} \end{bmatrix}.\tag{6.7}$$

This system has eigenvalues  $g = \pm \sqrt{\gamma_0^2 - (\Delta k/2)^2}$ . When  $\Re[g] > 0$ , i.e. when  $|\Delta k| < 2\gamma_0$ , exponential growth occurs. From the solutions to Eq. (6.7) with zero idler input, the output signal is given by

$$a_s(L) = a_s(0) \cosh(gL) e^{-i\Delta kz/2},\tag{6.8}$$

which for high values of  $gL$  corresponds to exponential growth of both the signal and idler waves.

### 6.4.2 Interactions Involving Pulsed Beams

In the experiments discussed above, pulsed beams were used to generate the mid-IR idler. The presence of non-uniform intensity profiles, the effects of diffraction and

dispersion, and depletion of the pump all modify the simple plane- and continuous-wave OPA process discussed in subsection 6.4.1.

To estimate the role played by these effects, in this subsection we consider the case of input signal and pump pulses which are Gaussian in both space and time, and have durations long enough that group velocity dispersion and higher-order terms in  $k(\omega)$  around each carrier frequency can be neglected. With these assumptions, the number of parameters in Eqs. (6.3) is reduced significantly. The dispersion relation is given, to first order, by

$$k(\omega_j + \Omega) \approx k(\omega_j) + \frac{n_g(\omega_j)}{c} \Omega \quad (6.9)$$

where  $\Omega$  is a frequency shift around carrier wave  $j$ . The group index  $n_g(\omega)$  is defined as  $n_g(\omega)/c = (dk/d\omega)$ ; the group velocity is given by  $v_g(\omega) = c/n_g(\omega)$ .

The pump  $1/e^2$  beam waist is denoted  $w_{p0}$ , and its  $1/e^2$  temporal duration is denoted  $\tau_{p0}$ ; we assume that there is no chirp on the input pulses. With these parameters, normalized coordinates  $X = x/w_{p0}$ ,  $Y = y/w_{p0}$ , and  $T = t/\tau_{p0}$  can be defined. In order to define a normalized coordinate for the propagation direction  $z$ , note that the characteristic interaction distance associated with Eqs. (6.3) is often given by the signal-pump group velocity mismatch (GVM) length  $|L_{\text{GVM}}^{(sp)}|$ , where the GVM distances  $L_{\text{GVM}}^{(ij)}$  are defined as

$$L_{\text{GVM}}^{(ij)} \equiv \frac{\tau_{p0} c}{n_g(\omega_i) - n_g(\omega_j)} \quad (6.10)$$

for any pair of carrier frequencies  $\omega_i$  and  $\omega_j$ . Over the length  $|L_{\text{GVM}}^{(sp)}|$ , pump and signal pulses of equal duration  $\tau_{p0}$  walk off each other in time. As a result, in a low-gain experiment, the signal and pump pulses interact very weakly after a certain number of such GVM lengths. In a high-gain experiment the dynamics can be somewhat more complicated, but the GVM length still limits the gain that can be obtained, since the other characteristic lengths (the diffraction length due to the focusing conditions and the length of the QPM grating itself) are free parameters (within certain bounds). Thus, when modeling pulses for which the GVM length satisfies  $|L_{\text{GVM}}^{(sp)}| \ll L_{\text{max}}$ ,

where  $L_{max}$  is the maximum grating length available, it is reasonable to normalize  $z$  to  $|L_{GVM}^{(sp)}|$ . This normalization is not suitable in general: for example, if the pump and signal group indices are the same, then  $|L_{GVM}^{(sp)}| \rightarrow \infty$ ; in such cases, another characteristic length of the problem should be chosen for normalization purposes. Another important example is when the signal and idler group velocities are on opposite sides of the pump group velocity: the signal and idler pulses can then “self trap”, leading to exponential amplification over arbitrary distances.

For numerical solutions it is also useful to define a moving coordinate system based on a particular reference group velocity  $v_{ref}$ , so that each of the pulses propagates slowly through the assumed time window (as discussed in chapter 2). Choosing  $v_{ref} = v_g(\omega_p)$ , we thus define a normalized propagation coordinate according to  $Z = (z - v_g(\omega_p)t)/|L_{GVM}^{(sp)}|$ . By normalizing each field to the peak field of the pump in space and time, as in Eq. (6.4), re-writing the coupled wave equations in terms of the above normalized coordinates, and multiplying both sides of each equation by  $|L_{GVM}^{(sp)}|$ , we obtain the following set of normalized coupled wave equations

$$\left[ \frac{\partial}{\partial Z} + \frac{\delta n_{ip}}{|\delta n_{sp}|} \frac{\partial}{\partial T} + \frac{ik_p}{2k_i} \xi_p^{diff} \bar{\nabla}_{\perp}^2 \right] a_i = -i\sqrt{\eta_{norm}} a_p a_s^* e^{-i\Delta kz} - iB_{norm} p_i \quad (6.11a)$$

$$\left[ \frac{\partial}{\partial Z} + \frac{\delta n_{sp}}{|\delta n_{sp}|} \frac{\partial}{\partial T} + \frac{ik_p}{2k_s} \xi_p^{diff} \bar{\nabla}_{\perp}^2 \right] a_s = -i\sqrt{\eta_{norm}} a_p a_i^* e^{-i\Delta kz} - iB_{norm} p_s \quad (6.11b)$$

$$\left[ \frac{\partial}{\partial Z} + \frac{i}{2} \xi_p^{diff} \bar{\nabla}_{\perp}^2 \right] a_p = -i\sqrt{\eta_{norm}} a_i a_s e^{i\Delta kz} - iB_{norm} p_p \quad (6.11c)$$

where  $\bar{\nabla}_{\perp}^2 = \partial^2/\partial X^2 + \partial^2/\partial Y^2$  is a normalized transverse diffraction operator, the pump diffraction length  $L_{diff} = k_p w_{p0}^2$  (twice the pump Rayleigh range), and  $\delta_{ij}$  are group index mismatch terms defined as  $\delta n_{ij} = n_g(\omega_i) - n_g(\omega_j)$ . The coefficients of the diffraction operators are proportional to the effective focusing factor  $\xi_p^{diff}$ , which is defined as

$$\xi_p^{diff} \equiv \frac{|L_{GVM}^{(sp)}|}{L_{diff}}. \quad (6.12)$$

This focusing factor indicates how rapidly the pump diffracts compared to the rate at which the signal and pump walk off each other in time.  $\xi_p^{diff}$  can take a wide range

of values via the beam waist  $w_{p0}$ . The normalized gain factor  $\eta_{\text{norm}}$  can be written in terms of the pump energy  $U_p$  as

$$\begin{aligned}\eta_{\text{norm}} &\equiv \left(\gamma_0 L_{\text{GVM}}^{(sp)}\right)^2 \\ &= \sqrt{\frac{2}{\pi}} \frac{4\omega_i\omega_s\omega_p d_1^2}{\pi\epsilon_0 c^3 n_i n_s |n_g(\omega_s) - n_g(\omega_p)|} (\xi_p^{\text{diff}} U_p)\end{aligned}\quad (6.13)$$

The  $B_{\text{norm}} p_j$  terms in Eq. (6.11) correspond to third-order nonlinear effects. The normalized nonlinear polarizations  $p_j$  are given by

$$p_j = \left[ \left(\frac{\omega_j n_p}{\omega_p n_j}\right)^2 |a_j|^2 + 2 \sum_{m \neq j} \frac{\omega_j \omega_m n_p^2}{\omega_p^2 n_j n_m} |a_m|^2 \right] a_j, \quad (6.14)$$

and the normalized  $\chi^{(3)}$  coefficient  $B_{\text{norm}}$  is given by

$$B_{\text{norm}} = \sqrt{\frac{2}{\pi}} \frac{3\omega_p^2 \chi^{(3)}}{2\pi\epsilon_0 n_p c^3} \frac{\xi_p^{\text{diff}} U_p}{\tau_{p0}}. \quad (6.15)$$

This coefficient depends on the ratio  $U_p/\tau_{p0}$  and hence scales with peak power. In contrast, the normalized  $\chi^{(2)}$  coefficient depends only on  $U_p$ , independent of the pulse duration. As a result, with decreasing pulse length SPM and XPM effects become more severe relative to the desired  $\chi^{(2)}$  effects

Provided that it is possible to choose grating lengths  $L \gg |L_{\text{GVM}}^{(sp)}|$  and any value of  $\xi_p^{\text{diff}}$ , the only remaining parameters in Eqs. (6.11) relating to  $\chi^{(2)}$  mixing are the pump energy and normalized input signal field  $a_s(z=0, t)$ . The signal gain that can be achieved, in the absence of  $\chi^{(3)}$  effects, is thus determined by the pump energy and the relative group velocities of the pump, signal and idler at the particular set of carrier frequencies involved in the interaction.

In order to estimate the significance of  $\chi^{(3)}$  effects on a high-gain OPA experiment, we first define a normalized coefficient  $h_{\text{OPA}}$  to express the OPA gain in relation to an estimate based on the value of  $\eta_{\text{norm}}$  alone. A simple estimate to the gain can be determined by considering plane- and continuous pump and signal waves. If we assume that the intensity of this (undepleted) pump equals the peak intensity of the

actual pulsed pump beam, and further assume a crystal of length equal to one GVM length,  $L = L_{\text{GVM}}^{(sp)}$ , then, based on Eqs. (6.11), an estimate for the signal power gain is given by  $\exp(2\sqrt{\eta_{\text{norm}}})$ ; exponential growth corresponds here to the high-gain limit of Eq. (6.8). Based on this estimate, we define  $h_{\text{OPA}}$  according to

$$h_{\text{OPA}} = \frac{\ln(G_s)}{2\sqrt{\eta_{\text{norm}}}} \quad (6.16)$$

where the signal gain  $G_s \equiv U(L)/U(0)$  (ratio of signal energies at  $z = L$  and  $z = 0$ ) is found from the solutions to Eqs. (6.11).

With Eqs (6.13) and (6.16), the pump energy required for a certain gain  $G_s$  can be obtained. Substituting this energy into  $B_{\text{norm}}$  and using Eq. (2.18) to replace  $\chi^{(3)}$  with  $n_2$  yields the following relation expression for the pump B-integral:

$$B_p = \frac{\tau_B}{\tau_{p0}} \frac{h_B}{h_{\text{OPA}}^2} \ln(G_s)^2 \quad (6.17)$$

where  $\tau_B$  is a characteristic time, given by

$$\tau_B = \frac{\omega_p n_i n_s n_p \epsilon_0 c |n_g(\omega_s) - n_g(\omega_p)| n_2}{8\omega_i \omega_s d_1^2}, \quad (6.18)$$

and the pump B-integral reduction factor is given by

$$h_B \equiv \frac{B_p}{B_{\text{norm}}} = \frac{\tan^{-1}(\xi_p)}{\xi_p^{\text{diff}}} \quad (6.19)$$

where  $\xi_p = L/(k_p w_{p0}^2)$ . Eq. (6.19) assumes that the resulting nonlinear phase only weakly perturbs the linear-optical diffraction of the pump, and hence that the total phase accumulated can be estimated by assuming that the Gaussian pump beam diffracts linearly. For a weakly-diffracting pump,  $h_B \approx 1$ .

The normalized coefficient  $h_{\text{OPA}}$  can be determined by numerical simulations of Eqs. (6.11), with results shown in Fig. 6.4(a). We limit these simulations to a parameter range corresponding to moderate signal gain of  $\approx 30$  dB, which is appropriate for amplification of a coherent seed pulse. Similar trends to those shown in Fig. 6.4

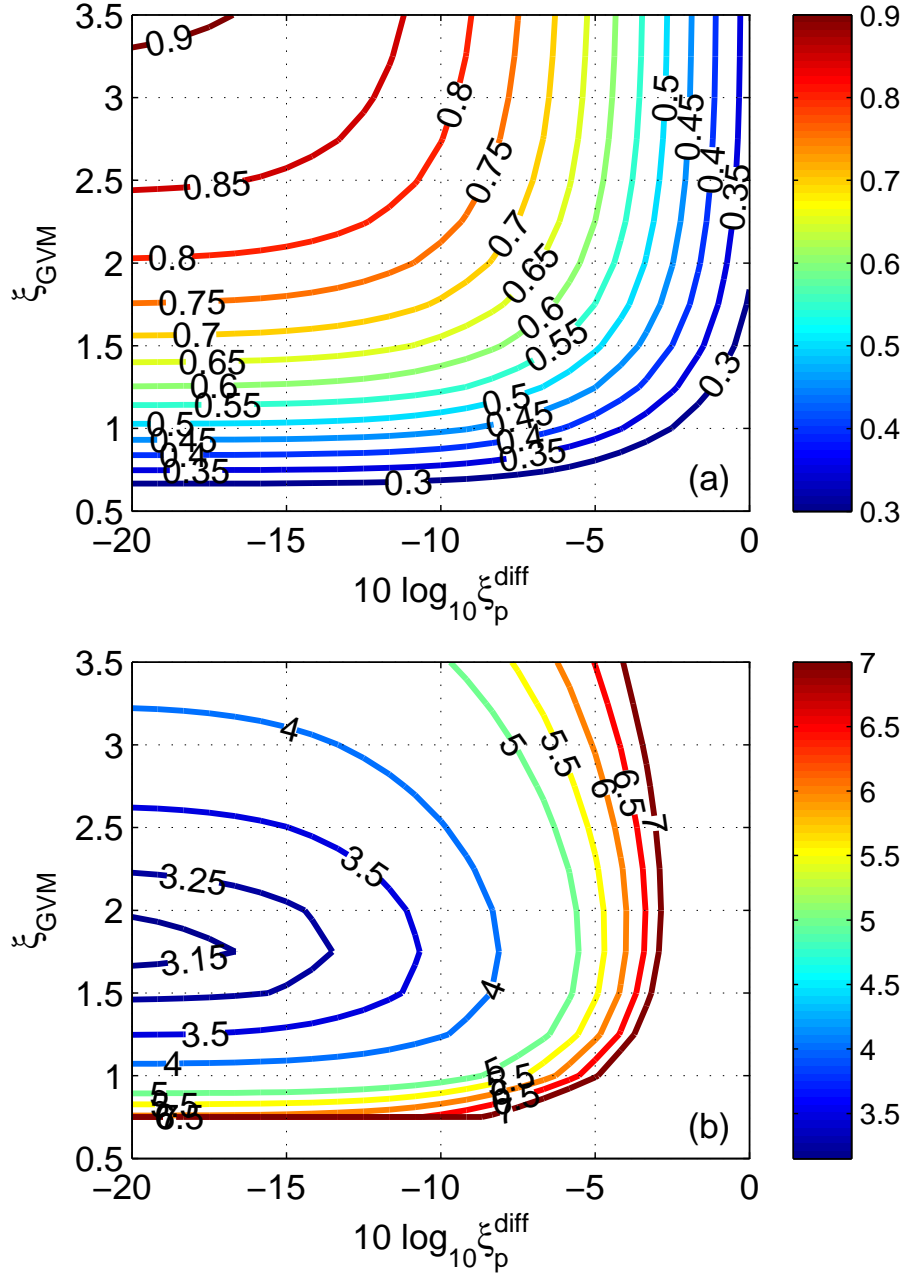


Figure 6.4: Normalized OPA parameters  $h_{\text{OPA}}$  [Eq. (6.16)] and  $h_B/h_{\text{OPA}}^2$  [Eq. (6.19)] as a function of normalized parameters  $\xi_{\text{GVM}} = L/L_{\text{GVM}}^{(\text{sp})}$  and  $\xi_p^{\text{diff}}$ , with  $\eta_{\text{norm}} = 30$  (a representative choice for amplifying a coherent seed pulse). (a)  $h_{\text{OPA}}$ , and (b)  $h_B/h_{\text{OPA}}^2$ , where  $h_B$  is given by Eq. (6.17).

occur with other values of  $\eta_{\text{norm}}$ . Based on Fig. 6.4(b), the optimal grating length is approximately  $L/L_{GVM}^{(is)} \approx 2$  (for the combination of pump and signal wavelengths being considered). The corresponding minimum of  $(h_B/h_{\text{OPA}}^2)$ , which appears in Eq. (6.17), is  $\pi$ . The remaining parameter  $\tau_B$  in Eq. (6.17) is a function only of known material and optical parameters, and can therefore be evaluated straightforwardly.

## 6.5 Design Example

To consider a specific design, we next evaluate the above expressions for GaAs, assuming a 1.95- $\mu\text{m}$  pump and a 2.5- $\mu\text{m}$  signal. The normalized gain factor satisfies  $\eta_{\text{norm}}/(\xi_p^{\text{diff}} U_p) \approx 3.6/\text{nJ}$ , which indicates that high gain is within reach of commercial few-nJ fiber lasers. However the corresponding normalized  $\chi^{(3)}$  coefficient satisfies  $B_{\text{norm}}\tau_{p0}/U_p \approx 0.26 \text{ ps/nJ}$ , and the characteristic time  $\tau_B \approx 18 \text{ fs}$ . Substituting this value of  $\tau_B$  into Eq. (6.17) and assuming  $h_B/h_{\text{OPA}}^2 = \pi$ , the B-integral can be approximated for GaAs and this particular choice of wavelengths as

$$B_p \approx \frac{0.3\text{ps}}{\tau_{p0}} \log_{10}(G_s)^2. \quad (6.20)$$

This expression shows that a large B integral will occur when using pump pulses of around 150-fs duration with sufficient energy to obtain high signal gain. In contrast, with 2-ps pump pulses, high gain ( $10^3$ - $10^4$ ) can be obtained with only a B integral of order  $\pi$ .

A realistic design criterion for achieving high output signal power is to obtain a high undepleted-pump signal-gain. Even if the pump is depleted, this criterion remains useful since an increase in signal gain will also correspond, in many cases, to an increase in pump depletion. Therefore, the above calculations are often sufficient for OPA design purposes. Based on these results, we next consider in Fig. 6.5 an example to demonstrate the advantages of using longer pump pulses.

We assume Gaussian pump pulses with a FWHM duration of 2 ps, a focused  $1/e^2$  free-space beam radius of 40  $\mu\text{m}$ , and energy up to 20 nJ (corresponding to 1.5 W at a 75 MHz repetition rate); the Gaussian signal has FWHM duration 100 fs, 40- $\mu\text{m}$

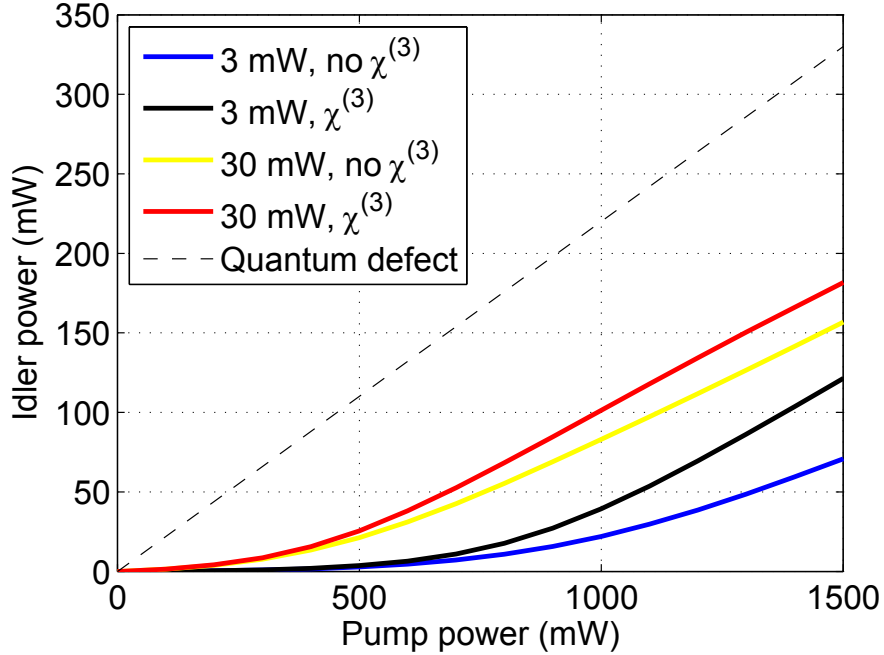


Figure 6.5: Design example with a long (2 ps) pump pulse, showing output idler power as a function of input pump power, for two different seed powers (40 and 400 pJ) with and without  $\chi^{(3)}$  effects (SPM and XPM). The dashed line represents the maximum idler power assuming full depletion of the pump.

beam radius, and with energy up to 0.4 nJ (30 mW). Fresnel losses are neglected. A 20-mm-long QPM grating is assumed, and the pulses are focused in the middle of the grating and overlapped temporally at 7 mm from the output end of the grating (this choice yields a slightly higher efficiency than the case with temporal overlap in the middle of the grating).

Fig. 6.5 shows the idler average power as a function of input average pump power for four cases (assuming a signal pulse energy of either 0.4-nJ or 40-pJ, with and without SPM and XPM effects included). Since a high signal parametric gain is supported and nonlinear phase shifts are kept within tolerable levels, a high idler output power can be obtained in each case, realistically in excess of 100 mW. The FWHM idler bandwidth is  $\approx 0.8$  THz, significantly narrower than the input signal bandwidth ( $\approx 4.4$  THz). This reduction in bandwidth occurs because the crystal length was

chosen to equal the pump-signal walk-off length; since the assumed pump pulse is of significantly longer duration than the signal, the corresponding acceptance bandwidths scale with the pump bandwidth and not the signal bandwidth. A narrower bandwidth is advantageous in many applications since it corresponds to a higher power spectral density.

## 6.6 Summary of This Chapter

In this chapter we have demonstrated tunable mid-IR generation through SFS of a Tm-doped-fiber laser system followed by DFG in a fan-out OP-GaAs crystal. This process was modeled numerically with high accuracy. Based on a simplified version of this model, we showed that high efficiencies can be obtained with longer pump pulses, typically several picosecond durations. With such designs, 6-12  $\mu\text{m}$  outputs in excess of 100 mW average power appear readily obtainable. In conclusion, DFG in OP-GaAs based on femtosecond Tm-fiber-lasers offers the potential for compact, broadly tunable, high-power mid-IR generation over the 5-18  $\mu\text{m}$  spectral region in a simple single-pass mixing geometry. Demonstration of such sources as well further theoretical and experimental investigation of fan-out angles and coherence properties are warranted to evaluate the suitability of these sources for different applications in the mid-IR.

# Chapter 7

## Theory of Efficient Optical Parametric Amplification using Chirped QPM Gratings

### 7.1 Introduction

In chapter 4, we discussed the importance of group velocity mismatch in ultra-broadband nonlinear interactions. With tightly confining waveguides, dispersion and hence GVM can be controlled through the dimensions of the structure. In weakly confining waveguides or in bulk interactions with collinear beams, group velocity matching occurs only at specific combinations of frequencies (for a given nonlinear medium). One way to support broad bandwidths in these cases is to use a chirped (aperiodic) QPM grating. There is a broad range of phase mismatches  $\Delta k$  associated with the pulse's spectral components, due to dispersion; we refer to this as the  $\Delta k$  bandwidth of the pulse. In order to amplify or convert each spectral component, the corresponding k-space bandwidth of the QPM grating must be greater than (or at least comparable to) that of the pulse. This broad grating k-space bandwidth can be obtained by using a chirped QPM grating, defined as one in which the grating k-vector is varied smoothly and monotonically over the length of the device. Since almost arbitrary QPM grating profiles can be designed and fabricated, the k-space

bandwidth of the grating can be matched to that of the pulse, allowing amplification over (almost) arbitrary optical bandwidths. As a result of the smooth QPM chirp profile, each spectral component is generated only around its phasematched region (the region where the local grating  $k$ -vector is close to the  $k$ -vector mismatch); this property allows a smooth and well-controlled amplitude and phase response.

There are a number of other ways to obtain a broad amplification bandwidth. For an interaction involving chirped pulses, it is possible to use an unchirped grating and high intensities, relying on pump saturation at the temporal (and hence spectral) center of the chirped pulse to amplify spectral wings [91]. Alternatively, in an unchirped grating or birefringently phasematched crystal, the Fourier bandwidth is inversely proportional to the length, so wide-bandwidth operation is always obtained with a very short crystal. In both of the above approaches, however, high-gain and broad-band OPA is difficult to achieve even with high-energy pulses since the material's damage threshold limits the maximum optical intensity. Another type of approach is to use noncollinear beams and satisfy noncollinear phasematching, thereby reducing the  $\Delta k$ -space bandwidth of the pulses. For green-laser-pumped parametric amplification of chirped pulses at Ti:Sapphire wavelengths, this noncollinear OPA (NOPA) method has been widely exploited, and supports ultra-wide bandwidths, due to the advantageous properties of beta-barium borate (BBO) for this application [92]. However, the added bandwidth from noncollinear operation comes at the cost of increased experimental complexity since noncollinear or even angularly dispersed pulses must be used. Furthermore, the idler waves generated in a NOPA scheme are not very useful (since each idler frequency is generated at a different angle), so the idler is usually discarded.

Another way to obtain group velocity matching in OPCPA is to operate at or near pump degeneracy [93]. In this configuration, the signal and idler are nearly the same, and hence even with a broad optical bandwidth, the corresponding range of phase mismatches can be narrow. However, operation at degeneracy constrains the choice of signal or pump wavelength. Laser sources with the required high peak powers are still scarce in the mid-IR, so operation at pump degeneracy is not always feasible. Based on the above discussion, we consider chirped QPM crystals, since they offer

the possibility of efficient and high-gain OPA, ultra-wide bandwidths, a convenient collinear experimental configuration, and obviate the need to constrain the pump and signal wavelengths.

Many of the essential properties of chirped-QPM devices can be understood by a coupled plane-wave model. Consider mixing process involving idler, signal and pump pulses. In the case of a narrow-band and undepleted pump, a negligibly-amplified signal, and zero input idler, there is a transfer function from the input signal wave to the generated idler wave [56]. This transfer function can be determined by evaluating Eq. (1.37a) in the frequency domain, with the assumption of a continuous-wave pump. Since we assume that the signal and pump envelopes are unperturbed by nonlinear mixing, the output idler is determined by integrating versus  $z$ ; it can be expressed in the form

$$\frac{\tilde{A}_i(L, \omega)}{\tilde{A}_s(0, \omega_p - \omega)^*} = -i \frac{\omega}{n(\omega)c} \tilde{d}_{\text{eff}} [\Delta k_0(\omega)], \quad (7.1)$$

where the right hand side is thus a transfer function relating the idler and signal spectra. In this equation, the frequency-dependent phase mismatch is given by  $\Delta k_0(\omega) = k(\omega_p) - k(\omega) - k(\omega_p - \omega)$ , and  $\tilde{d}_{\text{eff}}(k)$  is the spatial Fourier transform of the QPM grating:

$$\tilde{d}_{\text{eff}}(k) = \int_{-\infty}^{\infty} d_{\text{eff}}(z) e^{-ikz}. \quad (7.2)$$

We have extended the integration limits to  $\pm\infty$  by assuming that  $d_{\text{eff}}(z) = 0$  for  $z < 0$  and  $z > L$  (outside the crystal). Based on Eq. (7.1), a target amplitude and phase profile of the idler can be obtained by engineering the spatial frequency spectrum of the grating.

Chirped QPM gratings, in which the grating k-vector  $K_g(z)$  is varied monotonically through the length of the device, are of particular interest for this type of spatial frequency engineering. If  $\Delta k_0(\omega)$  is monotonic with respect to  $\omega$  over the frequency range of interest, then each spectral component is phasematched around a different

point  $z_{pm}(\omega)$  in the grating, which satisfies  $K_g[z_{pm}(\omega)] = \Delta k_0(\omega)$ . The idler is generated in the vicinity of this phasematching point, in the region within which the phase mismatch remains sufficiently small. The resulting spectral amplitude is thus determined by the local chirp rate around  $z_{pm}(\omega)$ . Similarly, each spectral component of the output idler can be viewed as having propagated at the signal group velocity  $v_g(\omega_p - \omega)$  before  $z_{pm}(\omega)$  and at the idler group velocity  $v_g(\omega)$  after  $z_{pm}(\omega)$ . Therefore, the idler's group delay spectrum is determined by the frequency-dependence of  $z_{pm}(\omega)$ . Similar results turn out to apply even to high-gain devices. These ideas were demonstrated experimentally in [94, 95] and theoretically in [51, 96].

Three-wave interactions in chirped QPM gratings have also been shown to exhibit minimal back-conversion [52, 97]. In phasematched media or periodic QPM gratings, the maximum pump depletion is usually reached after the fields propagate a certain distance which depends on the intensity of the input waves and on the phase mismatch [13]; after this distance, energy is back-converted to the pump. In contrast, this back-conversion can be avoided in chirped QPM gratings. For example, in the cases of SFG and DFG, the interaction between the idler and pump waves (assuming a strong and unamplified signal wave) exhibits adiabatic following, provided that the grating is long enough and the signal is sufficiently intense. In this adiabatic following process, the three waves closely follow a local plane-wave nonlinear eigenmode [97, 98, 99, 100, 101], which evolves smoothly with the QPM chirp. These eigenmodes are sets of amplitudes and phases of the three waves which, in the absence of a QPM chirp, would propagate through the crystal without any energy being transferred between the waves (i.e. only the phase of the waves changes during propagation, not their amplitudes). Up until recently [52], the nonlinear nature of the  $\chi^{(2)}$  coupled wave equations had received less attention when analyzing chirped QPM gratings, with the interaction being linearized by the assumption that at least one of the three waves remains unchanged during propagation. This assumption is often inappropriate for OPA schemes, since depletion of the pump is a key consideration.

In this chapter, we investigate the behavior of chirped QPM interactions for which the amplitudes of all three waves change significantly during propagation, and we give a generalized description of the adiabatic following process mentioned above. We find

that useful properties from the linear regime can nonetheless be maintained due to the localized conversion of each spectral component. Furthermore, the conversion efficiency of the pump monotonically approaches 100% with increasing pump intensity, even for high gain OPA. We discuss the factors affecting this conversion efficiency, as well as the nonlinear phase accumulation, which places constraints on the maximum pump intensity that can be used in a practical OPA device.

## 7.2 Coupled Wave Equations

We consider plane-, continuous-wave interactions involving incident signal and pump waves and a generated idler wave. This assumption is a useful approximation for understanding the amplification of individual spectral components in an optical parametric chirped pulse amplification (OPCPA) system employing wide beams and highly chirped signal pulses. The limits to the validity of this simplification are discussed in chapter 8. The coupled wave equations given in Eqs. (1.37) describe the evolution of the idler, signal, and pump in the presence of the  $\chi^{(2)}$  nonlinearity. As discussed in section 1.5.2, in order to model first-order ( $m = 1$ ) QPM interactions, the phase factors  $\Delta k_0 z$  appearing in Eqs. (1.37) are replaced with the first-order grating phase,

$$\phi_{\Delta k} \equiv \int_0^z \Delta k_1(z') dz', \quad (7.3)$$

where  $\Delta k_1 = k_p - k_s - k_i - K_g(z)$  [Eq. (1.38)] and the appropriate Fourier coefficient of the grating is given by  $\bar{d}_1$  [Eq. (1.26)].

In Eqs. (6.4), we defined normalized envelopes in order to help analyze the OPA solutions supported by the coupled-wave equations. In this chapter we consider cases where all three waves can vary significantly, so it is useful to take a slightly different approach to normalization. From Eqs. (1.37), there is a rate of coupling between the signal and idler due to the pump, given by  $\gamma_p(z) = g(z)\gamma_{p0}(z)$ , where  $\gamma_{p0}(z)$  is given

by

$$\gamma_{p0}(z) = \sqrt{\frac{\omega_i \omega_s}{n_i n_s c^2}} \left| \frac{2d_{\text{eff}}}{\pi} A_p(z) \right|. \quad (7.4)$$

and where the gain reduction factor  $g(z)$  is related to the QPM duty cycle  $D(z)$  by

$$g(z) = \sin(\pi D(z)). \quad (7.5)$$

Similarly, there is a rate of coupling between the idler and pump, given by  $\gamma_s(z) = g(z)\gamma_{s0}(z)$ , where

$$\gamma_{s0}(z) = \sqrt{\frac{\omega_i \omega_p}{n_i n_p c^2}} \left| \frac{2d_{\text{eff}}}{\pi} A_s(z) \right|. \quad (7.6)$$

If the signal or the pump remains unchanged during propagation due to a sufficiently weak nonlinear interaction, then the behavior of the remaining envelopes is determined entirely by either  $\gamma_s$  or  $\gamma_p$ , respectively. When all the envelopes are  $z$ -dependent, it is appropriate to define some coupling rate  $\gamma_{sp}$  which scales with both  $\gamma_s$  and  $\gamma_p$ . To choose the form of  $\gamma_{sp}$ , note that  $[\gamma_{s0}^2 + \gamma_{p0}^2]$  is proportional to the sum of the signal and pump photon fluxes, which can be seen by expressing  $\gamma_{s0}$  and  $\gamma_{p0}$  in terms of the envelopes  $a_j$  defined in Eq. (6.4), since  $|a_j|^2$  is proportional to the photon flux of wave  $j$ . The Manley-Rowe relations [102], which can be derived directly from the coupled wave equations, imply that  $\gamma_{s0}(z)^2 + \gamma_{p0}(z)^2$  is conserved (one photon is gained by the signal for each one lost by the pump). Based on the above considerations, we define  $\gamma_{sp}$  according to

$$\gamma_{sp} = \sqrt{\gamma_{s0}^2 + \gamma_{p0}^2}. \quad (7.7)$$

Note that, for the plane-wave interactions considered here,  $\gamma_{sp}$  is independent of  $z$ , and can be used to define a normalized propagation coordinate  $\zeta = \gamma_{sp}z$ . Similarly, a normalized phase mismatch can be defined as  $\delta k = \Delta k / \gamma_{sp}$ . As discussed in subsection 6.4.1, when the fields are scaled such that their square magnitude is proportional to

photon flux, the coupling coefficient (or rate of coupling) appearing in each coupled-wave equation has the same magnitude. If we also multiply each envelope by the factor  $\exp(-i\phi_{\Delta k}(z))$  [Eq. (7.3)], then the coupling coefficient also has the same phase in each of the three equations, and hence the three coupling coefficients are identical. For these reasons, we define envelopes  $b_j$  which satisfy

$$A_j = \left( \sqrt{\frac{\omega_j}{n_j}} \frac{\gamma_{sp}}{\kappa} e^{-i\phi_{\Delta k}} \right) b_j \quad (7.8)$$

where the field coupling coefficient  $\kappa$  is given by

$$\kappa = \sqrt{\frac{\omega_i \omega_s \omega_p}{n_i n_s n_p c^2}} \left| \frac{2d_{\text{eff}}}{\pi} \right|. \quad (7.9)$$

With the normalization given in Eq. (7.8), these envelopes satisfy

$$|b_s|^2 + |b_p|^2 = 1 \quad (7.10)$$

at all positions and for all input conditions. Assuming first-order QPM, and substituting the normalized coordinate  $\zeta$  and normalized fields  $b_j$  into Eqs. (1.37) results in the following set of normalized coupled wave equations

$$\begin{aligned} \frac{db_i}{d\zeta} - i\delta k(\zeta)b_i &= -ig(\zeta)b_s^*b_p \\ \frac{db_s}{d\zeta} - i\delta k(\zeta)b_s &= -ig(\zeta)b_i^*b_p \\ \frac{db_p}{d\zeta} - i\delta k(\zeta)b_p &= -ig(\zeta)b_ib_s, \end{aligned} \quad (7.11)$$

where  $0 \leq g(\zeta) \leq 1$  can be chosen, via the QPM duty cycle, to help apodize the grating [51, 103]; apodization is discussed in more detail later in this section, and also in section 8.3.3. To characterize the solutions of Eqs. (7.11), we denote the ratio of signal and pump input photon fluxes as  $\rho = |b_s(0)/b_p(0)|^2$  and the pump depletion at  $z = L$  as  $\eta = |b_p(L)/b_p(0)|^2$ , where  $L$  is the length of the grating; the photon conversion efficiency from pump to signal is then  $(1 - \eta)$ . Minor changes to the above

definitions could be performed for SFG cases, i.e. for cases with an input idler but no input pump.

For chirped QPM gratings, the interaction between the three waves is most simply illustrated by choosing a linear chirp profile of the form  $K_g(z) = K_{g0} - \Delta k'z$ , where  $\Delta k'$  is the chirp rate ( $\Delta k' = d\Delta k/dz = -dK_g/dz$ ) and  $K_{g0}$  is a constant. For OPA in the undepleted-pump limit and with a constant QPM duty cycle of 50%, Eqs. (7.11) can be solved (see section 7.3 and Ref. [51]) to show that the power gain for the signal is given by

$$G \approx \exp(2\pi\lambda_{R,p}) \quad (7.12)$$

where the gain factor  $\lambda_{R,p} \equiv \gamma_{p0}^2/|\Delta k'|$  [51].  $\lambda_{R,p}$  can be interpreted as the product of the gain rate  $2\gamma_{p0}$  times an effective gain length  $\pi\gamma_{p0}/|\Delta k'|$ . A more general interpretation is provided by WKB analysis (see section 7.3). For SFG in the unamplified-signal limit (i.e. with a strong input signal, a weak input pump, and no input idler), the pump depletion is given by

$$\eta \equiv |b_p(L)/b_p(0)|^2 \approx \exp(-2\pi\lambda_{R,s}), \quad (7.13)$$

where the pump depletion factor  $\lambda_{R,s} \equiv \gamma_{s0}^2/|\Delta k'|$  [97]. These results apply for sufficiently chirped QPM gratings (i.e. with chirp rates which are monotonic and not too large, and which correspond to a large initial and final phase mismatch; these sufficiency criteria can be quantified with the results discussed in this chapter). For other interactions, we can define a general coupling factor as

$$\begin{aligned} \lambda_R &= \lambda_{R,s} + \lambda_{R,p} \\ &= \lambda_{R,p}(1 + \rho). \end{aligned} \quad (7.14)$$

When  $\rho \ll 1$ ,  $\lambda_R \approx \lambda_{R,p}$ ; when  $\rho \gg 1$ ,  $\lambda_R \approx \lambda_{R,s}$ .

When all of the envelopes evolve significantly during propagation, Eqs. (7.11) are in general nonlinear (although linearization is still sometimes possible, as discussed in appendix 7.8.1). To help understand this regime in the context of chirped QPM

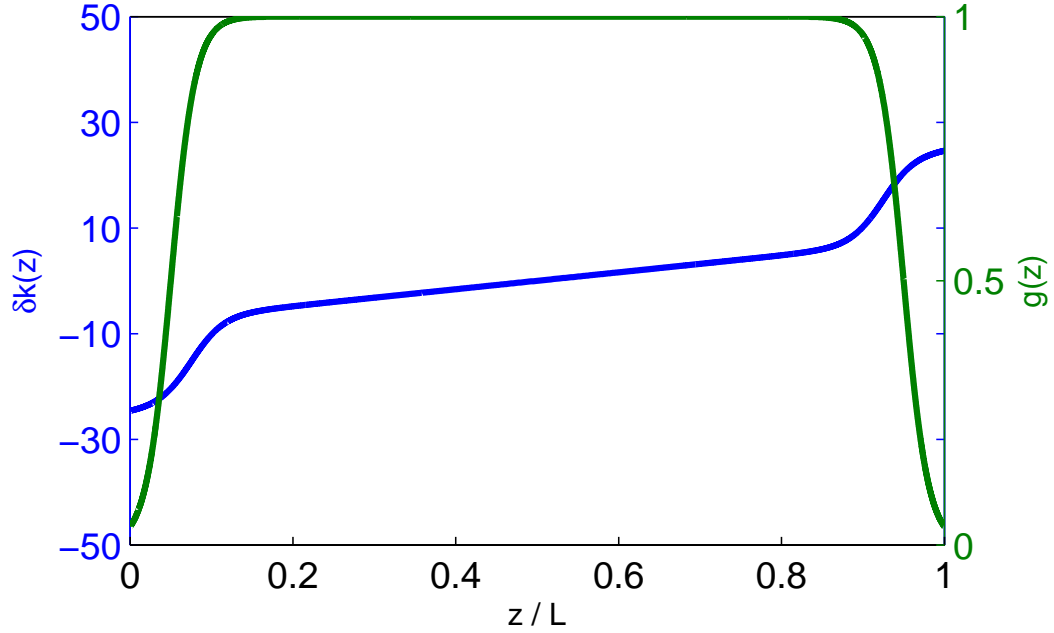


Figure 7.1: Spatial profile of the phase mismatch for a particular spectral component of the signal in a chirped QPM grating. For this example, phasematching occurs at  $z = L/2$ , i.e. in the middle of the device. The phase mismatch is nominally linear with respect to position. To apodize the gain at the ends of the grating, the phase mismatch is rapidly but smoothly increased, and the duty cycle is modified such that the first-order QPM coupling coefficient  $g(z)$  is evolved smoothly towards zero.

gratings, we consider OPA in the specific case of the example grating shown in Fig. 7.2. In this grating, approximately the first and last 7.5% of the grating is used for apodization [51], in order to ensure that  $|g/\delta k| \ll 1$  at  $z = 0$  and  $z = L$  and hence that the grating is highly chirped. The grating chirp profile  $K_g(z)$  is chosen such that

$$\begin{aligned} \Delta k(z) &= \Delta k'(z - L/2) + \text{sgn}(\Delta k') \\ &\times \left\{ \frac{K_s}{2} \left[ 1 - \tanh\left(\frac{z - z_{k1}}{L_{k1}}\right) \right] - \frac{K_e}{2} \left[ 1 - \tanh\left(\frac{L - z_{k2} - z}{L_{k2}}\right) \right] \right\}, \end{aligned} \quad (7.15)$$

and the grating duty cycle is chosen such that

$$g(z) = \frac{1}{4} \left[ 1 + \tanh\left(\frac{z - z_{g1}}{L_{g1}}\right) \right] \left[ 1 + \tanh\left(\frac{z_{g2} - z}{L_{g2}}\right) \right]. \quad (7.16)$$

The apodization parameters are given by  $z_{k1}/L = 0.075$ ,  $z_{k2}/L = 0.075$ ,  $L_{k1} = 0.04$ ,  $L_{k2} = 0.04$ ,  $z_{g1}/L = 0.05$ ,  $z_{g2}/L = 0.05$ ,  $L_{g1}/L = 0.03$ ,  $L_{g2}/L = 0.03$ ,  $K_s/\gamma_{sp} = 25$ ,  $K_e/\gamma_{sp} = 25$ . These parameters yield a smooth profile with small values of  $|g/\delta k|$  at the edges of the grating, and hence a weak coupling between the fields. These are typical parameters; their precise values are not critical. Apodization, which is facilitated in Fig. 7.1 by the rapid increase in  $|\Delta k(z)|$  and decrease in  $g(z)$  near the edges of the grating, is needed to avoid a ripple in the amplitude and phase of the output spectrum. Apodization is discussed in more detail in section 8.3.3. In a real grating, the coupling between the fields cannot be made arbitrarily small via changes in the duty cycle or period of the QPM grating, since the other QPM orders ( $m \neq 1$ ) eventually dominate, and therefore limit how well-apodized the interaction can be made. In the first-order QPM approximation assumed here, it is possible to obtain essentially perfect apodization for the purposes of numerical simulations.

Solutions for the three-wave interactions obtained by solving Eqs. (7.11) for several different initial conditions for the chirped QPM grating shown in Fig. 7.1 are shown in Fig. 7.2. In the different cases shown, the input photon flux ratio  $\rho = |b_s(0)/b_p(0)|^2$  is varied, assuming  $\lambda_{R,p} = 2$  in each case. The three-wave interaction is phasematched at  $z = z_{pm}$ , i.e. where  $\Delta k(z) = 0$ . In the absence of any pump depletion, amplification occurs over the region  $-1 < (z - z_{pm})/L_{deph} < 1$ , where the dephasing length is given by [51]

$$L_{deph} \equiv \frac{2\gamma_{p0}}{|\Delta k'|} \quad (7.17)$$

The  $\rho = 10^{-8}$  case of Fig. 7.2(a) shows that the pump is down-converted to the signal and idler within this amplification region. Fig. 7.2(b) shows how the conversion efficiency increases monotonically with the signal intensity at the input of the chirped QPM grating, which would not be the case in a uniformly phasematched device. Outside the amplification region the fields exhibit oscillatory behavior, with low net energy transfer.

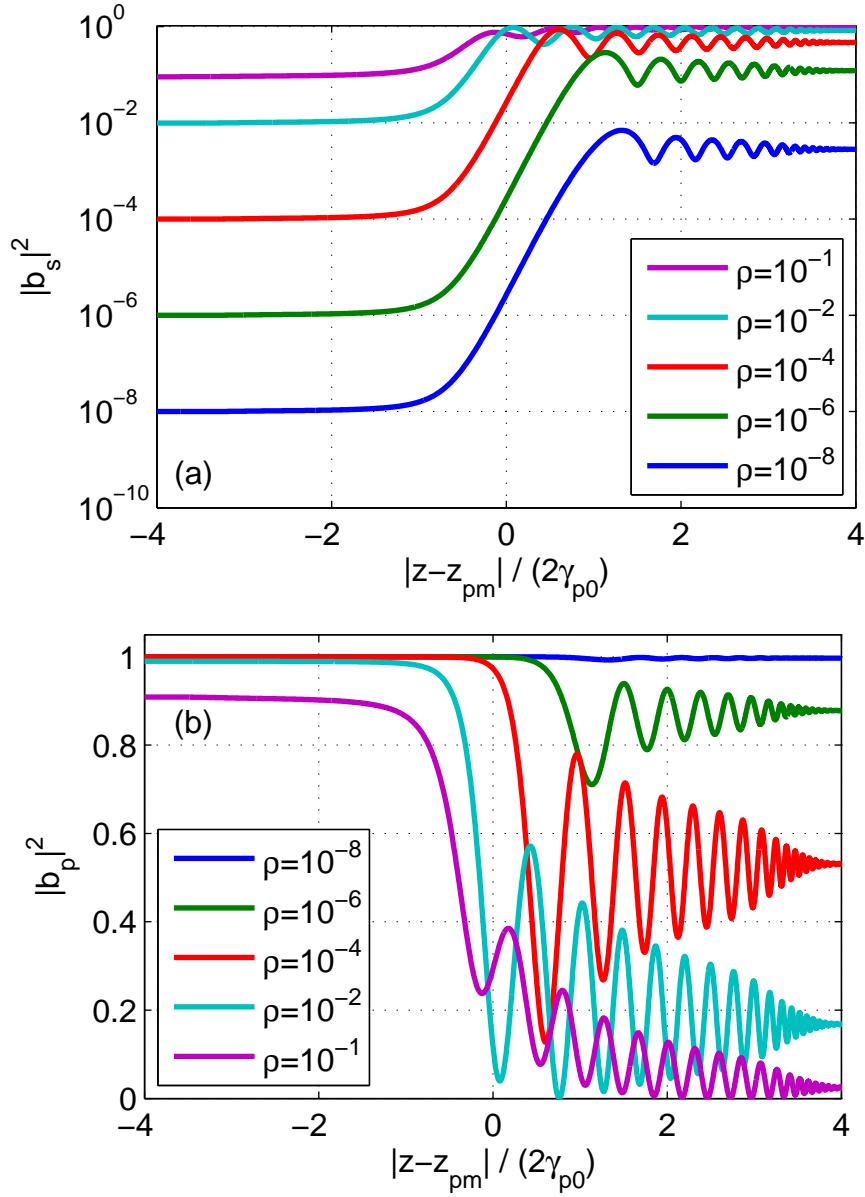


Figure 7.2: Signal gain and pump depletion in an apodized QPM grating, with undepleted-pump gain set by  $\lambda_{R,p} = 2$  and phasematched point  $z_{pm} = L/2$ , at increasing signal-pump photon flux ratio  $\rho$ . (a) Log-scale, illustrating exponential signal gain, (b) linear scale, illustrating pump depletion

### 7.3 Signal Amplification

The gain of the signal can be found by approximate solutions to Eqs. (7.11). If pump depletion is neglected ( $\rho \rightarrow 0$ ), then coupling between the signal and idler can be written as a position-dependent linear system. Furthermore, if we define signal and idler envelopes slightly modified from the  $b_j$  of Eq. (7.8), as

$$A_j = \left( \sqrt{\frac{\omega_j}{n_j}} \frac{\gamma_{sp}}{\kappa} e^{-i\phi_{\Delta k}/2} \right) a_j \quad (7.18)$$

and a pump envelope as  $a_p = A_p$ , then the evolution equation for the signal can be put into the following standard form [51]:

$$\frac{d^2 a_s}{d\zeta^2} + Q(\zeta) a_s = 0, \quad (7.19)$$

where the “potential”  $Q$  is given by

$$Q = -g^2 + \frac{1}{2} \frac{d}{d\zeta} \left( \frac{g'}{g} \right) - \frac{i\delta k'}{2} - \frac{1}{4} \left( \frac{g'}{g} - i\delta k \right)^2. \quad (7.20)$$

Equation (7.19) has a familiar form and can be solved asymptotically using the WKB method [104]. Based on the form of  $Q$  and assuming a constant value of  $g$ , there are two “turning points” where  $\text{Re}[Q] = 0$  ( $(\delta k/2)^2 = g^2$ ). At these points, the signal gain rate is approximately zero. The existence of such turning points indicates that there are three qualitatively different regions:  $\delta k < -2g$ ,  $-2g < \delta k < 2g$ , and  $\delta k > 2g$ . Inside these regions and away from the tuning points, the solutions to Eq. (7.19) can be approximated by the WKB solutions. The method of phase integrals can then be used to connect the coefficients of the WKB solutions in the three regions and thereby arrive at a solution which is accurate at all positions [51, 104]. The analysis for the present case was given in detail in Ref. [51]. Note that the WKB method actually involves the complex-valued turning points which satisfy  $Q = 0$ , not just the real-valued points where  $\text{Re}[Q] = 0$ . Nonetheless, an important result shown in Ref.

[51] is the following approximate formula for the signal field gain  $G_s$ :

$$G_s \approx \exp \left[ \int_{\zeta_{tp,1}}^{\zeta_{tp,2}} \sqrt{g^2 - (\delta k/2)^2} d\zeta \right], \quad (7.21)$$

where  $\zeta_{tp,j}$  denotes turning point  $\zeta_{tp,j}$ : these points satisfy  $\text{Re}[Q(\zeta_{tp,j})] = 0$ . Eq. (7.21) corresponds to Eq. (16) of Ref. [51]. For the specific case of a linear chirp, Eq. (7.21) yields Eq. (7.12).

A useful inequality which indicates the limits on the validity of the WKB solutions is [104]

$$\left| \frac{dQ}{d\zeta} \frac{1}{Q^{3/2}} \right| \ll 1. \quad (7.22)$$

We will use this inequality in chapter 8 to define optimal apodization profiles. The WKB approach is useful when the pump is undepleted, but is insufficient for more general cases involving both non-negligible signal gain and pump depletion, since the coupled wave equations are then nonlinear and therefore no longer have the standard WKB form. In particular, WKB analysis does not directly explain the monotonically-increasing pump depletion shown in Fig. 7.2(b). We consider this behavior in the next sections.

## 7.4 Adiabatic Following Solutions

Numerical solutions of Eqs. (7.11) show that the conversion efficiency at the output of a sufficiently well-apodized grating monotonically approaches 100% with respect to both  $\lambda_{R,p}$  and  $\rho$  (i.e. with respect to both the signal and pump intensity), and hence back-conversion to the pump is suppressed; this is in contrast to the usual oscillatory behavior exhibited by the Jacobi Elliptic function solutions to three-wave mixing processes in uniform nonlinear media [13]. The suppression of back-conversion can be understood as the adiabatic following of local nonlinear eigenmodes of the three-wave mixing process; these eigenmodes evolve if the local period of the QPM grating changes along the length of the device. Adiabatic following is exhibited by a wide

variety of physical systems, typically when a system begins in a certain instantaneous eigenstate, and that state is changed sufficiently slowly by some perturbation [97, 105, 106]

The nonlinear eigenmodes are solutions of Eqs. (7.11) for which, in the case of constant  $\delta k$ , propagation corresponds only to phase shifts of the three waves, with the magnitude of each wave remaining constant. Up to an overall phase, there are two such eigenmodes for a given value of  $\delta k/(2g)$  and set of input conditions. If  $|\delta k(0)/(2g(0))| \gg 1$  in a chirped grating, the input fields (with  $b_s(0)$  and  $b_p(0)$  finite, but  $b_i(0) = 0$ ) are close to one of these eigenmodes. Provided that  $\delta k/g$  is monotonic in  $z$ , then as  $\delta k$  (or  $g$ ) is varied, this eigenmode is swept from one corresponding to no photons at the idler frequency (input, with  $\pm[\delta k(0)/g(0)] \gg 1$ ) to one with no photons at the pump frequency (output, with  $\mp[\delta k(L)/g(L)] \gg 1$ ); the fields follow this eigenmode provided the chirp rate is slow enough. The eigenmodes depend on primarily on the parameter  $\nu$ , defined as

$$\nu \equiv \frac{\delta k}{2g}. \quad (7.23)$$

The three-wave adiabatic following process can be visualized using the geometrical description of  $\chi^{(2)}$  interactions given in Ref. [16]. In this description, a set of three real-valued reduced field variables  $X$ ,  $Y$ , and  $Z$  are introduced which are related to the complex electric-field envelopes. In [16], general QPM interactions were considered; in this section, we modify the analysis slightly to consider first-order QPM interactions. Here we briefly recapitulate the formulation given in more detail in [16], and give the modifications required for first-order QPM. The reduced field variables  $X$ ,  $Y$ , and  $Z$  are given by

$$\begin{aligned} X + iY &= b_i b_s b_p^* \\ Z &= |b_p|^2. \end{aligned} \quad (7.24)$$

The phase of  $X + iY$  specifies the relative phase between the envelopes and their driving polarizations, and hence the direction of energy transfer. The remaining

variable  $Z$  specifies the pump photon flux. These variables can be treated as specifying a “position” vector  $\mathbf{W}$  in an abstract 3-space, defined as

$$\mathbf{W} = [X, Y, Z]^T. \quad (7.25)$$

During propagation,  $\mathbf{W}$  evolves according to the evolving complex field amplitudes, but is constrained to lie on a surface whose shape is determined by the input conditions. This surface is given by the implicit relation  $\varphi = 0$ , where

$$\varphi = X^2 + Y^2 - Z(Z - K_{ip})(Z - K_{sp}), \quad (7.26)$$

and where the constants  $K_{ip}$  and  $K_{sp}$  are Manley-Rowe invariants, given by

$$K_{jp} = |b_j|^2 + |b_p|^2 \quad (7.27)$$

for  $j = i$  and  $j = s$ . With the envelope definitions used in this chapter [Eq. (7.8)],  $K_{sp} = 1$  and  $K_{ip} = |b_p(0)|^2$ . For cases with an input signal that is much larger than the pump ( $\rho \gg 1$ , and hence  $0 \leq Z \leq K_{ip} \ll 1$ ),  $\varphi = 0$  is a sphere; this case corresponds to the adiabatic following processes discussed in Refs. [97, 107] and is analogous to adiabatic following in two-level quantum systems [105]. For other input conditions ( $\rho \not\gg 1$ ), the conserved surface  $\varphi = 0$  is not spherical, but remains closed and convex [16]; as a result, adiabatic following can still occur (as discussed below).

The evolution of  $W$  is given by

$$\frac{d\mathbf{W}}{d\zeta} = \nabla H \times \nabla \varphi, \quad (7.28)$$

where  $\nabla = [\partial/\partial X, \partial/\partial Y, \partial/\partial Z]^T$ , and where the local Hamiltonian  $H$ , which is discussed in more detail in Ref. [16], can be expressed as

$$H = gX + \frac{\delta k}{2} (Z - (K_{ip} + K_{sp})). \quad (7.29)$$

Eq. (7.28) implies that  $\mathbf{W}$  is constrained to remain on the implicit surface  $\varphi = 0$ , since

the “force” acting on  $\mathbf{W}$  is perpendicular to the local surface normal  $\nabla\varphi$ . Eq. (7.28) also reveals the existence of the local nonlinear eigenmodes discussed above. These eigenmodes, which we denote as  $\mathbf{W}_m$ , satisfy  $d\mathbf{W}/d\zeta = 0$ , and hence correspond to the two points on  $\varphi = 0$  for which  $\nabla H$  is normal to the surface (the points where  $\nabla\varphi$  is in the same direction as  $\pm\nabla H$ ; there are two and only two such points because  $\varphi = 0$  is closed and convex).

The geometrical approach of [16], a key result of which is Eq. (7.28), greatly simplifies the interpretation of most three-wave mixing problems. For example, during propagation in a uniformly-phasematched medium,  $\mathbf{W}$  is constrained to lie the intersection between a plane ( $H = \text{constant}$ ) and a convex surface ( $\varphi = 0$ ), i.e. on a ring. The fields travel around this ring indefinitely; the distance required to fully traverse the ring is the period associated with the Jacobi-elliptic analytical solutions of the three-wave mixing problem, derived in [13]. The complicated structure of these analytical solutions can thus be replaced with a very simple geometrical construction. An example for a uniformly-phasematched device is shown in Fig. (7.3). In this example, the black arrow points in the direction of  $\nabla H$ ; its location has been chosen so that the point where it touches the conserved surface  $\varphi = 0$  corresponds to a nonlinear eigenmode (as described in the figure caption). In this unchirped example, this eigenmode is fixed (and hence represents a true eigenmode of the three-wave mixing problem). In a chirped device, the direction of  $\nabla H$ , and hence the local nonlinear eigenmode  $\mathbf{W}_m$ , would be swept from the top to the bottom of  $\varphi = 0$  as  $\nu$  is swept from  $\pm\nu \gg 1$  to  $\mp\nu \gg 1$ .

Since the nonlinear eigenmodes  $\mathbf{W}_m = \begin{bmatrix} X_m & 0 & Z_m \end{bmatrix}$  are points where  $\nabla H \times \nabla\varphi = 0$ , they can be found, for any given value of  $\nu$ , by solving the equations

$$\varphi = 0 \tag{7.30a}$$

$$\frac{\partial\varphi}{\partial Z} = \nu \frac{\partial\varphi}{\partial X} \tag{7.30b}$$

$$Y = 0. \tag{7.30c}$$

As stated above, in the case of SFG or DFG with a strong and unamplified signal wave, the coupled-wave equations are linear in the idler and pump, and  $\varphi = 0$  is a

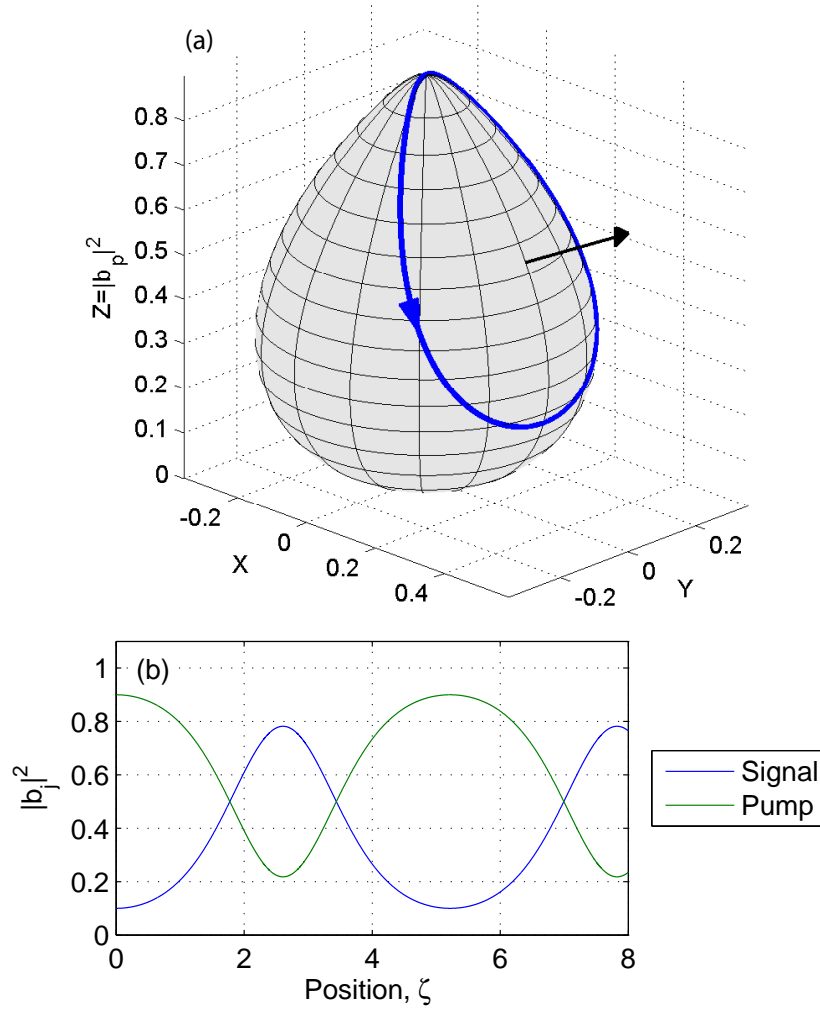


Figure 7.3: (a) Solution to an example three-wave-mixing problem, visualized with the geometric description of [16] [and Eq. (7.28) in particular]. The parameters for this example are  $K_{ip} = |b_p(0)|^2 = 0.9$ ,  $g = 1$  (50% duty cycle), and  $\delta k = g = 1$ . The surface is  $\varphi = 0$ , and the blue line represents the trajectory of  $\mathbf{W}$ . Since  $\delta k$  and  $g$  are both constant in this example, the blue line lies on a plane  $H = \text{constant}$ .  $\mathbf{W}$  is initially at the top of the surface ( $Z \equiv |b_p|^2 = K_{ip} = 0.9$ ), and the direction of  $\mathbf{W}$  (with increasing  $\zeta$ ) is shown by the blue arrow. In (b), photon fluxes  $|b_j|^2$  are shown for comparison. In (a), the direction of  $\nabla H$  is also shown (black arrow). The point where this arrow touches the surface is a nonlinear eigenmode associated with the chosen parameters (i.e. a point where  $\nabla H$  is in the direction of the surface normal to  $\varphi = 0$ ,  $\nabla\varphi$ ). Since  $\nu$  is constant in this example, this nonlinear eigenmode is fixed, and the solutions for input conditions not corresponding to the eigenmode orbit around it on the surface.

sphere. However, because  $\varphi = 0$  is convex for all input conditions, the eigenmodes and envelopes behave in a similar way to these linear cases even when the coupled-wave system is nonlinear: the relevant nonlinear eigenmode initially corresponds to low idler energy, and is swept smoothly (by changing  $g$  and  $\delta k$ ) to one corresponding to low pump energy. If the sweep rate is slow enough (conditions for which are discussed in section 7.5 and appendix 7.8), the fields follow this eigenmode, and as a result most of the pump energy is transferred to the signal and idler waves.

To illustrate this behavior, we show in Fig. 7.4 the trajectory of the reduced field vector  $\mathbf{W}$  (solid lines) and the local nonlinear eigenmode  $\mathbf{W}_m$  (dashed lines) for four example cases, with parameters (b)  $\lambda_{R,s} = 1$  and  $K_{ip} = 10^{-3}$ , (c)  $\lambda_{R,s} = 2$  and  $K_{ip} = 10^{-3}$ , (e)  $\lambda_{R,p} = 2$  and  $K_{ip} = 0.9$ , and (f)  $\lambda_{R,p} = 10$  and  $K_{ip} = 0.9$ . The structure of  $\varphi = 0$  is shown in Figs. 7.4(a) and (d) for the input conditions  $K_{ip} = 10^{-3}$  (0.1% of input photons in the pump, 99.9% in the signal) and  $K_{ip} = 0.9$  (90% of input photons in the pump, 10% in the signal), respectively.

For both choices of  $K_{ip}$ , the adiabatic following process requires a large coupling factor  $\lambda_R$ ; for smaller  $\lambda_R$ , a ripple in the components of  $\mathbf{W}$  [solid lines in Figs. 7.4(b), (c), (e), and (f)] around  $\mathbf{W}_m$  (dashed lines) is introduced. Such ripples occur when the chirp rate is too rapid for the fields to follow the local eigenmode; they are thus indications of non-adiabaticity. For the strong-signal case ( $K_{ip} = 10^{-3}$ ), the amplitude of these ripples scales as  $\exp(-2\pi\lambda_{R,s})$ ; for the strong-pump case ( $K_{ip} = 0.9$ ) the behavior is more complicated, but a faster-than-polynomial decay of the ripple amplitude with respect to  $\lambda_{R,p}$  is still obtained, as discussed in appendix 7.8. At larger values of the coupling factors, the fields  $\mathbf{W}$  can be seen in Fig. 7.4 to follow the local eigenmode  $\mathbf{W}_m$  more closely (the ripple amplitude is reduced). The noncircularity of  $\varphi = 0$  for the strong-pump case [Fig. 7.4(d)] means that a large coupling factor is required to achieve a (nearly) adiabatic interaction.

A ripple in  $\mathbf{W}(\zeta)$  also occurs if the fields are not launched properly into the input eigenmode, i.e. if  $|\nu(\zeta = 0)|$  is not large enough; unless  $|\nu(\zeta = 0)|^{-1} = 0$ , the input conditions ( $|b_i| = 0$ ) are different from that of the input eigenmode ( $|b_i| \neq 0$ ). These ripples are not noticeable in Fig. 7.4 because the apodization profile [see Eqs. (7.15) and (7.16)] ensures that  $|\nu|$  is very large at the edges of the grating.

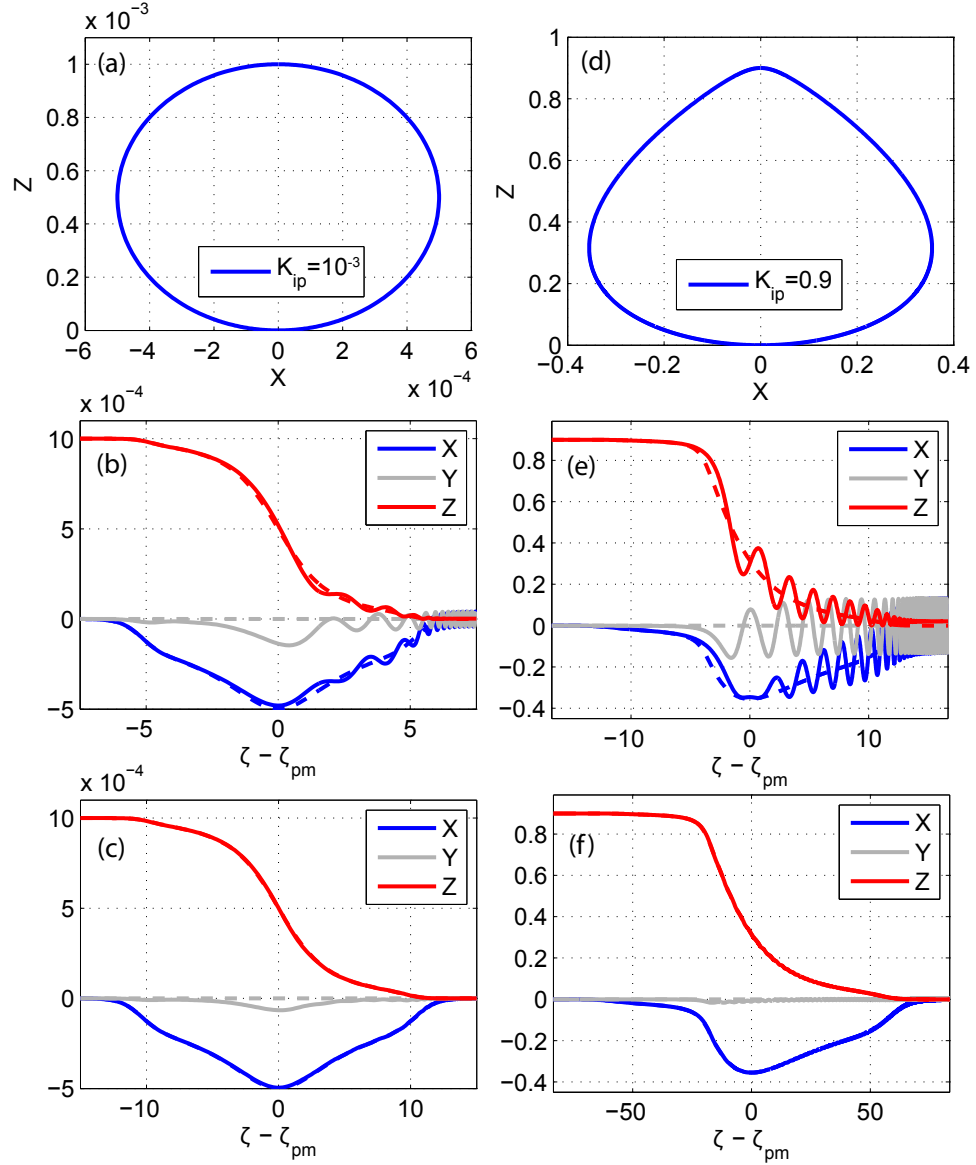


Figure 7.4: Propagation of field vector  $\mathbf{W}$  and eigenmode vector  $\mathbf{W}_m$  [the solid and dashed lines, respectively, in (b), (c), (e), and (f)], illustrating the adiabatic following process arising from Eq. (7.28). The left column is for  $K_{ip} \equiv |b_p(0)|^2 = 10^{-3}$  (strong input signal), while the right column is for  $K_{ip} = 0.9$  (strong input pump). The first row [Figs. (a) and (d)] are cuts through the surface  $\varphi = 0$  in the plane  $Y = 0$ , corresponding to these two input conditions. The second and third rows show the evolution of the field vectors under these input conditions, for two different coupling factors:  $\lambda_{R,s} = (1, 2)$  for Figs. (b) and (c), respectively, and  $\lambda_{R,p} = (2, 10)$  for Figs (e) and (f), respectively.

## 7.5 Adiabaticity Constraint

Adiabatic following solutions are obtained for all input conditions provided that the grating is sufficiently chirped, and the chirp rate is sufficiently slow (see Fig. 7.9 in section 7.8). In order to make use of these solutions in a practical setting, it is important to determine how rapidly the grating can be chirped while still maintaining adiabaticity. Towards this end, in this section we determine a heuristic constraint for the QPM chirp rate: if this constraint is satisfied, then the adiabatic following process can occur.

As  $\nu$  is varied (by changing  $\delta k$ ,  $g$  or both), the local eigenmode  $\mathbf{W}_m$  changes, but always remains in the  $X - Y$  plane ( $Y_m = 0$ ). When the reduced field vector  $\mathbf{W}$  is in the  $X - Z$  plane, each of the envelopes  $b_j$  is orthogonal to (i.e.  $\pm\pi/2$  radians out of phase with) its driving term in Eq. (7.11), which implies that  $d|b_j|/d\zeta = 0$ , and is why  $\mathbf{W}_m$  lies in the  $X - Z$  plane. Some physical insight into the meaning of this  $X - Z$  plane can be gained by considering an unchirped device:  $\mathbf{W}$  passes through the  $X - Z$  plane at points where the direction of energy flow changes (e.g. at any point where the pump is fully depleted, just before the onset of back-conversion).

In order for adiabatic following to occur, the reduced variable  $Z$  must keep up with the corresponding component  $Z_m$  of the local eigenmode, and hence it is necessary that

$$\frac{dZ}{d\zeta} \approx \frac{dZ_m}{d\zeta}. \quad (7.31)$$

From Eq. (7.28),  $dZ/d\zeta = 2gY$ , and therefore the required magnitude of  $Y$  increases with  $dZ_m/d\zeta$ , and  $dZ_m/d\zeta$  in turn increases with the chirp rate.

Since  $\varphi = 0$  is convex, an angle  $\theta_{\parallel}$  in the  $X - Z$  plane associated with the local eigenmode can be defined according to

$$\begin{aligned} \tan(\theta_{\parallel}) &= \left. \frac{\partial\varphi/\partial Z}{\partial\varphi/\partial X} \right|_{\mathbf{w}=\mathbf{w}_m} \\ &= \nu. \end{aligned} \quad (7.32)$$

To see why the latter equality holds, recall that  $\nu = \delta k/(2g)$ ,  $Y_m = 0$ , and that the eigenmodes  $\mathbf{W}_m$  are points for which  $\nabla\varphi = \begin{bmatrix} \partial\varphi/\partial X & \partial\varphi/\partial Y & \partial\varphi/\partial Z \end{bmatrix}$  is parallel or anti-parallel to  $\nabla H = \begin{bmatrix} g & 0 & \delta k/2 \end{bmatrix}$ .

Based on the curvature of  $\varphi = 0$ , an angle  $\theta_\perp$  associated with the value of  $Y$  can be defined according to

$$Y = R_\perp(\mathbf{W}_m) \sin(\theta_\perp), \quad (7.33)$$

where  $R_\perp$  is the local radius of curvature (RoC) of the surface in the direction perpendicular to the  $X - Z$  plane (i.e. approximately along  $Y$ ). In order for the interaction to be adiabatic, we expect that the condition  $|\theta_\perp| \ll 1$  must be satisfied in addition to  $dZ/d\zeta \approx dZ_m/d\zeta$ , since in the limit of an infinitely slow chirp rate (i.e.  $\lambda_R \rightarrow \infty$ ),  $Y \rightarrow 0$  and hence  $\theta_\perp \rightarrow 0$ . With the conditions  $|\theta_\perp| \ll 1$  and  $dZ/d\zeta = dZ_m/d\zeta$ , it is possible to obtain a heuristic constraint on the chirp rate required for the adiabatic following process.

To obtain this heuristic constraint, first consider the local curvatures of the surface  $\varphi = 0$ . Formulas for the curvatures of surfaces specified by implicit equations are given in [108]. We denote the in-plane ( $X - Z$  plane) curvature as  $k_\parallel$  (RoC  $R_\parallel = -k_\parallel^{-1}$ ), and the curvature in the orthogonal direction (approximately along  $Y$ ) as  $k_\perp$  (RoC  $R_\perp = -k_\perp^{-1}$ ). After some algebra it can be shown that, at the local eigenmode, these curvatures are given by

$$k_\parallel = - \frac{2}{|\nabla\varphi|} \frac{\bar{G}(Z_m) + \nu^2}{1 + \nu^2} \quad (7.34a)$$

$$k_\perp = - \frac{2}{|\nabla\varphi|}, \quad (7.34b)$$

where the parameter  $\bar{G}(Z)$  is given by

$$\bar{G}(Z) = 1 + K_{ip} - 3Z. \quad (7.35)$$

Given  $\text{sgn}(\nu(\zeta = 0))$ , the relevant local eigenmode and hence the (local) curvatures  $k_\parallel$  and  $k_\perp$  are functions of only  $\nu$ .

An expression for the evolution of the local eigenmode is also required. With Eq. (7.30a),  $X_m$  can be expressed in terms of  $Z_m$ ; substituting this result into Eq. (7.30b), an implicit equation for  $Z_m$  is obtained, of the form  $f(Z_m(\nu), \nu) = 0$  for function  $f$ . By taking the derivative of this equation with respect to  $\nu$ , it can be shown that

$$\frac{dZ_m}{d\nu} = -\text{sgn} \left( \frac{d\nu}{d\zeta} \right) \frac{|\nabla\varphi|}{2(\bar{G} + \nu^2)(1 + \nu^2)^{1/2}}, \quad (7.36)$$

where the sgn prefactor assumes  $\nu(\zeta)$  is monotonic. With the above relations and the condition  $dZ_m/d\zeta = dZ/d\zeta$ , the inequality  $|\theta_\perp| \ll 1$  can be expressed as

$$\begin{aligned} \left| \frac{d}{d\zeta} \left( \frac{\delta k}{2g} \right) \right| &\ll 2g (1 + \nu^2)^{1/2} (\bar{G} + \nu^2) \\ &= \frac{(4g^2 + \delta k^2)^{1/2} (4g^2 \bar{G} + \delta k^2)}{4g^2}, \end{aligned} \quad (7.37)$$

which is the required adiabaticity condition. The right hand side is a function only of  $\delta k$  and  $g$ . If we define a new propagation coordinate  $\Xi = \int_0^\zeta \sqrt{4g(\zeta)^2 + \delta k(\zeta)^2} d\zeta$ , then Eq. (7.37) can be expressed in a purely geometrical form:

$$\left| \frac{d\theta_\parallel}{d\Xi} \right| \ll \frac{k_\parallel}{k_\perp}, \quad (7.38)$$

where the form of  $\Xi$  arises from Eq. (7.28): the rate of change of  $\mathbf{W}_m$  has an overall scaling with  $|\nabla H| = \sqrt{g^2 + (\delta k/2)^2}$ .

In the undepleted-pump limit (in which adiabatic following does not occur), the signal is amplified in the region where  $|\nu| < 1$  [51]. Since this limit can be described accurately by the complex WKB method, the points  $|\nu| = 1$  are referred to as turning points. For small signal input compared to the pump, i.e. small  $\rho$ , the first turning point is also an important point in the adiabatic following process: as  $K_{ip}$  is increased towards unity ( $\rho \rightarrow 0$ , i.e. the signal input is much weaker than the pump), the ratio  $k_\parallel/k_\perp \rightarrow 0$  near this point, and hence in order to maintain adiabaticity, the chirp rate at this point must be very slow. Physically, the signal must experience a large enough gain to begin depleting the pump over the small region near  $|\nu| = 1$  in order

to follow the eigenmode. The geometrical explanation for this requirement, provided by Eq. (7.38), is that the rate at which the eigenmode is swept in the  $X - Z$  plane, and hence the required value of  $Y$ , scales with  $k_{\parallel}^{-1}$ , while the deviation of the angle  $\theta_{\perp}$  from zero scales (for a given value of  $Y$ ) with  $k_{\perp}$ .

In order to show the implications of Eq. (7.37) for different cases, it is useful to re-write the inequality in terms of the coupling factor  $\lambda_R$ . If  $g = 1$ , then  $\lambda_R = |(d\delta k/d\zeta)^{-1}|$ , and hence Eq. (7.37) can be re-written as

$$4\lambda_R \gg \Lambda \equiv \frac{1}{(1 + \nu^2)^{1/2} (\bar{G} + \nu^2)}. \quad (7.39)$$

If  $\rho \gg 1$ ,  $\lambda_R \approx \lambda_{R,s}$  and it is reasonable to consider the interaction adiabatic when  $\lambda_{R,s} > 1$  [since the pump depletion in this limit, given in Eq. (7.13), is  $\exp(-2\pi\lambda_{R,s})$ ]. Therefore, the following adiabaticity heuristic is obtained in the general case:

$$\lambda_R > \Lambda. \quad (7.40)$$

Note that both  $\lambda_R$  and  $\Lambda$  can be treated as functions of either the position  $\zeta$  or the ratio  $\nu$ , since  $\nu$  itself is a monotonic function of  $\zeta$ .

In Fig. 7.5,  $\Lambda$  is plotted as a function of  $\delta k$  for several values of  $\rho$ . In the limit  $\rho^{-1} \rightarrow 0$  (strong signal, weak pump),  $\bar{G} = 1$  and  $\Lambda$  therefore has a very simple form. Away from this limit,  $\bar{G}$  becomes more complicated and changes with  $\delta k$ . In the opposite limit of  $\rho \rightarrow 0$ , the maximum of  $\Lambda$  as a function of  $\delta k$  approaches infinity, and its maximum occurs near  $|\delta k| = 2g$ ; these trends can be seen in Fig. 7.5. Based on Eq. (7.37), the divergence of  $\Lambda$  with respect to  $\rho$  makes it increasingly difficult to maintain adiabaticity as the input signal intensity is decreased. For example, for the  $\rho = 10^{-3}$  case in Fig. 7.5,  $\max(\Lambda) \approx 60$ , which is an extremely large value [consider, for example, that the exponential signal gain in the undepleted-pump limit is  $G = \exp(2\pi\lambda_{R,p})$ ]. It is highly unlikely that such a large value of  $\lambda_R$  could be used in practice without the onset of other, unwanted effects.

In appendix 7.8, we develop another adiabaticity constraint by analogy to two- and three-level quantum systems, and test the validity of both that constraint and

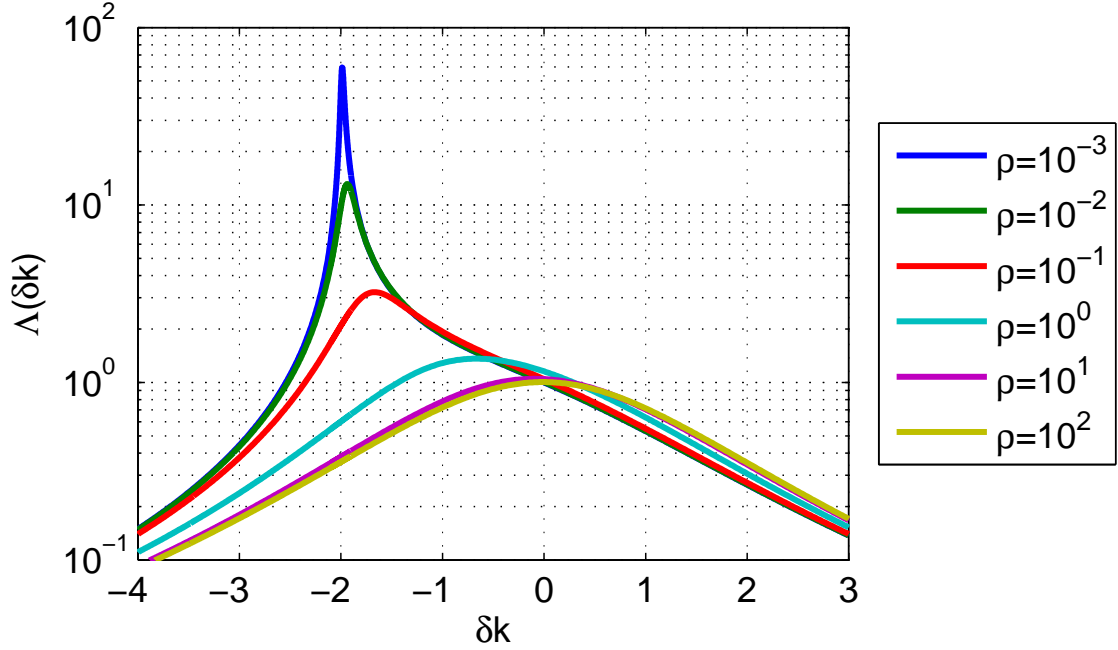


Figure 7.5:  $\Lambda$  [defined in Eq. (7.39)] as a function of  $\delta k$ , for several values of  $\rho$ , assuming  $g = 1$ . For small  $\rho$ , the maximum of  $\Lambda$  occurs near the first turning point ( $|\delta k| \approx 2g$ ) and diverges as  $\rho \rightarrow 0$ .

Eq. (7.37) derived above, by comparison to numerical simulations of Eqs. (7.11).

## 7.6 Efficiency and Phase

For practical applications, it will not always be feasible to maintain a truly adiabatic interaction, particularly for cases with  $\rho \ll 1$ . Instead, quantifying the dependence of conversion efficiency and output phase on the input intensities is more important. In this section, we first determine the effects of pump and signal intensity on conversion efficiency by solving Eqs. (7.11) numerically. We then develop approximate equations for the rates at which the idler, signal and pump acquire nonlinear phase, and compare these equations to the numerically-determined phases.

Fig. (7.6) shows contours of the pump depletion  $\eta$  as a function of coupling factor  $\lambda_{R,p}$  and ratio of input signal to pump in photon units,  $\rho$ . The grating length is

chosen such that  $L/L_{\text{deph}} = 8$ , which means that the grating is four times longer than the amplification region. For high signal gain and low conversion efficiency, the exponential gain predicted by Eq. (7.12) is accurate, and the hence contours of constant  $\eta$  are approximately straight lines in  $[\log(\rho) - \lambda_{R,p}]$  space. The straight contours of Fig. (7.6) mean that, even when a significant proportion of the pump is depleted, the exponential gain behavior persists, but with a reduction in gain. More specifically, for output pump depletion  $\eta$ , straight contours imply the following relation:  $\rho \exp(2\pi\lambda_{R,p}h(\eta)) = 1 - \eta$ . This relation means that the slope in signal gain versus  $\lambda_{R,p}$  is reduced by a factor  $h$  which depends on the pump depletion, a property at the *output* of the grating. By performing simulations with different grating lengths  $L$ , it can be shown that  $\eta$ , for wavelengths within the phasematching bandwidth, is almost independent of  $L$ , as long as  $L \gg L_{\text{deph}}$  and a suitable apodization profile is applied.

Given an upper limit on  $\lambda_{R,p}$ , Fig. (7.6) shows that high conversion efficiency (small  $\eta$ ) cannot be achieved unless  $\rho$  is sufficiently large. To achieve high conversion efficiency for a fixed and small  $\rho$ , multiple amplification stages are then required such that  $\rho$  is large enough in the final power amplifier. In experiments, one will usually be limited to the moderate range of  $\lambda_{R,p}$  considered in Fig. (7.6) due to a variety of considerations, including the damage threshold of the medium and the accumulation of nonlinear phase (which is considered below) and several other effects (discussed in chapter 8).

The contours of  $\eta$  [as a function of  $\log(\rho)$  and  $\lambda_{R,p}$ ] are not straight at larger values of  $\rho$ . For example, for  $\rho \gg 1$ , the interaction should be viewed as DFG rather than OPA, Eq. (7.13) applies and leads to a pump depletion that is almost independent of pump intensity. Furthermore, the contours are not straight when both  $\rho$  and  $\eta$  are sufficiently small [ $\ln(\eta) \ll -\pi$ ], due to the adiabatic following process. In these cases, Eq. (7.37) can be used to estimate the shape of the conversion efficiency contours, as shown in subsection 7.8.2.

Next, we consider the accumulation of signal phase in the QPM grating. This phase, which depends primarily on  $\lambda_{R,p}$  and  $\eta$ , has application-dependent constraints associated with, for example, the requirements to avoid nonlinear focusing and to

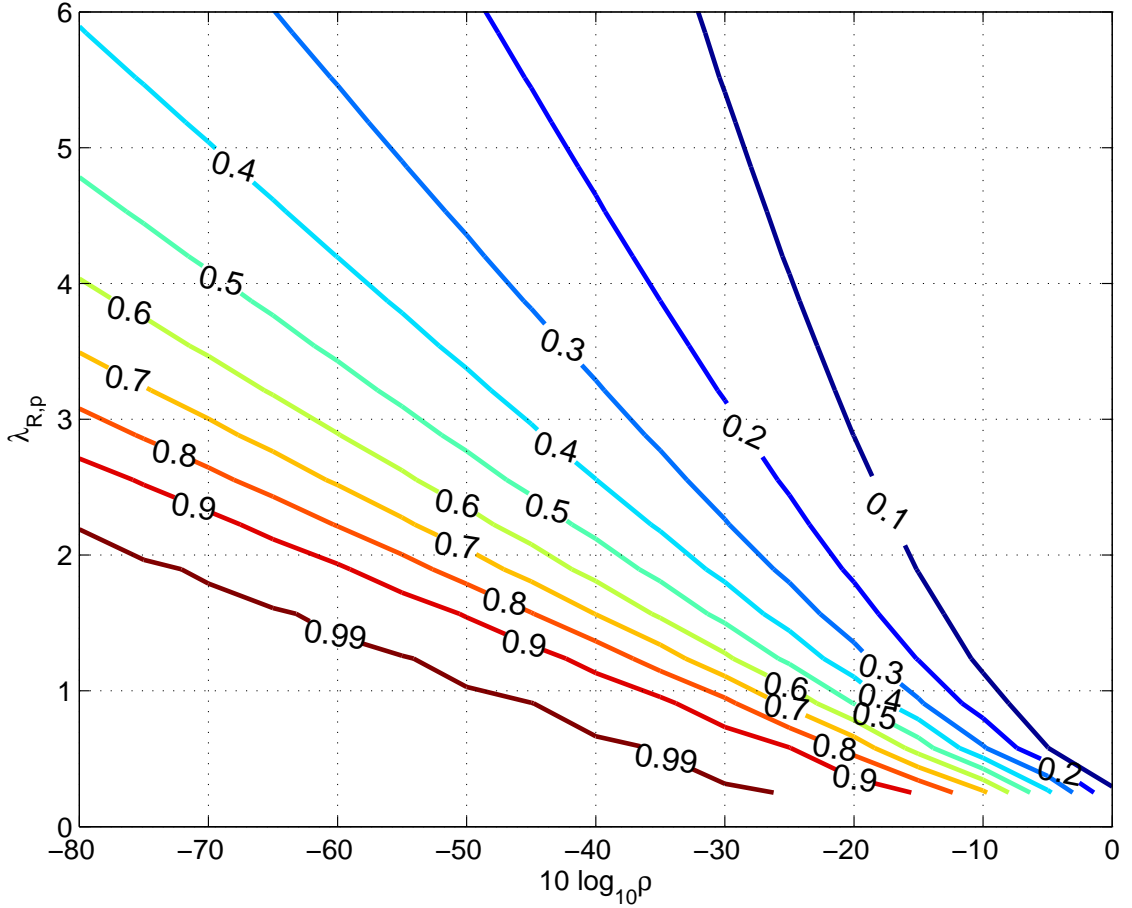


Figure 7.6: Pump depletion  $\eta$  as a function of gain factor  $\lambda_{R,p} \equiv |\gamma_{p0}^2/|\Delta k'|$  and photon flux ratio  $\rho \equiv |b_s(0)/b_p(0)|^2$ , with  $z_{pm} = L/2$  and using  $\sqrt{|\Delta k'|}L = 45$  so that  $L \gg 2L_{deph}$  for all values of  $\lambda_{R,p}$  simulated. Contours are labeled with values of  $\eta$ .

produce compressible amplified chirped pulses. Both of these requirements place a limit on the nonlinear phase accumulated by the signal and idler (or on the complexity of the compensating optical system).

The phase shifts accumulated can be understood, in regions where  $|\delta k| > 1$ , by a multiple scale analysis of Eqs. (7.11) [32]. With  $g = 1$ , the analysis yields the following set of coupled effective nonlinear Schrödinger equations for leading-order

fields  $b_j^{(0)}$ , which vary slowly compared to  $1/\delta k$  (except for the  $\exp(-i\phi_G)$  envelope):

$$\begin{aligned}\frac{db_i^{(0)}}{d\zeta} - i\delta k(\zeta)b_i^{(0)} &= -i\frac{1}{\delta k(\zeta)} \left[ |b_p^{(0)}|^2 - |b_s^{(0)}|^2 \right] b_i^{(0)} \\ \frac{db_s^{(0)}}{d\zeta} - i\delta k(\zeta)b_s^{(0)} &= -i\frac{1}{\delta k(\zeta)} \left[ |b_p^{(0)}|^2 - |b_i^{(0)}|^2 \right] b_s^{(0)} \\ \frac{db_p^{(0)}}{d\zeta} - i\delta k(\zeta)b_p^{(0)} &= -i\frac{1}{\delta k(\zeta)} \left[ |b_i^{(0)}|^2 + |b_s^{(0)}|^2 \right] b_p^{(0)}.\end{aligned}\quad (7.41)$$

This equation, which has a Kerr-like form, shows that the rate of phase accumulation depends on both  $\delta k$  and the relative number of photons in the three waves. There is a sign change for the rate of signal phase accumulation from  $\delta k$  on passing through the phasematched point  $z_{pm}$  [since  $\delta k(z_{pm}) = 0$ ], and also from the  $|b_p|^2 - |b_i|^2$  factor at the position where the pump becomes more than 50% depleted. We illustrate this behavior in Fig. (7.7), which shows numerical solutions of Eqs. (7.11) with  $z_{pm} = L/2$ . The approximate phases calculated using Eqs. (7.41) (dashed lines) agree with numerical solutions outside the amplification region, and hence they can be used to estimate the phases accumulated once  $\eta$  has been determined. The dashed lines are approximations to the phase, based on Eqs. (7.41) with  $b_j^{(0)}(0) = b_j(0)$  and  $b_j^{(0)}(L) = b_j(L)$ , respectively. For the latter case, this substitution means that the values of  $b_j(L)$  are first calculated numerically via Eqs. (7.11), and then these values are equated with  $b_j^{(0)}(L)$  on the assumption that the apodization present at the ends of the grating removes the rapidly-varying  $b_j^{(1)}$  and higher-order components of the fields, and then these values of  $b_j^{(0)}(L)$  are substituted into Eqs. (7.41) to obtain an estimate for the signal phase in Fig. 7.7.

If  $\rho$  is adjusted to keep the pump depletion  $\eta$  constant as the gain factor  $\lambda_{R,p}$  is varied, the phase is approximately proportional to  $\lambda_{R,p}$ , while the bandwidth of the device depends primarily on the total length  $L$ , as in the undepleted-pump case [51]. To compare the phase with different pump intensities, consider a grating whose length is specified by a normalized chirp-length  $\zeta_L \equiv \sqrt{|\Delta k'|}L = 30$ . We assume a similar apodization profile to the one defined above in Eqs. (7.15) and (7.16). From Fig. (7.6), two combinations of parameters resulting in  $\eta \approx 0.1$  are (1)  $\rho = 10^{-1}$

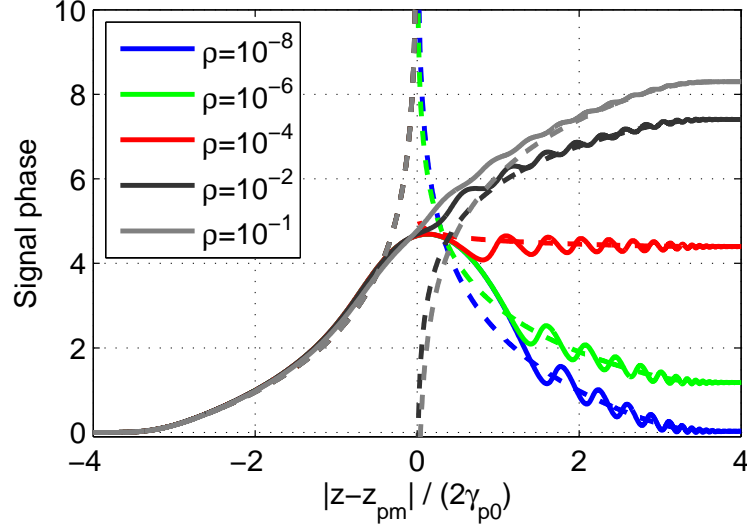


Figure 7.7: Signal phase accumulation during propagation with  $\lambda_{R,p} = 2$  and  $z_{pm} = L/2$  at increasing signal to pump photon flux ratio  $\rho$ , obtained with numerical solution of Eqs. (7.11).

and  $\lambda_{R,p} = 1$ , and (2)  $\rho = 10^{-3}$  and  $\lambda_{R,p} = 5.5$ . The output signal phase for these cases, with  $\zeta_L = 30$ , is  $\approx 1.5\pi$  and  $\approx 6.85\pi$ , respectively. These phases indicate an approximately linear phase slope with respect to  $\lambda_{R,p}$  (and hence with respect to pump intensity, since the chirp rate was kept constant in the two cases). The signal phase for the  $\rho = 10^{-3}$  case may exceed the phase tolerances of the system; if so, multiple amplification stages would then be required. One way to reduce the nonlinear phase is to reduce the grating length (at fixed chirp rate), but this change would also reduce the amplification bandwidth. A detailed discussion of the bandwidth and other system constraints is given in chapter 8.

The exact rate of phase of phase accumulation can also be determined via the reduced field variables  $X$ ,  $Y$ , and  $Z$  introduced above. Substituting  $b_j = |b_j| \exp(i\phi_j)$  into Eqs. (7.11), multiplying both sides by  $b_j^*$ , and taking the imaginary part of the resulting equations yields  $d\phi_j/dz$ . With this procedure, it can be shown that the

phases evolve according to

$$\begin{aligned}\frac{d\phi_i}{d\zeta} &= \delta k - \frac{gX}{K_{ip} - Z} \\ \frac{d\phi_s}{d\zeta} &= \delta k - \frac{gX}{1 - Z} \\ \frac{d\phi_p}{d\zeta} &= \delta k - \frac{gX}{Z}.\end{aligned}\tag{7.42}$$

The denominator in the final term of each of these equations is  $|b_j|^2$  (since  $|b_i|^2 = K_{ip} - Z$ ,  $|b_s|^2 = 1 - Z$ , and  $|b_p|^2 = Z$ ). When the fields follow a local eigenmode, the approximations  $X \approx X_m$  and  $Z \approx Z_m$  can be made; the right hand side of each equation is then a known function of  $\zeta$  which can be integrated directly to find the nonlinear phase. This result could provide useful insights into the nonlinear phase accumulated by the three waves, but will not be pursued further here. Note that with  $X = X_m$  and  $Z = Z_m$ , Eqs. (7.42) imply that  $d(\phi_p - \phi_s - \phi_i)/d\zeta = 0$ , as required for a nonlinear eigenmode.

## 7.7 Summary of This Chapter

In this chapter, we have considered the general three-wave nonlinear interaction in chirped QPM gratings. The remarkable efficiency and bandwidth properties seen previously in the undepleted-pump SFG regime are shown to be preserved in the nonlinear regime, with conversion efficiency approaching 100% with increasing input pump and signal intensities. Achieving high gain and efficiency simultaneously in a single chirped QPM grating may not be practical, for example due to restrictions on the accumulated phase or other system constraints (which will be discussed in chapter 8). The phase of each wave can be understood in terms of Kerr-like approximations, with the rate of phase accumulation changing sign when one of the input waves is depleted. When the pump or signal is strong enough, the waves adiabatically follow a nonlinear eigenmode which evolves as the QPM period changes over the length of a chirped grating. The geometrical description of three-wave mixing introduced in Ref. [16] can be utilized to understand and quantify this adiabatic following process.

The plane- and continuous wave model given by Eqs. (7.11) is applicable to optical parametric chirped pulse amplification (OPCPA), and hence serves as a starting point for the OPCPA design discussed in chapter 8. We will show that a number of unwanted effects can cause this minimal model to break down, giving rise to various design constraints. Despite these limitations, the understanding of nonlinear interactions in chirped QPM gratings developed here will help enable the design of high-gain, high-efficiency, and wide-bandwidth amplifier systems with engineered phase response, representing a promising approach to optical frequency conversion.

## 7.8 Appendix: Linearization and Adiabaticity of Reduced Equations

Three-wave mixing processes can be solved via Eqs. (7.28). These equations describe the evolution of the idler, signal and pump waves via reduced field variables  $X$ ,  $Y$  and  $Z$  [Eq. (7.24)]. The propagation of the reduced field vector  $\mathbf{W} = [X \ Y \ Z]$  is determined by Eq. (7.28); this equation is nonlinear because  $\partial\varphi/\partial Z$  is quadratic in  $Z$ . However, the existence of adiabatic-following solutions suggests that  $Z - Z_m$  can become arbitrarily small at all  $\zeta$ , provided the chirp rate is sufficiently slow; this suggests that  $(Z - Z_m)^2$  may be negligible, which would allow the propagation equations to be linearized.

In this appendix, we determine a linear and homogeneous system of equations which provide a good approximation to the general nonlinear system in the limit of a slow chirp rate. This form is then used to determine another adiabaticity constraint by analogy to atomic systems. Finally, we compare the two adiabaticity constraints [Eqs. (7.37) and (7.55)] to fully numerical simulations.

### 7.8.1 Linearization

Motivated by the facts that  $\varphi = 0$  is a closed and convex surface and that  $\mathbf{W}$  is driven by  $\nabla\varphi$ , we define a new vector of reduced variables according to

$$\mathbf{U} = \nabla\varphi. \quad (7.43)$$

There is a one-to-one mapping between  $\mathbf{W}$  and  $\mathbf{U}$  due to convexity. It can be shown from Eq. (7.28) that the evolution of  $\mathbf{U}$  is given by

$$\frac{d\mathbf{U}}{d\zeta} = \mathbf{A}\mathbf{U} \quad (7.44)$$

where the matrix  $\mathbf{A}$  is given by

$$\mathbf{A} = \begin{bmatrix} 0 & -\delta k & 0 \\ \delta k & 0 & -2g \\ 0 & 2g\bar{G} & 0 \end{bmatrix}, \quad (7.45)$$

where  $\bar{G}(Z) = 1 + K_{ip} - 3Z$  [defined in Eq. (7.35)]. The nonlinearity of Eq. (7.44) arises from the  $Z$ -dependence of  $\bar{G}(Z)$ . However, for nearly-adiabatic solutions,  $Z \approx Z_m$ , and hence we make the approximation

$$\bar{G}(Z) \approx \bar{G}(Z_m) \quad (7.46)$$

when  $\lambda_R$  is sufficiently large. Since the relevant eigenmode is a function of  $\nu = \delta k/(2g)$ , and since  $\nu$  is assumed to be monotonic in  $\zeta$  for a chirped QPM grating,  $Z_m$  is a single-valued function of  $\zeta$ . Thus, with this approximation, Eq. (7.44) becomes a homogeneous and position-dependent linear system. It can be tested numerically that the errors introduced by Eq. (7.46) become small when  $\lambda_R$  is sufficiently large. In the rest of this appendix, we assume that Eq. (7.46) holds.

The matrix  $\mathbf{A}$  can be diagonalized according to

$$\mathbf{A} = \mathbf{S}\mathbf{J}\mathbf{S}^{-1}. \quad (7.47)$$

The diagonal matrix  $\mathbf{J}$  is given by

$$\mathbf{J} = \text{diag} \left[ 0 \quad -i\sqrt{q} \quad i\sqrt{q} \right], \quad (7.48)$$

where  $q$  is given by

$$q = 4g^2\bar{G} + \delta k^2. \quad (7.49)$$

This expression also appeared in the numerator of Eq. (7.37). The eigenvector matrix  $\mathbf{S}$  is given, up to an overall scale factor and for  $\delta k \neq 0$ , by

$$\mathbf{S} = \begin{bmatrix} 4g^2\bar{G}/\delta k & -\delta k & -\delta k \\ 0 & -i\sqrt{q} & i\sqrt{q} \\ 2g\bar{G} & 2g\bar{G} & 2g\bar{G} \end{bmatrix}. \quad (7.50)$$

The eigenvalues  $\pm i\sqrt{q}$  play an important role in the adiabatic following process.

The function  $q$  is always real and positive, provided that  $\bar{G}$  is evaluated at a nonlinear eigenmode. This result emerges from the convexity of  $\varphi = 0$ : the intersections of the strictly convex surface  $\varphi = 0$  and the planes  $H = \text{constant}$  are either empty (corresponding to values of the reduced variables that are not physically realizable), a single point (corresponding to one of the two nonlinear eigenmodes), or a closed path (corresponding to oscillation around the eigenmode). Propagation in the absence of a QPM chirp is confined to such intersections [as implied by Eq. (7.28)], and is hence oscillatory. Locally (near  $\mathbf{W}_m$ ), the linearized equations provide a good approximation to the oscillatory behavior of the full nonlinear equations. To obtain oscillatory solutions, it is necessary that  $q > 0$ . A useful interpretation of this linearization is that  $\varphi = 0$  is approximated as an ellipsoid in the neighborhood of  $\mathbf{W}_m$ . When  $\rho \ll 1$ ,  $\min(q)$  becomes small but remains positive, and the minimum occurs around the first turning point, where  $|\delta k| = 2g$  [see Fig. (7.5)].

The dynamics of other types of mixing problems can be predicted via  $q$ . For example, in undepleted-pump OPA (with  $\rho \ll 1$ ),  $\bar{G} \approx -1$  and hence  $-iq \approx \sqrt{4g^2 - \delta k^2}$ , which is the formula for the signal gain. Eq. (7.44) is thus of use whenever  $\bar{G}$  can be

approximated as a known function of position.

### 7.8.2 Analogy to Quantum Systems

The matrix  $\mathbf{A}$  has a similar form to the Hamiltonians describing three-level quantum systems [99, 100, 101, 109, 110, 111]. In particular, when  $\bar{G} = 1$ ,  $\mathbf{A}$  has the same form as the Hamiltonians of the three-level systems used for the stimulated Raman adiabatic passage (STIRAP) method of population transfer. It can be shown that such three-level systems are equivalent to a two-level system when there is no detuning between the initial and final energy states [101]. Such two-level systems support adiabatic following solutions if the states are swept sufficiently slowly; an important result is that the amplitude of a non-adiabatic transition (i.e. the scattering out of the desired adiabatic state into the other state) is determined purely by an integral involving the time-dependent eigenvalues of the Hamiltonian [106, 112].

In the case considered here, position  $\zeta$  corresponds to time  $t$  in atomic systems, and  $\sqrt{q(\zeta)}$  corresponds to the local splitting of the energy eigenstates. The case with  $\bar{G}(\zeta) = 1$  occurs when  $K_{ip} \rightarrow 0$  (i.e. SFG, or DFG), and is completely analogous to a two-level system, with the complex-valued envelopes  $b_i$  and  $b_p$  playing the role of the two components of the wavefunction. The effective two-level system can be derived from Eqs. (7.11) by assuming that the signal envelope propagates linearly. For other cases, when  $\bar{G}(\zeta)$  is not always equal to 1, the coupled-wave system is not fully analogous to quantum systems. However, since the local eigenvalues  $q > 0$  in all cases, it is still possible to define a slowly-varying adiabatic basis. The existence of such a basis, and the observation of adiabatic following solutions, motivates the application of the analytical result of Ref. [106] to the linearized three-wave mixing problem of Eq. (7.44).

In Eq. (4.29) of Ref. [106], the following result is given for the amplitude of non-adiabatic transitions in two-level systems:

$$a_2(t \rightarrow \infty) = a_1(t \rightarrow -\infty) \exp \left[ \frac{i}{\hbar} \int_0^{t_c} \delta E(\tau) d\tau \right] \quad (7.51)$$

where  $a_1$  and  $a_2$  are components of the wavefunction, and where  $\delta E(t)$  is the difference

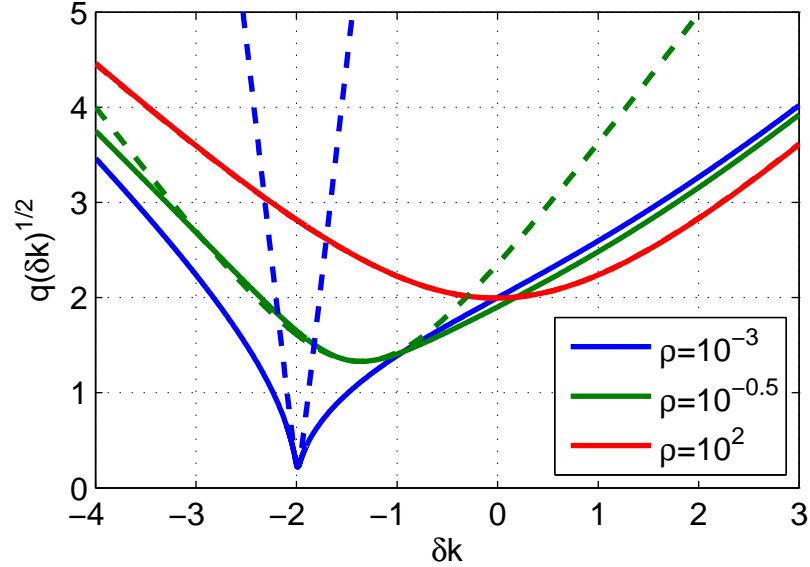


Figure 7.8: Eigenvalue function  $q$  defined in Eq. (7.49) as a function of normalized phase mismatch  $\delta k$  for several values of  $\rho$ , assuming  $g = 1$ . The solid lines correspond to the exact values of  $\sqrt{q(\delta k)}$ , while the dashed lines correspond to the quadratic approximation given in Eq. (7.53). For the case  $\rho = 10^2$ , the quadratic approximation is indistinguishable from the exact form on the scale of the figure.

between the two time-dependent instantaneous eigenvalues of the system.  $\delta E(t)$  is assumed to be positive on the real line. The complex-valued time  $t_c$  is the zero of  $\delta E(t)$  closest to the real line. Eq. (7.51) assumes that there is a single dominant avoided crossing of energy levels. By analogy to Eq. (7.51), we can obtain an approximation for the pump depletion of three-wave mixing processes in chirped QPM gratings:

$$\ln(\eta) \approx \text{Im} \left[ 2i \int_0^{\zeta_c} \sqrt{q(\zeta)} d\zeta \right], \quad (7.52)$$

where  $q(\zeta_c) = 0$  and  $\zeta_c$  the closest such point to the real line. In order to apply Eq. (7.51),  $\delta E(t)$  must be an analytic function in the complex plane, and obey certain relatively unrestrictive technical conditions [106]; the same condition thus applies to  $q(\zeta)$  in Eq. (7.52).

If we assume  $g = 1$ ,  $q$  can be written as a function of  $\delta k$ . In Fig. 7.8, we show  $q(\delta k)$  for several values of  $\rho$ . Except in certain limiting cases, there is not a simple

functional form for  $q(\zeta)$ , because  $Z_m$  is found by solving two nonlinear equations. For example,  $q$  involves a fourth-order polynomial even for a simple linearly chirped grating. However, by assuming a much simpler form for  $q(\zeta)$  which nonetheless maintains the most important features, we can obtain a simple analytical result with which the difficulty in obtaining an adiabatic interaction can be estimated. Motivated by the form taken by  $q$  for SFG ( $\bar{G} \rightarrow 1$  as  $\rho \rightarrow 0$ ), which also corresponds to the well-known Landau-Zener model [105], we approximate  $q$  as second-order in  $\delta k$ . Thus,

$$q(\delta k) \approx q_0 + q_2 (\delta k - \delta k_0)^2 \quad (7.53)$$

where  $\delta k_0$  is the phase mismatch at which  $dq/d\delta k = 0$ ,  $q_0 = q(\delta k_0)$ , and  $q_2 = d^2q(\delta k_0)/d\delta k^2$ . This approximate form of  $q$  is shown as dashed lines in Fig. 7.8. For small  $\rho$  and away from the minimum, the quadratic approximation becomes inaccurate. Given Eq. (7.53), the zero of  $q(\delta k)$ ,  $\delta k_c$ , is given by

$$\delta k_c = \delta k_0 + i \frac{q_0}{q_2}. \quad (7.54)$$

By substituting the approximate form of  $q$  into Eq. (7.52) and performing a change of variables in the integration, we can obtain

$$\ln(\eta) \approx -2\pi\lambda_R \left( \frac{q_0}{4g^2\sqrt{q_s}} \right). \quad (7.55)$$

For large  $\rho$  (weak pump, strong signal), the factor in parenthesis approaches unity, and, according to Eq. (7.14),  $\lambda_R \approx \lambda_{R,p}$ . Therefore, this limiting case corresponds to Eq. (7.13), which is the same as the well-known Landau-Zener formula. In contrast, for small  $\rho$  (strong pump, weak signal), the factor in parentheses can be small, which means that a much larger  $\lambda_R$  is required in order to maintain adiabaticity. This trend is illustrated in Fig. 7.9, which shows contours of constant efficiency similar to those plotted in Fig. 7.6 but including much larger values of  $\lambda_R$ . The contour predicted by the adiabaticity condition given in section 7.5 is also shown. Both conditions deviate somewhat from the full numerical solutions, but are accurate enough to provide a quantitative estimate of the difficulty in obtaining an adiabatic interaction.

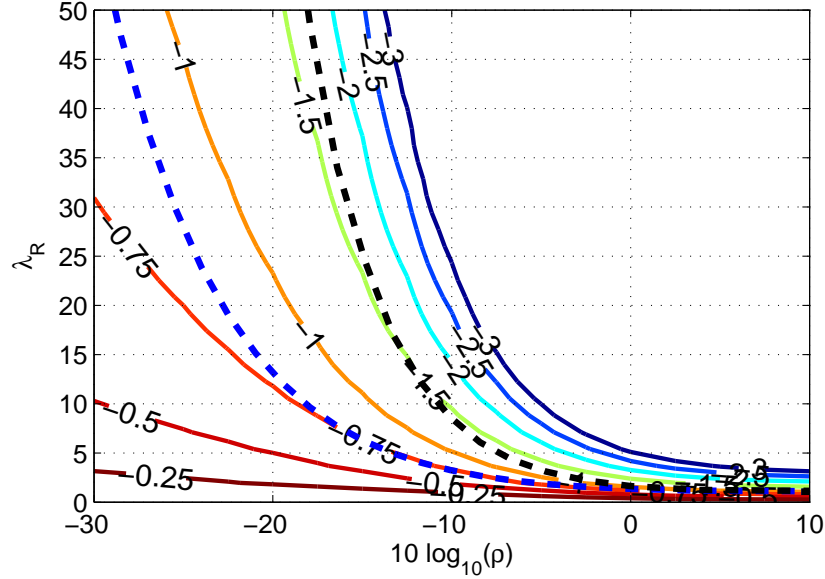


Figure 7.9: Contours of constant conversion efficiency, as a function of input photon flux ratio  $\rho = |b_s(0)|^2/|b_p(0)|^2$  and coupling factor  $\lambda_R = \lambda_{R,p} + \lambda_{R,s}$ . The contours correspond to values of  $\ln(\eta)/(2\pi)$ . The dashed blue and black lines show estimates of the conversion efficiency based on the geometric and eigenvalue-based adiabaticity conditions [Eqs. (7.37) and (7.55)], respectively. The absolute scale of the geometric estimate was determined by matching the curve to the  $\rho \rightarrow \infty$  case corresponding to SFG [for which the conversion efficiency is given by Eq. (7.13)]. The dashed curve corresponding to a perfect adiabaticity condition would lie exactly on the  $\ln(\eta)/(2\pi) = -1$  contour.

Eq. (7.55) provides a relatively simple intuitive picture: adiabaticity is violated because the effective energy levels are too close to each other (small  $q_0$ ) and they pass through the effective “avoided crossing” too rapidly (large  $q_2$ ). This explanation is complementary to Eq. (7.37), in which adiabaticity is violated if the eigenmodes are swept too quickly for the fields to keep up. In designing QPM gratings, Eq. (7.37) is likely to be more useful: because it provides a local adiabaticity condition, it can be used to form a differential equation for the  $\delta k$  and  $g$  profiles. In contrast, while the non-adiabaticity could in principle be estimated via Eq. (7.55), the response of the complex zeros of the general form of  $q(\zeta)$  to a nonlinear chirp apodization profile of  $\delta k(\zeta)$  is not as intuitively clear.

## Chapter 8

# Design of Optical Parametric Chirped Pulse Amplifiers Based on Chirped QPM Gratings

In chapter 7, we discussed some of the advantageous properties of chirped QPM gratings. In this chapter, we consider the design of a practical optical parametric chirped pulse amplification (OPCPA) system employing chirped QPM gratings as the gain media. We find that several QPM and system design constraints emerge, usually due to additional physical effects which cause the ideal plane- and continuous-wave mixing behavior to break down when pulsed beams are involved. In section 8.1, we give an outline of OPCPA using chirped QPM gratings, in order to introduce the key concepts. In section 8.2, we discuss the experimental system which motivated a detailed design study and summarize our experimental results. In section 8.3, we develop design constraints and procedures based on the results of chapter 7. In later sections, we discuss additional parasitic or unwanted effects, and quantify the constraints they impose on the system. In section 8.8, we collect and summarize the key results of this chapter. Experimental parameters are given in table 8.1. Design parameters and constraints are given in table 8.3.

## 8.1 OPCPA Using Chirped QPM Gratings

The goal of an OPCPA system is to transfer energy from a narrow-bandwidth, high-energy pump laser to a broadband, initially low-energy seed laser [53, 91, 92, 93, 113, 114, 115, 116]. The high-energy amplified seed is then compressed in time, and often also focused in space, allowing the energy to be packed into a very small volume, which results in the extremely high intensities essential for high-field experiments [117]. The reason for the name, and why OPCPA is so effective, is that the broadband pulse is first chirped (stretched) so that it has a comparable duration to the pump pulse. This approach has two key advantages: first, it allows for a large fraction of the pump energy to be extracted. Second, excessively high intensities (and all the problems they cause) are avoided, because the signal energy is not confined to a short temporal duration within the OPCPA system itself. It is important that a clean spectral and spatial phase be maintained throughout the system, so that the chirped signal pulse can be compressed and focused down to a bandwidth- and diffraction-limited spot.

In the limit of wide beams and long pulse durations, the plane-wave processes discussed in chapter 7 apply at each point in space and time. With a highly chirped signal pulse of comparable duration to the long pump pulse, each spectral component of the signal can be approximated as interacting with a corresponding temporal component of the pump. This temporal component is determined via the group delay spectrum of the signal. Given a pump frequency  $\omega_p$  and an instantaneous signal frequency  $\omega_s(t)$ , the generated instantaneous idler frequency is given by  $\omega_i(t) = \omega_p - \omega_s(t)$ . The mapping between time and frequency is illustrated in Fig. 8.1, which shows an idealized OPCPA scheme.

Our focus here is on using chirped QPM gratings as the gain medium in OPCPA systems. There are several factors motivating this choice:

1. An essentially arbitrary phasematching bandwidth can be obtained simply by imposing a corresponding spatial frequency bandwidth onto the grating. This design freedom means that we can pump and seed the OPA with wavelengths available from well-developed lasers and still obtain gain over an ultrabroad bandwidth.

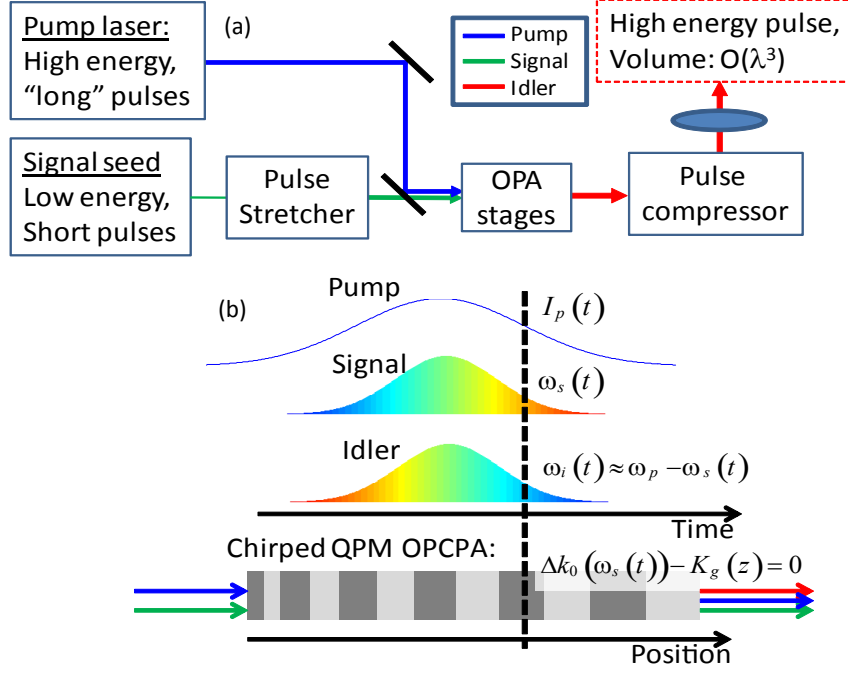


Figure 8.1: (a) Schematic for an OPCPA system. Signal pulses are generated, stretched to comparable temporal duration to the pump, then sent into one or more optical parametric amplifier (OPA) stages, and finally are compressed in time and focused in space. Ideally, this process results in a concentration of the amplified signal or idler pulse energy into a volume of order  $\lambda^3$  (i.e. a single-cycle unchirped pulse, focused down to a beam size equal its wavelength).

(b) Illustration of OPA in a chirped QPM grating involving chirped pulses. The vertical dashed line indicates a mapping between time, frequency, and position. At each point in time there is a corresponding instantaneous signal frequency  $\omega_s(t)$ , and the instantaneous idler frequency is given (in the highly-chirped-pulse limit) by  $\omega_i(t) = \omega_p - \omega_s(t)$ . Therefore, the idler has approximately opposite chirp to the signal, as indicated in the figure. Given the set of frequencies  $\omega_p$ ,  $\omega_s(t)$ , and  $\omega_i(t)$ , there is a material phase mismatch  $\Delta k_0[\omega_s(t)] = k[\omega_p] - k[\omega_s(t)] - k[\omega_i(t)]$ . Quasi-phasematching is therefore satisfied at the position in the chirped QPM grating where the grating k-vector  $K_g(z)$  satisfies  $K_g(z) = \Delta k_0(\omega_s(t))$ ; we denote this phasematching point as  $z_{pm}(\omega_s)$ . The gain of the signal and idler components ( $\omega_s$  and  $\omega_p - \omega_s$ , respectively) is determined primarily by the local intensity of the pump,  $I_p(t)$ , and by the chirp rate of  $K_g(z)$  near  $z_{pm}(\omega_s)$ .

2. By using a monotonic chirp profile (that is,  $K_g(z)$  is monotonic in  $z$ ) the resulting spectral phase is clean, smooth, and compressible.
3. The QPM chirp profile can be engineered in order to obtain desired spectral gain and phase profiles. For example, gain narrowing can be compensated.
4. The system is in principle experimentally simple, since only collinear beams are involved, without any need for noncollinear or angularly dispersed beams.
5. Both the seeded signal and the generated idler are useful beams.
6. A related advantage is that we can start with a commercial laser system in the near-IR as a seed signal, manipulate the pulse using well-developed and widely available optical elements, and then generate a mid-IR idler automatically from the amplification process which also inherits any spectral or spatial phase imposed onto the input signal. This phase transfer from the signal to the idler means that we can pre-distort the near-IR seed's spectral phase (using e.g. a pulse shaper) in order to optimize the compression of the mid-IR output pulse.
7. The adiabatic following process discussed in chapter 7 means that in a properly designed system, it should be possible to obtain high conversion efficiencies. Furthermore, this high conversion efficiency is possible even without precise beam-shape engineering, due to the monotonic conversion efficiency behavior.

These advantages come at a cost: chirped QPM gratings are susceptible to several additional parasitic effects. These effects arise primarily due to the difficulty in maintaining the desired plane- and continuous-wave mixing behavior. In this chapter, we explore in detail these parasitic effects as well as the above advantages. With careful design of both the system and the QPM grating, these effects can be avoided or at least mitigated. These techniques have enabled construction of a high-energy, short-pulse mid-IR OPCPA system with many novel and advantageous properties. We discuss this system in the following section, which is then used to motivate our design study in the remaining sections of this chapter.

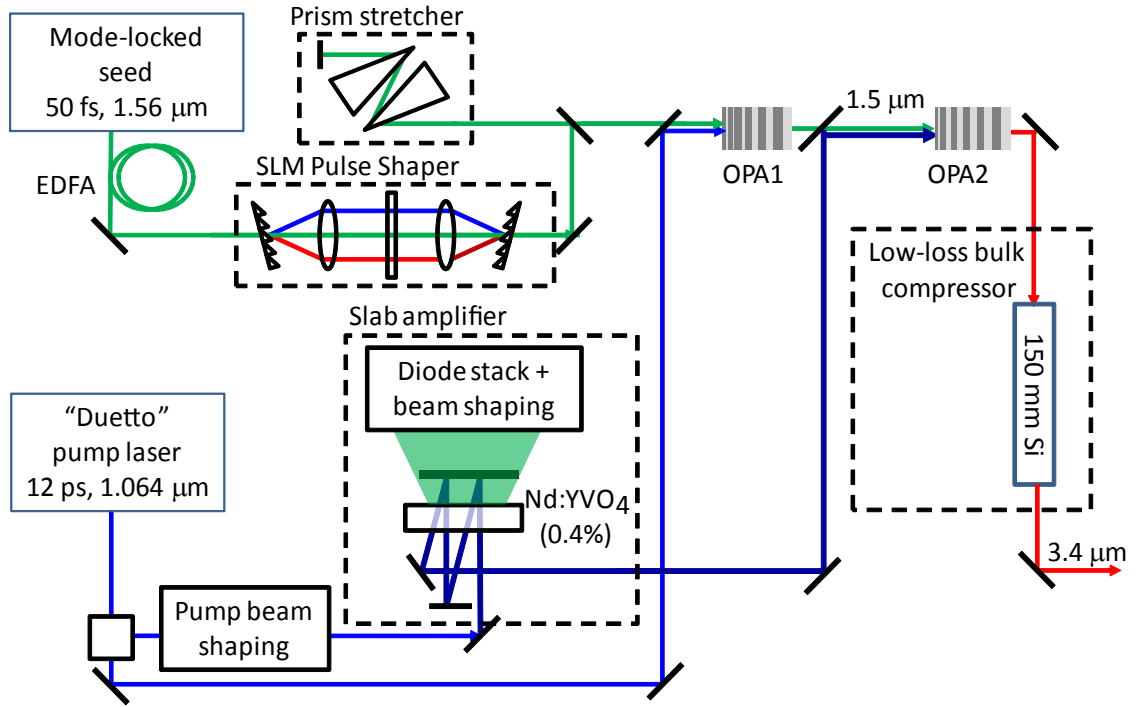


Figure 8.2: Experimental schematic of a mid-IR OPCPA system. System parameters are given in Table 8.1.

## 8.2 Experimental System

In this section, we discuss a mid-infrared OPCPA system in which we are using chirped QPM gratings as the amplifiers [53, 62]. The goal of the system is to generate high repetition rate, high-energy pulses in the mid-infrared; such pulses are of significant interest for high-field experiments [117]. To accomplish this goal, we need both a wide amplification bandwidth (supporting few-cycle pulses), high gain, and good overall conversion efficiency. Reducing system complexity while still meeting these goals is, of course, also advantageous.

The current system setup is shown in Fig. 8.2. The experiments were performed in Professor Ursula Keller’s group at ETH Zurich. The pump is a commercial 12-ps, 1.064- $\mu\text{m}$  laser with a repetition rate of 100 kHz and pulse energies of up to 120  $\mu\text{J}$  (average power 12 W). We seed the OPCPA system with a 50-fs 1.56- $\mu\text{m}$  mode-locked

fiber laser which emits pulses of energy 2.5 nJ at a repetition rate rate of 82 MHz. The pump and seed lasers are synchronized to each other. Most of the pump is sent to the OPCPA pre-amplifier (OPA1), while the remaining energy (10  $\mu$ J) is sent to a custom-built Nd:YVO<sub>4</sub> laser amplifier [118]. This laser amplifier, which is based on the InnoSlab concept [119, 120], yields a pump energy of 466  $\mu$ J (46.6 W) with rms energy fluctuations of 0.8% over 30 minutes. These amplified pump pulses are sent to the OPCPA power amplifier (OPA2).

Before OPA1, the signal seed is sent through a spatial light modulator (SLM) to impose a programmable spectral phase, and is then chirped using a silicon prism pair, resulting in a 2.6-ps FWHM duration of the signal. The pump and seed energies reaching OPA1 are 100  $\mu$ J and 87 pJ, respectively. We take the near-IR output pulses generated in OPA1 (which are centered at 1.56  $\mu$ m) as the seed for OPA2. The pump energy reaching OPA2 is 300  $\mu$ J. The OPA1 and OPA2 crystals are MgO:LiNbO<sub>3</sub>, and are uncoated. Both OPA1 and OPA2 have a nominal linear chirp profile, with a chirp rate of  $-2.5 \text{ mm}^{-2}$ . Apodization is performed in the first and last 10% of the grating via a nonlinear chirp apodization profile similar to that given in Eq. (7.15). The local QPM periods at the input and output side of the gratings are 38 and 24  $\mu$ m, respectively (for both OPA1 and OPA2). The mid-IR idler pulses (centered at 3.4  $\mu$ m) generated along with the amplification of the 1.5  $\mu$ m seed in OPA2, are sent through two AR-coated bulk silicon slabs with total length 150 mm in order to accomplish pulse compression. The compressed pulses are characterized by SHG frequency resolved optical gating (FROG) and used for subsequent experiments. The system parameters are summarized in table 8.1.

The best performance was obtained with a grating having a nonlinear chirp apodization and no duty cycle apodization. However, because of the limited number of gratings we have available, the variations in poling quality from one grating to the next, and the presence of additional parasitic effects which depend strongly on the poling quality (see section 8.4), this result does not rule out the utility of duty cycle apodization in general.

The amplified and compressed pulses have duration 75 fs and energy 7  $\mu$ J, and have been used to ionize Xenon in on-going high-field experiments. With losses of

Table 8.1: Current OPCPA system parameters. Durations correspond to full width at half maximum (FWHM).

Symbol	Value	Description
$\lambda_p$	1.064 $\mu\text{m}$	Pump wavelength
$\lambda_{\text{seed}}$	1.56 $\mu\text{m}$	Seed wavelength
$\lambda_{\text{MIR}}$	3.4 $\mu\text{m}$	Mid-IR output wavelength
$\tau_p$	12 ps	Pump duration
$\tau_{s0}$	50 fs	Compressed seed duration
$\tau_{s,1}$	2.6 ps	1.56- $\mu\text{m}$ seed pulse duration before OPA1
$\tau_{\text{out}}$	75 fs	Final 3.4- $\mu\text{m}$ duration after compression
$U_{p,i}$	120 $\mu\text{J}$	Pump energy from Duetto laser
$U_{p,\text{amp}}$	466 $\mu\text{J}$	Pump energy after Nd:YVO <sub>4</sub> amplifier
$U_{p,1}$	100 $\mu\text{J}$	Pump energy sent to OPA1
$U_{p,2}$	300 $\mu\text{J}$	Pump energy sent to OPA2
$U_{s,i}$	2.5 nJ	Seed energy directly from fiber laser
$U_{s,1}$	87 pJ	1.56- $\mu\text{m}$ seed energy reaching OPA1
$U_{\text{out}}$	7 $\mu\text{J}$	Final 3.4- $\mu\text{m}$ energy after compression
$P_{pk,1}$	6.4 MW	Pump peak power inside OPA1
$P_{pk,2}$	19.1 MW	Pump peak power inside OPA2
$f_{\text{rep},p}$	100 kHz	Pump laser repetition rate
$f_{\text{rep},s}$	82 MHz	Seed laser repetition rate
$w_{p,1}$	250 $\mu\text{m}$	$1/e^2$ radius of pump at OPA1
$w_{p,2}$	400 $\mu\text{m}$	$1/e^2$ radius of pump at OPA2
$L_1$	10 mm	OPA1 crystal length
$L_2$	10 mm	OPA2 crystal length
$\Delta k'_1$	-2.5 $\text{mm}^{-2}$	OPA1 chirp rate
$\Delta k'_2$	-2.5 $\text{mm}^{-2}$	OPA2 chirp rate
$w_{\text{ap}}$	1 mm	OPA crystal aperture (along c-axis)
$L_{Si}$	150 mm	length of bulk silicon compressor

10% from the bulk Si compressor, 13% from Fresnel losses at the MgO:LiNbO<sub>3</sub> facets, and 10% system losses between OPA2 and the compressor, we can infer an internal conversion efficiency  $1 - \eta$  in OPA2 of approximately 12.5%. The experimental setup and results are discussed further in Refs. [53, 62, 118, 121, 122, 123, 124, 125, 126].

The system relies on parametric transfer, where the conjugate of any phase imposed onto the 1.56- $\mu\text{m}$  seed before OPA1 is transferred to the mid-IR output. This property was a motivating factor for our re-design of the OPCPA system into its

current form: by modifying the spectral phase of the seed with a pulse shaper, we can optimize the compression of the output mid-IR pulses without the need for a lossy grating or prism system after OPA2. In previous system layouts, losses of as much as 70% were incurred in a prism compressor after OPA2; in the new layout, losses of  $< 10\%$  from the bulk Si compressor are obtained. This approach is possible because the chirped QPM OPA process produces useful and broadband idler pulses (in contrast to noncollinear systems, where the idler is difficult to use due to its large angular dispersion). This system layout yields a significant reduction in complexity and improvement in performance compared with our earlier system implementation, which also involved separate SC generation and DFG stages to obtain a mid-IR seed [53, 91].

Although the use of a bulk compression scheme enabled a significant reduction in losses after OPA2, the overall pump-to-idler conversion efficiency it is still limited by the 12.5% internal conversion efficiency in OPA2 (12.5% of pump photons are converted into idler photons). From full numerical simulations including dispersion to all orders, diffraction, both OPA stages, and several additional processes (such as those included in the plane- and continuous-wave simulations discussed in section 8.4), an internal conversion efficiency of approximately 14.5% is predicted, in good agreement with the experiment. The simulations do not account for QPM fabrication errors. As we will show in section 8.5, such errors can scatter significant amounts of light out of the desired idler, signal and pump waves; these errors therefore provide a likely explanation for the discrepancy between the measured and simulated conversion efficiencies. The simulations help to motivate the use of a coupled-wave formalism to predict the performance of the OPCPA system. Based on the adiabatic conversion processes discussed in chapter 7, there are therefore a number of potential ways to increase the conversion efficiency, including increasing the pump intensity, adding additional amplification stages to obtain a higher seed energy at the input to the final OPA stage, and exploiting QPM design techniques to suppress gain narrowing effects. To achieve such improvements in practice, however, it is necessary to understand the design constraints and opportunities associated with chirped QPM OPCPAs. These issues are the subject of the remaining sections of this chapter. Our results, together

with ongoing system upgrades, help explain the current system design and show how the remaining limitations of the system can be resolved, pointing the way towards higher mid-IR energies and few-cycle pulse durations.

### 8.3 Design in the Limit of Non-Diffracting Beams and Highly Chirped Signal Pulses

In this and the following sections, we study the design constraints and opportunities for chirped QPM OPCPA devices. Our results are summarized in section 8.8; in table 8.3, we numerically evaluate the various constraints and parameters defined throughout the chapter.

#### 8.3.1 Pump Intensity and QPM Chirp Rate

We begin our design study with the results given in chapter 7. Based on these results, several constraints must be met when designing chirped QPM gratings in an OPCPA system. The amplification bandwidth is usually comparable to the k-space bandwidth of the grating, which is given by

$$\Delta K_g \approx |\Delta k'|L \quad (8.1)$$

for constant chirp rate  $\Delta k'$  and grating length  $L$ . This equation applies in the case of a highly-chirped grating (one whose k-space bandwidth significantly exceeds the bandwidth ( $\approx \pi/L$ ) of an unchirped grating of the same length).

The k-space amplification bandwidth  $\Delta k_{OPA}$  is the range of carrier phase mismatches  $\Delta k_0 = k_p - k_s - k_i$  which are fully amplified. Amplification for a given carrier phase mismatch occurs in the region where the first-order phase mismatch satisfies  $|\Delta k_1| < 2\gamma_p$ , where  $\gamma_p$  was defined in Eq. (7.4) and is the coupling between the signal and idler due to the pump (which we assume for now to be undepleted), and  $\Delta k_1 = \Delta k_0 - K_g$  [defined in Eq. (1.38)]. Spectral components are not fully amplified unless  $\Delta k_1$  is swept from  $\mp 2\gamma_p$  to  $\pm 2\gamma_p$  within a region of the grating with

a constant (or slowly varying) chirp rate. Taking this consideration into account, the OPA bandwidth is given by

$$\Delta k_{OPA} \approx |\Delta k'|L - 4\gamma_0. \quad (8.2)$$

When an apodization region is included,  $L$  in this expression should correspond to the length of the unapodized central region of the grating. Apodization is discussed in more detail in subsection 8.3.3.

The output signal intensity is determined primarily by the input pump and signal intensities via the gain factor  $\lambda_{R,p} = \gamma_{p0}^2/|\Delta k'|$  [with undepleted-pump gain  $G = \exp(2\pi\lambda_{R,p})$ , given by Eq. (7.12)] and the input photon flux ratio  $\rho \equiv |b_s(0)/b_p(0)|^2$ . The parameters  $\lambda_{R,p}$  and  $\rho$  are sufficient to determine the output intensities provided that the grating is long enough [as discussed in chapter 7]. These parameters can be treated as functions of position and time (or frequency) in the idealized OPCPA scheme depicted in Fig. 8.1.

The types of interactions that can be achieved in a particular experimental configuration (e.g. high gain OPA) are determined primarily by the duration and peak power of the pump, the required gain bandwidth, and the dispersion of the nonlinear medium. To show the role these parameters play, it is useful to express the gain factor  $\lambda_{R,p}$  in terms of the peak power of the pump. Assuming a Gaussian pump beam and a 50% QPM duty cycle and using Eq. (7.4),  $\lambda_{R,p}$  can be written as

$$\lambda_{R,p} = \frac{4\omega_i\omega_s\omega_p d_1^2 \xi_p P_{pk}}{\pi\epsilon_0 c^4 n_i n_s \Delta K_g}. \quad (8.3)$$

In this equation,  $P_{pk}$  is the peak power of the pump, and the pump focusing factor  $\xi_p$  is defined as

$$\xi_p = \frac{L}{k_p w_0^2}, \quad (8.4)$$

where  $w_0$  is the  $1/e^2$  intensity radius of the pump beam.  $d_1 = 2d_{\text{eff}}/\pi$  is the relevant nonlinear coefficient for first-order QPM with a 50% duty cycle. The value of  $\xi_p$

in Eq. (8.3) is also constrained. In nonlinear optics experiments, one often selects confocal focusing, i.e.  $\xi_p \approx 1$ , as a tradeoff between tight focusing for high intensity and loose focusing for long interaction length, in order to maximize the conversion efficiency. However, we show in subsequent sections of this chapter that loose focusing, i.e.  $\xi_p \ll 1$ , is usually required for chirped-QPM OPA in order to avoid unwanted nonlinear focusing effects. Given a constraint on  $\xi_p$ , Eq. (8.3) indicates that in order to obtain a high OPA gain for a particular signal bandwidth, a certain pump peak power is required. For broadband OPCPA, this peak power can correspond to tens of megawatts.

The design of each amplification stage in the OPCPA system can be parameterized by three parameters, the peak gain coefficient  $\gamma_{p0}$ , the peak gain factor  $\lambda_{R,p}$ , and the k-space amplification bandwidth  $\Delta k_{OPA}$ , introduced in Eqs. (7.4), (7.12) and (8.2) respectively. For a linearly chirped grating, given  $\gamma_{p0}$  and  $\lambda_{R,p}$ ,  $\Delta k'$  is fixed. Together, these parameters determine the required crystal length,

$$L = \left( \frac{\Delta k_{OPA}}{\gamma_{p0}^2} + \frac{4}{\gamma_{p0}} \right) \lambda_{R,p}. \quad (8.5)$$

The ratio of the grating length to the amplification length for a given spectral component of the signal is given by  $L/(2L_{\text{deph}})$ , where  $L_{\text{deph}}$  is defined in Eq. (7.17). Given Eq. (8.5), this ratio is given by

$$\frac{L}{2L_{\text{deph}}} = 1 + \frac{\Delta k_{OPA}}{4\gamma_{p0}}. \quad (8.6)$$

If  $\gamma_{p0} \rightarrow 0$ , there are many amplification regions contained in the grating. On the other hand, if  $\Delta k_{OPA} < 4\gamma_{p0}$ , all spectral components are amplified over the whole length of the device; in this case, the grating cannot be considered highly chirped for the purposes of OPA.

From fabrication constraints, there is some maximum grating length  $L_{\text{max}}$  available, and hence

$$L \leq L_{\text{max}}. \quad (8.7)$$

Similarly, there is an upper bound on  $\gamma_{p0}$ :

$$\gamma_{p0} \leq \gamma_{\max}, \quad (8.8)$$

where  $\gamma_{\max}$  is the gain coefficient for a pump whose intensity equals the damage threshold of the material (or from a practical standpoint, the highest pump intensity at which damage can reliably be avoided). The damage threshold can depend on the pump pulse duration. Note that the grating length must also be significantly longer than the (average) QPM period in order for the first-order-QPM approximation used in chapter 7 to be accurate. We consider systems for which designs with only a few QPM periods are not appropriate, and therefore evade this issue.

The quasi-CW limit we have assumed so far breaks down when the relative group delay between the idler, signal and pump accumulated during propagation through the QPM grating is non-negligible compared to their (stretched) durations. This breakdown can lead to pronounced ripples in the output signal spectrum. Therefore, excessive group delay between the pulses should be avoided. While the resulting spectral ripples can be suppressed by improved apodization, in practice they cannot be suppressed entirely due to the limitations on the apodization process. To minimize these effects (and more generally to obtain a tractable interaction in which there is minimal cross-talk between different spectral components), the grating should be made as short as possible, while still meeting the other constraints of the system. Therefore, it is often appropriate to choose

$$\gamma_{p0} = \gamma_{\max}, \quad (8.9)$$

since this choice minimizes the required grating length. Note, however, that some other parasitic effects discussed in this chapter (section 8.5) favor *longer* grating lengths, and so  $\gamma_{p0} = \gamma_{\max}$  is not always optimal.

If we take the maximum useful length of the QPM grating to correspond to several GVM lengths of the form given in Eq. (6.10), then we obtain from Eq. (8.5) the

following (heuristic) constraint for the pump duration  $\tau_p$ :

$$\tau_p \gg \left( \frac{\Delta k_{\text{OPA}}}{\gamma_{p0}^2 c} + \frac{4}{\gamma_{p0} c} \right) \delta n_g \lambda_{R,p}, \quad (8.10)$$

where  $\delta n_g$  is a characteristic group index difference, corresponding to the largest group index minus the smallest group index involved in the three-wave interaction. With this inequality, the required pump duration can be estimated given the required gain and bandwidth. The shortest minimum pump duration is obtained with  $\gamma_{p0} = \gamma_{\text{max}}$ . Given a constraint on  $\xi_p$  (see sections 8.6 and 8.7), Eq. (8.3) yields an inequality for the pump peak power. Thus, with Eqs. (8.3) and (8.10), the minimum pulse energy can also be determined.

These constraints are evaluated in section 8.8; several other design constraints are first established in the following sections.

### 8.3.2 Nonlinear Chirp Profile

In order to obtain high conversion efficiency across a spatiotemporal pulse profile with a linearly chirped QPM grating, the peak of the pump must be driven well into saturation in order to also saturate the wings. A relatively large value of  $\lambda_{R,p}$  is therefore required. Driving the peak of the pump too far into depletion can lead to a number of unwanted effects, such as detrimental cascaded processes or a large nonlinear phase. One way to help avoid these effects is by designing a grating with a nonlinear chirp profile in order to obtain a flat gain spectrum even with a non-uniform profile of the pump intensity versus time.

For chirped signal pulses, there is a mapping between time and signal frequency, which can be expressed via the instantaneous frequency,  $d\phi_s(t)/dt = \omega_{\text{inst}}(t)$ , where  $\phi_s(t)$  is the time-dependent phase of the signal. Spectral components of the signal overlapped with the wings of the pump pulse experience a reduction in gain, since they “see” a lower pump intensity than spectral components near the center of the signal (and hence pump) pulse. In most cases, there is also a one-to-one mapping between signal frequency and phasematching k-vector. This mapping means that a

function  $z_{pm}(\omega)$  can be defined which specifies the phasematched point in the QPM grating for signal component at frequency  $\omega$ .

One way to approximately compensate for the reduction in gain due to the non-uniform pump intensity profile (and hence obtain a frequency-independent gain) is by matching the grating chirp rate at each position in the grating to the coupling coefficient  $\gamma^2$  at the point in time where the corresponding phasematched signal frequency is localized. In this way, the ratio  $\gamma^2/|\Delta k'|$  can be rendered constant. If changes to  $\gamma^2/|\Delta k'|$  are small over the amplification length, this choice results in a frequency-independent gain.

A differential equation can be formulated to construct a grating with the appropriate nonlinear chirp (NLC) profile. Given the above mapping between signal frequency and pump intensity, the coupling coefficient  $\gamma^2$  [see Eq. (7.4)] can be expressed as a function of frequency according to

$$\gamma(\omega)^2 = \frac{2\omega(\omega_p - \omega)d_1^2}{n(\omega)n(\omega_p - \omega)n(\omega_p)\epsilon_0 c^3} I_p(t_{\text{inst}}(\omega)) \quad (8.11)$$

where,  $t_{\text{inst}}(\omega)$  is the point in time (delay with respect to the peak of the pump pulse) where signal frequency  $\omega$  is localized, and hence satisfies  $t_{\text{inst}}(\omega_{\text{inst}}(t)) = t$ . Similarly, the signal frequency  $\omega$  can be mapped to the grating k-vector by the function  $\omega_{pm}(K_g)$  which specifies the phasematched signal frequency given a grating k-vector  $K_g$ . This function hence satisfies  $\Delta k(\omega_{pm}(K_g)) = K_g$ . In cases where these functions exist,  $\gamma^2$  can be written as a function of  $K_g$ . Since  $\Delta k' = -dK_g/dz$ , the following differential equation is obtained

$$\frac{dz}{dK_g} = \frac{s\lambda_{R,p}}{\gamma(\omega_{pm}(K_g))^2} \quad (8.12)$$

where  $s = \pm 1$  determines the sign of the chirp rate. The solution to this equation can be expressed in the form

$$z_{\text{sol}}(K_g) = -\frac{1}{\Delta k'_0} \int_{K_{g,i}}^{K_g} \frac{dK'_g}{\bar{\gamma}(\omega_{pm}(K'_g))^2} \quad (8.13)$$

where  $K_{g,i}$  is the initial grating k-vector,  $\bar{\gamma} = \gamma/\gamma_{p0} \leq 1$ , and  $\Delta k'_0 = \pm\gamma_{p0}^2/\lambda_{R,p}$  is the maximum chirp rate present in the grating, and is given in terms of the design parameters  $\gamma_{p0}$  and  $\lambda_{R,p}$  discussed in section 8.3.1. The function  $z_{\text{sol}}(K_g)$  can be inverted to yield the grating k-vector profile  $K_{g,\text{sol}}(z)$ . The QPM grating itself can then be constructed according to Eq. (1.23), i.e.  $\bar{d}(z) = \text{sgn}(\cos(\int_0^z K_{g,\text{sol}}(z')dz'))$ . The above procedure can be applied provided that one-to-one mappings exist between time, frequency, and grating k-vector (specific forms of these functions are not required).

The primary condition required for the effectiveness of the above ‘‘local’’ NLC design is that the changes to  $\gamma^2/|\Delta k'|$  are small over the amplification length. In practice, this condition is not always met, and so while Eq. (8.12) provides a reasonably intuitive picture of how the grating chirp can compensate for the non-uniform intensity profile, an improved design is required. A much more versatile approach involves using Eq. (7.21) to approximate the frequency-dependent field gain. This equation, expressed here in physical units, is given by

$$G_s \approx \exp \left[ \int_{z_{tp,1}}^{z_{tp,2}} \sqrt{|\gamma(\omega)|^2 - \left( \frac{\Delta k_0(\omega) - K_g(z)}{2} \right)^2} dz \right], \quad (8.14)$$

Since we assume monotonic  $K_g$  profiles,  $\ln(G_s)$  can be written as an integral versus  $K_g$ , with a  $(dz/dK_g)$  factor in the integrand. The limits of integration are the frequency-dependent k-space turning points, which satisfy  $|\Delta k_0(\omega) - K_{tp,j}(\omega)| = 2\gamma(\omega)$ . Provided that both of these turning points lie within the range of  $K_g$  (i.e. provided that the amplification region of a particular spectral component is fully contained within the grating), the integration limits can be extended to cover the entire range of  $K_g$  by taking the real part of the integrand. That is, the gain can be re-written as

$$\ln(G_s(\omega)) = \int_{K_i}^{K_f} \frac{dz}{dK_g} \Gamma(\omega, K) dK, \quad (8.15)$$

where  $K_i$  and  $K_f$  are the initial and final grating k-vectors, respectively. The local

gain rate  $\Gamma$  is given by

$$\Gamma(\omega, K) = \text{Re} \left[ \sqrt{\gamma(\omega)^2 - \left( \frac{\Delta k_0(\omega) - K}{2} \right)^2} \right]. \quad (8.16)$$

Equation (8.15) is valid for a frequency  $\omega$  provided that the zeros of  $\Gamma(\omega, K)$  with respect to  $K$  lie within the range spanned by  $K_i$  and  $K_f$ . Since  $\Delta k_0$  and  $\gamma$  are known functions of frequency, values of  $K_i$  and  $K_f$  can be chosen which contain the amplification regions of all the spectral components of interest.

If we specify discrete grids for frequency  $\omega$  and  $K_g$ , then  $\Gamma(K_g, \omega)$  is a matrix and Eq. (8.15) is a linear equation in the variable

$$z_K \equiv \frac{dz}{dK_g}. \quad (8.17)$$

We can therefore formulate an appropriate convex optimization problem by imposing smoothness and monotonicity of  $z_K$ , comparing  $\ln(G_s(\omega))$  to an arbitrary target gain profile, and applying other constraints as needed. Once  $z_K$  is known, the position can be expressed as a function of  $K_g$ :

$$z(K_g) = \int_{K_i}^{K_f} z_K dK. \quad (8.18)$$

The function  $z(K_g)$  can be inverted to find a grating profile,  $K_g(z)$ . Apodization regions can then be appended to the ends of this grating profile in order to yield a smooth amplification spectrum.

We next show a specific example of this approach. The assumed Gaussian pump has a center wavelength of  $1.064 \mu\text{m}$ , a FWHM duration of 10 ps, and an intensity such that  $\gamma_{p0} = 3 \text{ mm}^{-1}$ . The Gaussian signal has center wavelength  $3.5 \mu\text{m}$ , bandwidth supporting a 35-fs FWHM duration, with a purely quadratic spectral phase such that the actual FWHM duration is 3.5 ps. We consider an undepleted-pump example, so the amplified signal intensity is negligible compared with the pump.

The NLC profile is designed to support amplification over the  $1/e^2$  pulse bandwidth (corresponding to spectral components between 3.1- and 4.0- $\mu\text{m}$ ). A grid of 100 frequency points spanning this range is chosen. The k-vectors phasematching the ends of this spectrum are  $K_{min} = 2.037 \times 10^5 \text{ m}^{-1}$  and  $K_{max} = 2.189 \times 10^5 \text{ m}^{-1}$ . A linear  $K_g$  grid is defined with end-points  $K_{min} - 2\gamma_{p0}$  and  $K_{max} + 2\gamma_{p0}$ , to ensure that the entire amplification region of each spectral component is contained within the grating. A frequency-independent gain factor  $\lambda_{R,p0} = 2.2$  is chosen, which corresponds to approximately 60 dB power gain. Before proceeding, it is useful to estimate the minimum required length. Substituting  $\Delta k_{OPA} = K_{max} - K_{min}$  and  $\gamma_{p0} = 3 \text{ mm}^{-1}$  into Eq. (8.5) yields a length  $L = 6 \text{ mm}$ . A grating exceeding this length is required, since  $\gamma(\omega) \leq \gamma_{p0}$ .

In specifying the optimization problem, we use subscripts  $n$  to indicate index  $n$  of the variables. The grid spacing is  $\delta K = K_{g,n+1} - K_{g,n} = (K_{max} - K_{min} + 4\gamma_{p0})/n_K$ , where  $n_K$  is the chosen number of points in  $K_g$ . The log of the gain is given by matrix multiplication,

$$\ln(G_s) = \Gamma z_K, \quad (8.19)$$

and we denote the target gain as  $G_T$  (which is equal to  $\exp(\pi\lambda_{R,p0})$ ). A tolerance  $\delta G$  is used: we allow  $\ln(G_s)$  to differ from  $\ln(G_T)$  by this amount. The length of the grating is given by summing  $z_K = dz/dK_g$  over  $K_g$ :

$$L = \delta K \sum z_K. \quad (8.20)$$

For definiteness, we assume a positive chirp rate. A finite-difference approximation to the derivative of  $z_K$  is denoted  $\Delta z_K$ , and satisfies

$$\Delta z_{K,n} = z_{K,n+1} - z_{K,n}. \quad (8.21)$$

With these definitions, we arrive at the following convex optimization problem:

$$\text{minimize } \|\Delta z_K\|_2^2 \quad (8.22a)$$

subject to:

$$-\delta G \geq \Gamma z_K - \ln(G_T) \leq \delta G \quad (8.22b)$$

$$L \leq L_{\max} \quad (8.22c)$$

$$\lambda_{R,\min} \leq \gamma_{p0}^2 z_K \leq \lambda_{R,\max}. \quad (8.22d)$$

To solve Eq. (8.22) we use **CVX**, a package for specifying and solving convex programs [127, 128]. Eq. (8.22) is a quadratic program. The objective function ensures smoothness of the solutions. The parameters  $\lambda_{R,\min} = 1$  and  $\lambda_{R,\max} = 10$  indicate bounds on the local gain parameters, and are chosen to ensure a sensible solution. In particular, these parameters were selected such that  $0 \ll \lambda_{R,\min} \leq \lambda_{R,p0}$  and  $\lambda_{R,\max} \gg \lambda_{R,p0}$ . As long as these conditions are met, the solution is not too sensitive to these parameters; note that the  $\lambda_{R,\min} > 0$  constraint ensures monotonicity of the  $z_K$  and hence  $K_g(z)$ . We choose  $\delta G = 0.05$ , since this tolerance is typically satisfactory for applications.  $\delta G$  can be made smaller, but eventually the problem may become infeasible. The length  $L_{\max}$  is treated as a parameter of the fit: we solve Eq. (8.22) for a range of choices of  $L_{\max}$ , simulate an OPCPA process in the resulting grating fully numerically, and select a feasible value of  $L_{\max}$  which yields a useful output spectrum. For the present example, we chose  $L_{\max} = 12$  mm [twice the minimum length indicated by Eq. (8.5)]. In the solution, both this maximum length inequality (8.22c) and the chirp rate bounds (8.22d) are inactive, which emphasizes that very little information is needed *a priori* to arrive at a sensible solution. Finally, we also need to apply apodization to the grating profile returned by the optimization routine. Profiles similar to those defined in Eqs. (7.15) and (7.16) are appended to the ends of the grating for this purpose. The resulting total length of the grating is  $L \approx 9.55$  mm.

The optimized grating and simulated gain spectrum is shown in Fig. 8.3. The simulations are based on coupled plane-wave equations similar to those defined in Eqs. (6.3), but modified by neglecting  $\chi^{(3)}$  and treating the frequency-dependence of the coupling coefficients  $\gamma_j(\omega)$  exactly. The dashed horizontal line in Fig. 8.3(b) indicates

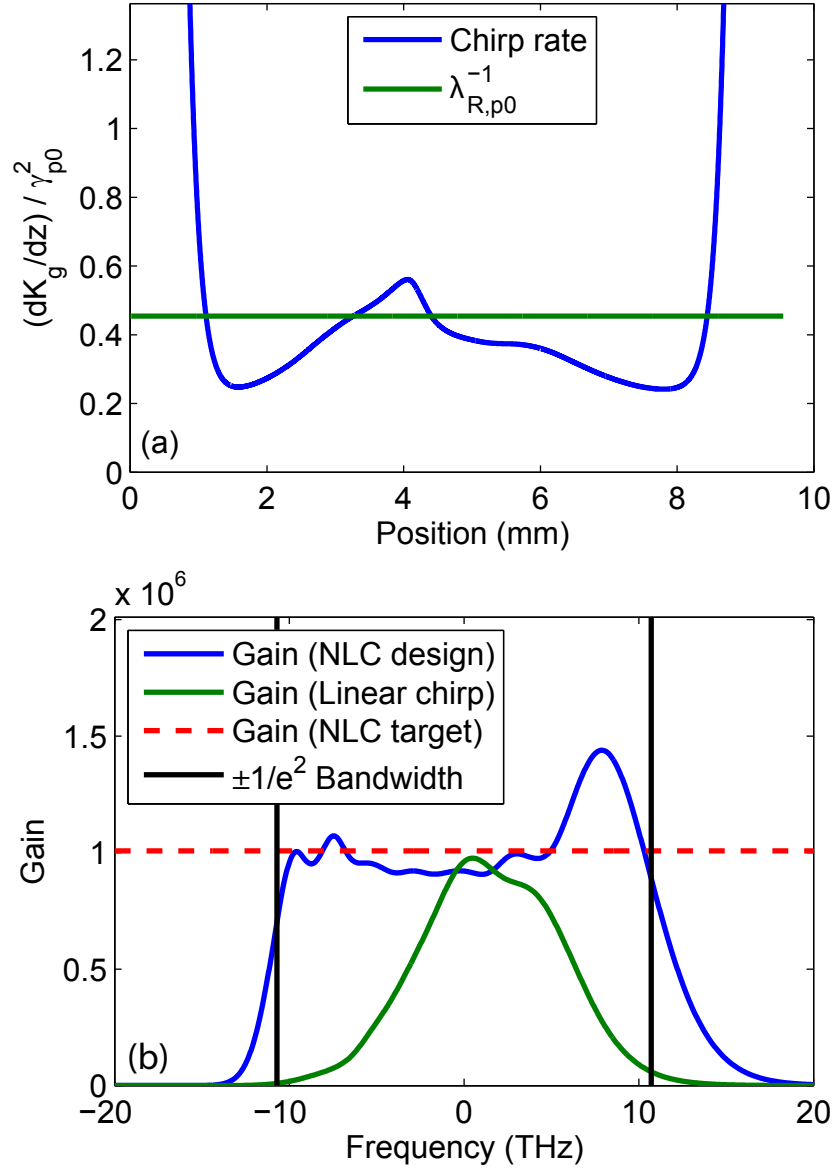


Figure 8.3: Nonlinear chirp design example using convex optimization. (a) Optimized chirp rate, normalized to the peak gain coefficient of the pump,  $\gamma_{p0}$ . The horizontal line indicates the constant chirp rate needed for Eq. (8.14) to yield the target gain spectrum if  $\gamma(\omega) = \gamma_{p0}$ . (b) Simulated output spectrum. The spectrum with a nominally linear, apodized chirp profile is shown for comparison.

the target gain. The actual simulated gain differs slightly from the predictions of Eq. (8.14), but is close enough to represent a useful design example. The gain spectrum

of a nominally linear, apodized grating design supporting the same OPA bandwidth (for a top-hat pump intensity profile versus time) is shown for comparison; the gain narrowing which occurs for such a design can easily be seen in the figure.

A number of other convex formulations of this grating design problem are possible, but Eq. (8.22) has several advantageous properties. First, it involves only a small number of free parameters, appropriate values of which can be estimated by inspection. Only  $L_{\max}$  may be difficult to guess in some cases, but the problem can be solved in a few seconds, so testing a range of values of a single parameter is straightforward. Furthermore, our objective function has two particularly advantageous properties. First, it ensures that  $z_K$  is a good approximation to an underlying continuous variable. Second, recall that this whole approach relies on the validity of Eq. (8.14), which in turn relies on having a sufficiently slowly-varying grating chirp: by using smoothness as an objective, we maximize the validity of the approximation upon which the optimization relies.

To summarize the NLC design: we chose a ratio of signal and pump durations, a target value of the gain plus an acceptable tolerance range around this gain, and very forgiving bounds on the chirp rate and grating length. These choices were sufficient to find a nominal grating design.

It is worth emphasizing that the convex optimization approach allows us to add additional convex constraints as needed. For example, by adding extra constraints to the problem, we can ensure that the gain spectrum is flat at multiple transverse spatial components of the beam. That is, if we neglect diffraction and consider some transverse component  $r$  of the pump beam, then the gain spectrum for that point is still determined by a matrix  $\Gamma(r)$ . The only difference is that the pump intensity, and hence  $\gamma(\omega)$ , is reduced compared to the peak of the beam. We can just take this matrix  $\Gamma(r)$  and specify that the gain  $\ln(G_s(r)) = \Gamma z_K$  should not fluctuate too much, i.e.  $-\delta G(r) \leq \Gamma(r) z_K - \kappa \leq \delta G(r)$  for some scalar  $\kappa$ . In this inequality,  $\kappa$  is just an unconstrained scalar variable: we do not need to know anything about it. An arbitrary number of these constraints (or, of course, any other convex constraint) can be added to Eq. (8.22).

### 8.3.3 Apodization

Another reason to use a nonlinear chirp profile besides the engineering of broad gain spectra discussed in section 8.3.2 is to apodize the QPM grating. We have used such nonlinear chirp apodization profiles in devices described in chapter 7 and subsection 8.3.2, but have not yet discussed these profiles in detail. In this section, we discuss optimal apodization designs for a specific type of interaction (high-gain OPA). The general approach we take is to start from a nominal grating design, such as a linear chirp or a nonlinear chirp design of the type discussed in subsection 8.3.2. Apodization regions are then appended to this nominal design, with the grating k-vector and duty cycle matched at the joining points. To construct the apodization regions, we take an inequality involving the chirp rate which must be satisfied in order for a particular type of solution to apply, and then turn this inequality into a differential equation for the grating parameters.

Apodization consists of smoothly turning the three-wave mixing interaction “off” at the input and output sides of the grating. Without apodization, the output spectrum exhibits a pronounced and unwanted ripple in amplitude and phase. Mathematically, the goal of apodization is generally to adiabatically evolve the ratio of phase mismatch to coupling coefficient, defined as  $\nu$  in Eq. (7.23), such that  $|\nu| \gg 1$  at the edges of the grating [in physical units,  $|\Delta k/(2\gamma)| \gg 1$ ]. If this condition is not met, then the nonlinear eigenmodes are not matched to the known input and desired output conditions (zero input idler and zero output pump, respectively).

A similar condition should be met in other interactions as well. For example, in the context of DFG interactions when changes to both the signal and pump are negligible, the output idler spectrum is described by a transfer function involving the spatial Fourier transform of the grating. Without apodization, the hard edges of the crystal (where  $\chi^{(2)}$  is abruptly turned on and off) give rise to a ripple in the Fourier spectrum. Another important example is the undepleted-pump OPA case discussed in section 7.3, which can be accurately described by WKB solutions. Without apodization, the fields are not properly launched into the desired WKB solution, and there is unwanted interference (see appendix E of [51]). This interference gives rise to a ripple in the gain spectrum.

The optimal choice of apodization profile depends on the type of interaction the device is designed for. With the results of chapter 7, apodization regions can be designed for both low and high pump depletion chirped-QPM OPA interactions. In a high-pump-depletion device, a sufficient goal is to obtain the adiabatic following solutions for each spectral component of interest; the key inequality for this constraint is Eq. (7.37). For a low-pump-depletion device, a sufficient goal is to maintain the WKB solutions of the undepleted-pump propagation equations; the key inequality for this constraint is Eq. (7.22). In Fig. 7.6, we showed that simultaneously obtaining high gain and conversion efficiency is usually impractical. Fig. 7.6 also shows that the contours of constant pump depletion  $\eta$  (which are plotted versus  $\ln(\rho)$  and  $\lambda_{R,p}$  in the figure) are straight even for moderate values of  $\eta$ ; these contours change shape only in the high-pump-depletion regime ( $\ln \eta < -\pi$ ). For these reasons the WKB-based constraint is likely to be of greater interest for practical applications, and is therefore the focus of this section. We usually want to perform apodization over as small a region as possible in order to minimize the severity of various parasitic effects, such as those discussed in sections 8.4 and 8.5.

We first repeat the relevant results of section 7.3 here for convenience, using physical units. Propagation of the signal is governed by the equation

$$\frac{d^2 a_s}{dz^2} + Q(z)a_s, \quad (8.23)$$

where the ‘‘potential’’  $Q(z)$  is given by

$$Q = -\gamma_p^2 + \frac{1}{2} \frac{d}{dz} \left( \frac{\gamma_p'}{\gamma_p} \right) - \frac{i\Delta k'}{2} - \frac{1}{4} \left( \frac{\gamma_p'}{\gamma_p} - i\Delta k \right)^2, \quad (8.24)$$

where the coupling coefficient  $\gamma_p$  is assumed to be real. The WKB solutions of Eq. (8.23) are valid provided that

$$\left| \frac{dQ}{dz} \frac{1}{Q^{3/2}} \right| \ll 1. \quad (8.25)$$

In a linearly chirped grating, the left hand side of this inequality becomes very small

far from the turning points, i.e. for  $\Delta k \ll -2\gamma_p$  and  $\Delta k \gg 2\gamma_p$ . The use of a linear chirp in these regions is inefficient: the chirp rate can be increased while still satisfying Eq. (8.25). By turning Eq. (8.25) into an equality, a differential equation for  $K_g$  or  $\gamma_p^2$  can be obtained which maintains the WKB solutions to some chosen fidelity. Therefore, we write the inequality as

$$\left| \frac{dQ}{dz} \frac{1}{Q^{3/2}} \right| \leq \epsilon, \quad (8.26)$$

for “small”  $\epsilon$ . This condition yields an implicit differential equation which as stated is difficult to solve. A much simpler equation is obtained by writing the coupling coefficient  $|\gamma_p|^2$  and the chirp rate  $K_z \equiv dK_g/dz$  as functions of  $K_g$ , and integrating versus  $K_g$  (note that this approach is possible because we always assume that  $K_g$  is monotonic in  $z$ ). For notational convenience, we suppress the  $g$  subscript on  $K_g$ . For simplicity, we also assume that  $\gamma_p$  is real and constant versus position and frequency. With this notation, the following equation can be obtained from Eq. (8.26)

$$\begin{aligned} \left( \frac{dK_z}{dK} \right)^2 &\leq \frac{4\epsilon^2}{K_z^2} \left| \left( \frac{\Delta k}{2} \right)^2 - \gamma_p^2 + i \frac{K_z}{2} \right|^3 - \Delta k^2 \\ &\equiv f_\epsilon(K, K_z, \Delta k) \end{aligned} \quad (8.27)$$

where  $\Delta k = \Delta k_0 - K$ , and  $\Delta k_0$  is the material phase mismatch. Eq. (8.27) must be satisfied for the range of  $\Delta k_0$  corresponding to the spectral bandwidth of the device. Close to the turning points (which satisfy  $\Delta k = \pm 2\gamma_p$ ), the right hand side is negative (except for large values of  $\epsilon$ ), which means that  $|dQ/dz| > \epsilon|Q^{3/2}|$ . The function  $f$  has been introduced as a shorthand to identify the frequency-dependence of the inequality.

If we move far enough from the turning points (towards the edges of the nominal grating profile) then equality is obtained. The minimum and maximum values of  $\Delta k_0$ , in particular, define the closest pair of grating k-vectors for which Eq. (8.27) is satisfied (for the nominal grating profile) for the entire range of values of  $\Delta k_0$  corresponding to the amplification bandwidth. We denote these two k-vectors as

$K_{\text{apod},s}$  and  $K_{\text{apod},e}$ . We assume that the (inverse) grating profile  $z(K)$  corresponds to the nominal profile  $z_{\text{nom}}(K)$  for  $K$  between  $K_{\text{apod},s}$  and  $K_{\text{apod},e}$ , and is determined via Eq. (8.27) outside this region. Eq. (8.27) can be turned into a differential equation by taking the worst-case value of  $\Delta k_0$  (the one for which  $|\Delta k|$  is smallest).

Based on the above discussion, we first determine  $K_{\text{apod},s}$  and  $K_{\text{apod},e}$  by solving the following pair of equations:

$$\begin{aligned} f_\epsilon(K_{\text{apod},j}, K_{z,\text{nom}}, \min_{\Delta k_0} [|\Delta k(K_{\text{apod},j})|]) &= 0, \\ \min_{\Delta k_0} [|\Delta k(K_{\text{apod},j})|] &> 2\gamma_p \end{aligned} \quad (8.28)$$

where subscript “nom” denotes the nominal grating profile, and where minimization with respect to  $\Delta k_0$  consists of choosing the value of  $\Delta k_0$ , within the spectral bandwidth, for which the magnitude of  $\Delta k(K)$  is smallest. For a linearly chirped grating,  $K_{z,\text{nom}}(K)$  is constant. It is convenient to define the k-space domain of the nominal grating:

$$\text{dom}(K_{\text{nom}}) = \left\{ K : \min_j(K_{\text{apod},j}) \leq K \leq \max_j(K_{\text{apod},j}) \right\}. \quad (8.29)$$

We now use  $K_{\text{apod},j}$  to define the rest of the grating by solving the following equations for  $K_z(K)$ :

$$\begin{aligned} K_g(z) &= K_{\text{nom}}(z) & K \in \text{dom}(K_{\text{nom}}) \\ \frac{dK_z}{dK} &= \min_{\Delta k_0}(f) & K \notin \text{dom}(K_{\text{nom}}) \end{aligned} \quad (8.30)$$

with the initial condition

$$K_z(K_{\text{apod},j}) = K_{z,\text{nom}}(K_{\text{apod},j}). \quad (8.31)$$

We then determine  $z(K)$  by

$$z(K) = \int_{K_i}^{K_f} K_z(K)^{-1} dK, \quad (8.32)$$

and invert this function to find  $K_g(z)$ .

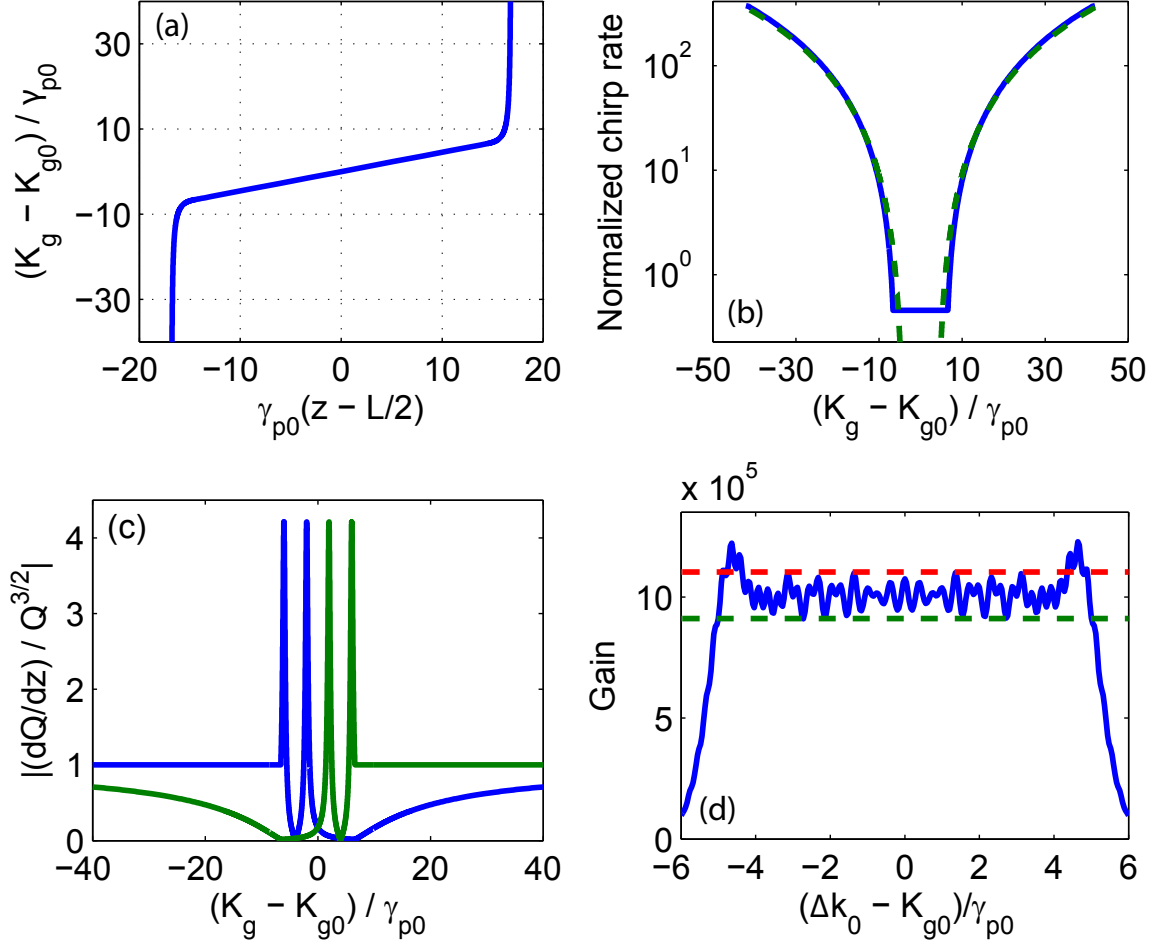


Figure 8.4: WKB-based apodization example. (a) Grating k-vector profile, (b) Grating chirp rate. The dashed lines show  $\min(\delta k^2)\epsilon$ , indicating that the optimal normalized chirp rate in the apodization region approximately satisfies  $|\delta k'| = \min(\delta k^2)\epsilon$ . (c)  $|(dQ/dz)/Q^{3/2}|$ , bounded above by  $\epsilon = 1$  for positions sufficiently far from the range of amplification regions. The two curves correspond to the ends of the target amplification spectrum (d) Amplified signal spectrum. The dashed lines indicate the fluctuations in the gain due to the finite value of  $|\gamma_{p0}/\Delta k|$  at the ends of the grating.

An example implementation of this design procedure is shown in Fig. 8.4. We plot the results in terms of the normalized parameters introduced in chapter 7 since the results are easier to interpret in this form. The parameters we assumed for the simulation were  $\lambda_{R,p} = 2$ ,  $\rho \rightarrow 0$ , and  $\epsilon = 1$ . The range of carrier phase mismatches

to be amplified satisfies  $\max(\Delta k_0) - \min(\Delta k_0) = 8\gamma_{p0}$ . The minimum and maximum grating k-vectors satisfy  $K_g(L) - K_{g0} = -40\gamma_{p0}$  and  $K_g(0) - K_{g0} = +40\gamma_{p0}$ , where  $K_{g0}$  is the grating k-vector required to phasematch the center frequency; it is useful to introduce the parameter  $\delta$  to describe the range of grating k-vectors,

$$|K_g - K_{g0}|/\gamma_{p0} \leq \delta, \quad (8.33)$$

where  $\delta = 40$  for the present example. This value is chosen to yield a large value of  $|\nu|$  [Eq. (7.23)] at the ends of the device.

The k-vector profile is shown in Fig. 8.4(a). In Fig. 8.4(b), the grating chirp rate is compared to  $\delta k^2$ , illustrating that optimal normalized chirp rate is proportional to the square of the minimum phase mismatch. The value of  $|(dQ/d\zeta)/Q^{3/2}|$  is shown in Fig. 8.4(c) for the end-points of the amplification bandwidth; this figure illustrates that Eq. (8.30) is satisfied. The resulting output gain spectrum as a function of  $\delta k_0 = (\Delta k_0 - K_{g0})/\gamma_{p0}$  is shown in Fig. 8.4(d). The finite value of  $\delta^{-1}$  defined above results in a ripple in the gain, such that  $|\ln(G_s) - 2\pi\lambda_{R,p}| \leq 4\delta^{-1}$  for frequencies within the amplification region [51]. The dashed lines in (d) were calculated using this expression; they bound the signal gain within the designed amplification range [i.e. within the range  $\max(\Delta k_0) - \min(\Delta k_0) = 8\gamma_{p0}$ ].

To suppress the gain ripple further, we could specify a function  $G(K)$  which is equal to  $|\gamma_{p0}|^2$  at  $K_{\text{apod},j}$  and equal to 0 at the ends of the grating, and substitute this function into Eq. (8.24) to arrive at an inequality of the same form as Eq. (8.26). This approach could yield better apodization (by increasing the value of  $|\nu|$  at the edges of the device). One could in principle choose an optimal  $\gamma_p(K)$  profile, but we have found that the apodization process is not too sensitive to different choices of  $\gamma_p(K)$ . Furthermore, control of  $\gamma_p$  is difficult in practice, since it requires precise control of the QPM duty cycle [26]. We therefore omit a more detailed analysis of this aspect of the problem.

Before concluding this section, we re-iterate that a similar procedure to the one detailed above could be applied based on Eq. (7.37) to define an optimal grating satisfying the adiabatic following constraint for all the spectral components involved.

We can therefore fully specify a plane- and quasi-continuous-wave design for all the cases of interest.

## 8.4 Coincidentally-Phasematched Processes

A number of factors can cause the minimal plane-coupled-wave model to break down. For example, many components of the nonlinear polarization are neglected by the three-wave mixing equations (7.11). In deriving these equations, the only components of the nonlinear polarization that were retained were those with carrier frequency equal to that of the idler, signal, or pump. The significance of the neglected components for a chirped-QPM OPCPA design can be estimated by performing a series of phasematching calculations, assuming a pump with a single-frequency component  $\omega_p$ . For each frequency  $\omega_s$ , all sum and difference frequencies involving  $\omega_i = \omega_p - \omega_s$ ,  $\omega_s$ , and  $\omega_p$  are generated (and in turn, all processes involving sums and differences of the resulting set also occur, and so on).

### 8.4.1 Phasematching

The most relevant DFG-like process (excluding the desired OPA process itself) is the generation of frequency  $\omega_{DF} = |\omega_s - \omega_i|$ ; the corresponding phase mismatch for this process is

$$\Delta k_{si}^{DFG} = k(\max(\omega_i, \omega_s)) - k(|\omega_s - \omega_i|) - k(\min(\omega_i, \omega_s)). \quad (8.34)$$

Many SFG processes also occur, generating frequencies

$$\omega_{pq}^{SFG} = \omega_p + \omega_q \quad (8.35)$$

for indices  $p$  and  $q$  in  $\{i, s, p\}$ . The corresponding phase mismatches are given by

$$\Delta k_{pq}^{SFG} = k(\omega_p + \omega_q) - k(\omega_p) - k(\omega_q). \quad (8.36)$$

Subsequent mixing processes involving these waves can also occur. A notable example is OPA of the idler SH by the pump.

The phase mismatches can be compared to the range of grating k-vectors required to quasi-phasematch the desired OPA process ( $\Delta k_{is}^{SFG}$  in this notation) by plotting each  $\Delta k_{pq}(\omega_s)$  over the frequency range of interest. In Fig. 8.5, we plot the phase-matching period  $\Lambda$  for several processes, assuming a pump wavelength of  $1.064\text{-}\mu\text{m}$  and all-*e*-wave polarized interactions in a MgO:LiNbO<sub>3</sub> crystal operated at  $150^\circ\text{C}$ . For the purposes of the figure we assume  $\omega_s > \omega_i$  (that is, signal refers to the short wave); in the other sections of this chapter, signal refers to the seeded wave. Some processes are quasi-phasematched by an order  $m \neq 1$  of the grating, so in these cases the quantity  $\Delta k/m$  is plotted, where  $m$  is the integer for which  $|\Delta k - mK_g|$  is smallest.

To interpret Fig. 8.5, consider an example case where OPA phasematching must be satisfied for idler wavelengths between  $3\text{-}4\ \mu\text{m}$ : the corresponding range of grating periods is approximately  $28.6\text{-}30.9\ \mu\text{m}$  (solid blue curve). Consider the  $3.8\text{-}\mu\text{m}$  idler component. If the grating is positively chirped ( $\Delta k' > 0$ ; short QPM periods near the input end of the crystal) then this component is first amplified where the local period is  $\approx 29.1\ \mu\text{m}$ . Near the end of the grating, where the period is  $\approx 30.5\ \mu\text{m}$ , SHG of this component is satisfied. If the amplified idler is sufficiently intense, this process can be efficient, leading to distortions of the pulse. If an even wider range of periods is present, for example  $28\text{-}32\ \mu\text{m}$ , then the idler is first amplified where the period  $\Lambda \approx 29.1\ \mu\text{m}$ , up-converted to its SH around  $\Lambda \approx 30.5\ \mu\text{m}$ , and this SH is itself amplified (by the pump of frequency  $\omega_p$ ) around  $\Lambda \approx 31.7\ \mu\text{m}$  (dashed curve). If the SHG process is reasonably efficient, then the idler SHG can effectively experience OPA twice, and hence have very high gain. Similar arguments can be made for the other spectral components and processes illustrated. When the QPM periods for different processes are quite close, the k-space extent of these processes is important (for example, OPA occurs over the region for which  $|\Delta k| < 2\gamma$ ).

In apodizing the grating, a highly nonlinear chirp profile is imposed in order to achieve a weak interaction and the ends of the grating (section 8.3.3). Such a profile entails a wide range of QPM periods, and hence the period is swept through the various processes illustrated in 8.5. For example, the period may be swept through

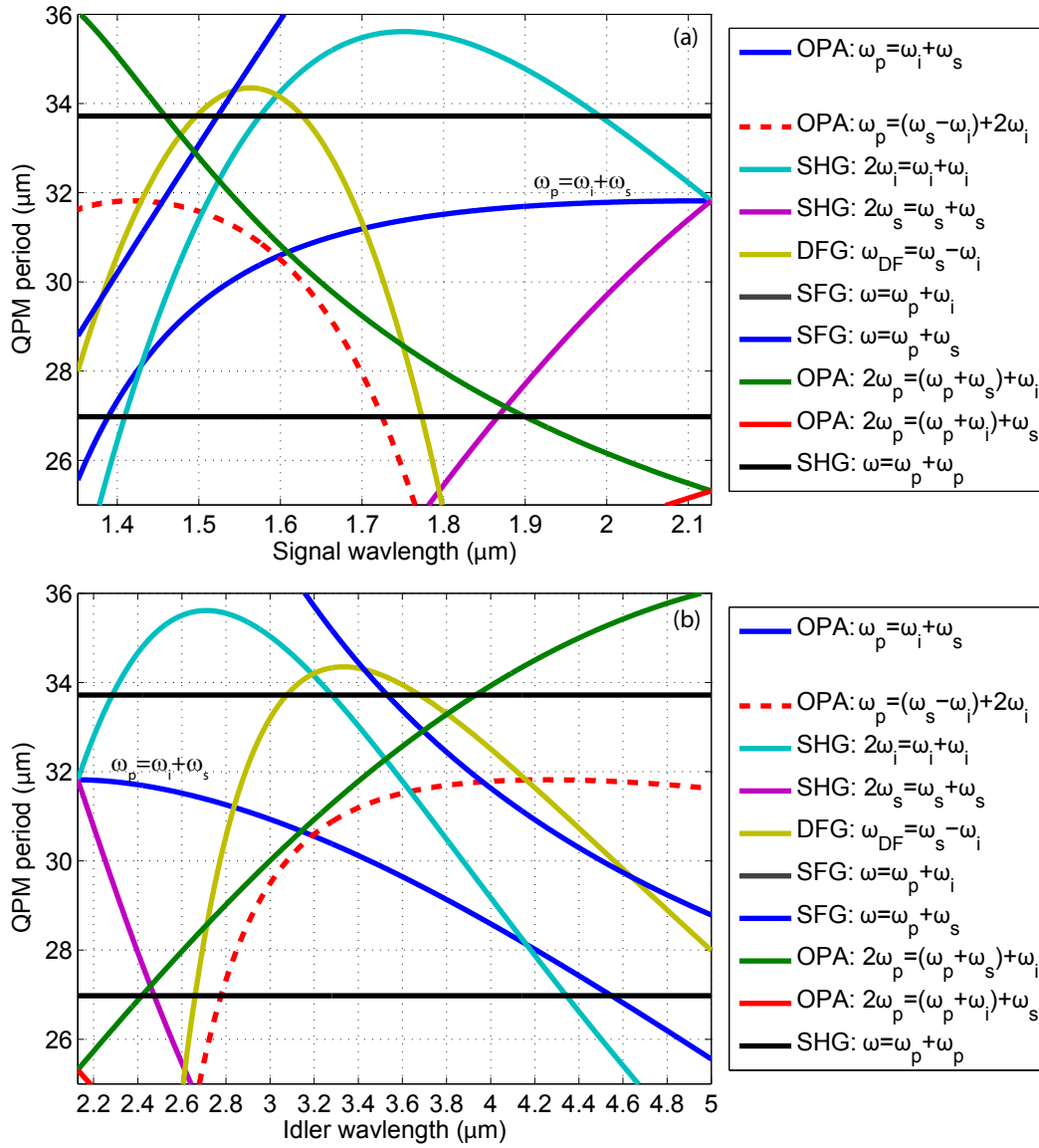


Figure 8.5: Coincidentally phasematched processes, assuming a pump wavelength of  $1.064 \mu\text{m}$ , as a function of (a) the smaller of the signal and idler wavelengths, and (b) the longer of the signal and idler wavelengths. For this figure we assume  $\omega_s > \omega_i$ . The legend indicates the type of interaction (SHG, OPA, or SFG) and the frequencies involved. The desired OPA interaction is  $\omega_p = \omega_i + \omega_s$ ; the corresponding curve is indicated. For each process, we consider phasematching for the nearest-odd-order of QPM (except for pump SHG process, for which we show 4<sup>th</sup>- and 5<sup>th</sup>-order QPM).

pump SHG phasematching. Even though the chirp rate is rapid, the pump may be intense enough for the SHG process to have non-negligible efficiency. The efficiency of this process can be estimated by integrating Eq. (1.33b). Since pump SHG occurs at 4<sup>th</sup>- and 5<sup>th</sup>-order QPM, it is possible in principle to suppress this process by an appropriate choice of QPM duty cycle in the regions where SHG phasematching is satisfied (50% for 4<sup>th</sup>-order, and 40% or 60% for 5<sup>th</sup>). This level of control of the duty cycle can be challenging in practice, however [26].

Based on Fig. 8.5, in order to avoid efficient long-wave SHG ( $2\omega_i = \omega_i + \omega_i$ ) in an amplifier designed for wavelengths between 3 and 4  $\mu\text{m}$ , the chirp rate should be negative ( $\Delta k' < 0$ ), since with this choice SHG of the long-wave idler is phasematched before that idler has been amplified via the OPA process, and so the parasitic SHG process has low efficiency.

## 8.4.2 Numerical Example

When the phasematching regions for the different processes are sufficiently separated, simple expressions for their efficiency can be obtained. This is not always the case, however, so it is useful to simulate all of the processes which are close to or pass through phasematching using a generalized coupled-wave model similar to the one given in chapter 5 but for an OPA process and the resulting additional carrier waves generated through the various mixing processes (instead of the harmonic-generation processes which were discussed in chapter 5).

Such coupled-wave models can be obtained using the approach described in section 1.5, but keeping a larger number of carrier waves and all of the corresponding polarization terms. In the examples shown in Fig. 8.6 and 8.7, we consider CW interactions involving several different spectral components. The set of frequencies included in these simulations is as follows:  $\omega_i$ ,  $\omega_s$ ,  $\omega_p$ ,  $2\omega_i$ ,  $2\omega_s$ ,  $2\omega_p$ ,  $\omega_i + \omega_p$ ,  $\omega_s + \omega_p$ , and  $\omega_s - \omega_i$ . The assumed parameters are  $\lambda_{R,p} = 2$  and  $\rho = 10^{-6}$ . The chirp rate  $|\Delta k'| = 3 \times 10^6$ , and grating length  $L = 10$  mm. Similar apodization profiles to those defined in Eqs. (7.15) and (7.16) are used.

Several features are apparent from these figures. In Fig. 8.6(a), where the chirp

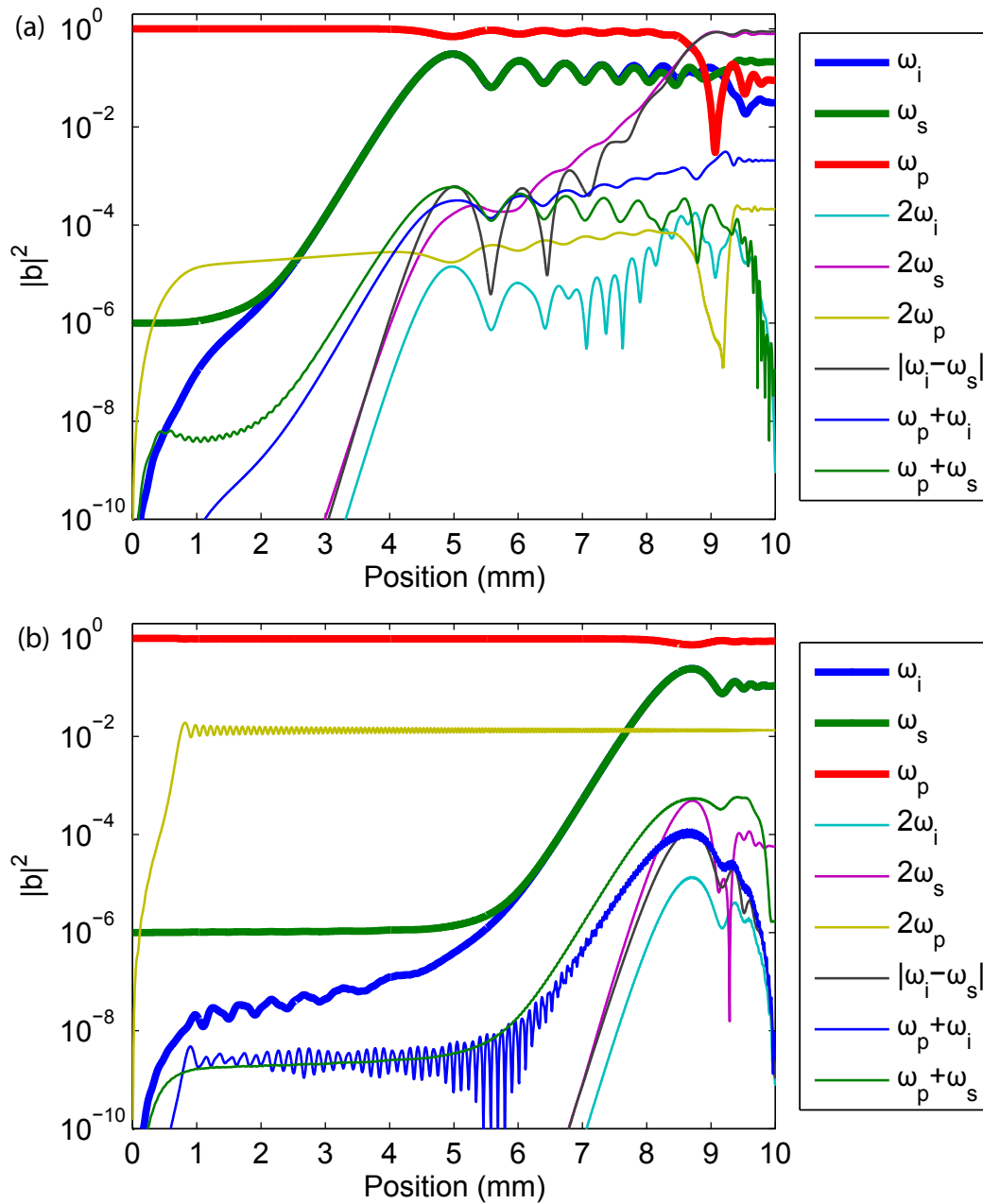


Figure 8.6: Numerical example including several carrier waves. The pump and idler wavelengths are  $1.064\text{-}\mu\text{m}$  and  $3.8\text{-}\mu\text{m}$ , respectively. The legend shows the frequency of each wave included in the model. The chirp rate ( $\text{sgn}(\Delta k')$ ) is (a) positive, and (b) negative. The parameters are given in the text

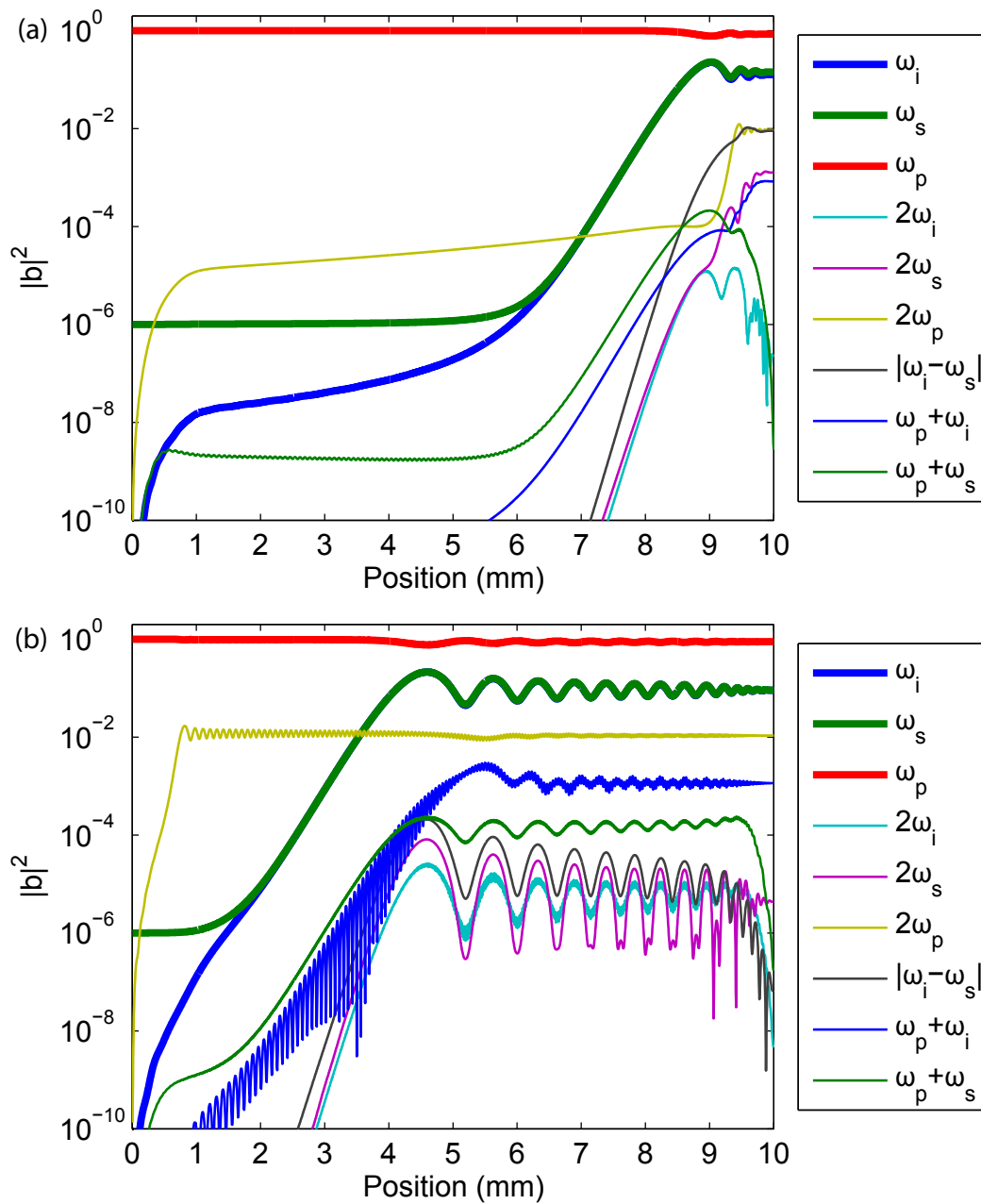


Figure 8.7: Numerical example including several carrier waves, with a 3.0- $\mu\text{m}$  idler wavelength. The other parameters are the same as Fig. 8.6. The legend shows the frequency of each wave included in the model.

rate is positive, the signal and idler are fully amplified around 5 mm from the input. Shortly after this point, the idler SHG process is phasematched, and then the idler-SH OPA process is phasematched. This latter process leads to exponential growth of the  $(\omega_s - \omega_i)$  and  $(2\omega_i)$  spectral components. Near the end of the grating, these components actually become stronger than the idler and signal themselves, and can even deplete the pump. The other curves in Fig. 8.6(a) exhibit no particularly prominent features, except an overall growth for up-converted components, since these are driven by waves which are amplified.

The behavior of Fig. 8.6(b), where the chirp rate is negative, is quite different. The only non-negligible waves at the output are the desired signal and idler, the pump, and a significant but still comparatively small pump second harmonic. Since idler SHG and idler-SH-OPA occur before idler OPA, these former two processes are inefficient and do not play a significant role. Therefore, the undesired coincidentally-phasematched processes which occur in 8.6(a) have been avoided by using a negative chirp rate. Note also that pump SHG is satisfied early in the grating, within the nonlinear chirp apodization region. This process could in principle be suppressed by using a 40% or 60% QPM duty cycle.

## 8.5 Statistical Phasematching

Even when one of the processes discussed in subsection 8.4 is phase mismatched, it can still be significant due to non-idealities in the QPM grating. In an ideal QPM grating, highly phase-mismatched interactions are weak and couple only a negligible amount of light out of the waves of interest. In practice, however, the actual positions where  $\bar{d}(z)$  is inverted differ slightly from the ideal (designed) positions. In lithographically-defined gratings in LiNbO<sub>3</sub>, where QPM is obtained by inversion of ferroelectric domains, these offsets are random from one tooth of the grating to the next, and (to good approximation) independent and identically distributed, with a normal distribution. Such errors are termed random duty cycle (RDC) errors. One consequence of their distribution is that, if we perform an ensemble average over many gratings with different random errors, there is a white “noise pedestal” in the

magnitude of the spatial Fourier transform. This pedestal in the SHG phasematching spectrum can be estimated by assuming a plane- and continuous wave interaction, as in Eqs. (1.33), and neglecting changes to the FH. The SH can then be approximated via Eq. (1.33b):

$$A_2 = -i \frac{2}{\pi} \frac{\omega_1 d_{\text{eff}}}{n_2 c} A_1^2 L \tilde{h}(\Delta k) \quad (8.37)$$

where  $d_{\text{eff}}$  is the relevant nonlinear tensor element,  $L$  is the length of the grating, and  $\tilde{h}(k)$  is an appropriately normalized spatial Fourier transform of the grating, given by

$$\tilde{h}(k) = i \frac{\pi}{kL} \sum_{n=1}^N (-1)^n e^{-ik\mathbf{z}[n]} \quad (8.38)$$

where  $\mathbf{z}$  is the vector of domain boundary positions. This expression for  $\tilde{h}$  is accurate when the number of domains  $N$  is large [14]. The SHG efficiency normalized to that of a first order QPM process in an ideal 50% duty cycle grating is given by  $|\tilde{h}(\Delta k)|^2$  for phase mismatch  $\Delta k$ . For an ideal grating of period  $2\pi/K_g$ ,  $|\tilde{h}(K_g)|^2 = 1$ . The normalized SHG efficiency averaged over an ensemble of gratings with the same normal distribution of random position errors is given by  $\langle |\tilde{h}(\Delta k)|^2 \rangle$  for SHG phase mismatch  $\Delta k$  [14], where

$$\langle |\tilde{h}(k)|^2 \rangle = e^{-(k\sigma_z)^2} |\tilde{h}_0(k)|^2 + N \left( \frac{\pi}{kL} \right)^2 \left( 1 - e^{-(k\sigma_z)^2} \right). \quad (8.39)$$

In this equation,  $\sigma_z$  is the standard deviation of the domain boundary positions and  $\tilde{h}_0(k)$  is the spatial Fourier transform of the ideal grating. The first term in this equation represents the ideal (error-free) efficiency reduced by a factor which depends on the size of the domain boundary errors, and the second term represents a noise “pedestal” that depends on the number of domains in the grating. This pedestal can be viewed either as the random-walk sum of the contributions from each of the narrow “error” regions at each boundary, or in the spatial frequency domain as the incoherent sum of the  $N$  very broad ( $\approx \pi/\sigma_l$ ) Fourier transforms of each of the error regions at each of the  $N$  boundaries. Processes for which  $|\tilde{h}_0(\Delta k)| \ll 1$  are inefficient

in the ideal structure, but can be enhanced in the actual structure by the presence of the noise pedestal. One class of applications where this enhancement is significant is single-photon frequency conversion [129, 130, 131, 132, 133, 134, 135, 136].

In the context of OPCPA, the enhancement of pump SHG due to RDC errors can be important. When the pump SHG process is highly phase mismatched in the ideal grating, RDC errors lead to an approximately linear growth of the pump SH intensity with respect to position  $z$  (as compared to the quadratic growth that would obtain in a perfectly phasematched grating in which the contributions from the  $N$  domains add coherently). If the pump is intense enough, its SH can become intense enough to exhibit significant two-photon absorption (TPA). In turn, this TPA can lead to a large thermal load and/or photorefractive beam distortions, which can cause a number of detrimental effects including thermal lensing that distorts the interacting beams, or in more extreme cases can even include fracture of the crystal itself.

A similar ensemble-averaging procedure can be applied to estimate the absorption of the SH. The absorbed intensity due to TPA is given by

$$I_{\text{abs}} = \int_0^z \beta_{TPA} I_2(z')^2 dz', \quad (8.40)$$

where  $\beta_{TPA}$  is the TPA coefficient and  $I_2$  is the SH intensity. It is convenient to approximate this integration as a summation over the ensemble-averaged intensities within each domain,

$$\begin{aligned} \langle I_{\text{abs}} \rangle &\approx \left\langle \sum_{m=1}^N \Lambda_{D,m} \beta_{TPA} I_2(\mathbf{z}[m])^2 \right\rangle \\ &\approx \beta_{TPA} I_{\text{max}}^2 \frac{L}{N} \left\langle \sum_{m=1}^N |\tilde{h}^{(m)}(k)|^4 \right\rangle, \end{aligned} \quad (8.41)$$

where  $\Lambda_{D,m}$  is the length of domain  $m$ . We have approximated each  $\Lambda_{D,m}$  coefficient according to  $\Lambda_{D,m} \approx \Lambda_D \equiv L/N$ , on the assumption that the total range of QPM

periods is relatively small.  $\tilde{h}^{(m)}(k)$  is the normalized SH amplitude at position  $\mathbf{z}[m]$ ,

$$\tilde{h}^{(m)}(k) = \frac{\pi}{kL} \sum_{n=1}^m (-1)^n e^{-ik\mathbf{z}[m]}, \quad (8.42)$$

and hence  $\tilde{h} = \tilde{h}^{(N)}$ . The “maximum” SH intensity, denoted  $I_{\max}$ , is the SH intensity which would be predicted for a perfectly quasi-phasematched interaction in an ideal periodic grating if pump depletion effects were neglected, and is given by

$$I_{\max} = \frac{n_2 \epsilon_0 C}{2} \left| \frac{2 \omega_1 d_{\text{eff}}}{\pi n_2 c} A_1^2 L \right|^2. \quad (8.43)$$

In order to evaluate Eq. (8.41), we need to find  $\langle |\tilde{h}^{(n)}|^4 \rangle$ . After some algebra, it can be shown that

$$\begin{aligned} \left\langle |\tilde{h}^{(n)}(k)|^4 \right\rangle &\approx 2n^2 \left( \frac{\pi}{kL} \right)^4 \left( 1 - e^{-(k\sigma_z)^2} \right)^2 \\ &\quad + 4n \left( \frac{\pi}{kL} \right)^2 \left( 1 - e^{-(k\sigma_z)^2} \right) e^{-(k\sigma_z)^2} |\tilde{h}_0^{(n)}(k)|^2 \\ &\quad + e^{-2(k\sigma_z)^2} |\tilde{h}_0^{(n)}(k)|^4 \end{aligned} \quad (8.44)$$

To estimate the SH TPA, we keep only the noise pedestal term in each  $\tilde{h}^{(n)}$  [the first term in Eq. (8.44)], under the assumption that the SHG process is highly phase mismatched. By substituting Eqs. (8.43) and (8.44) into Eq. (8.41), summing over the intensity absorbed within each domain, and assuming  $N^3 \gg N^2$ , the following expression for the total, ensemble-averaged TPA can be obtained:

$$\langle I_{\text{abs}} \rangle \approx \frac{2}{3} \beta_{TPA} I_{\Lambda}^2 \Lambda_D \left( \frac{L}{\Lambda_D} \right)^3 \left( \frac{\pi \sigma_z}{\Lambda_D} \right)^4 \left( \frac{1 - e^{-k^2 \sigma_z^2}}{k^2 \sigma_z^2} \right)^2 \quad (8.45)$$

where  $\Lambda_D$  is the average domain size, and  $I_{\Lambda} = I_{\max}(\Lambda_D/L)^2$  is the “maximum” intensity from a single domain of size  $\Lambda_D$ ; this substitution is made so that Eq. (8.45) gives the length-dependence of  $\langle I_{\text{abs}} \rangle$  explicitly. For sufficiently small errors, the final factor in parentheses is equal to 1. Eq. (8.45) thus indicates that  $I_{\text{abs}}$  is

proportional to  $L^3$  and  $I_1^4$ , where  $I_1$  is the FH intensity (which, in the context of OPCPA, would also be the pump), and hence using Eq. (7.4) to relate the coupling coefficient  $\gamma_{p0}$  to the pump intensity,

$$\langle I_{\text{abs}} \rangle \propto \frac{(\gamma_{p0}^2 L)^4 \sigma_z^4}{L}, \quad (8.46)$$

where the factor in parentheses is approximately proportional to the gain-bandwidth product [see Eq. (8.5)], which is usually constrained for an OPCPA system. Therefore, this equation shows that  $I_{\text{abs}}$  has an overall scaling with  $\sigma_z^4/L$  once other system constraints are met.

We next evaluate Eq. (8.45) with system parameters comparable to those considered in subsection 8.3.2. The pump wavelength is 1.064  $\mu\text{m}$ , the material is MgO:LiNbO<sub>3</sub>, the average domain size is assumed to be  $\Lambda_D = 14.94 \mu\text{m}$  (corresponding to OPA for a 3.5- $\mu\text{m}$  idler), and the crystal length is 10 mm. The SHG phase mismatch determines the spatial frequency at which Eq. (8.45) should be evaluated, and hence  $k = 9.317 \text{ m}^{-1}$ . We assume RDC errors such that  $\sigma_z = 1 \mu\text{m}$  [131]. The two-photon absorption coefficient of LiNbO<sub>3</sub> at 532 nm ( $\lambda_p/2$ ) is  $\beta_{TPA} = 0.38 \text{ cm/W}$  [54], the effective nonlinear coefficient for 1064-nm SHG involving the  $d_{33}$  tensor element is  $d_{\text{eff}} = 25.2 \text{ pm/V}$  [30], and the dispersion relation is given in Ref. [137]. For a first calculation, we assume a CW pump with an intensity of 10 GW/cm<sup>2</sup>. With these parameters, we find from Eq. (8.45) that  $\langle I_{\text{abs}} \rangle \approx 2.865 \text{ GW/cm}^2$  (a remarkably large fraction of the pump).

To determine the thermal load in the presence of a pulsed pump beam, the SH absorption must be integrated over both space and time. To perform this integration, we can make use of the transfer function result of Ref. [56], which implies that as long as GVD of the pump can be neglected, the SH is driven in the frequency domain by the Fourier transform of the square of the FH envelope. This result implies that Eq. (8.37) can be written as a more general frequency-domain equation:

$$\tilde{A}_2(\omega, L) \approx -i \frac{2 \omega_1 d_{\text{eff}} L}{\pi n_2 c} \mathcal{F} [A_1^2](\omega) \tilde{h}(\Delta k_{\text{SHG}}(\omega)) \quad (8.47)$$

where  $\omega_1$  is now treated as the carrier frequency of the FH.  $\Delta k(\omega)$  is the frequency-dependent phase mismatch for the SHG process; since GVD of the FH has been neglected, this phase mismatch is given by

$$\begin{aligned}\Delta k_{\text{SHG}}(2\omega_1 + \Omega) &= k(2\omega_1 + \Omega) - 2k(\omega) - \frac{\Omega}{v_g(\omega_1)} \\ &\approx \Delta k_{\text{SHG}}(2\omega_1) + \left( \frac{1}{v_g(2\omega_1)} - \frac{1}{v_g(\omega_1)} \right) \Omega,\end{aligned}\quad (8.48)$$

where  $v_g$  is the group velocity. The second expression neglects GVD of both the FH and SH (which is usually a good approximation when dealing with the narrow-bandwidth pumps typically used in OPCPA systems). The ensemble-averaged absorbed energy can be estimated as follows: we first modify Eq. (8.47) to find the local SH field  $\tilde{A}_2(\omega, z)$ , and take the inverse Fourier transform of  $\tilde{A}_2$  to determine the time- and position-dependent SH intensity,  $I_2(z, t)$ . This intensity is then substituted into Eq. (8.40), and the resulting integral over  $z$  is approximated as a summation over the domain boundary positions, analogously to Eq. (8.41). Next, consider the  $\Delta k$  bandwidth of the SHG interaction, denoted  $\Delta k_{BW}$ ; this bandwidth is approximately  $\Delta k_{BW} \approx |v_g^{-1}(2\omega_1) - v_g^{-1}(\omega_1)|\Omega_{BW}$ , where  $\Omega_{BW}$  is the optical frequency bandwidth of the FH. If this bandwidth is narrow, we can approximate the ensemble averages involving  $\tilde{h}^{(n)}(k)$  using Eq. (8.44) by just evaluating them at the carrier phase mismatch. With this approximation, the ensemble-averaged absorbed energy  $\langle U_{\text{abs}} \rangle$  is given by the following simple equation:

$$\langle U_{\text{abs}} \rangle = \left\langle I_{\text{abs}}^{(CW)} \right\rangle \iiint \bar{I}_1^4(x, y, t) dx dy dt, \quad (8.49)$$

where  $\bar{I}_1 \equiv I_1/I_{pk}$  denotes the normalized FH intensity (maximum equal to 1) and  $I_{\text{abs}}^{(CW)}$  denotes the absorbed intensity for a plane- and continuous wave case involving a FH of intensity  $I_{pk}$ .  $I_{\text{abs}}^{(CW)}$  can be directly calculated from Eq. (8.45). For Gaussian pulses in space and time ( $1/e^2$  radius  $w$ , FWHM duration  $\tau$ ), the integral in Eq.

(8.49) is given by

$$\iiint \bar{I}_1^4(x, y, t) dx dy dt = \left(\frac{\pi}{8}\right)^{3/2} \frac{w^2 \tau}{\sqrt{2 \ln(2)}}. \quad (8.50)$$

For the example considered above, where we assumed a peak pump intensity of  $I_{pk} = 10 \text{ GW/cm}^2$ , the CW ensemble-averaged absorbed intensity was  $\langle I_{\text{abs}}^{(CW)} \rangle = 2.865 \text{ GW/cm}^2$ . If we assume a Gaussian pump beam with a FWHM duration of 12 ps and an energy of 300  $\mu\text{J}$  (corresponding to a beam radius of 387  $\mu\text{m}$ ), Eq. (8.49) implies an ensemble-averaged absorbed energy of 7.18  $\mu\text{J}$ . At a repetition rate of 100 kHz (30 W pump power), this implies a thermal load of 718 mW, which is very large. With RDC errors of  $\sigma_z = 0.5 \mu\text{m}$  instead of 1  $\mu\text{m}$ , the predicted thermal load is reduced to 81 mW.

RDC-enhanced two-photon absorption effects can be suppressed in a number of ways, including: (1) use of a longer QPM grating (while still constraining the gain-bandwidth product), (2) improve fabrication to reduce RDC errors, (3) reduce the repetition rate of the pump to reduce the average power, (4) move to a material which can tolerate the predicted amount of absorbed pump SH, (5) split the system into additional amplifier stages to reduce the gain-bandwidth product per stage. The most straightforward approach is to increase the grating length  $L$  while keeping  $\gamma_{p0}^2 L$  constant, but this may not always be feasible due to the GVM-related constraints discussed in relation to Eq. (8.10).

## 8.6 Noncollinear Processes

The plane-wave model assumed in chapter 7 is appropriate for interactions involving beams of sufficient width that different transverse beam components do not interact. However, when the pump beam is too narrow, this approximation can break down, resulting in deleterious effects. In a chirped QPM OPA experiment, there can exist noncollinearly-phasematched modes of the signal and idler which can experience a gain that greatly exceeds that of the collinear signal seed. These modes can be seeded by quantum noise, and can hence lead to a significant reduction in noise

contrast of an OPCPA system. In extreme cases, noise can be amplified to the level of the pump itself, corresponding to optical parametric generation (OPG). These noncollinear modes were discussed in detail in Refs. [94, 138]; in the rest of this section, we summarize the most relevant results from these papers, and then determine their implications to the design of OPCPA systems.

### 8.6.1 Noncollinear Phasematching

We first discuss noncollinear phasematching, which refers to phasematching involving beams whose  $\mathbf{k}$ -vectors are in different directions. Consider a plane-wave interaction with  $\mathbf{k}$ -vectors  $\mathbf{k}_j$  for  $j \in \{i, s, p\}$  and a grating  $\mathbf{K}_g$ . Each  $\mathbf{k}_j$  satisfies  $|\mathbf{k}_j| = k(\omega_j)$ , where  $k(\omega_j)$  is one of the linear-optical eigenvalues (propagation constants) corresponding to Eqs. (1.7). The vector phase mismatch is given by

$$\Delta\mathbf{k} = \mathbf{k}_p - \mathbf{k}_s - \mathbf{k}_i - \mathbf{K}_g \quad (8.51)$$

This equation supports phasematching ( $\Delta\mathbf{k} = \mathbf{0}$ ) for both collinear and noncollinear signal and idler waves. In this section, we consider interactions in which  $\mathbf{k}_p = k_p \hat{\mathbf{z}}$  and  $\mathbf{K}_g = K_g \hat{\mathbf{z}}$  for scalars  $k_p = k(\omega_p)$  and  $K_g$ . Phasematching along the transverse coordinates  $x$  and  $y$  therefore implies that the transverse components of  $\mathbf{k}_i$  and  $\mathbf{k}_s$  must be equal and opposite. In order to express the  $z$ -component of the resulting phase mismatch as a function of the transverse spatial frequency components of the signal, Eqs. (1.7) must be used in order to determine the relevant linear-optical propagation constants; these constants depend on the propagation angle for an anisotropic medium. We assume a uniaxial crystal with permittivity given by Eq. (1.8) [crystalline  $c$ -axis along  $\hat{\mathbf{x}}$ ] and assume that the signal and idler  $\mathbf{k}$ -vectors are at small angles with respect to  $\hat{\mathbf{z}}$ . With this approximation and Eq. (1.7), the  $z$ -component of  $\mathbf{k}_j$  can be expressed as

$$\frac{\mathbf{k}_j \cdot \hat{\mathbf{z}}}{k_e} \approx 1 - \frac{1}{2} \left[ \left( \frac{\mathbf{k}_j \cdot \hat{\mathbf{x}}}{k_o} \right)^2 + \left( \frac{\mathbf{k}_j \cdot \hat{\mathbf{y}}}{k_e} \right)^2 \right]. \quad (8.52)$$

Since the magnitudes of the transverse spatial frequencies for the signal and idler are equal, it is useful to define  $k_x = \mathbf{k}_s \cdot \hat{\mathbf{x}}$  and  $k_y = \mathbf{k}_s \cdot \hat{\mathbf{y}}$ . By applying these definitions and substituting Eq. (8.52) into Eq. (8.51), the  $z$  component of the phase mismatch can be written as

$$\Delta \mathbf{k} \cdot \hat{\mathbf{z}} \approx \Delta k_0 + \sum_{j=i,s} \left[ \frac{k_e(\omega_j)}{2k_o(\omega_j)^2} k_x^2 + \frac{1}{2k_e(\omega_j)} k_y^2 \right] \quad (8.53)$$

where  $\Delta k_0 = k_e(\omega_p) - k_e(\omega_s) - k_e(\omega_i) - K_g$  is the collinear phase mismatch. With some additional assumptions, Eq. (8.53) can be simplified significantly. If we neglect the anisotropy of the material (via the substitution  $k_o \rightarrow k_e$ ), define the resulting magnitude of the transverse components of the  $\mathbf{k}$ -vectors as  $k_\perp = (k_x^2 + k_y^2)^{1/2}$ , simplify the resulting coefficients of  $k_\perp$  with the approximation  $k_i + k_s \approx k_p$ , and define a geometric mean angle according to

$$\theta_{is} = \pm \frac{|k_\perp|}{\sqrt{k_e(\omega_i)k_e(\omega_s)}}, \quad (8.54)$$

then Eq. (8.53) can be simplified as

$$\Delta \mathbf{k} \cdot \hat{\mathbf{z}} \approx \Delta k_0 + \frac{k_e(\omega_p)}{2} \theta_{is}^2. \quad (8.55)$$

From Eqs. (8.53) and (8.55),  $\Delta \mathbf{k} \cdot \hat{\mathbf{z}} > \Delta k_0$ . Hence, noncollinear phasematching can be obtained whenever  $\Delta k_0 < 0$  (within the limits of the small-angle approximation). The small-angle approximations made in this subsection are useful for understanding important trends, but are not necessary for numerical calculations.

### 8.6.2 Noncollinear Gain: Outline

In the presence of an undepleted and plane-wave pump, each transverse spatial frequency component of the signal interacts with a corresponding spatial frequency component of the idler. The OPA process is essentially the same for each component, except for a modification to the gain rate  $\gamma$  that occurs at large angles, and a modification to the phase mismatch according to Eq. (8.53). When the collinear phase

mismatch  $\Delta k_0 < 0$ , there is a set of finite transverse spatial frequencies which satisfy noncollinear phasematching; these and all nearby spatial frequencies experience gain.

With a pump beam of finite size, the gain is reduced due to spatial walk-off, since the phasematched or nearly-phasematched signal and idler beam components move across the finite spatial profile of the pump beam. This walk-off occurs over a characteristic length  $L_{wo} = w_p / \tan(\theta_{is})$ , for pump beam width  $w_p$  [see Fig. 8.8]. If  $L_{wo}$  is shorter than the gain length  $\gamma^{-1}$ , i.e.  $\tan(\theta_{is}) > w_p \gamma$ , the signal and idler walk off the pump faster than they can be amplified, and parasitic OPA is suppressed. When  $\tan(\theta_{is}) < w_p \gamma$ , gain-guided modes are supported, but the gain rate depends on the QPM profile. In particular, for chirped QPM gratings, noncollinear gain is suppressed both for sufficiently small and large angular components. In subsections 8.6.3 and 8.6.4 we explain this behavior by considering the gain guided modes supported by uniform and linearly chirped phasematching media, respectively.

### 8.6.3 Noncollinear Gain: Uniform Medium

Consider first the case of a uniform phasematching medium (for example, an unchirped QPM grating). When  $L_{wo}\gamma > 1$  and  $\Delta k_0 < 0$ , gain is supported indefinitely, even though the signal and idler propagate at a finite angle with respect to the pump. Gain can be sustained in this case because the signal and idler propagate at opposite angles, which gives rise to a self-trapping effect: the signal is amplified and generates idler components as it walks across the pump; these idler components in turn walk back across the pump in the opposite direction, experiencing amplification and generating signal components, and so on. This self trapping process results in a gain-guided mode.

The gain can be estimated by defining a reduced model in which diffraction and pump depletion are neglected. If we assume a particular collinear phase mismatch  $\Delta k_0 < 0$ , then there is a spatial frequency  $k_x$  for which noncollinear phasematching is satisfied. In the following analysis, we consider envelopes centered around this spatial frequency, set  $k_y = 0$ , neglect diffraction and birefringence [ $\delta = 0$  in Eq. (1.13)], and assume small angles. We use normalized position coordinates  $\zeta = \gamma_{p0} z$  and  $\bar{x} = x/w_{p0}$ .

With these assumptions, the coupled-wave equations [e.g. Eqs. (6.3)] can be put into the form

$$\begin{aligned}\frac{\partial a_i}{\partial \zeta} - \Theta \sqrt{\frac{k_s}{k_i}} \frac{\partial a_i}{\partial \bar{x}} &= -i a_s^* a_p \\ \frac{\partial a_s}{\partial \zeta} + \Theta \sqrt{\frac{k_i}{k_s}} \frac{\partial a_s}{\partial \bar{x}} &= -i a_s^* a_p,\end{aligned}\tag{8.56}$$

where the fields are normalized according to Eq. (7.8), but without the  $\exp(-i\phi_{\Delta k})$  phase factor. In particular, the pump is normalized such that  $\max(|a_p|) = 1$ , and we assume  $a_i(\bar{x}, \zeta = 0) = 0$ . We assume Gaussian signal and pump input beams. The ratio  $k_s/k_i$  represents the non-degeneracy of the problem (at degeneracy,  $k_s = k_i$ ). The only remaining parameter in Eqs. (8.56) is  $\Theta$ , which is defined as

$$\Theta \equiv \pm \frac{\sqrt{|\tan(\theta_i) \tan(\theta_s)|}}{\gamma_{p0} w_p},\tag{8.57}$$

where the sign is chosen to obtain the correct direction for the two beams, and  $\tan(\theta_j) = k_{\perp}/k_j$  are angles corresponding to the directions of the signal and idler wave-vectors.  $\Theta$  is the ratio of the gain length to the distance over which the signal and idler walk off the pump: when  $|\Theta| \gg 1$ , spatial walk-off occurs much more rapidly than gain.

Equations (8.56) are linear in the signal  $a_s$  and idler conjugate  $a_i^*$ . These equations support gain-guided signal-idler modes. The reduction in gain as a function of  $|\Theta|$  is shown by the  $\lambda_{R,p}^{-1} = 0$  curve in Fig. 8.9. When  $\Theta = 0$ , the normalized gain rate is unity (physical gain rate equal to  $\gamma_{p0}$ ). When  $\Theta > 1.1$ , gain guiding is suppressed.

#### 8.6.4 Noncollinear Gain: Linearly Chirped Medium

Next, we consider a medium with a linear chirp (such as a chirped QPM grating). In this case, slowly-evolving gain-guided modes can still be supported, but their gain is reduced compared to their gain in a uniform medium.

In the presence of a QPM chirp, there is a characteristic dephasing length for collinear interactions  $L_{\text{deph}} = 2\gamma_0/|\Delta k'|$  [defined in Eq. (7.17)]:  $L_{\text{deph}}$  is the distance

over which the phase mismatch is changed by  $\pm 2\gamma_0$ . In an initially phasematched plane-wave interaction ( $\Delta k = 0$ ), gain occurs over a distance  $L_{\text{deph}}$ , after which the interaction becomes too phase mismatched and gain is suppressed. In contrast, gain can be sustained over lengths greater than  $L_{\text{deph}}$  in a noncollinear interaction even with a chirped QPM grating provided that components of the signal and idler walk off the pump beam more rapidly than they are dephased. However, if the beams walk off the pump too rapidly, then gain is also suppressed, as in the unchirped-grating case discussed above. These effects are illustrated in Fig. 8.8

The resulting trade-off between gain, walk-off, and dephasing can be quantified by adding a linear chirp to the driving terms in Eqs. (8.56):

$$\begin{aligned}\frac{\partial a_i}{\partial \zeta} - \Theta \sqrt{\frac{k_s}{k_i}} \frac{\partial a_i}{\partial \bar{x}} &= -i a_s^* a_p e^{-i\phi(\zeta)} \\ \frac{\partial a_s}{\partial \zeta} + \Theta \sqrt{\frac{k_i}{k_s}} \frac{\partial a_s}{\partial \bar{x}} &= -i a_s^* a_p e^{-i\phi(\zeta)},\end{aligned}\quad (8.58)$$

where the phase  $\phi(\zeta)$  in these equations is given by

$$\phi(\zeta) = \frac{1}{2\lambda_{R,p}} [(\zeta - \zeta_{pm})^2 - (\zeta_0 - \zeta_{pm})^2], \quad (8.59)$$

where  $\zeta_{pm}$  is the collinear phasematched point and  $\zeta_0$  is the initial point. The appearance of  $\lambda_{R,p}$  in the coupled wave equations adds another parameter to the problem. For the purposes of addressing the most important results, we omit a formal analysis or a discussion of subtleties with simulating these equations; these aspects are discussed extensively in Ref. [138]. In Fig. 8.9, gain rates for noncollinear modes, extracted from numerical solutions of Eqs. (8.58), are plotted vs normalized angle  $\Theta$  for several values of  $\lambda_{R,p}$ .

To understand the trends illustrated in Fig. 8.9, it is useful to consider three characteristic lengths of the problem: the gain length  $\gamma_0^{-1}$ , the walk-off length  $L_{wo}$ , and the dephasing length  $L_{\text{deph}}$ . Gain is suppressed for both small and large angles unless  $\lambda_R^{-1} = 0$  (no QPM chirp). For large angles, the behavior with  $\lambda_{R,p}^{-1} \neq 0$  is similar to the  $\lambda_{R,p}^{-1} = 0$  case, with a slight additional reduction in gain due to the

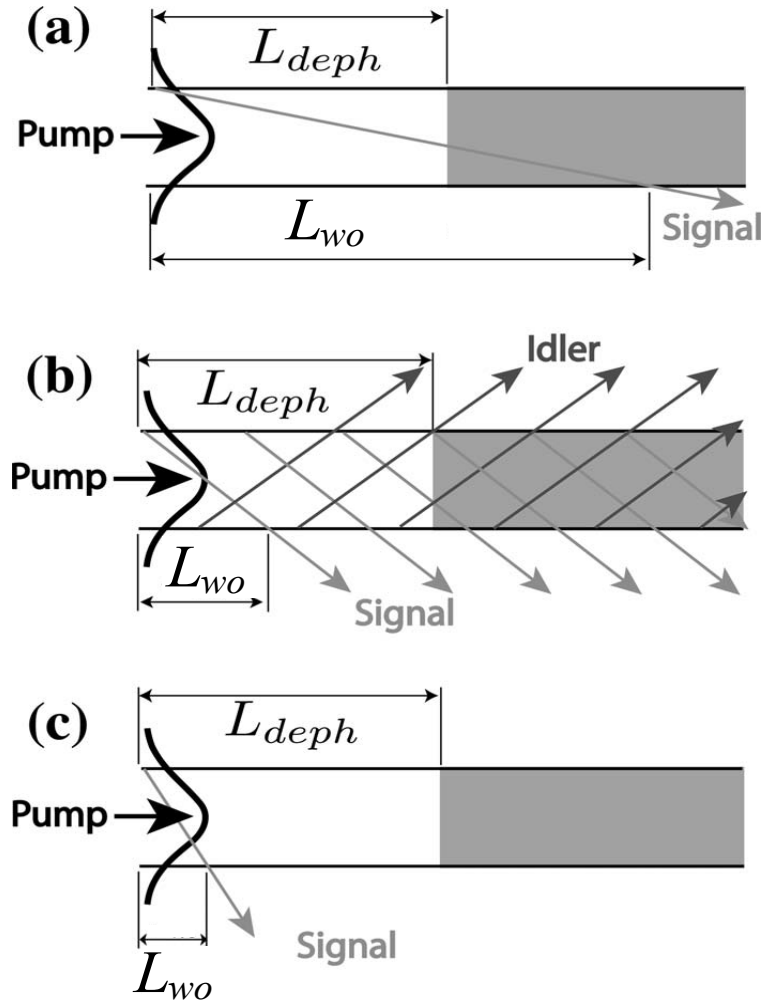


Figure 8.8: Schematic of gain-guided noncollinear modes in chirped QPM gratings. This figure is copied from Fig. 15 of Ref. [138] with minor modifications. (a) When  $L_{wo} > L_{deph}$ , gain-guided modes do not exist because they are suppressed by the dephasing. (b) When  $L_{wo} < L_{deph}$ , gain-guided modes exist because the waves escape the pump before experiencing dephasing. (c) However, when the angle is too large, gain-guided modes do not exist because the rate at which energy walks out of the pump region per unit length in  $z$  falls below the rate that energy is added by OPA (i.e. the waves escape the pump too quickly to experience amplification).

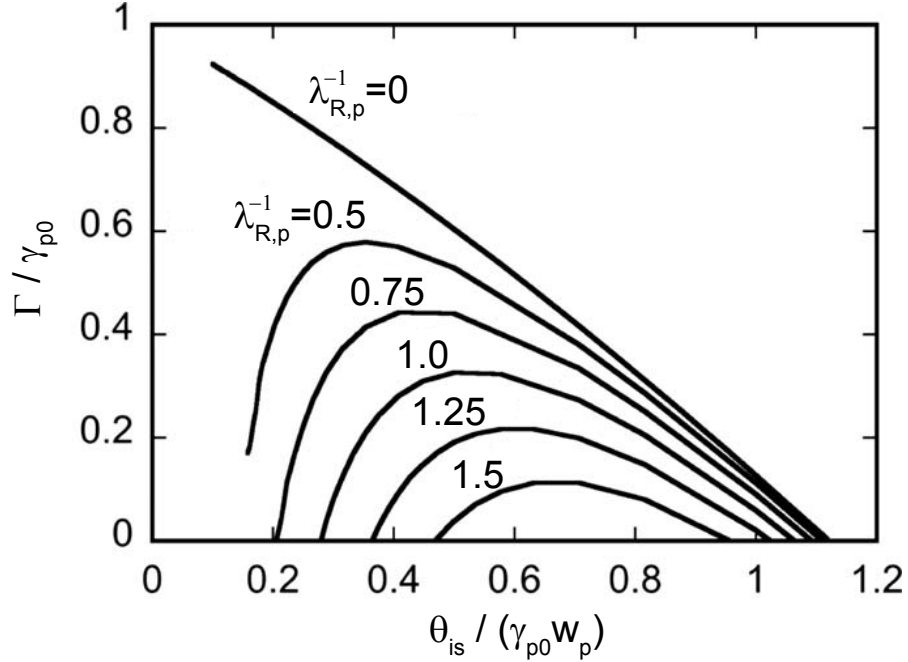


Figure 8.9: Simulated normalized gain rate  $\Gamma/\gamma_{p0}$  of noncollinear gain guided modes, for different normalized angles and values of  $\lambda_{R,p}$ . The  $\lambda_{R,p}^{-1} = 0$  case corresponds to an unchirped grating, discussed in subsection 8.6.3. This figure is copied from Fig. 2 of [94] and Fig. 12 of [138], with minor modifications to notation.

QPM chirp. For smaller angles, the behavior differs substantially: gain-guided modes do not exist for small angles, because the OPA process is dephased before the signal and idler walk off the pump. Dephasing occurs more rapidly than walk-off when  $L_{\text{deph}} < L_{\text{wo}}$ . This condition can be expressed, for small angles, as  $\Theta < \frac{1}{2\lambda_{R,p}}$ ; as a result, the minimum angle at which gain-guided modes exist scales as  $1/\lambda_{R,p}$ . Fig. 8.9 shows that gain is suppressed when the normalized angle is less than such a cut-off angle, denoted  $\Theta < \Theta_{co}$ . A reasonable approximation to  $\Theta_{co}$  for the Gaussian pump beam case simulated is

$$\Theta_{co} \approx \frac{1}{\pi\lambda_{R,p}}. \quad (8.60)$$

This approximation slightly overestimates the cut-off angles illustrated, except for small values of  $\lambda_{R,p}$ .

In the reduced coupled-wave model defined by Eqs. (8.58), gain can be sustained indefinitely. However, the ability of the equations to support gain indefinitely is an artificial consequence of neglecting the diffraction operator. When diffraction is included, the phasematched angle, and hence the corresponding value of  $\Theta$ , evolves as the grating period changes. Provided this angle changes sufficiently slowly compared to the gain rate, the gain-guided modes evolve adiabatically such that they closely resemble the local gain-guided mode, and experience amplification according to the *local* value of  $\Theta(\zeta)$ . Therefore, roughly speaking, gain occurs for each spectral component for positions  $z$  for which

$$\Theta_{co} < |\Theta(\zeta)| < 1. \quad (8.61)$$

In the absence of pump depletion, a useful heuristic for the total gain is obtained by integrating the local gain rate  $\Gamma$ , i.e.  $\ln(G_s) \approx \int \Gamma(\Theta(\zeta))d\zeta$ .

When the chirp rate is positive (negative), the phasematched beam angles decrease (increase) monotonically with position [see Eq. (8.53), or Fig. 21 of [138]]. If the collinear phasematched point  $\zeta_{pm}$  for a particular spectral component is contained within the grating, then  $\theta = 0$  at this point. Noncollinear phasematching is not possible after (before) this point, so noncollinear gain-guiding can only occur in the region  $\zeta < \zeta_{pm}$  ( $\zeta > \zeta_{pm}$ ).

### 8.6.5 System Implications

In a practical OPCPA system, the noncollinear gain guided modes discussed above must be suppressed in order to avoid amplifying high spatial frequency components (of either the input beam or of quantum noise). We show below that this suppression can be accomplished by increasing the peak power of the pump.

For a particular pump frequency and range of  $K_g(z)$ , there is a trajectory of phasematched angles for each signal frequency [the range of angles satisfying  $\Delta\mathbf{k} \cdot \hat{\mathbf{z}} = 0$  according to Eq. (8.53) given the range of  $K_g$  present in the grating]. The product  $(w_p \gamma_{p0})^2$  is proportional to the peak power of the pump. Therefore, if the peak power of the pump is sufficiently high, all of the normalized angles  $\Theta$  corresponding to the

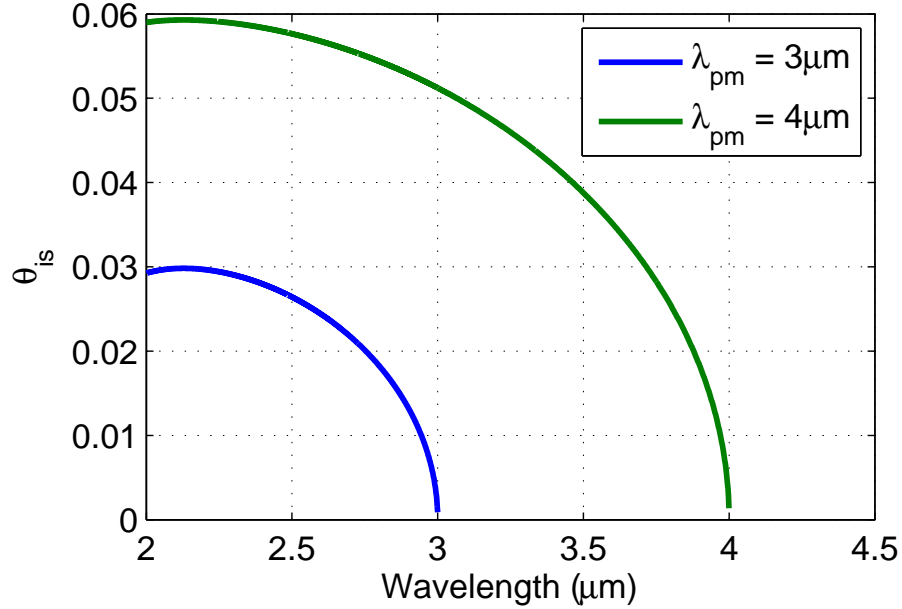


Figure 8.10: Geometric mean angle  $\theta_{is}$  versus idler wavelength, for two particular grating k-vectors (chosen to satisfy collinear phasematching for 3 or 4  $\mu\text{m}$ ). The maximum angle occurs at pump degeneracy.

range of phasematching angles (e.g. the range of  $\theta_{is}$ ) can lie below the normalized cut-off angle  $\Theta_{co}$ . From Eq. (8.60), the condition that the normalized phasematching angles must satisfy in order that noncollinear modes be suppressed can be expressed as

$$\Theta(z, \omega_s) < \frac{1}{\pi \lambda_{R,p}(z, \omega_s)} \quad (8.62)$$

for all  $z$  and  $\omega_s$ . To illustrate the implications of this constraint, we show in Fig. 8.10 the geometric mean angle  $\theta_{is}$  as a function of signal frequency  $\omega_s$  for several values of  $K_g$  (using the dispersion relation given in [137]). Given signal and idler frequencies within the transparency window of the material, and the required range of grating periods to amplify the spectral range of interest, the maximum value of  $\theta_{is}$ ,  $\theta_{is,(\max)}$ , can be determined. For Fig. 8.10,  $\theta_{is,(\max)} \approx 0.06$  rad for an amplifier designed for

operation between 3 and 4  $\mu\text{m}$ . A simple estimate for this angle is

$$\theta_{is,\max} = \theta_{is}\left(\frac{\omega_p}{2}, \max(K_g)\right). \quad (8.63)$$

That is, the maximum angle is obtained (in this case) at pump degeneracy, and involves the shortest QPM period present in the nominal (non-apodizing) region of the grating. Given  $\theta_{is} < \theta_{is,\max}$ , the condition for suppressing the gain guided modes is

$$\Theta_{\max} = \frac{\theta_{is,\max}}{\gamma_{p0}w_p} < \frac{1}{\pi\lambda_{R,p}}. \quad (8.64)$$

By expressing the factor  $\gamma_{p0}w_p$  in terms of the peak power of the pump, the following constraint on the peak power can be obtained:

$$P_{pk} > \frac{\pi^3 \epsilon_0 n_i n_s n_p c^3}{4\omega_i \omega_s d_{\text{eff}}^2 \bar{d}_1^2} (\lambda_{R,p} \theta_{is,\max})^2, \quad (8.65)$$

where the signal and idler quantities in this equation should be evaluated at the frequencies corresponding to  $\theta_{is,\max}$ ,  $d_{\text{eff}}$  denotes the relevant tensor element in the unmodulated material, and  $\bar{d}_1 = 2 \sin(\pi D)/\pi$  for QPM duty cycle  $D$  [Eq. (1.26)]. With Eqs. (8.63) and (8.65), we can determine the peak power required to suppress noncollinear gain-guided modes for a chirped-QPM OPA device. We have written Eq. (8.65) in terms of  $\lambda_{R,p}$  since this gain factor is constrained by the desired OPA process.

As in previous subsections of this chapter, we consider an example with a 1.064- $\mu\text{m}$  pump pulse and a 50%-duty-cycle QPM grating in an  $\text{MgO}:\text{LiNbO}_3$  crystal. The relevant nonlinear coefficient for OPA is  $d_{\text{eff}} \approx 19.5$  pm/V [30]. For a range of  $K_g$  satisfying phasematching between 3- and 4- $\mu\text{m}$ ,  $\max K_g \approx 2.198 \times 10^5$  m<sup>-1</sup>, which results in a maximum angle  $\theta_{is,\max} \approx 0.06$ . This angle occurs at degeneracy, so the corresponding signal and idler frequencies are  $\omega_i = \omega_s = \omega_p/2$ . For these parameters,

Eq. (8.65) can be expressed as

$$\frac{P_{pk}}{\lambda_{R,p}^2} > 0.56 \text{ MW}. \quad (8.66)$$

For peak powers below this level, there will exist a finite range of signal frequencies which can experience high gain through noncollinear phasematching. If these frequencies lie outside the spectral range of interest, and if their gain is insufficient to deplete the pump, then they can be spectrally filtered after the amplifier, thereby maintaining a high quality signal. Calculation of  $\theta_{is,max}$  could be restricted in this case to frequencies lying within the amplification range. However, if the noncollinear gain is high enough to cause depletion of the pump (from amplified quantum noise, for example), then this approach is not feasible, and  $\theta_{is,max}$  should be calculated by considering the whole transparency window of the material. Note that Eq. (8.66) should be satisfied for both the pre- and power-amplifier stages.

For Gaussian pump pulses with 12-ps FWHM duration and an energy of 400  $\mu\text{J}$ , the peak power is 31.3 MW. If 10% of the pulse is used for a pre-amplifier stage, Eq. (8.66) can be satisfied while still obtaining high gain. In contrast, with the 100- $\mu\text{J}$  used in our earlier OPCPA experiments [53], Eq. (8.65) could not be satisfied in the high-gain pre-amplifier stage. As a result, these experiments were susceptible to amplified quantum noise.

## 8.7 Collinear Focusing

In chapter 7, we showed that there is an accumulation of intensity-dependent phase by the pump, signal and idler waves during plane-wave interactions involving chirped QPM gratings. In an OPA experiment with non-uniform spatial intensity profiles, this process results in a non-uniform phase profile across the beams, and hence a lensing effect. If this lensing effect becomes too large, significant diffraction can occur before the end of the grating, potentially spoiling the desired OPA process. Furthermore, since different spectral components accumulate different amounts of phase, and hence experience lensing effects of different strength and around different phasematching

positions, a spatiotemporal coupling can be introduced, in which different spectral components have different beam parameters at the output of the grating. In this section, we show how the severity of these effects can be estimated, and discuss how they can be mitigated. We will show that avoiding these lensing effects can necessitate the use of very wide pump beams.

### 8.7.1 Effective Lensing

A number of different  $z$ -dependent signal and idler phase profiles can arise depending on the input conditions and position of the phasematched point within the QPM grating. To identify cases where significant diffraction within the crystal is anticipated, it is useful to consider the peak nonlinear phase shift of each wave, which we denote as  $\phi_{j,\max}$ . Depending on the pump depletion, this maximum phase shift may occur near the phasematched point ( $z \approx z_{pm}$ ), or at the end of the grating ( $z = L$ ) [see Fig. 7.7]. The cascading approximation, given in Eqs. (7.41), shows that the nonlinear phases scale linearly with various sums and differences of photon fluxes. By deriving Eqs. (7.41) with a multiple-scale method introduced in Ref. [32], a diffraction operator can also be included. This process yields the following set of leading-order equations:

$$\frac{da_i^{(0)}}{dz} + \frac{i}{2k_i} \nabla_{\perp}^2 a_i^{(0)} = -i \frac{\gamma_{sp}^2}{\Delta k(z)} [ |a_p^{(0)}|^2 - |a_s^{(0)}|^2 ] a_i^{(0)} \quad (8.67a)$$

$$\frac{da_s^{(0)}}{dz} + \frac{i}{2k_s} \nabla_{\perp}^2 a_s^{(0)} = -i \frac{\gamma_{sp}^2}{\Delta k(z)} [ |a_p^{(0)}|^2 - |a_i^{(0)}|^2 ] a_s^{(0)} \quad (8.67b)$$

$$\frac{da_p^{(0)}}{dz} + \frac{i}{2k_p} \nabla_{\perp}^2 a_p^{(0)} = -i \frac{\gamma_{sp}^2}{\Delta k(z)} [ |a_i^{(0)}|^2 + |a_s^{(0)}|^2 ] a_p^{(0)}, \quad (8.67c)$$

where we have introduced envelopes  $a_j^{(0)}$  which are the same as the  $b_j^{(0)}$  envelopes in Eq. (7.41) except for the grating phase factor; specifically, each  $a_j^{(0)}$  is assumed to vary slowly compared to  $\Delta k$ . Recalling that  $\gamma_{sp}$  is defined in Eq. (7.7), these equations show that there is an approximately linear dependence of the output phase of the signal and idler on the pump intensity in cases when the pump is either strongly or

weakly depleted. Although many cases can occur (different input conditions, conversion efficiencies, crystal lengths, signs of chirp rate, and so on), the notion of phase shifts which are proportional to the pump intensity is useful in general since it is analogous to SPM and XPM effects in  $\chi^{(3)}$  media.

When a Gaussian beam acquires a nonlinear phase proportional to its intensity (SPM) or the intensity of a beam of similar size (XPM) there is simultaneously a reduction in  $M^2$  beam quality and a lensing effect which changes the complex curvature  $q$  of the embedded Gaussian beam. These effects, and the properties of Gaussian beams, have been discussed extensively [4, 139]. If the beam undergoing phase shifts is too narrow, then significant diffraction will occur within the nonlinear medium. For example, in the case of a focusing nonlinearity, beam collapse can occur, leading to a significant increase in intensity and other unwanted effects [76]. In the context of an OPCPA system, it is preferable to avoid these types of effects, since they result in complicated dynamics and reduced beam and pulse quality.

The significance of diffractive effects can be estimated by comparing the focal length of the effective lens associated with the peak phase shift  $\phi_{j,\max}$  and the crystal length. The maximum phase can be estimated from plane-wave simulations such as those shown in Fig. 7.7. Consider for simplicity a nonlinear phase proportional to the (Gaussian) pump intensity, which results in a phase profile given by

$$\begin{aligned}\phi_{j,NL}(r) &\approx \phi_{j,\max} e^{-2(r/w_p)^2} \\ &\approx \phi_{j,\max} (1 - 2(r/w_p)^2)\end{aligned}\tag{8.68}$$

where the second approximation applies near to the peak of the pump beam. This approximation to the phase can be compared to the phase imparted by an ideal thin lens,  $\phi_{TL}$ :

$$\phi_{TL} = \frac{kr^2}{2f}\tag{8.69}$$

Comparing Eqs. (8.68) and (8.69), we obtain the following effective focal length for

wave  $j$  due to the nonlinear phase:

$$f_{j,\text{eff}} = -\frac{k_j w_p^2}{4\phi_{j,\text{max}}} \quad (8.70)$$

The remaining non-parabolic terms in Eq. (8.68) cause a reduction in beam quality. The severity of any diffractive effects scales with the ratio  $L/f_{\text{eff}}$ . To avoid diffraction within the crystal, we therefore require that

$$\left| \frac{f_{j,\text{eff}}}{L} \right| = \left| \frac{k_j}{4k_p \phi_{j,\text{max}}} \frac{1}{\xi_p} \right| \gg 1, \quad (8.71)$$

for each wave  $j$ , where we have assumed a collimated pump (beam radius  $w_p$  approximately equal to beam waist  $w_{p0}$ ). Eq. (8.71) implies that a small value of the pump focusing factor  $\xi_p = L/(k_p w_{p0}^2)$  is required. The amount by which the left hand side must exceed unity depends quite strongly on the amount of pump depletion involved and on the sign of the chirp rate. The gain factor  $\lambda_{R,p}$  can be related to the pump focusing factor  $\xi_p$  and peak power  $P_{pk}$  by Eq. (8.3). Using this relation, we can express Eq. (8.71) in terms of the peak power of the pump:

$$P_{pk} \gg \frac{\pi \epsilon_0 c^4 n_i n_s k_p}{\omega_i \omega_s \omega_p d_{\text{eff}}^2 d_1^2} \max_j \left| \frac{\phi_{j,\text{max}}}{k_j} \right| \Delta K_g \lambda_{R,p} \quad (8.72)$$

This equation provides, as in Eq. (8.65) of section 8.6.5, a constraint on the peak power of the pump. As an example, consider the following system parameters: a signal and pump wavelength of 1.064  $\mu\text{m}$  and 3.5  $\mu\text{m}$ , respectively, MgO:LiNbO<sub>3</sub> as the material ( $d_{\text{eff}} = 19.5$  pm/V [30]), a 50% duty cycle, and a grating bandwidth  $\Delta K_g = 2.5 \times 10^4$  m<sup>-1</sup>. With these parameters, Eq. (8.72) implies that

$$\frac{P_{pk}}{\phi_{\text{max}} \lambda_{R,p0}} \gg 0.485 \text{MW}. \quad (8.73)$$

If we have a case with  $\lambda_{R,p} = 2$ , a maximum phase of  $2\pi$ , and need to maintain the  $\gg$  inequality by a margin 5, the pump power constraint becomes  $P_{pk} > 30.5$  MW. In the following subsections, we consider two important cases involving chirped gratings

in order to illustrate the types of effects that can occur and their severity.

### 8.7.2 Example: Positive Chirp Rate, Undepleted-pump

The effective lensing effects are simplest in the case of a positive chirp rate and an undepleted pump. An example simulation of this case is shown in Fig. (8.11). The behavior exhibited by the signal and idler beams can be understood with the help of Eqs. (8.67). Since the pump is undepleted, the  $|a_s^{(0)}|^2$  and  $|a_i^{(0)}|^2$  terms are negligible in comparison to  $|a_p^{(0)}|^2$  and can be neglected. When  $z \ll z_{pm}$ , the idler is out of phase with its driving polarization (it corresponds to one of the eigenmodes discussed in chapter 7). As a result, its phase is determined by the product  $a_p a_s^*$ . That is, in the region before  $z_{pm}$ , the signal undergoes a pump-intensity-dependent phase shift due to Eq. (8.67b), and the conjugate of *that* phase is imposed onto the idler. Put differently,  $a_i^{(0)} \approx 0$  for  $z \ll z_{pm}$ : the leading-order idler term is negligible, and the idler instead corresponds to the first-order term in the multiple scale analysis, which is given by

$$a_i^{(1)} = \frac{\gamma_{sp}}{\Delta k} a_s^{(0)*} a_p \exp\left(-i \int_0^z \Delta k(z') dz'\right) \quad (8.74)$$

and thus the idler phase evolution is not approximated by Eq. (8.67a) until *after*  $z_{pm}$ . In contrast, for  $z \gg z_{pm}$ , the idler has been generated, and so the signal and idler phases evolve according to Eqs. (8.67b) and (8.67a), respectively. Understanding how the phase of both the signal and idler evolves allows us to interpret the diffraction effects which are predicted by the coupled-wave equations. Before considering an example, it is convenient to first define normalized complex curvatures

$$\bar{q}_j(z_{pm}) = \frac{q_j(z_{pm})}{z_{R,p}}, \quad (8.75)$$

for subscripts  $j = i$  and  $j = s$  corresponding to the idler and signal, respectively.  $z_{R,p}$  denotes the input Rayleigh range of the pump.

Consider the positively chirped, undepleted-pump example shown in Fig. 8.11 (parameters given in the caption). Since the chirp rate is positive,  $\Delta k < 0$  for

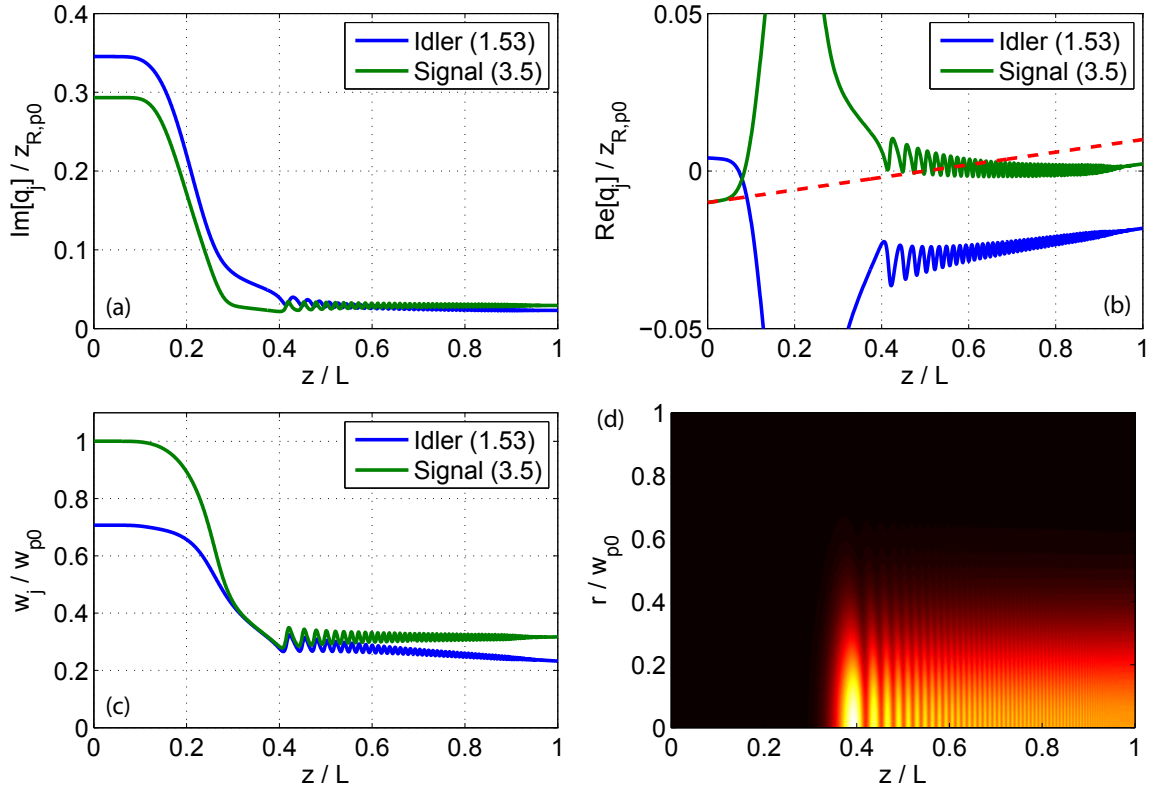


Figure 8.11: Simulation example for a positively chirped QPM grating. The parameters were as follows:  $\lambda_{R,p0} = 2$ ,  $w_{s,0}/w_{p,0} = 1$ ,  $\rho \rightarrow 0$ ,  $\zeta_L = 40$ ,  $\xi_p = 0.01$ , and  $z_{pm}/L = 0.3$ ,  $\lambda_p = 1.064 \mu\text{m}$ ,  $\lambda_s = 3.5 \mu\text{m}$  (the seeded signal wavelength). (a)  $\text{Im}[q_j]$ , (b)  $\text{Re}[q_j]$ , (c) Beam radii  $w_j$ , and (d) magnitude of the signal electric field.

$z < z_{pm}$ , which means that the signal initially experiences a negative lensing effect. Around  $z_{pm}$ , the signal is amplified and the idler is generated. As a result, the signal beam is narrowed (the center of the beam experiences a higher gain), and so  $\bar{q}_j$  are decreased substantially, as shown in Fig. 8.11(a). Because the idler is approximately the conjugate of the signal immediately after it is generated,  $\text{Re}[\bar{q}_i] < 0$  while  $\text{Re}[\bar{q}_s] > 0$ , as shown near  $z/L = 0.4$  in Fig. 8.11(b); this phase means that the generated  $1.53\text{-}\mu\text{m}$  idler converges towards its focus, causing the reduction in beam radius  $w_i$  shown in 8.11(c). Since both the beams have been narrowed after the gain region, they diffract more rapidly. However, when  $z > z_{pm}$ ,  $\Delta k > 0$ , which means that the pump imposes a positive effective lens on both the signal and idler.

This positive lensing reduces the rate at which the signal diverges; this can be seen by comparing the real part of  $\bar{q}_j$  to the dashed line of Fig. 8.11(b), whose slope corresponds to linear diffraction. Because diffractive effects are mitigated by lensing effects, Eq. (8.71) does not need to be strict: for example in Fig. 8.11,  $f_{\text{eff}}/L \approx 1.6$ , and the focusing effects are relatively minor.

With the above arguments, all of the qualitative features of Fig. 8.11 can be identified. Similar arguments can be applied to other cases (different amounts of pump depletion, either sign of the chirp rate, and different phasematching positions).

### 8.7.3 Example: Negative Chirp Rate, High Pump Depletion

In section 8.4, we found that a negative chirp rate is sometimes required in order to avoid coincidentally-phasematched processes such as SHG of the long-wavelength idler. In this subsection, we consider an example with high ( $> 50\%$ ) pump depletion and a negative chirp rate, in order to illustrate the focusing effects that can occur in this case. After  $z_{pm}$ , most of the pump is depleted over most of its spatial profile. In a region with 100% pump depletion, Eqs. (8.67a) and (8.67b) become

$$\frac{da_i^{(0)}}{dz} + \frac{i}{2k_i} \nabla_{\perp}^2 a_i^{(0)} = i \frac{\gamma_{sp}^2}{\Delta k(z)} |a_s^{(0)}|^2 a_i^{(0)} \quad (8.76a)$$

$$\frac{da_s^{(0)}}{dz} + \frac{i}{2k_s} \nabla_{\perp}^2 a_s^{(0)} = i \frac{\gamma_{sp}^2}{\Delta k(z)} |a_i^{(0)}|^2 a_s^{(0)}. \quad (8.76b)$$

As a result of these equations, there is a cross-focusing between the idler and signal waves. Because each wave focuses the other wave, this effect is self-reinforced. In analogy with self-reinforcing SPM in a pure  $\chi^{(3)}$  medium, this self-reinforcing behavior can result in rapid beam collapse unless sufficiently wide beams are used. An example of this behavior is illustrated in Fig. 8.12 (parameters given in the caption). The signal and idler begin to cross-focus each other after  $z_{pm}$ , and continue to do so until the end of the crystal. If the crystal is significantly longer or the pump focusing is tighter, the beams collapse until the cascading approximation breaks down, after which oscillatory behavior of the beam waist can ensue (not shown).

For negatively chirped gratings involving significant pump depletion, the margin

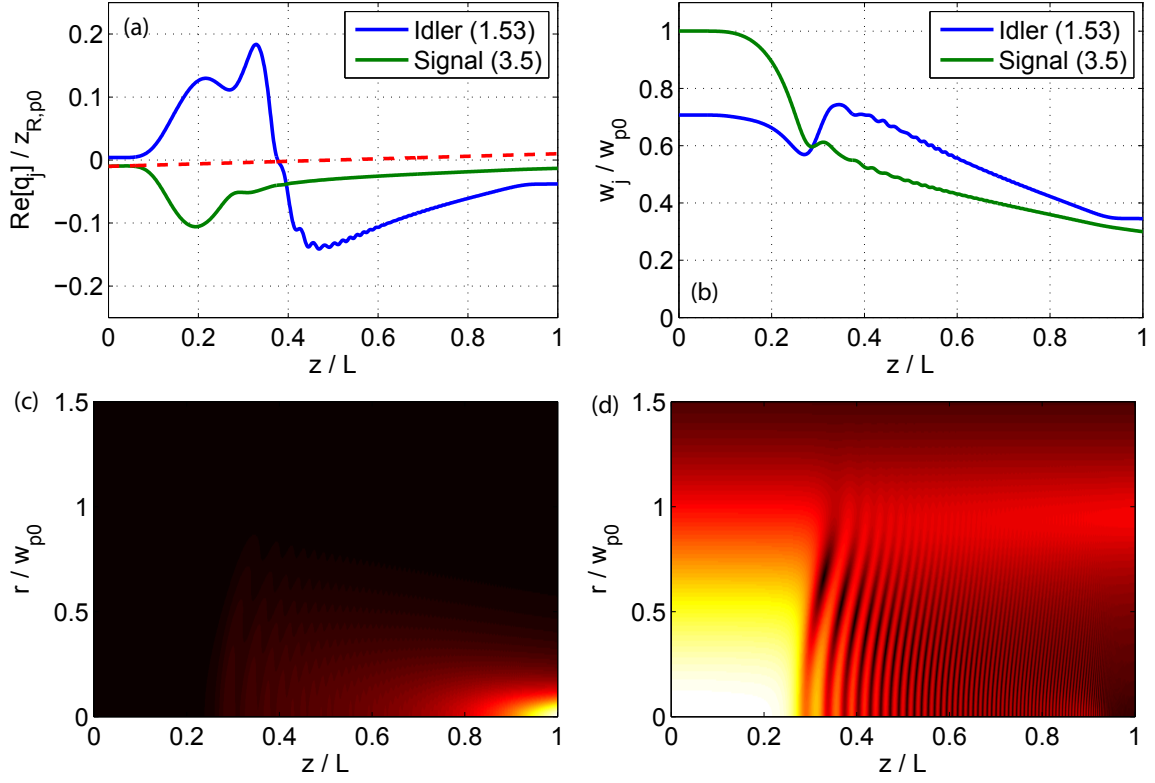


Figure 8.12: Simulation example for a negatively chirped QPM grating. The parameters were as follows:  $\lambda_{R,p0} = 2$ ,  $w_{s,0}/w_{p,0} = 1$ ,  $\rho = 0.1$ ,  $\zeta_L = 40$ ,  $\xi_p = 0.01$ , and  $z_{pm}/L = 0.3$ ,  $\lambda_p = 1.064 \mu\text{m}$ ,  $\lambda_s = 3.5 \mu\text{m}$  (the seeded signal wavelength). (a)  $\text{Re}[q_j]$ , (b) Beam radii  $w_j$ , (c) and (d): magnitude of the signal and pump electric fields, respectively.

by which the inequality (8.71) must be satisfied (i.e. how much greater than unity  $f_{\text{eff}}/L$  must be) is more severe than in the positively-chirped, undepleted-pump case considered in subsection 8.7.2. This stricter constraint is a result of the XPM reinforcing any diffractive effects (the idler focuses the signal simultaneously with the signal focusing the idler). A heuristic criterion to ensure that beam collapse is avoided is  $f_{\text{eff}}/L > 2$ . This constraint can be substituted into Eq. (8.72) to obtain an inequality for the pump peak power.

### 8.7.4 Spatiotemporal Coupling: Concept

The rate of phase accumulation depends on the local phase mismatch, which is a function of both position and frequency. Therefore, different spectral components can acquire different spatial phase profiles, which represents a source of spatiotemporal coupling. The frequency dependence of  $z_{pm}$  results in a variety of such spatiotemporal coupling effects. As a simple example, consider a positively chirped grating and an undepleted pump with wide enough beams that negligible diffraction occurs within the length of the device. Over most of the device, the intensity-dependent phase shifts acquired by signal components phasematched near  $z = 0$  are negative while those for signal components phasematched near  $z = L$  are positive. Thus, in this example, the higher intensities on axis create a positive effective lens for signal components phasematched near  $z = 0$ , but a negative one for those phasematched near  $z = L$ .

To understand spatiotemporal coupling effects in more detail, we determine the complex curvature  $q_j$  of the output waves as a function of the frequency-dependent phasematching point  $z_{pm}$ . If we increase the pump Rayleigh range  $z_{R,p}$  enough that  $f_{\text{eff}}/L \gg 1$  (while maintaining a fixed ratio of signal and pump width), then the normalized curvatures  $\bar{q}_i(z_{pm})$  and  $\bar{q}_s(z_{pm})$  [defined in Eq. (8.75)] approach forms that are independent of further increases to  $z_{R,p}$ .  $q_i$  and  $q_s$  can be used to quantify the change in beam parameters across the spectrum of the pulse (via the frequency-dependence of  $z_{pm}$ ). It is also important to consider the  $M^2$  beam quality of each spectral component of the pulses [140], which we denote as  $M_j^2(z_{pm})$  for wave  $j$ . By determining  $\bar{q}_j(z_{pm})$  and  $M_j^2(z_{pm})$ , the severity of the spatiotemporal distortions can be determined. If the pulse is too highly distorted, it cannot be compressed (time) and focused (space) into a diffraction-limited spot (or “bullet”). These distortions thus reduce the peak intensity, which is detrimental to high-field experiments.

We defer a detailed discussion of all the different cases to future work, and state here the most important points. For pre-amplifier stages involving a high gain and a low amount of pump depletion, the distortions on the beam are not too severe provided that Eqs. (8.65) and (8.72) are satisfied. One reason for the weakness of the distortions is that the beams “sample” a narrower region of the pump, since the gain is much higher near the peak than in the wings of the pump. Furthermore, any resulting

distortions can be reduced significantly in subsequent amplifier stages, for example by making the signal beam slightly wider than the pump. With this approach, the most significant amplitude and phase distortions of the signal are pushed onto the wings of the pump, and hence are not significantly amplified. In this way, the pump can act as a smooth amplitude filter, thereby improving beam and pulse quality. Since the conversion efficiency is monotonic in both the signal and pump intensities in a sufficiently-chirped grating, high overall conversion efficiency can still be achieved.

### 8.7.5 Spatiotemporal Coupling Example

Based on the above argument, we next consider a power amplifier stage and examine  $M^2$  and  $q_j$  as a function of  $z_{pm}$  for a high-pump-depletion, negative-chirp-rate, weakly focused ( $\xi_p \ll 1$ ) case such as the example discussed in subsection 8.7.3. The resulting dependence on  $z_{pm}$  of several key parameters related to the beam quality are shown in Fig. 8.13 for several values of the input signal complex curvature. The parameters are given in the caption; our parameterization of the curvature is given below. Figs. 8.13(a) and (c) show that we can change the slope of the output idler curvature with respect to  $z_{pm}$  by the choice of a (frequency-independent) input signal curvature

To specify the curvature, consider the Gaussian beam parameters of wave  $j$  at  $z = L/2$  in the absence of any nonlinear coupling (i.e. if the only effect is linear diffraction); the corresponding complex curvatures and beam radii at this position are denoted as  $q_{j,c}$  and  $w_{j,c}$  (subscript  $c$  indicating the center of the crystal). The corresponding beam waists (i.e. beam radius at the focus)  $w_{j,0}$  satisfy  $\text{Im}[q_{j,c}] = k_j w_{j,0}^2/2$ . In the simulations, we keep  $w_{s,c}$  fixed, but vary the signal beam waist  $w_{s,0}$  such that

$$w_{s,c} = w_{s,0} \sqrt{1 + N_s^2} \quad (8.77)$$

for a chosen value of signal curvature parameter  $N_s$ . Since the beam radius of a Gaussian beam can be expressed as  $w = w_0 \sqrt{1 + (\text{Re}[q]/\text{Im}[q])^2}$ ,  $N_s = \text{Re}[q_{s,c}]/\text{Im}[q_{s,c}]$ ; assuming linear propagation through a single homogeneous medium,  $\text{Re}[q_{s,c}]$  is the distance between the center of the crystal and the beam focus, and  $\text{Im}[q_{s,c}]$  is the

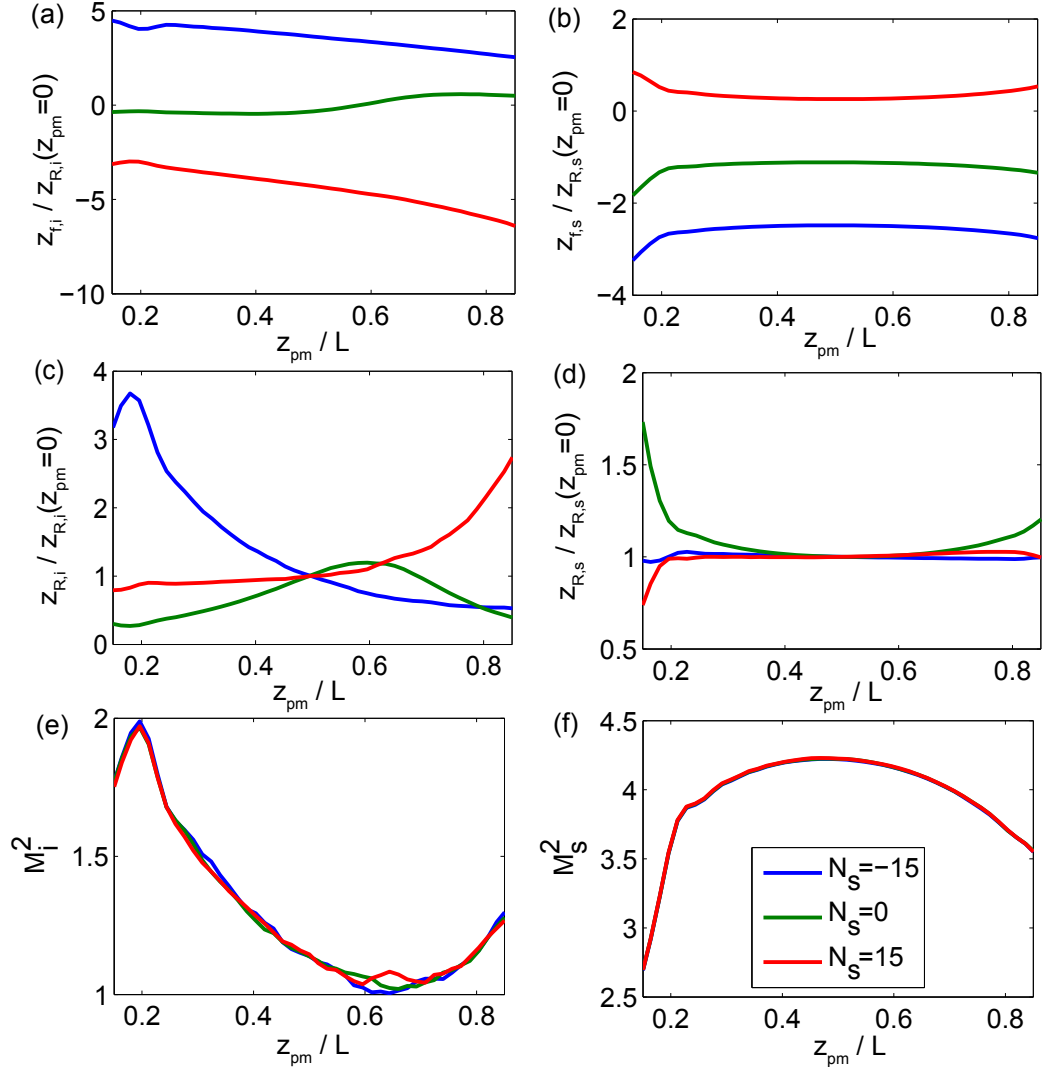


Figure 8.13: Spatiotemporal coupling effects for an example case with high pump depletion and a negative chirp rate, found via full numerical simulations. Figures (a), (c), and (e) correspond to the idler; figures (b) and (d) and (f) correspond to the signal. In (a)-(d), we consider the components of  $q_j$  at the output of the device. These components are given by  $z_{f,j}(z_{pm}) = \text{Re}[q_j(z_{pm}, z = L)]$  and  $z_{R,j}(z_{pm}) = \text{Im}[q_j(z_{pm}, z = L)]$ . We normalize each component to the Rayleigh range corresponding to  $z_{pm} = L/2$ . (a) and (b):  $z_f(z_{pm})/z_R(z_{pm} = L/2)$ , (c) and (d):  $z_R(z_{pm})/z_R(z_{pm} = L/2)$ , (e) and (f):  $M^2$  beam quality. The parameters for this simulation were  $w_{s,c}/w_{p,c} = 1.5$ ,  $\xi_p = 10^{-4}$ ,  $\zeta_L = 25$ ,  $\lambda_{R,p} = 2$ ,  $\rho = 10^{-1}$ ,  $\Delta k' < 0$ ,  $\lambda_p = 1.064 \mu\text{m}$ ,  $\lambda_s = 3.5 \mu\text{m}$ . The conversion efficiency is  $\approx 70\%$  for each value of  $z_{pm}$ .

Rayleigh range. The parameter  $N_s$  is therefore a convenient way to express how far the foci of the beams are from the center of the crystal. The signal beam radius  $w_{s,c}$  can be expressed in terms of  $q_{s,c}$  as  $k_s w_{s,c}^2/2 = \text{Im}[-q_{s,c}^{-1}]^{-1}$ . The pump input conditions are chosen such that  $w_{p,c} = w_{p,0}$  (i.e.  $N_p = 0$ , in the absence of nonlinear effects, the minimum pump waist lies at  $z = L/2$ ). The ratio of signal and pump beam radii at the center of the crystal in the absence of nonlinear effects,  $w_{s,c}/w_{p,c}$ , is kept fixed.

We can get a rough estimate the slope (versus  $z_{pm}$ ) in idler curvature at the output of the crystal that is obtained for a given value of  $N_s$ . For simplicity, we first imagine that the idler is just the conjugate of the Gaussian signal beam after it is generated, and neglect nonlinear phase shifts. By assuming a Gaussian signal, with wavefront  $\phi_j(r, z) = -\text{Re}[k_s r^2/(2q_s(z))]$ , and that the idler phase is conjugate of the signal phase at the phasematched point  $z_{pm}$ , i.e. that  $\phi_i(r, z_{pm}) = -\phi_s(r, z_{pm})$ , we can therefore obtain an estimate for the changes in  $q_i$  across the gain spectrum; we assume in the following oversimplified analysis that the signal propagates linearly ( $dq_s/dz = 1$ ), and the idler propagates linearly after  $z_{pm}$ . Consider two spectral components of this (very approximate) idler, generated at  $z_{pm} = 0$  and  $z_{pm} = L$ , respectively. Given the above assumptions, the difference in the two resulting output idler curvatures can be expressed in terms of  $N_s$ :

$$\left( \frac{q_i(z_{pm} = L, z = L) - q_i(z_{pm} = 0, z = L)}{\text{Im}[q_{s,c}]} \right) = -\frac{2k_p}{k_s} \left( 1 + \frac{k_i}{k_s} \right) \left( \frac{w_{p,0}}{w_{s,c}} \right)^2 \xi_p (1 + N_s^2) \quad (8.78)$$

Due to the  $N_s^2$  factor, significant changes in the idler curvature can be obtained even though  $\xi_p \ll 1$ . The relative change in beam size of the signal due to linear-optical propagation, which should not be too large if a good overlap between the signal and pump beams is to be maintained, is given by

$$\frac{w_s(L)^2 - w_s(0)^2}{w_s(L/2)^2} = 4 \frac{k_p w_{p,0}^2}{k_s w_{s,c}^2} \xi_p N_s. \quad (8.79)$$

Since this normalized change in signal beam size due to diffraction is proportional to

$\xi_p N_s$  but the normalized change in idler curvature is proportional to  $\xi_p(1 + N_s^2)$ , if we choose a large value of  $N_s$  (i.e. a small signal beam waist, located far from the center of the amplifier crystal), the curvature of the idler can be manipulated without substantially changing the overlap between the signal and pump beams. Note that the transverse spatial frequency bandwidth of the signal also scales as  $\xi_p(1 + N_s^2)$ , since

$$\left(\frac{2}{k_s w_{s,0}}\right)^2 = \frac{4k_p}{k_s^2 L} \frac{w_{p,0}^2}{w_{s,c}^2} \xi_p (1 + N_s^2). \quad (8.80)$$

Therefore, this approach for idler-curvature-compensation can be scaled to large beams, since the spatial frequency bandwidth of the signal is proportional to the relative change in idler curvature, Eq. (8.78), which means that the phasematching conditions are maintained.

The above heuristic approach predicts that the slope of  $\text{Re}[q_i(z_{pm})]$  should be negative and that  $\text{Im}[q_i(z_{pm})]$  should be independent of  $z_{pm}$ . From Fig. 8.13, we see that neither of these properties holds in general, and hence this heuristic picture is very inaccurate. In fact, the signal and idler simultaneously diffract *and* undergo a lensing effect, which leads to changes in both the real and imaginary part of  $q_j$ , as seen in Fig 8.13(c). Eq. (8.78) just provides a rough estimate of the scale of changes to  $q_i$  as a function of  $N_s$ . For a more accurate heuristic (the details of which will be given in future work), we can approximate the problem as a lens duct. This slightly more complex effective lensing model can explain the features seen in Fig. 8.13. In the following paragraphs, we explain the  $N_s = -15$  case shown, in order to connect the lens-like behavior arising from cascaded phase shifts [see Eqs. (8.67)] with the actual beam properties returned by full numerical simulations.

For phasematched points  $z_{pm}$  close to the input of the OPA (e.g.  $z_{pm}/L = 0.2$ ), the idler is first generated as the conjugate of the input signal, which corresponds to a diverging phase (that is, the idler would be diverging if it propagated linearly for  $z > z_{pm}$ ). The pump is highly depleted, so Eqs. (8.67) predict an effective lensing which focuses the idler, cancelling out some of its diverging phase. This phase cancellation leads to the increase in  $z_R$  (i.e. better collimation) of the idler in

Fig. 8.13(c) for phasematching points near the input of the crystal. For  $z_{pm}$  close to the output of the OPA (e.g.  $z_{pm}/L = 0.8$ ), the signal, which is converging since  $N_s < 0$ , first undergoes diffraction and a positive lensing effect [see Eqs. (8.67): before  $z_{pm}$ ,  $\Delta k > 0$  and the pump is undepleted]. This lensing adds to the curvature of the signal, and hence reduces the embedded Gaussian beam's waist,  $w_{s,0}$ . The corresponding idler is generated near the output where it acquires the opposite of this large signal curvature; as a result, the idler's beam waist  $w_{i,0}$  is also small, which explains the changes in  $z_R$  of the idler shown in Fig. 8.13(c) for  $N_s = -15$ .

The slope  $\text{Re}[q_i(z_{pm})]$  can be explained in a similar way. For  $z_{pm} \sim 0$ , the idler first acquires the opposite curvature to the signal,  $\text{Re}[q_i] \gg 0$ . Diffraction causes  $\text{Re}[q_i]$  to increase, but the effective lensing causes it to decrease, so there is a competition between focusing and diffraction. In contrast, for  $z_{pm} \sim L$ , the signal first is focused as it converges, both of which cause  $\text{Re}[q_s]$  to increase towards zero (since  $\text{Re}[q_s] \ll 0$ ). Then, around  $z_{pm}$ , the idler acquires a phase opposite to that of the signal. Therefore,  $\text{Re}[q_i]$ , which is positive, has also been brought towards zero. These two cases ( $z_{pm} \sim 0$  and  $z_{pm} \sim L$ ) help explain why the slope of  $\text{Re}[q_s](z_{pm})$  is negative.

The behavior of the signal is somewhat simpler. Because the pump is highly depleted, the signal acquires phase of the same sign both before and after  $z_{pm}$  [see Fig. 7.7 for  $\rho = 10^{-1}$ ]. As a result, each spectral component acquires a comparable curvature, which in turn means that  $q_s$  is weakly-dependent on  $z_{pm}$ . However, because each spectral component acquires a relatively large nonlinear phase, each  $M_s^2(z_{pm})$  beam quality is reduced. The phase giving rise to these reductions is weakly-dependent on  $z_{pm}$  (frequency), and so the beam quality of the entire signal pulse could in principle be restored by applying an appropriate phase mask before the nonlinear crystal.

The final qualitative feature of the  $N_s = -15$  curve is the dependence of  $M_i^2$  on  $z_{pm}$ . This profile has a simple explanation in terms of the nonlinear phases imparted onto the idler wave during the three-wave mixing process. A convenient way to identify the nonlinear phase of the idler is by comparing the phases predicted by a pair of simulations: one with the nominal value of  $\lambda_R$  and the other with  $\lambda_R \rightarrow 0$ . This approach is convenient because the overall grating phase accumulated prior to  $z_{pm}$  is imparted onto the idler in both cases, and by subtracting the phase of the

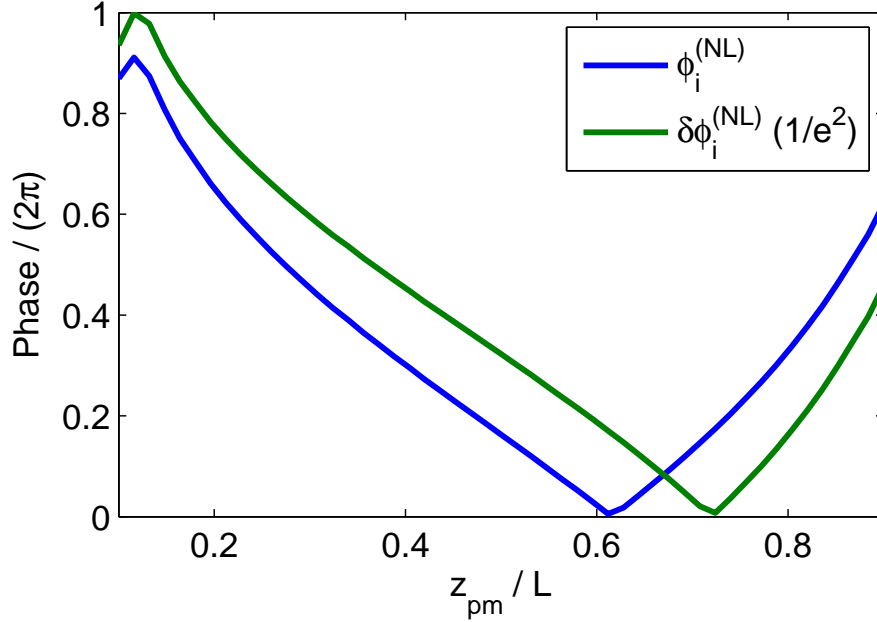


Figure 8.14: Nonlinear idler phase. The nonlinear idler phase is defined as  $\phi_i^{(NL)} = \phi_i - \phi_{i0}$ , where  $\phi_{i0}$  is the idler phase in the  $\lambda_R \rightarrow 0$  limit. The phase difference  $\delta\phi_i^{(NL)} = \phi_{i,1} - \phi_{i,2}$  for two arbitrary cases labeled 1 and 2. In the figure,  $\delta\phi_i^{(NL)} (1/e^2)$  denotes the difference in idler phases between cases with  $\lambda_R = 2$  and  $\lambda_R = 2e^{-2}$ ; this corresponds to the difference in nonlinear phase between the peak of the idler ( $\lambda_R = 2$ ) and the  $1/e^2$  intensity radius ( $\lambda_R = 2e^{-2}$ ), assuming for simplicity that all the beams have the same width after amplification. The profile of the two  $\phi_i^{(NL)}$  closely resembles the profile of  $M_i^2$  in Fig. 8.13(e).

$\lambda_R \rightarrow 0$  simulation (for which the nonlinear phase is zero) from the nominal  $\lambda_R$  case, we can identify just the nonlinear part without the need for any separate calculations. Each such pair of simulations yields the nonlinear phase as a function of position  $z$  for a given value of  $z_{pm}$ . In Fig. 8.14, we determine the output ( $z = L$ ) nonlinear phase as a function  $z_{pm}$ . The  $M_i^2$  profile in Fig. 8.13(e) corresponds very well to the nonlinear phase predicted by Fig. 8.14. There is a minimum in the idler (nonlinear) phase (and hence  $M_i^2$ ) when the nonlinear phase shifts before and after  $z_{pm}$  cancel each other; such cancellation occurs when the signal phase shifts before  $z_{pm}$  have the same sign as the idler phase shifts after  $z_{pm}$ , which occurs when the (local) pump depletion exceeds 50% (which it does in the example under discussion).

The other curves in Fig. 8.13 can be explained by similar arguments. The dependence of these  $q_j$  profiles on  $\xi_p$  can also be explained in this way.

### 8.7.6 Summary of This Section

It is clear from the above discussion that there are many input and grating parameters and that many different types of interactions that can occur. The same type of analysis - combining full numerical simulations including diffraction, full numerical simulations of plane-wave interactions, cascaded phase shifts, concepts related to the plane-wave adiabatic following or approximate WKB solutions (for example, with the idler acquiring opposite phase to the signal in the vicinity of  $z_{pm}$ ), and heuristic analyses based on lens-duct models - can be applied to each of these cases as needed. This analysis allows us to identify important variables (such as the pump focusing factor  $\xi_p$  and the signal curvature parameter  $N_s$ ) which can then be explored numerically.

Since both nonlinear phases and frequency-dependent phasematching points are essential aspects of chirped QPM OPA devices, some spatiotemporal distortion is inevitable. By identifying the most critical parameters, these distortions can be minimized or even corrected, for example by sending the signal seed through a phase mask. A critical parameter is  $\xi_p$ , and hence pump peak power  $P_{pk}$  [see Eqs. (8.3) and (8.72)]. We summarize the most relevant trends in table 8.2. Since the primary goal of this chapter is to determine a set of OPCPA design procedures and constraints, we defer a more extensive study of these focusing and spatiotemporal coupling effects to future work.

## 8.8 Summary of Design Constraints

In this section, we collect and summarize the design constraints developed throughout this chapter. In table 8.3, we give relevant design parameters for the OPA experiments described in section 8.2. Since only a small portion of the total pump power is typically used for pre-amplifier stages, the peak power constraints could only be met after the pump laser upgrade depicted in Fig. 8.2 [118]. The other constraints define the

Table 8.2: Overview of spatiotemporal effects in chirped QPM OPCPAs. The “role of  $\xi_p$ ” column indicates the severity of the diffractive effects which occur as  $\xi_p$  is increased; in all cases, it is advantageous to limit the effective nonlinear focal length to  $f_{\text{eff}}/L > 1$ ; these effects also become minor when  $f_{\text{eff}}/L \gg 1$ . For this table, we assume  $N_s = 0$ . The “signal” and “idler” columns refer to the spatiotemporal distortions that occur for these waves with  $\xi_p \rightarrow 0$ . “Undistorted” means that changes to  $\text{Re}[q_j]$ ,  $\text{Im}[q_j]$ , and  $M_j^2$  all have a very weak dependence of  $z_{pm}$ , and that  $M_j^2 \approx 1$ . We re-iterate that “signal” and “idler” refer here to the seeded and generated waves, respectively, regardless of which has shorter wavelength.

Conditions	Signal	Idler	Role of $\xi_p$
$\Delta k' < 0, \eta = 1$	$d\text{Re}[q_s]/dz_{pm} < 0,$ $M_s^2 \approx 1$	Undistorted	Moderate (noncollinear phasematching)
$\Delta k' < 0, \eta \rightarrow 0$	Large $M_s^2$ , phase weakly-dependent on $z_{pm}$ , $M_s^2 > M_i^2$	Modulation of $\text{Im}[q_i]$ , $\text{Re}[q_i](z_{pm})$ increasing, $dM_i^2/dz_{pm} < 0$	Significant (cross-focusing)
$\Delta k' > 0, \eta = 1$	$d\text{Re}[q_s]/dz_{pm} > 0,$ $M_s^2 \approx 1$	Undistorted	Minor (diffraction reduced by lensing)
$\Delta k' > 0, \eta \rightarrow 0$	Large $M_s^2$ , phase weakly-dependent on $z_{pm}$ , $M_s^2 > M_i^2$	Modulation of $\text{Im}[q_i]$ , $\text{Re}[q_i](z_{pm})$ decreasing, $dM_i^2/dz_{pm} < 0,$	Moderate: (cross- defocusing)

feasible range of chirp rates and crystal lengths. The parameters in the table explain the actual parameters used in the current experiments (see table 8.1).

The gain coefficient  $\gamma_{p0}$  is constrained by the material damage threshold. The crystal length  $L$  has an upper bound due to fabrication. Therefore,

$$0 \leq \gamma_{p0} \leq \gamma_{\text{max}} \quad (8.81a)$$

$$0 \leq L \leq L_{\text{max}}. \quad (8.81b)$$

Given an optical amplification bandwidth, there is a corresponding phase mismatch bandwidth  $\Delta k_{\text{OPA}}$ . Given this bandwidth, the length of a linearly chirped grating

Table 8.3: OPCPA design constraints and parameters. Quantities are evaluated assuming MgO:LiNbO<sub>3</sub> as the amplification medium, using Table 8.1 for any system parameters. For a quantity A that depends on a quantity B in this table or in table 8.1, the given value of B is assumed, e.g.  $\gamma_{\max}$  is evaluated at the approximate value of  $I_{\max}$  given below. We assume  $\lambda_{R,p0} = 3$ .

Quantity	Value	Description
$I_{\max}$	10 GW/cm <sup>2</sup>	Approx. damage threshold intensity <sup>a</sup>
$\gamma_{\max}$	2920 m <sup>-1</sup>	Max. value of $\gamma_{p0}$
$\Delta k_{\text{OPA}}$	$1.66 \times 10^4$ m <sup>-1</sup>	OPA bandwidth, with 3-4 $\mu\text{m}$ wavelength range [137]
$L/(2L_{\text{deph}})$	$\geq 2.4$	Min. ratio of length and amplification distance
$L_{\max}$	50 mm	Max. crystal length (fabrication)
$L_{\min}$	9.95 mm	Min. linearly-chirped-crystal length for $\lambda_{R,p} = 3$ <sup>b</sup>
$L_{\text{GVM}}/10$	11 mm	Min. GVM length (scaled <sup>c</sup> )
$P_{pk}^{(NC)}$	5 MW	Min. peak power: gain-guided noncollinear modes
$P_{pk,1}^l$	10 MW	Min. OPA1 peak power to avoid lensing effects
$P_{pk,2}^l$	19 MW	Min. OPA2 peak power to avoid lensing effects
$\xi_{p,1}^{(l)}$	$1.2 \times 10^{-2}$	Max. OPA1 pump focusing factor before lensing effects
$\xi_{p,2}^{(l)}$	$0.6 \times 10^{-2}$	Max. OPA2 pump focusing factor before lensing effects <sup>d</sup>
$w_{ap}$	1 mm	Current crystal aperture
$w_{ap,\min}$	1.2 mm	Min. OPA2 crystal aperture <sup>e</sup>
$\sigma_z$	1 $\mu\text{m}$	Estimate of RDC error standard deviation
$P_{\text{abs}}$	718 mW	Estimate of SH power absorbed by TPA <sup>f</sup>
$\Delta k'$	$< 0$	Chirp rate <sup>g</sup>

<sup>a</sup>This estimate is quite conservative. Operation at  $\approx 14$  GW/cm<sup>2</sup> has sometimes been possible

<sup>b</sup>Corresponding chirp rate of  $2.85$  mm<sup>-2</sup>

<sup>c</sup> $L_{\text{GVM}}$  calculated based on 12-ps pump duration. Factor of 10 chosen heuristically: stretched signal duration is often 0.2 – 0.3 times pump duration, and we require small temporal walk-off compared to the signal duration

<sup>d</sup>This case corresponds to both a negative chirp rate and a high pump depletion, so lensing effects are significant

<sup>e</sup>For a pump of radius  $w_{ap}/\pi$ , with 300  $\mu\text{J}$  and  $I_{pk} = I_{\max}$

<sup>f</sup>Assumes an energy of 300  $\mu\text{J}$

<sup>g</sup>To avoid coincidentally-phaseshifted SHG of amplified spectral components near 3.8  $\mu\text{m}$ .

should satisfy

$$L = \left( \frac{\Delta k_{\text{OPA}}}{\gamma_{p0}^2} + \frac{4}{\gamma_{p0}} \right) \lambda_{R,p} \quad (8.82)$$

In order to avoid GVM effects, the duration should satisfy

$$\tau_p \gg \left( \frac{\Delta k_{\text{OPA}}}{\gamma_{p0}^2 c} + \frac{4}{\gamma_{p0} c} \right) \delta n_g \lambda_{R,p}. \quad (8.83)$$

This inequality can alternatively be expressed in terms of the length  $L$  instead of  $\gamma_{p0}$ . If the pump duration is fixed or highly constrained (as is often the case), then this inequality provides a constraint on the gain coefficient  $\gamma_{p0}$ .

It is possible to use a nonlinear chirp design to obtain a flat gain spectrum even in the presence of a non-uniform temporal profile of the pump intensity. The length of the grating in such designs will be somewhat longer than with a linearly chirped grating having the same peak signal gain. The increase in length can be estimated by solving Eq. (8.12) (the local NLC design) or by determining the optimal design according to Eq. (8.22). The nonlinear chirp design is facilitated by the WKB approximation to the signal gain derived in [51], which can be written as an integral over the grating k-vector,

$$\ln(G_s(\omega)) = \int_{K_i}^{K_f} \frac{dz}{dK_g} \Gamma(\omega, K) dK, \quad (8.84)$$

where  $\Gamma$  is defined in Eq. (8.16). By discretizing  $\omega$  and  $K_g$  and specifying a set of constraints, the grating profile can then be determined via convex optimization.

Given a nominal design (whether a linear or nonlinear chirp), apodization regions should be appended to the ends of the grating to obtain a flat gain spectrum. This apodization can be done heuristically (for example, via the functions given in Eqs. (7.15) and (7.16), or optimally. The optimal approach for the case of undepleted-pump OPA was discussed in subsection 8.3.3; within the apodization region, the

optimal chirp rate scales, approximately, as

$$\left| \frac{dK_g(z)}{dz} \right| \propto \min_{\omega} (\Delta k(z, \omega)^2). \quad (8.85)$$

The same procedure could be generalized to obtain optimal apodization profiles for adiabatic following interactions as well, based on the geometric adiabaticity constraint given in Eq. (7.37).

The plane and continuous coupled-wave model used to derive the above designs can break down in a number of ways. Because the grating has a broad k-space bandwidth, it is possible to phasematch unwanted processes. For example, with a 1.064- $\mu\text{m}$  pump and a 3.5- $\mu\text{m}$  idler, the phase mismatch for the OPA process ( $\omega_i + \omega_s = \omega_p$ ) is comparable to the phase mismatch for idler SHG ( $\omega_i + \omega_i = 2\omega_i$ ). In a positively chirped grating, idler OPA can be followed by idler SHG, resulting in distortions to the output spectrum. Avoiding this effect favors negatively chirped gratings. Therefore, the following constraint can often apply:

$$\Delta k' < 0. \quad (8.86)$$

Examples are given in section 8.4.2.

The pump SHG phase mismatch differs substantially from that of the desired OPA process, so pump SHG is a relatively minor effect in an ideal grating structure. However, in practice, QPM gratings are perturbed by fabrication non-idealities. A sufficient way to model this effect in LiNbO<sub>3</sub> is to assume that errors in the positions of the domain boundaries are independent of each other and are normally distributed around their nominal (designed) positions. These perturbations are referred to as random duty cycle (RDC) errors. RDC errors give rise to a phasematching pedestal that is spectrally flat, in an ensemble-averaged sense. As a consequence, the efficiency of the nominally phase mismatched pump SHG process is enhanced. With a 1064-nm pump, this enhancement can give rise to an intense green pulse, which is then strongly two-photon absorbed in the LiNbO<sub>3</sub> material (since green is above the two-photon

edge in LiNbO<sub>3</sub>). The ensemble-averaged TPA is given by [Eq. (8.49)]

$$\begin{aligned} \langle U_{\text{abs}} \rangle &\approx \frac{32\beta_{TPA}}{3} \left( \frac{\omega_1^2 d_{\text{eff}}^2}{\epsilon_0 n_1^2 n_2 c^3} \right)^2 \\ &\times \frac{I_{pk}^4 L^3 \sigma_z^4}{\Lambda_D^2} \left( \frac{1 - e^{-k^2 \sigma_z^2}}{k^2 \sigma_z^2} \right)^2 \iiint \bar{I}_1^4(x, y, t) dx dy dt, \end{aligned} \quad (8.87)$$

With realistic values for the pulse parameters and RDC errors, as much as 700 mW can be absorbed, corresponding to a high thermal load. It is difficult to precisely specify an upper limit on the TP-absorbed SH, since a wide variety of effects can occur in photorefractive materials due to this type of absorption. The pump intensities which can be supported in our OPCPA system, and hence the conversion efficiencies which can be achieved, are currently limited by this process. With higher intensities, the large thermal load can lead to beam instabilities and even fracture of the crystals. With realistic improvements in the RDC errors, pump SH absorption could be reduced substantially, thereby enabling higher pump intensities in both stages, and hence significantly higher overall conversion efficiency.

The collinear plane-wave assumption can also break down. One way this breakdown can occur is due to non-collinear phasematching: if the normalized widths of the beams are not large enough, quantum noise can experience extremely high gain. In order to avoid noise amplification due to this process, the pump peak power must be large enough [Eq. (8.65)]

$$P_{pk} > \frac{\pi^3 \epsilon_0 n_i n_s n_p c^3}{4 \omega_i \omega_s d_{\text{eff}}^2 d_1^2} (\lambda_{R,p} \theta_{is,\text{max}})^2, \quad (8.88)$$

where  $\theta_{is,\text{max}}$  is the maximum phasematched angle, and can be estimated via Eq. (8.63). Another way for the plane-wave assumption to break down is due to collinear focusing effects. A basic consequence of interactions in chirped QPM gratings is that the three waves accumulate nonlinear phase shifts; these phases are approximately proportional to the pump intensity. With non-uniform intensity profiles, these nonlinear phase shifts lead to a lensing effect, with an effective focal length,  $f_{\text{eff}}$ . In order

to avoid changes to the beam profiles within the length of the device, we require

$$\left| \frac{f_{\text{eff}}}{L} \right| \gg 1. \quad (8.89)$$

The margin by which this inequality should be satisfied depends on the conversion efficiency and the sign of the chirp rate. The most relevant cases were summarized in table 8.2. The inequality can be expressed as a constraint on the peak power of the pump [Eq. (8.72)]:

$$P_{pk} \gg \frac{\pi \epsilon_0 c^4 n_i n_s k_p}{\omega_i \omega_s \omega_p d_{\text{eff}}^2 d_1^2} \max_j \left| \frac{\phi_{j,\text{max}}}{k_j} \right| \Delta K_g \lambda_{R,p} \quad (8.90)$$

As a result, transverse-beam-related distortions (both noncollinear and collinear effects) can be evaded by increasing the peak power of the pump and suitably adjusting its spot size. However, as the pump peak power is increased, the beam width also increases (if we keep the peak intensity fixed). The sample aperture  $w_{ap}$  must be large enough to support the beam sizes [139]:

$$w_{ap} > \pi w \quad (8.91)$$

where  $w$  refers to the beam *radius*. Since the factor  $(w\gamma_{p0})^2$  is proportional to the peak power of the pump, this equation can be expressed in terms of the design parameter  $\gamma_{p0}$ .

The constraints summarized in table 8.3 and the rest of this section are sufficient to specify an OPCPA system design. The most restrictive constraints will often be the peak pump power (since increasing this quantity requires upgrades to the pump laser itself), the sample aperture (which is limited by QPM fabrication technology), and unwanted pump SHG followed by TPA (which may also require fabrication improvements). These constraints are not decoupled: for example, LiTaO<sub>3</sub> can support large poling apertures and higher intensities [24], but its nonlinear coefficient is lower, and therefore the minimum peak power needed to avoid detrimental transverse beam effects is increased.

## 8.9 Conclusions

The design and operation of chirped QPM OPCPAs can be subtle and complex. Initially unexpected effects can arise and amplify noise, distort the pulses, or even damage the nonlinear crystals. With the analysis performed here, the necessary constraints to the system (peak pump power) and QPM fabrication (crystal aperture and poling quality, measured in terms of random duty cycle errors) can be determined. In our earlier experiments, the peak power was insufficient to avoid the various transverse beam effects we have discussed. After the pump upgrade, enough peak power is now available for both the pre- and power amplifier stages. Improvements to the poling quality of the samples is needed in order to allow for higher pump intensities and hence higher conversion efficiency. There is room for improvement, but our system is much more sensitive than most to QPM fabrication errors, and so it can be difficult to meet the fabrication tolerances with commercially-available samples.

Coincidentally phasematched processes are also difficult to overcome. The present system layout, in which the crystals are oriented such that the chirp rate is negative, does not appear to suffer from any severe coincidental phasematching issues. However, in terms of beam quality, a positive chirp rate could be advantageous (since we cannot fully suppress lensing effects at the current OPA2 peak power, and the beam distortions arising from these effects are more severe with a negative chirp rate). One way to avoid this issue is with noncollinear QPM gratings (while still maintaining collinear pump and signal beams). This is an approach we plan to explore in the future.

Usually, the signal and idler should walk off of each other and the pump by at most a small fraction of their duration within the length of the device. We have seen in simulations that failure to meet this criterion can lead to pronounced spectral ripples, and in severe cases can lead to other deleterious effects unique to the case of chirped QPM OPCPAs (for example, the idler can be compressed during the amplification process, thereby concentrating all of its energy in a small temporal region). Additionally, it is difficult to design devices in which GVM effects are substantial, because our only recourse is then to perform full numerical simulations of the nonlinear

system. In contrast, as long as the different spectral components stay overlapped in time, the convex optimization approach given in Eq. (8.22) can be applied. Indeed, the design shown in Fig. 8.3 indicates that our current configuration is currently close enough to this quasi-CW limit. However, the GVM-based length constraint given in table 8.3 indicates that the current devices are close to the boundary between “highly chirped” and “not chirped enough”. If samples of improved poling quality cannot be obtained, then suppressing two-photon absorption of pump SHG will favor longer devices with lower peak intensities. In contrast, the GVM constraint favors shorter devices. In a system with longer pump pulses, it would be relatively straightforward to increase the crystal length without causing excessive GVM. Given our 12-ps pump pulses, however, and the high degree of complexity already exhibited by the system, improving poling quality and having a grating length much shorter than the GVM length is likely to be the more reliable approach towards a tractable system (in terms of both experiment and theory).

Despite any remaining difficulties, the experimental results are very promising, and the design concepts discussed in section 8.3.2 and 8.3.3 should allow us to take full advantage of the versatility promised by QPM gratings, while still maintaining a computationally tractable design procedure (i.e. without having to use as a design metric the fidelity of the output pulses from a full 3+1D numerical simulation). By resolving gain narrowing effects using nonlinear chirp designs, the system will no longer need to be driven too far into depletion, and the mid-IR output could be made sufficiently chirped to “see” more of the pump pulse. These improvements, combined with higher-quality samples to reduce RDC errors, should enable significantly higher overall conversion efficiencies to be obtained. To reach few-cycle pulse durations, the seed bandwidth must be increased. Such increases should not be an intractable problem, since the seed pulses are in the 1.5- $\mu\text{m}$  wavelength range. The goals of high pump depletion and two- or three-cycle pulse durations appear feasible.

# Chapter 9

## Conclusions

### 9.1 Summary of this dissertation

The three main topics discussed in this dissertation are supercontinuum (SC) generation in  $\chi^{(2)}$  media, DFG in OP-GaAs, and OPCPA using chirped QPM gratings. In the context of SC generation, we constructed generalized models for highly nonlinear processes in  $\chi^{(2)}$  and  $\chi^{(3)}$  media, and used these models to quantitatively explain the existing SC generation experiments. We showed that the dynamics involved are unexpectedly subtle, with a highly sensitive cancellation of the effective  $\chi^{(3)}$  susceptibility arising from cascaded  $\chi^{(2)}$  processes by the true  $\chi^{(3)}$  susceptibilities. This work forms a baseline for the analysis and design of  $\chi^{(2)}$  SC generation experiments. Furthermore, the numerical models we developed and calibrated will be of great use in designing and evaluating the performance of many different types of devices. We performed SC generation experiments in reverse proton exchanged (RPE) waveguides using a Tm-doped fiber laser as the pump source, demonstrating multiple-octave-spanning spectra,  $f_{\text{CEO}}$  detection directly from the waveguide, and good agreement with our numerical model. This work represented the first self-referencing of a Tm-fiber laser source, an important step in utilizing Tm-fiber lasers for generating frequency combs in the mid-IR. We also took another step towards this goal by demonstrating tunable and moderate-power mid-IR generation using OP-GaAs. We were able to model the experimental results with high accuracy, and

used this model to propose a new system design utilizing longer pump pulses in order to facilitate high-power mid-IR generation.

The cancellation between  $\chi^{(2)}$  and  $\chi^{(3)}$  effects motivated an advanced design concept based on group velocity dispersion (GVD) engineering. The type of waveguides needed to accomplish this GVD engineering have been constructed for other applications, but have not been put towards the purpose of SC generation or GV-engineered interactions in general. Furthermore, LiNbO<sub>3</sub> ridge waveguides with sufficiently small dimensions for use with a 1.55- $\mu\text{m}$  pump have not yet, to our knowledge, been built. Our theoretical results are extremely promising, and indicate that  $\chi^{(2)}$ -based SC generation should be genuinely competitive with  $\chi^{(3)}$ -based schemes, particularly since there exist QPM media with transparency far into the mid-IR (e.g. 17  $\mu\text{m}$ ). Another substantial advantage is that octave spanning  $\chi^{(2)}$  SC generation inherently involves the generation of overlapping envelope spectra, and hence the detection of the carrier envelope offset frequency is possible directly at the output of the waveguide (just a filter is required, so that the detector is not saturated by the non-overlapping parts of the output spectrum). This capability combined with the 50-pJ-level SC generation predicted for ridge waveguides would be a significant step in simplifying frequency comb technology.

The single-envelope approach to modeling ultrabroadband  $\chi^{(2)}$  and  $\chi^{(3)}$  has a number of drawbacks, including its inability to separate out the different sub-processes involved, and loss of information about the carrier envelope phase. In order to reconstruct the individual harmonics involved (first, second, third harmonic, and so on) it is necessary to perform a series of simulations with different CEP and interfere the results. Furthermore, individual processes such as third or fourth harmonic generation cannot be turned off in order to identify the most important properties of the nonlinear interaction. To resolve these issues, we developed a generalized coupled-wave (GCW) model which accounts for all harmonic components explicitly and can be applied to both  $\chi^{(2)}$  and  $\chi^{(3)}$  mixing processes. With our approach, simplified models can be defined automatically (that is, we can neglect all but some subset of harmonic components, and all but some subset of the nonlinear interactions between those harmonics). The choice of such models is constrained, and we have shown how

those constraints can be met. This GCW approach should be of great use in designing devices and understanding the physical processes involved (since it is possible to turn off perturbative, time-consuming, or complicated effects to identify the most important features), and in analyzing experimental results (since the model is more general than single-envelope approaches).

In the context of OPCPA, we explored in detail the physics, design opportunities, and constraints which arise when implementing chirped QPM devices for real OPCPA systems. Chirped-QPM OPA offers the possibility of high gain or high conversion efficiency across the spatiotemporal profile of the pump beam, due to the monotonic conversion efficiency and adiabatic following behavior we examined in chapter 7. The amplification bandwidth is determined primarily by the QPM grating's spatial frequency bandwidth, which we can increase almost arbitrarily. With a combination of analytical results, convex optimization, and full numerical simulations, QPM gratings with optimized gain properties can be designed. This design approach should allow us to overcome gain narrowing effects, without the need to implement complex and lossy pump beam and pulse shaping techniques. Apodization is a key ingredient in chirped QPM gratings: since they rely on various types of adiabaticity, achieving a smooth transition from “off” (before the grating) to “on” (where the beams are amplified) to “off” (after the grating) is essential. We identified both optimal and heuristic approaches to apodization. The optimal approach (which we derived for the undepleted-pump case) will allow us to minimize any parasitic effects arising due to the length of the device without the need to artificially tweak any parameters. Heuristic approaches (where we use tanh profiles) are useful since they are both effective and very easy to implement.

Several issues can arise in a real OPCPA system. These impose constraints on the peak power of the pump, its focusing conditions, and its pulse duration. We showed that recent upgrades to the pump power available in our experimental apparatus helped to resolve a number of unwanted transverse beam effects which degraded the performance of our previous system. The imperfect poling quality of the crystals can lead to excessive green generation and absorption, which can in turn lead to a host of photorefractive and thermal issues. The constraints placed on the QPM

duty cycle errors to avoid excessive green generation ( $\sigma_z \leq 0.5 \mu\text{m}$ , for example) are not excessive, but can still be difficult to achieve in purchased samples since most applications are not as sensitive to these types of fabrication errors as is ours. It is certainly difficult to optimize a system when there is a high risk of the crystals breaking, so improving the poling quality is important. We also quantified several other constraints, and used them to design the existing gratings and point the way towards further system improvements. With realistic improvements to the gratings and the seed laser, obtaining high conversion efficiency and two- or three-cycle pulse durations appears feasible.

## 9.2 Other contributions

I have worked on a number of projects while at Stanford [38, 52, 53, 62, 64, 74, 107, 121, 122, 124, 125, 126, 132, 133, 134, 135, 136, 141, 142, 143, 144, 145, 146, 147, 148, 149, 150, 151, 68, 152], only some of which have been discussed in this dissertation. Although not discussed in the preceding chapters, a major theme of my research has been on optical parametric oscillators (OPOs).

In Ref. [142], we demonstrated the first monolithic PPLN OPO. This architecture offers the possibility of increased stability without the need for active cavity control, and is a compact format for building CW OPOs. While developing this OPO, we identified several key device constraints. We quantified a parasitic process involving a backwards generated THz wave which can lead to degraded OPO stability. This process has quite far-reaching implications for QPM OPOs, particularly those operating near to degeneracy. In our first monolithic OPO devices, oscillation degraded over time-scales of several minutes, after which the linear-optical modes of the cavity were suppressed; oscillation was only possible after letting the MgO:LiNbO<sub>3</sub> crystal “recover” at a high temperature for several hours. This type of behavior is usually expected in photorefractive crystals, but was expected to have been suppressed by the use of MgO:LiNbO<sub>3</sub>. We showed that the effect was consistent with beam distortions arising due to the pyroelectric effect (which can induce photorefractive effects, even in MgO:LiNbO<sub>3</sub>). We studied these pyroelectric effects experimentally

and theoretically [151]. In the context of OPOs, absorption of the resonant signal leads to a non-uniform temperature profile, which can in turn lead to a redistribution of charges and hence to a non-uniform refractive index profile due to the electro-optic effect. This non-uniform index profile then distorts the cavity modes, preventing oscillation until the charges equilibrate. This effect can be suppressed by ensuring that the entire resonant path of the signal is within the poled (QPM) region of the crystal, as the periodic poling causes the pyroelectric charges to change sign with the QPM period, which in turn reduces the magnitude of the electric field induced in the vicinity of the beam axis [151, 153].

We also performed extensive studies of the stability of OPOs. We used a linear stability analysis to develop the theory of singly-resonant OPO stability, deriving conditions which must be met in order to achieve stable, single mode operation [74]. In particular, if we define  $N$  as the ratio of the pump power to the oscillation threshold, then the OPO becomes unstable when  $N$  exceeds some instability threshold. This instability threshold, denoted  $N_{th}$ , depends strongly on the group velocity mismatch and dispersion between the pump, signal and idler waves. This behavior is in contrast to previous work [154], in which time-dependent changes to the pump were (inconsistently) neglected. Our OPO theory predicts regions of low stability in certain operating regions, for example in long-wave resonant 1.064- $\mu\text{m}$ -pumped MgO:LiNbO<sub>3</sub> OPOs. Several singly-resonant OPO instabilities have been observed in recent years, and are often attributed to various thermal effects. We showed that these instabilities are in fact consistent with a plane-wave model neglecting thermal effects entirely.

Based on our studies of both chirped QPM gratings and OPOs, we proposed a novel type chirped-QPM OPO which exploits the adiabatic following process discussed in chapter 7 to achieve a high conversion efficiency [107]. However, unless additional steps are taken, such OPOs are unstable at all values of  $N$ . We showed theoretically that with a suitable intracavity etalon, this instability could be suppressed, and very high conversion efficiency could be obtained. This OPO design could find application in nanosecond-pumped OPOs, especially when a narrow linewidth is not critical, but a high conversion efficiency is required.

Recently, we have considered the properties of singly-resonant OPOs operating near pump degeneracy. Our results so far indicate that a substantial decrease in OPO stability is predicted once the OPO is close enough to degeneracy that the usual three-wave-mixing OPO process can interact coherently with a backwards THz-OPA process. This work should clarify, and help to resolve, the degradation in OPO performance near that is often observed when operating close to degeneracy. In order to perform the calculations, we had to generalize the linear stability analysis performed for the non-degenerate OPO case to include several different nonlinear effects (both  $\chi^{(2)}$  and  $\chi^{(3)}$ ), and an arbitrary number of carrier waves.

In other work, we have performed studies of the properties of random duty cycle (RDC) errors in QPM gratings. In particular, we have shown that these RDC errors are responsible for the parasitic visible light generation that is often observed in QPM devices such as OPOs. An example of this work is given in subsection 8.5, where we showed that a parasitic enhancement of green generation due to RDC errors can be a limiting factor in chirped-QPM OPCPAs. RDC errors also play a critical role in the performance of PPLN-based single-photon up- and down-conversion devices [132, 133, 134, 135, 136].

In chapter 8, we discussed collinear chirped QPM OPCPA system design in detail. We have also explored other QPM designs, including the use of non-collinear chirped QPM gratings with collinear input beams. Based on theoretical considerations, these devices could facilitate an octave-spanning OPCPA while avoiding many of the parasitic processes discussed in chapter 8. For example, with these devices it should be possible to avoid the coincidentally phasematched processes discussed in section 8.4. Prototype non-collinear chirped QPM devices were recently fabricated, and we plan to experimentally test the predicted performance improvements in the near future.

### 9.3 Future work

There are a number of future directions based on the result of this dissertation. In the context of QPM supercontinuum generation, the next step is to experimentally

demonstrate the ridge waveguide designs discussed in chapter 4. Existing ridge waveguide technology should be suited to the purpose. It is likely that the main difficulty lies in obtaining waveguides that are both tightly confining and low-loss. Turning our theoretical results into real devices would open up the possibility of a number of very interesting applications. One example would be the emergence of QPM as a strong competitor to  $\chi^{(3)}$ -based supercontinuum generation. Such waveguides could become the standard method of performing carrier envelope detection, since  $f_{\text{CEO}}$  can be measured directly from the output of the waveguide (in contrast to most  $\chi^{(3)}$ -based approaches), and with GVD-engineering, only tens of pJ are required.

It would be interesting to extend some of our supercontinuum- and OPA-related results to OP-GaAs, in order to reach the mid-IR. While the fabrication requirements to obtain the necessary GVD-shifting in an AlGaAs material platform are quite stringent, this type of waveguide could in principle support mid-IR generation directly from a femtosecond pulse with just a simple single-pass traveling-wave interaction.

In the context of OPCPAs, chirped QPM gratings still have much potential left to be unlocked experimentally. With upgrades to both the OPCPA system and the QPM gratings themselves, the goal of high-energy, nearly-single-cycle, nearly-diffraction-limited, high-repetition-rate mid-IR pulses should be attainable.

In the context of OPOs, we have shown that singly-resonant OPO performance is both subtler and richer than previously thought. However, our analysis has been restricted to plane-wave interactions, whereas most experiments use Gaussian input beams. Implementing and evaluating a generalized modulation instability analysis for OPOs including transverse beam effects would be a significant step forward. Such a tool would help to alleviate the speculation that sometimes ensues in explaining the seemingly-mysterious behavior which OPOs frequently exhibit. Furthermore, many OPOs are synchronously-pumped. Determining the role played in pico- or femto-second pulsed experiments by the continuous-wave modulation instabilities we examined theoretically may be valuable, and is a topic we are beginning to explore.

# Bibliography

- [1] Takao Fuji, Jens Rauschenberger, Alexander Apolonski, Vladislav S. Yakovlev, Gabriel Tempea, Thomas Udem, Christoph Gohle, Theodor W. Hensch, Walter Lehnert, Michael Scherer, and Ferenc Krausz. Monolithic carrier-envelope phase-stabilization scheme. *Opt. Lett.*, 30(3):332–334, February 2005.
- [2] Carsten Langrock, M. M. Fejer, I. Hartl, and Martin E. Fermann. Generation of octave-spanning spectra inside reverse-proton-exchanged periodically poled lithium niobate waveguides. *Opt. Lett.*, 32(17):2478–2480, 2007.
- [3] Amnon Yariv and Pochi Yeh. *Photonics*. Oxford University Press, 2007.
- [4] Robert W. Boyd. *Nonlinear Optics, Third Edition*. Academic Press, 3 edition, April 2008.
- [5] W. Sellmeier. Zur erklärung der abnormen farbenfolge im spectrum einiger substanzen. *Annalen der Physik und Chemie*, 219:272–282, 1871.
- [6] Ilya Fushman, Dirk Englund, Andrei Faraon, Nick Stoltz, Pierre Petroff, and Jelena Vuckovic. Controlled phase shifts with a single quantum dot. *Science*, 320(5877):769–772, May 2008.
- [7] Jr. Fleck and M. D. Feit. Beam propagation in uniaxial anisotropic media. *Journal of the Optical Society of America*, 73(7):920–926, July 1983.
- [8] M. M Fejer. *Single crystal fibers: growth dynamics and nonlinear optical interactions*. PhD dissertation, Stanford University, Stanford, CA, 1986.

- [9] Hermann A. Haus. *Waves and fields in optoelectronics*. Prentice-Hall, 1984.
- [10] Salah Obayya. *Computational Photonics*. John Wiley & Sons, June 2011.
- [11] A.B. Fallahkhair, K.S. Li, and T.E. Murphy. Vector finite difference modesolver for anisotropic dielectric waveguides. *Lightwave Technology, Journal of*, 26(11):1423–1431, June 2008.
- [12] Dietrich Marcuse, American Telephone Company, and Telegraph. *Theory of dielectric optical waveguides*. Academic Press, 1991.
- [13] J. A. Armstrong, N. Bloembergen, J. Ducuing, and P. S. Pershan. Interactions between light waves in a nonlinear dielectric. *Physical Review*, 127(6):1918–1939, 1962.
- [14] M. M. Fejer, G.A. Magel, D.H. Jundt, and R. L. Byer. Quasi-phase-matched second harmonic generation: tuning and tolerances. *Quantum Electronics, IEEE Journal of*, 28(11):2631–2654, 1992.
- [15] K. Rustagi, S. Mehendale, and S. Meenakshi. Optical frequency conversion in quasi-phase-matched stacks of nonlinear crystals. *IEEE Journal of Quantum Electronics*, 18(6):1029–1041, June 1982.
- [16] G. G. Luther, M. S. Alber, J. E. Marsden, and J. M. Robbins. Geometric analysis of optical frequency conversion and its control in quadratic nonlinear media. *Journal of the Optical Society of America B*, 17(6):932–941, June 2000.
- [17] Duan Feng, Nai-Ben Ming, Jing-Fen Hong, Yong-Shun Yang, Jin-Song Zhu, Zhen Yang, and Ye-Ning Wang. Enhancement of second-harmonic generation in LiNbO<sub>3</sub> crystals with periodic laminar ferroelectric domains. *Appl. Phys. Lett.*, 37(7):607, 1980.
- [18] A. Feisst and P. Koidl. Current induced periodic ferroelectric domain structures in LiNbO<sub>3</sub> applied for efficient nonlinear optical frequency mixing. *Appl. Phys. Lett.*, 47(11):1125–1127, December 1985.

- [19] Y.S. Luh, R.S. Feigelson, M. M. Fejer, and R. L. Byer. Ferroelectric domain structures in LiNbO<sub>3</sub> single-crystal fibers. *Journal of Crystal Growth*, 78(1):135–143, October 1986.
- [20] E. J. Lim, M. M. Fejer, and R. L. Byer. Second-harmonic generation of green light in periodically poled planar lithium niobate waveguide. *Electronics Letters*, 25(3):174–175, February 1989.
- [21] G. A Magel, M. M Fejer, and R. L Byer. Quasi-phase-matched second-harmonic generation of blue light in periodically poled LiNbO<sub>3</sub>. *Appl. Phys. Lett.*, 56(2):108–110, January 1990.
- [22] L. E. Myers and W. R. Bosenberg. Periodically poled lithium niobate and quasi-phase-matched optical parametric oscillators. *IEEE J. Quantum. Electron.*, 33(10):1663–1672, October 1997.
- [23] Eric Lim, S. Matsumoto, Michael L Bortz, and M. M Fejer. Quasi-phase-matched frequency conversion in lithium niobate and lithium tantalate waveguides. In *Society of Photo-Optical Instrumentation Engineers (SPIE) Conference Series*, volume 1561, pages 135–142, December 1991.
- [24] David Hum. *Frequency conversion in near-stoichiometric lithium tantalate fabricated by vapor transport equilibration*. PhD dissertation, Stanford University, Stanford, CA, 2007.
- [25] L. Gordon, G.L. Woods, R.C. Eckardt, R.R. Route, R.S. Feigelson, M. M. Fejer, and R. Byer. Diffusion-bonded stacked GaAs for quasiphase-matched second-harmonic generation of a carbon dioxide laser. *Electronics Letters*, 29(22):1942–1944, October 1993.
- [26] Gregory David Miller. *Periodically poled lithium niobate: modeling, fabrication, and nonlinear-optical performance*. PhD dissertation, Stanford University, Stanford, CA, 1998.

- [27] Paulina Susan Kuo. *Thick film, orientation-patterned gallium arsenide for nonlinear optical frequency conversion*. PhD dissertation, Stanford University, Stanford, CA, 2008.
- [28] David S. Hum and Martin M. Fejer. Quasi-phasematching. *Comptes Rendus Physique*, 8(2):180–198, March 2007.
- [29] R. Eckardt and J. Reintjes. Phase matching limitations of high efficiency second harmonic generation. *Quantum Electronics, IEEE Journal of*, 20(10):1178–1187, October 1984.
- [30] Ichiro Shoji, Takashi Kondo, Ayako Kitamoto, Masayuki Shirane, and Ryoichi Ito. Absolute scale of second-order nonlinear-optical coefficients. *Journal of the Optical Society of America B*, 14(9):2268–2294, 1997.
- [31] G. I. Stegeman, D. J. Hagan, and L. Torner.  $\chi^{(2)}$  cascading phenomena and their applications to all-optical signal processing, mode-locking, pulse compression and solitons. *Optical and Quantum Electronics*, 28(12):1691–1740, 1996.
- [32] C. Conti, S. Trillo, P. Di Trapani, J. Kilius, A. Bramati, S. Minardi, W. Chianaglia, and G. Valiulis. Effective lensing effects in parametric frequency conversion. *Journal of the Optical Society of America B*, 19(4):852, April 2002.
- [33] John M. Dudley, Gory Genty, and Stphane Coen. Supercontinuum generation in photonic crystal fiber. *Reviews of Modern Physics*, 78(4):1135, October 2006.
- [34] J.H.V. Price, T.M. Monro, H. Ebendorff-Heidepriem, F. Poletti, P. Horak, V. Finazzi, J.Y.Y. Leong, P. Petropoulos, J.C. Flanagan, G. Brambilla, Xian Feng, and D.J. Richardson. Mid-IR supercontinuum generation from nonsilica microstructured optical fibers. *Selected Topics in Quantum Electronics, IEEE Journal of*, 13(3):738–749, June 2007.
- [35] Carsten Langrock, Saurabh Kumar, John E. McGeehan, A. E. Willner, and M. M. Fejer. All-Optical signal processing using  $\chi^{(2)}$  nonlinearities in guided-wave devices. *J. Lightwave Technol.*, 24(7):2579, July 2006.

- [36] X. Yu, L. Scaccabarozzi, Jr. J. S. Harris, P. S. Kuo, and M. M. Fejer. Efficient continuous wave second harmonic generation pumped at  $1.55\ \mu\text{m}$  in quasi-phase-matched AlGaAs waveguides. *Opt. Express*, 13(26):10742–10748, December 2005.
- [37] Matteo Conforti, Fabio Baronio, and Costantino De Angelis. Nonlinear envelope equation for broadband optical pulses in quadratic media. *Physical Review A*, 81(5):053841, May 2010.
- [38] C. R. Phillips, Carsten Langrock, J. S. Pelc, M. M. Fejer, I. Hartl, and Martin E. Fermann. Supercontinuum generation in quasi-phases-matched waveguides. *Opt. Express*, 19(20):18754–18773, 2011.
- [39] M Kolesik and J V Moloney. Nonlinear optical pulse propagation simulation: from maxwell’s to unidirectional equations. *Physical Review. E*, 70:036604, 2004.
- [40] G. Genty, P. Kinsler, B. Kibler, and J. M. Dudley. Nonlinear envelope equation modeling of sub-cycle dynamics and harmonic generation in nonlinear waveguides. *Opt. Express*, 15(9):5382–5387, April 2007.
- [41] S. Wabnitz and V. V. Kozlov. Harmonic and supercontinuum generation in quadratic and cubic nonlinear optical media. *Journal of the Optical Society of America B*, 27(9):1707–1711, 2010.
- [42] Rostislav V. Roussev. *Optical-Frequency Mixers in Periodically Poled Lithium Niobate: Materials, Modeling and Characterization*. PhD dissertation, Stanford University, Stanford, CA, December 2006.
- [43] M.L. Bortz, S.J. Field, M. M. Fejer, D.W. Nam, R.G. Waarts, and D.F. Welch. Noncritical quasi-phase-matched second harmonic generation in an annealed proton-exchanged LiNbO<sub>3</sub> waveguide. *Quantum Electronics, IEEE Journal of*, 30(12):2953–2960, December 1994.

- [44] Xiang Liu, Liejia Qian, and Frank Wise. High-energy pulse compression by use of negative phase shifts produced by the cascade  $\chi^{(2)} : \chi^{(2)}$  nonlinearity. *Opt. Lett.*, 24(23):1777–1779, December 1999.
- [45] Jeffrey Moses and Frank W. Wise. Soliton compression in quadratic media: high-energy few-cycle pulses with a frequency-doubling crystal. *Opt. Lett.*, 31(12):1881–1883, June 2006.
- [46] S. Ashihara, J. Nishina, T. Shimura, and K. Kuroda. Soliton compression of femtosecond pulses in quadratic media. *Journal of the Optical Society of America B*, 19(10):2505–2510, October 2002.
- [47] M. Bache, O. Bang, J. Moses, and F. W. Wise. Nonlocal explanation of stationary and nonstationary regimes in cascaded soliton pulse compression. *Opt. Lett.*, 32(17):2490–2492, 2007.
- [48] Morten Bache and Frank W. Wise. Type-I cascaded quadratic soliton compression in lithium niobate: Compressing femtosecond pulses from high-power fiber lasers. *Physical Review A*, 81(5):053815, May 2010.
- [49] Rick Trebino and Daniel J. Kane. Using phase retrieval to measure the intensity and phase of ultrashort pulses: frequency-resolved optical gating. *J. Opt. Soc. Am. A*, 10(5):1101–1111, May 1993.
- [50] J. P. Gordon. Theory of the soliton self-frequency shift. *Opt. Lett.*, 11(10):662–664, October 1986.
- [51] Mathieu Charbonneau-Lefort, Bedros Afeyan, and M. M. Fejer. Optical parametric amplifiers using chirped quasi-phase-matching gratings I: practical design formulas. *J. Opt. Soc. Am. B*, 25(4):463–480, April 2008.
- [52] C. R. Phillips and M. M. Fejer. Efficiency and phase of optical parametric amplification in chirped quasi-phase-matched gratings. *Opt. Lett.*, 35(18):3093–3095, 2010.

- [53] C. Heese, C. R. Phillips, L. Gallmann, M. M. Fejer, and U. Keller. Ultrabroadband, highly flexible amplifier for ultrashort midinfrared laser pulses based on aperiodically poled Mg:LiNbO<sub>3</sub>. *Opt. Lett.*, 35(14):2340–2342, July 2010.
- [54] R. DeSalvo, A.A. Said, D.J. Hagan, E.W. Van Stryland, and M. Sheik-Bahae. Infrared to ultraviolet measurements of two-photon absorption and  $n_2$  in wide bandgap solids. *Quantum Electronics, IEEE Journal of*, 32(8):1324–1333, August 1996.
- [55] M. Bache, O. Bang, B. B. Zhou, J. Moses, and F. W. Wise. Optical cherenkov radiation in ultrafast cascaded second-harmonic generation. *Physical Review A*, 82(6):063806, December 2010.
- [56] G. Imeshev, M. M. Fejer, A. Galvanauskas, and D. Harter. Pulse shaping by difference-frequency mixing with quasi-phase-matching gratings. *J. Opt. Soc. Am. B*, 18(4):534–539, April 2001.
- [57] A. S. Barker and R. Loudon. Dielectric properties and optical phonons in LiNbO<sub>3</sub>. *Phys. Rev.*, 158(2):433–&, 1967.
- [58] P. Delfyett, R. Dorsinville, and R. Alfano. Spectral and temporal measurements of the third-order nonlinear susceptibility of LiNbO<sub>3</sub> using picosecond raman-induced phase-conjugation spectroscopy. *Physical Review B*, 40(3):1885–1891, July 1989.
- [59] N. Surovtsev, V. Malinovskii, A. Pugachev, and A. Shebanin. The nature of low-frequency raman scattering in congruent melting crystals of lithium niobate. *Physics of the Solid State*, 45(3):534–541, 2003.
- [60] Roland Schiek, Robert Stegeman, and George I. Stegeman. Measurement of Third-Order nonlinear susceptibility tensor elements in lithium niobate. In *Frontiers in Optics*, OSA Technical Digest Series, page JWA74. Optical Society of America, October 2005.

- [61] Dieter H. Jundt. Temperature-dependent Sellmeier equation for the index of refraction,  $n_e$ , in congruent lithium niobate. *Opt. Lett.*, 22(20):1553–1555, October 1997.
- [62] Clemens Heese, Christopher R. Phillips, Nick Hartmann, Lukas Gallmann, M. M. Fejer, and Ursula Keller. High repetition rate, 93-MW mid-infrared optical parametric-chirped pulse amplifier based on apodized aperiodically poled Mg:LiNbO<sub>3</sub>. In *Lasers, Sources, and Related Photonic Devices*, OSA Technical Digest (CD), page AM1A.7. Optical Society of America, January 2012.
- [63] E Palik. *Handbook of optical constants of solids*, volume I. Academic Press, 1985.
- [64] C. R. Phillips, Carsten Langrock, J. S. Pelc, M. M. Fejer, J. Jiang, Martin E. Fermann, and I. Hartl. Supercontinuum generation in quasi-phase-matched LiNbO<sub>3</sub> waveguide pumped by a tm-doped fiber laser system. *Opt. Lett.*, 36(19):3912–3914, October 2011.
- [65] Frithjof Haxsen, Axel Ruehl, Martin Engelbrecht, Dieter Wandt, Uwe Morgner, and Dietmar Kracht. Stretched-pulse operation of a thulium-doped fiber laser. *Opt. Express*, 16(25):20471–20476, December 2008.
- [66] G. Imeshev and M. Fermann. 230-kW peak power femtosecond pulses from a high power tunable source based on amplification in Tm-doped fiber. *Opt. Express*, 13(19):7424–7431, 2005.
- [67] Ming-Hsien Chou. *Optical frequency mixers using three-wave mixing for optical fiber communications*. PhD dissertation, 1999.
- [68] J. R. Schwesyg, C. R. Phillips, K. Ioakeimidi, M. C. C. Kajiyama, M. Falk, D. H. Jundt, K. Buse, and M. M. Fejer. Suppression of mid-infrared light absorption in undoped congruent lithium niobate crystals. *Opt. Lett.*, 35(7):1070–1072, April 2010.

- [69] I. Hartl, G. Imeshev, M. Fermann, C. Langrock, and M. Fejer. Integrated self-referenced frequency-comb laser based on a combination of fiber and waveguide technology. *Opt. Express*, 13(17):6490–6496, August 2005.
- [70] O. Levi, T. J. Pinguet, T. Skauli, L. A. Eyres, K. R. Parameswaran, Jr. J. S. Harris, M. M. Fejer, T. J. Kulp, S. E. Bisson, B. Gerard, E. Lallier, and L. Becouarn. Difference frequency generation of 8- $\mu\text{m}$  radiation in orientation-patterned GaAs. *Opt. Lett.*, 27(23):2091–2093, December 2002.
- [71] Q. Lin, Oskar J. Painter, and Govind P. Agrawal. Nonlinear optical phenomena in silicon waveguides: modeling and applications. *Opt. Express*, 15(25):16604–16644, December 2007.
- [72] Kiminori Mizuuchi, Tomoya Sugita, Kazuhisa Yamamoto, Tatsuo Kawaguchi, Takeshi Yoshino, and Minoru Imaeda. Efficient 340-nm light generation by a ridge-type waveguide in a first-order periodically poled MgO:LiNbO<sub>3</sub>. *Opt. Lett.*, 28(15):1344–1346, 2003.
- [73] Sunao Kurimura, Yuji Kato, Masayuki Maruyama, Yusuke Usui, and Hirochika Nakajima. Quasi-phase-matched adhered ridge waveguide in LiNbO<sub>3</sub>. *Appl. Phys. Lett.*, 89(19):191123, November 2006.
- [74] C. R. Phillips and M. M. Fejer. Stability of the singly resonant optical parametric oscillator. *Journal of the Optical Society of America B*, 27(12):2687–2699, December 2010.
- [75] Steven T. Cundiff and Jun Ye. Colloquium: Femtosecond optical frequency combs. *Reviews of Modern Physics*, 75(1):325–342, March 2003.
- [76] Amnon Yariv. *Quantum Electronics*. Wiley, 1989.
- [77] Florian Adler, Piotr Maslowski, Aleksandra Foltynowicz, Kevin C. Cossel, Travis C. Briles, Ingmar Hartl, and Jun Ye. Mid-infrared fourier transform spectroscopy with a broadband frequency comb. *Opt. Express*, 18(21):21861–21872, October 2010.

- [78] David G. Winters, Philip Schlup, and Randy A. Bartels. Subpicosecond fiber-based soliton-tuned mid-infrared source in the 9.7-14.9  $\mu\text{m}$  wavelength region. *Opt. Lett.*, 35(13):2179–2181, July 2010.
- [79] Tyler W. Neely, Todd A. Johnson, and Scott A. Diddams. High-power broadband laser source tunable from 3.0  $\mu\text{m}$  to 4.4  $\mu\text{m}$  based on a femtosecond yb: fiber oscillator. *Opt. Lett.*, 36(20):4020–4022, October 2011.
- [80] M. J. Angell, R. M. Emerson, J. L. Hoyt, J. F. Gibbons, L. A. Eyres, M. L. Bortz, and M. M. Fejer. Growth of alternating  $\langle 100 \rangle / \langle 111 \rangle$ -oriented II-VI regions for quasi-phase-matched nonlinear optical devices on GaAs substrates. *Appl. Phys. Lett.*, (64):3107, 1994.
- [81] C. Lynch, D.F. Bliss, T. Zens, A. Lin, J.S. Harris, P. S. Kuo, and M. M. Fejer. Growth of mm-thick orientation-patterned GaAs for IR and THZ generation. *Journal of Crystal Growth*, 310(24):5241–5247, December 2008.
- [82] Konstantin L. Vodopyanov, O. Levi, P. S. Kuo, T. J. Pinguet, J. H. Harris, M. M. Fejer, B. Gerard, L. Becouarn, and E. Lallier. Optical parametric oscillation in orientation-patterned GaAs. In *Nonlinear Optics: Materials, Fundamentals and Applications*, page TuA4. Optical Society of America, 2004.
- [83] P. S. Kuo, K. L. Vodopyanov, M. M. Fejer, D. M. Simanovskii, X. Yu, J. S. Harris, D. Bliss, and D. Weyburne. Optical parametric generation of a mid-infrared continuum in orientation-patterned GaAs. *Opt. Lett.*, 31(1):71–73, January 2006.
- [84] Joseph E. Schaar, Konstantin L. Vodopyanov, and M. M. Fejer. Intracavity terahertz generation in a synchronously pumped optical parametric oscillator using Quasi-Phase-matched GaAs. In *Conference on Lasers and Electro-Optics/Quantum Electronics and Laser Science Conference and Photonic Applications Systems Technologies*, page CThI6. Optical Society of America, 2007.

- [85] W. C. Hurlbut, Yun-Shik Lee, K. L. Vodopyanov, P. S. Kuo, and M. M. Fejer. Multiphoton absorption and nonlinear refraction of GaAs in the mid-infrared. *Opt. Lett.*, 32(6):668–670, March 2007.
- [86] Guanshi Qin, Xin Yan, Chihiro Kito, Meisong Liao, Chitrarekha Chaudhari, Takenobu Suzuki, and Yasutake Ohishi. Ultrabroadband supercontinuum generation from ultraviolet to 6.28  $\mu\text{m}$  in a fluoride fiber. *Appl. Phys. Lett.*, 95(16):161103, 2009.
- [87] Joseph Eden Schaar. *Terahertz sources based on intracavity parametric frequency down-conversion using quasi-phase-matched gallium arsenide*. PhD dissertation, Stanford University, Stanford, CA, 2009.
- [88] F. M. Mitschke and L. F. Mollenauer. Discovery of the soliton self-frequency shift. *Opt. Lett.*, 11(10):659–661, Oct 1986.
- [89] Kazi S. Abedin and Fumito Kubota. Widely tunable femtosecond soliton pulse generation at a 10-ghz repetition rate by use of the soliton self-frequency shift in photonic crystal fiber. *Opt. Lett.*, 28(19):1760–1762, Oct 2003.
- [90] Ming-Che Chan, Shih-Hsuan Chia, Tzu-Ming Liu, Tsung-Han Tsai, Min-Chen Ho, A.A. Ivanov, A.M. Zheltikov, Jiun-Yi Liu, Hsiang-Lin Liu, and Chi-Kuang Sun. 1.2- to 2.2- $\mu\text{m}$  tunable raman soliton source based on a cr:forsterite laser and a photonic-crystal fiber. *Photonics Technology Letters, IEEE*, 20(11):900–902, 2008.
- [91] C. Erny, C. Heese, M. Haag, L. Gallmann, and U. Keller. High-repetition-rate optical parametric chirped-pulse amplifier producing 1-J, sub-100-fs pulses in the mid-infrared. *Opt. Express*, 17(3):1340–1345, February 2009.
- [92] A. Shirakawa, I. Sakane, M. Takasaka, and T. Kobayashi. Sub-5-fs visible pulse generation by pulse-front-matched noncollinear optical parametric amplification. *Appl. Phys. Lett.*, 74(16):2268–2270, April 1999.

- [93] Giedrius Andriukaitis, Tadas Balinas, Skirmantas Aliauskas, Audrius Puglys, Andrius Baltuka, Tenio Popmintchev, Ming-Chang Chen, Margaret M. Murnane, and Henry C. Kapteyn. 90 GW peak power few-cycle mid-infrared pulses from an optical parametric amplifier. *Opt. Lett.*, 36(15):2755–2757, 2011.
- [94] Mathieu Charbonneau-Lefort, Bedros Afeyan, and M. M. Fejer. Competing collinear and noncollinear interactions in chirped quasi-phase-matched optical parametric amplifiers. *J. Opt. Soc. Am. B*, 25(9):1402–1413, September 2008.
- [95] L. Gallmann, G. Steinmeyer, U. Keller, G. Imeshev, M. M. Fejer, and J.-P. Meyn. Generation of sub-6-fs blue pulses by frequency doubling with quasi-phase-matching gratings. *Opt. Lett.*, 26(9):614–616, May 2001.
- [96] M. Charbonneau-Lefort, M. M. Fejer, and Bedros Afeyan. Tandem chirped quasi-phase-matching grating optical parametric amplifier design for simultaneous group delay and gain control. *Opt. Lett.*, 30(6):634–636, March 2005.
- [97] Haim Suchowski, Vaibhav Prabhudesai, Dan Oron, Ady Arie, and Yaron Silberberg. Robust adiabatic sum frequency conversion. *Opt. Express*, 17(15):12731–12740, July 2009.
- [98] M. D. Crisp. Adiabatic-Following approximation. *Physical Review A*, 8(4):2128–2135, October 1973.
- [99] K Bergmann, H Theuer, and BW Shore. Coherent population transfer among quantum states of atoms and molecules. *Reviews of Modern Physics*, 70(3):1003–1025, 1998.
- [100] J. R. Kuklinski, U. Gaubatz, F. T. Hioe, and K. Bergmann. Adiabatic population transfer in a three-level system driven by delayed laser pulses. *Physical Review A*, 40(11):6741–6744, December 1989.
- [101] Timo A. Laine and Stig Stenholm. Adiabatic processes in three-level systems. *Physical Review A*, 53(4):2501–2512, April 1996.

- [102] J. M. Manley and H. E. Rowe. General energy relations in nonlinear reactances. *P. I. Radio Eng.*, 47:2115–2116, 1959.
- [103] Jie Huang, X. P. Xie, Carsten Langrock, R. V. Roussev, D. S. Hum, and M. M. Fejer. Amplitude modulation and apodization of quasi-phase-matched interactions. *Opt. Lett.*, 31(5):604–606, March 2006.
- [104] R. B. White. *Asymptotic Analysis of Differential Equations*. World Scientific, 2005.
- [105] Clarence Zener. Non-Adiabatic crossing of energy levels. *Proceedings of the Royal Society of London. Series A*, 137(833):696–702, 1932.
- [106] Jon P Davis and Philip Pechukas. Nonadiabatic transitions induced by a time-dependent hamiltonian in the semiclassical/adiabatic limit: The two-state case. *The Journal of Chemical Physics*, 64(8):3129–3137, April 1976.
- [107] C. R. Phillips and M. M. Fejer. Adiabatic optical parametric oscillators: steady-state and dynamical behavior. *Opt. Express*, 20(3):2466–2482, January 2012.
- [108] Ron Goldman. Curvature formulas for implicit curves and surfaces. *Computer Aided Geometric Design*, 22(7):632–658, October 2005.
- [109] C. E. Carroll and F. T. Hioe. Analytic solutions for three-state systems with overlapping pulses. *Physical Review A*, 42(3):1522–1531, 1990.
- [110] N.V. Vitanov and S. Stenholm. Non-adiabatic effects in population transfer in three-level systems. *Optics Communications*, 127:215–222, June 1996.
- [111] Jie Liu, Libin Fu, Bi-Yiao Ou, Shi-Gang Chen, Dae-Il Choi, Biao Wu, and Qian Niu. Theory of nonlinear Landau-Zener tunneling. *Physical Review A*, 66(2):023404, 2002.
- [112] A. M. Dykhne. Adiabatic perturbation of discrete spectrum states. *Sov. Phys. JETP*, (14):941, 1962.

- [113] S. Witte and K.S.E. Eikema. Ultrafast optical parametric Chirped-Pulse amplification. *Selected Topics in Quantum Electronics, IEEE Journal of*, 18(1):296–307, February 2012.
- [114] A. Dubietis, R. Butkus, and A.P. Piskarskas. Trends in chirped pulse optical parametric amplification. *Selected Topics in Quantum Electronics, IEEE Journal of*, 12(2):163–172, April 2006.
- [115] R. Butkus, R. Danielius, A. Dubietis, A. Piskarskas, and A. Stabinis. Progress in chirped pulse optical parametric amplifiers. *Applied Physics B: Lasers and Optics*, 79(6):693–700, 2004.
- [116] Gunnar Arisholm, Jens Biegert, Philip Schlup, Christoph Hauri, and Ursula Keller. Ultra-broadband chirped-pulse optical parametric amplifier with angularly dispersed beams. *Opt. Express*, 12(3):518–530, February 2004.
- [117] P. Colosimo, G. Doumy, C. I. Blaga, J. Wheeler, C. Hauri, F. Catoire, J. Tate, R. Chirila, A. M. March, G. G. Paulus, H. G. Muller, P. Agostini, and L. F. DiMauro. Scaling strong-field interactions towards the classical limit. *Nature Physics*, 4(5):386–389, March 2008.
- [118] C. Heese, A. E. Oehler, L. Gallmann, and U. Keller. High-energy picosecond Nd:YVO4 slab amplifier for OPCPA pumping. *Applied Physics B*, 103(1):5–8, April 2011.
- [119] P. Russbuedt, T. Mans, J. Weitenberg, H. D. Hoffmann, and R. Poprawe. Compact diode-pumped 1.1 kW Yb:YAG Innoslab femtosecond amplifier. *Opt. Lett.*, 35(24):4169–4171, December 2010.
- [120] Keming Du, Nianle Wu, Jiandong Xu, J. Gieseke, P. Loosen, and R. Poprawe. Partially end-pumped Nd:YAG slab laser with a hybrid resonator. *Opt. Lett.*, 23(5):370–372, March 1998.

- [121] Clemens Heese, Christopher R. Phillips, Lukas Gallmann, M. M. Fejer, and Ursula Keller. High-Power Mid-Infrared optical parametric Chirped-Pulse amplifier based on aperiodically poled Mg:LiNbO<sub>3</sub>. In *CLEO:2011 - Laser Applications to Photonic Applications*, OSA Technical Digest (CD), page CMR5. Optical Society of America, May 2011.
- [122] Clemens Heese, Christopher R. Phillips, Lukas Gallmann, M. M. Fejer, and Ursula Keller. High-power mid-infrared optical parametric chirped-pulse amplifier based on aperiodically poled mg:linbo<sub>3</sub>. In *CLEO/Europe and EQEC 2011 Conference Digest*, OSA Technical Digest (CD), page CF6.1. Optical Society of America, May 2011.
- [123] Clemens Heese, Andreas E. H. Oehler, Lukas Gallmann, and Ursula Keller. 50-MW, 12-ps Nd:YVO<sub>4</sub> slab amplifier for OPCPA pumping. In *CLEO:2011 - Laser Applications to Photonic Applications*, OSA Technical Digest (CD), page CWG4. Optical Society of America, May 2011.
- [124] Clemens Heese, Lukas Gallmann, Ursula Keller, Christopher R. Phillips, and M. M. Fejer. Ultra-Broadband optical parametric Chirped-Pulse amplifier based on aperiodically poled Mg:LiNbO<sub>3</sub> in the Mid-Infrared at high repetition rates. In *Advanced Solid-State Photonics*, OSA Technical Digest Series (CD), page AME4. Optical Society of America, February 2010.
- [125] Clemens Heese, Lukas Gallmann, Ursula Keller, Christopher Richard. Phillips, and M. Fejer. Ultra-Broadband optical parametric Chirped-Pulse amplifier based on aperiodically poled Mg:LiNbO<sub>3</sub> in the Mid-Infrared. In *Conference on Lasers and Electro-Optics*, OSA Technical Digest (CD), page CWH3. Optical Society of America, May 2010.
- [126] Clemens Heese, Christopher R. Phillips, Lukas Gallmann, M. M. Fejer, and Ursula Keller. Ultrabroadband optical parametric Chirped-Pulse amplifier in the Mid-Infrared using aperiodically poled Mg:LiNbO. In *International Conference on Ultrafast Phenomena*, page TuE27. Optical Society of America, 2010.

- [127] M. Grant and S. Boyd. *CVX: Matlab Software for Disciplined Convex Programming, version 1.21*. April 2011.
- [128] M. Grant and S. Boyd. Graph implementations for nonsmooth convex programs. In V. Blondel, S. Boyd, and H. Kimura, editors, *Recent Advances in Learning and Control*, Lecture Notes in Control and Information Sciences, pages 95–110. Springer-Verlag Limited, 2008. <http://stanford.edu/boyd/graph.dcp.html>.
- [129] Carsten Langrock, Eleni Diamanti, Rostislav V. Roussev, Yoshihisa Yamamoto, M. M. Fejer, and Hiroki Takesue. Highly efficient Single-Photon detection at communication wavelengths using upconversion in reverse proton exchanged PPLN waveguides. In *Conference on Lasers and Electro-Optics/Quantum Electronics and Laser Science and Photonic Applications Systems Technologies*, page QThJ1. Optical Society of America, 2005.
- [130] Jason S. Pelc, Carsten Langrock, Qiang Zhang, and M. M. Fejer. Efficient Down-Conversion of single photons for quantum communication. In *Nonlinear Optics: Materials, Fundamentals and Applications*, page NTuB1. Optical Society of America, 2009.
- [131] J. S. Pelc, C. Langrock, Q. Zhang, and M. M. Fejer. Influence of domain disorder on parametric noise in quasi-phase-matched quantum frequency converters. *Opt. Lett.*, 35(16):2804–2806, 2010.
- [132] Jason S. Pelc, Chris R. Phillips, Carsten Langrock, Derek Chang, and M. M. Fejer. White phasematching noise: Random Duty-Cycle errors in Quasi-Phase-Matching devices. In *Conference on Lasers and Electro-Optics*, OSA Technical Digest (CD), page CThEE6. Optical Society of America, May 2010.
- [133] J. S. Pelc, C. R. Phillips, D. Chang, C. Langrock, and M. M. Fejer. Efficiency pedestal in quasi-phase-matching devices with random duty-cycle errors. *Opt. Lett.*, 36(6):864–866, March 2011.
- [134] J. S. Pelc, L. Ma, C. R. Phillips, Q. Zhang, C. Langrock, O. Slattery, X. Tang, and M. M. Fejer. Long-wavelength-pumped upconversion single-photon detector

- at 1550 nm: performance and noise analysis. *Opt. Express*, 19(22):21445–21456, October 2011.
- [135] Jason Pelc, Christopher R. Phillips, Carsten Langrock, Qiang Zhang, Lijun Ma, Oliver Slattery, Xiao Tang, and M. M. Fejer. Single-Photon detection at 1550 nm via upconversion using a tunable Long-Wavelength pump source. In *CLEO:2011 - Laser Applications to Photonic Applications*, OSA Technical Digest (CD), page CMC4. Optical Society of America, May 2011.
- [136] J. S. Pelc, Q. Zhang, C. R. Phillips, L. Yu, Y. Yamamoto, and M. M. Fejer. Cascaded frequency upconversion for high-speed single-photon detection at 1550nm. *Opt. Lett.*, 37(4):476–478, February 2012.
- [137] O. Gayer, Z. Sacks, E. Galun, and A. Arie. Temperature and wavelength dependent refractive index equations for MgO-doped congruent and stoichiometric LiNbO<sub>3</sub>. *Appl. Phys. B: Lasers Opt.*, 91(2):343–348, 2008.
- [138] Mathieu Charbonneau-Lefort, Bedros Afeyan, and M. M. Fejer. Theory and simulation of gain-guided noncollinear modes in chirped quasi-phase-matched optical parametric amplifiers. *J. Opt. Soc. Am. B*, 27(4):824–841, April 2010.
- [139] Anthony E. Siegman. *Lasers*. University Science Books, 1St edition edition, May 1986.
- [140] Anthony E. Siegman. New developments in laser resonators. volume 1224, pages 2–14. SPIE, 1990.
- [141] C. R. Phillips, J. Jiang, A. C. Lin, C. Langrock, M. Snure, D. Bliss, M. Zhu, I. Hartl, J. S. Harris, M. E. Fermann, and M. M. Fejer. Tunable Mid-Infrared source based on difference frequency generation of a femtosecond tm-fiber system in orientation patterned GaAs. In *Conference on Lasers and Electro-Optics*, page CF3B.2. Optical Society of America, 2012.
- [142] C. R. Phillips, J. S. Pelc, and M. M. Fejer. Continuous wave monolithic quasi-phase-matched optical parametric oscillator in periodically poled lithium niobate. *Opt. Lett.*, 36(15):2973–2975, 2011.

- [143] C R. Phillips, J S. Pelc, and M M. Fejer. Monolithic Continuous-Wave optical parametric ring oscillator in periodically poled lithium niobate. In *Frontiers in Optics*, page PDPB7. Optical Society of America, 2010.
- [144] Chris R. Phillips, M. M. Fejer, Clemens Heese, Lukas Gallmann, and Ursula Keller. Aperiodic Quasi-Phase-Matched gratings for efficient and broadband optical parametric chirped pulse amplification. In *Conference on Lasers and Electro-Optics*, OSA Technical Digest (CD), page CTuGG4. Optical Society of America, May 2010.
- [145] Christopher R. Phillips and M. M. Fejer. Modulation instability of continuous wave optical parametric oscillators. In *CLEO:2011 - Laser Applications to Photonic Applications*, OSA Technical Digest (CD), page CTuK1. Optical Society of America, May 2011.
- [146] Christopher R. Phillips, Jie Jiang, Carsten Langrock, M. M. Fejer, and Martin E. Fermann. Self-Referenced frequency comb from a tm-fiber amplifier via PPLN waveguide supercontinuum generation. In *CLEO:2011 - Laser Applications to Photonic Applications*, OSA Technical Digest (CD), page PDPA5. Optical Society of America, May 2011.
- [147] Christopher R. Phillips, Jie Jiang, Carsten Langrock, Ingmar Hartl, M. M. Fejer, and Martin Fermann. Self frequency shift near  $2 \mu\text{m}$  in periodically poled lithium niobate waveguides. In *CLEO/Europe and EQEC 2011 Conference Digest*, OSA Technical Digest (CD), page CF6-4. Optical Society of America, May 2011.
- [148] Christopher R. Phillips, Carsten Langrock, M. M. Fejer, Jie Jiang, Ingmar Hartl, and Martin E. Fermann. Supercontinuum generation near  $2 \mu\text{m}$  in periodically poled lithium niobate waveguides. In *CLEO:2011 - Laser Applications to Photonic Applications*, OSA Technical Digest (CD), page CTuQ2. Optical Society of America, May 2011.

- [149] Christopher R. Phillips, Carsten Langrock, M. M. Fejer, Jie Jiang, Ingmar Hartl, and Martin E. Fermann. Supercontinuum generation near  $2 \mu\text{m}$  in periodically poled lithium niobate waveguides. In *CLEO:2011 - Laser Applications to Photonic Applications*, page CTuQ2. Optical Society of America, 2011.
- [150] K. Ioakeimidi, Judith R. Schwesyg, Chris R. Phillips, Konstantin L. Vodopyanov, and M. M. Fejer. Singly resonant CW Mid-IR optical parametric oscillator pumped by a tunable C-Band source for free space coherent optical communications. In *Conference on Lasers and Electro-Optics*, OSA Technical Digest (CD), page CThH1. Optical Society of America, May 2010.
- [151] Judith R. Schwesyg, Matthias Falk, Chris R. Phillips, Dieter H. Jundt, Karsten Buse, and M. M. Fejer. Pyroelectrically induced photorefractive damage in magnesium-doped lithium niobate crystals. *Journal of the Optical Society of America B*, 28(8):1973–1987, 2011.
- [152] Judith R. Schwesyg, M. M. Fejer, Matthias Falk, Carsten Langrock, Roger K. Route, Chris R. Phillips, Maria Claudia C. Kajiyama, Dieter H. Jundt, and Karsten Buse. Light absorption and pyroelectrically induced optical damage in nominally undoped and Magnesium-Doped lithium niobate crystals. In *Advances in Optical Materials*, OSA Technical Digest (CD), page AWC2. Optical Society of America, October 2009.
- [153] Minoru Taya, Matthew C. Bashaw, and M. M. Fejer. Photorefractive effects in periodically poled ferroelectrics. *Opt. Lett.*, 21(12):857–859, June 1996.
- [154] L. B. Kreuzer. Single and multimode oscillation of the singly resonant optical parametric oscillator. *Proceedings of the Joint Conference on Lasers and Opto-Electronics*, pages 52–63, 1969.